

DEPARTAMENTO DE ASTROFÍSICA

Universidad de La Laguna

*Using CMB, LSS and Galaxy Clusters as
Cosmological Probes*

Memoria que presenta
D. Denis Tramonte
para optar al grado de Doctor
por la Universidad de La Laguna.



INSTITUTO DE ASTROFÍSICA DE CANARIAS
junio de 2017

Este documento incorpora firma electrónica, y es copia auténtica de un documento electrónico archivado por la ULL según la Ley 39/2015.
Su autenticidad puede ser contrastada en la siguiente dirección <https://sede.ull.es/validacion/>

Identificador del documento: 973742

Código de verificación: Jfg6xBh0

Firmado por: DENIS TRAMONTE UNIVERSIDAD DE LA LAGUNA	Fecha: 30/06/2017 15:10:10
RAFAEL DELFIN BARRENA DELGADO UNIVERSIDAD DE LA LAGUNA	30/06/2017 15:21:31
JOSE ALBERTO RUBIÑO MARTIN UNIVERSIDAD DE LA LAGUNA	30/06/2017 15:34:17
ERNESTO PEREDA DE PABLO UNIVERSIDAD DE LA LAGUNA	06/07/2017 13:51:19

Examination date: July 28, 2017

Thesis supervisors: Dr. José Alberto Rubiño Martín, Rafael Barrena Delgado

© Denis Tramonte 2017

Este documento incorpora firma electrónica, y es copia auténtica de un documento electrónico archivado por la ULL según la Ley 39/2015.
Su autenticidad puede ser contrastada en la siguiente dirección <https://sede.ull.es/validacion/>

Identificador del documento: 973742

Código de verificación: Jfg6xBh0

Firmado por: DENIS TRAMONTE
UNIVERSIDAD DE LA LAGUNA

Fecha: 30/06/2017 15:10:10

RAFAEL DELFIN BARRENA DELGADO
UNIVERSIDAD DE LA LAGUNA

30/06/2017 15:21:31

JOSE ALBERTO RUBIÑO MARTIN
UNIVERSIDAD DE LA LAGUNA

30/06/2017 15:34:17

ERNESTO PEREDA DE PABLO
UNIVERSIDAD DE LA LAGUNA

06/07/2017 13:51:19

*Ai miei genitori,
a Glenda e a Damiano.*

Este documento incorpora firma electrónica, y es copia auténtica de un documento electrónico archivado por la ULL según la Ley 39/2015.
Su autenticidad puede ser contrastada en la siguiente dirección <https://sede.ull.es/validacion/>

Identificador del documento: 973742

Código de verificación: Jfg6xBh0

Firmado por: DENIS TRAMONTE <i>UNIVERSIDAD DE LA LAGUNA</i>	Fecha: 30/06/2017 15:10:10
RAFAEL DELFIN BARRENA DELGADO <i>UNIVERSIDAD DE LA LAGUNA</i>	30/06/2017 15:21:31
JOSE ALBERTO RUBIÑO MARTIN <i>UNIVERSIDAD DE LA LAGUNA</i>	30/06/2017 15:34:17
ERNESTO PEREDA DE PABLO <i>UNIVERSIDAD DE LA LAGUNA</i>	06/07/2017 13:51:19

Este documento incorpora firma electrónica, y es copia auténtica de un documento electrónico archivado por la ULL según la Ley 39/2015.
Su autenticidad puede ser contrastada en la siguiente dirección <https://sede.ull.es/validacion/>

Identificador del documento: 973742

Código de verificación: Jfg6xBh0

Firmado por: DENIS TRAMONTE UNIVERSIDAD DE LA LAGUNA	Fecha: 30/06/2017 15:10:10
RAFAEL DELFIN BARRENA DELGADO UNIVERSIDAD DE LA LAGUNA	30/06/2017 15:21:31
JOSE ALBERTO RUBIÑO MARTIN UNIVERSIDAD DE LA LAGUNA	30/06/2017 15:34:17
ERNESTO PEREDA DE PABLO UNIVERSIDAD DE LA LAGUNA	06/07/2017 13:51:19

Resumen

En esta tesis hemos estudiado tres herramientas independientes para obtener información sobre parámetros cosmológicos: la estructura a gran escala de la materia en el Universo (LSS), los cúmulos de galaxias y el fondo cósmico de microondas (CMB).

En el estudio de la LSS hemos proporcionado una parametrización para la función de masa condicional (CMF), es decir, la distribución en masa de la abundancia de halos en regiones sobredensas y subdensas. Hemos considerado un formalismo ya descrito en la literatura e introducido un parámetro adicional para asegurar la normalización de la CMF. Hemos comparado la abundancia de halos predicha por esta CMF con la predicción de simulaciones numéricas de N-cuerpos, para condiciones con radio Euleriano de 5 a $30 h^{-1}$ Mpc, y para halos de masa entre 10^{11} y $10^{14} h^{-1} M_{\odot}$. Con la parametrización propuesta hemos encontrado un acuerdo excelente con las abundancias simuladas en regiones subdensas para todo el rango de escalas explorado, y en regiones sobredensas para escalas grandes. Finalmente, hemos presentado un ajuste analítico para la función de sesgo de halos en regiones subdensas, que puede ser de interés para acelerar el cálculo de la abundancia de halos a la hora de estudiar la estadística de los vacíos. Este ajuste es capaz de reproducir el sesgo de halos con un error menor del 2% para la cosmología de referencia, y menor del 9% para distintos valores del desplazamiento al rojo y de σ_8 .

En lo que respecta a la cosmología con cúmulos de galaxias, hemos considerado la abundancia de cúmulos en función del desplazamiento al rojo como una herramienta para restringir los parámetros cosmológicos Ω_m y σ_8 . Hemos implementado el cálculo de la distribución en desplazamiento al rojo de los cúmulos dependiendo de la cosmología, y hemos desarrollado una herramienta estadística basada en un método de cadenas de Markov Monte Carlo (MCMC) para recuperar los parámetros cosmológicos dada la abundancia de cúmulos. Hemos aplicado nuestro código al subconjunto cosmológico del catálogo PSZ1 de cúmulos detectados por el satélite *Planck* con señal a ruido mayor que siete. Hemos obtenido estimaciones de Ω_m y σ_8 basadas en la abundancia de cúmulos en combinación con estudios de la nucleosíntesis primordial del *Big Bang* (BBN) y de las oscilaciones acústicas de bariones (BAO), considerando el sesgo en la estimación de la masa de cúmulos b como un parámetro fijo o libre. Fijando el sesgo en $b = 0.2$, hemos encontrado $\Omega_m = 0.293 \pm 0.020$ y $\sigma_8 = 0.760^{+0.018}_{-0.017}$ (68% C.L.). Dejando el sesgo b como un parámetro libre, con un *prior* plano definido por el intervalo $[0, 0.3]$, hemos obtenido $\Omega_m = 0.289^{+0.022}_{-0.020}$ y $\sigma_8 = 0.750 \pm 0.028$. Estos resultados están en muy buen acuerdo con los obtenidos por la colaboración Planck a partir del mismo catálogo de cúmulos. Esto demuestra la

Este documento incorpora firma electrónica, y es copia auténtica de un documento electrónico archivado por la ULL según la Ley 39/2015.
Su autenticidad puede ser contrastada en la siguiente dirección <https://sede.ull.es/validacion/>

Identificador del documento: 973742

Código de verificación: Jfg6xBh0

Fecha: 30/06/2017 15:10:10

Firmado por: DENIS TRAMONTE UNIVERSIDAD DE LA LAGUNA	30/06/2017 15:21:31
RAFAEL DELFIN BARRENA DELGADO UNIVERSIDAD DE LA LAGUNA	30/06/2017 15:34:17
JOSE ALBERTO RUBIÑO MARTIN UNIVERSIDAD DE LA LAGUNA	06/07/2017 13:51:19
ERNESTO PEREDA DE PABLO UNIVERSIDAD DE LA LAGUNA	

fiableidad de nuestro método, que por lo tanto podría ser aplicado en el futuro a catálogos más amplios, lo que permitirá reducir significativamente las barras de error en las estimaciones de estos parámetros. Un ejemplo es el subconjunto cosmológico extendido del PSZ1, que contiene alrededor de tres veces el número de cúmulos utilizados para el análisis en este trabajo, y que estará pronto disponible al público.

Por otro lado, hemos explotado el efecto Sunyaev-Zel'dovich como una herramienta cosmológica. Para ello hemos calculado la función de distribución de probabilidad en una dimensión (PDF) del parámetro de Compton y medido por el satélite *Planck* en todo el cielo, la cual es fuertemente dependiente del parámetro σ_8 . Hemos modelado la contribución de los cúmulos de galaxias a la PDF y testeado nuestro formalismo con mapas simulados del parámetro de Compton. Hemos aplicado este formalismo para ajustar el valor de σ_8 , comparando su predicción con la PDF extraída de los datos de *Planck*. Hemos considerado solo valores $y \gtrsim 4.5 \times 10^{-6}$ para excluir contaminaciones de ruido instrumental y otras contribuciones astrofísicas, y hemos obtenido la estimación final $\sigma_8 = 0.77 \pm 0.02$ (68% C.L.). Este resultado es compatible con otras estimaciones basadas en cúmulos, y está en tensión con el valor obtenido con el análisis del CMB (~ 0.83). Esta tensión puede ser debida a efectos sistemáticos en el modelado o en la calibración instrumental, o puede ser la primera pista para una necesaria extensión del modelo cosmológico estándar.

Los estudios relacionados con CMB presentados en esta tesis se basan en el experimento QUIJOTE, y en los datos obtenidos con el instrumento multifrecuencia (MFI). Hemos llevado a cabo la calibración del apuntado del primer telescopio de QUIJOTE, desarrollando un conjunto de transformaciones de coordenadas para corregir las imperfecciones del telescopio. Estas transformaciones se han implementado en el paquete de reducción de datos del MFI, y son utilizadas diariamente para alcanzar una corrección al apuntado con errores por debajo de 1 minuto de arco. Hemos considerados observaciones del MFI en las regiones galácticas W49, W51 (nubes moleculares) e IC443 (remanente de supernova), y valorado la contribución relativa de diferentes mecanismos de emisión. En particular, hemos detectado indicios de emisión anómala de microondas (AME) en intensidad en todas las regiones, con una detección más robusta en W49. Hemos detectado emisión sincrotrón en W49 e IC443. Esta información es relevante para modelar las propiedades del sincrotrón en nuestra Galaxia, y así facilitar la separación de la señal cosmológica de modos B en los datos futuros de éste y otros experimentos.

Este documento incorpora firma electrónica, y es copia auténtica de un documento electrónico archivado por la ULL según la Ley 39/2015.
Su autenticidad puede ser contrastada en la siguiente dirección <https://sede.ull.es/validacion/>

Identificador del documento:	973742	Código de verificación:	Jfg6xBh0
Firmado por:	DENIS TRAMONTE UNIVERSIDAD DE LA LAGUNA	Fecha:	30/06/2017 15:10:10
	RAFAEL DELFIN BARRENA DELGADO UNIVERSIDAD DE LA LAGUNA		30/06/2017 15:21:31
	JOSE ALBERTO RUBIÑO MARTIN UNIVERSIDAD DE LA LAGUNA		30/06/2017 15:34:17
	ERNESTO PEREDA DE PABLO UNIVERSIDAD DE LA LAGUNA		06/07/2017 13:51:19

Summary

In this thesis we have studied three independent tools to get information on cosmological parameters: the large scale structure (LSS) of matter in the Universe, galaxy clusters and the cosmic microwave background (CMB).

In the study of the LSS we have provided an analytical recipe for computing the conditional mass function (CMF), i.e. the mass distribution of the halo abundance in overdense and underdense regions. We have considered a formalism already discussed in the literature and introduced an additional parameter to ensure the CMF normalisation. We have compared the predicted halo abundance from this CMF recipe with the one obtained from numerical N-body simulations, for conditions with Eulerian radii from 5 to $30 h^{-1}$ Mpc, and for halo masses between 10^{11} and $10^{14} h^{-1} M_{\odot}$. We have found excellent agreement with simulated abundances in underdense regions at all scales, and in overdense regions at large scales; we have also confirmed that the CMF normalisation is satisfied at all scales. We have finally presented an analytical fit to the matter-to-halo bias function in underdense regions, which could be of special interest to speed-up the computation of the halo abundance when studying void statistics. This fit is capable of reproducing the computed halo bias with an error below 2% for the reference cosmology, and below 9% when considering different values of redshift and σ_8 .

With respect to the cosmology with galaxy clusters, we have considered the abundance of clusters as a function of redshift as a tool to estimate the cosmological parameters Ω_m and σ_8 . We have implemented the computation of the cluster redshift distribution according to a specified cosmology, and developed a statistical tool based on a Markov Chains Monte Carlo (MCMC) method to retrieve the cosmological parameters starting from the cluster abundance. We have applied our code to the cosmological subsample of the PSZ1 catalogue of clusters detected by the *Planck* satellite with signal-to-noise ratio above seven. We have obtained estimates of Ω_m and σ_8 based on the cluster abundance in combination with BBN and BAO likelihoods, considering the bias b in the determination of the cluster mass as a fixed or free parameter. With the bias parameter fixed to the value $b = 0.2$ we found $\Omega_m = 0.293 \pm 0.020$ and $\sigma_8 = 0.760^{+0.018}_{-0.017}$ (68% C.L.). With b free to vary with a flat prior in the range [0.0, 0.3] we found $\Omega_m = 0.289^{+0.022}_{-0.020}$ and $\sigma_8 = 0.750 \pm 0.028$. These results are in very good agreement with the ones obtained by the Planck Collaboration using the same cluster catalogue. This proves the reliability of our method, that can therefore be applied in the future to broader catalogues, resulting in a significant reduction of the error bars in the estimation of these parameters. An example is the extended cosmological subsample of the PSZ1, that contains

Este documento incorpora firma electrónica, y es copia auténtica de un documento electrónico archivado por la ULL según la Ley 39/2015.
Su autenticidad puede ser contrastada en la siguiente dirección <https://sede.ull.es/validacion/>

Identificador del documento:	973742	Código de verificación:	Jfg6xBh0
Firmado por:	DENIS TRAMONTE UNIVERSIDAD DE LA LAGUNA	Fecha:	30/06/2017 15:10:10
	RAFAEL DELFIN BARRENA DELGADO UNIVERSIDAD DE LA LAGUNA		30/06/2017 15:21:31
	JOSE ALBERTO RUBIÑO MARTIN UNIVERSIDAD DE LA LAGUNA		30/06/2017 15:34:17
	ERNESTO PEREDA DE PABLO UNIVERSIDAD DE LA LAGUNA		06/07/2017 13:51:19

nearly three times the number of clusters employed for the analysis in this work and that will soon be made publicly available.

We have employed the Sunyaev-Zel'dovich effect as a cosmological probe. To this aim we computed the one dimensional probability distribution function (PDF) of the Compton parameter y measured by the *Planck* satellite over the whole sky; this PDF is strongly dependent on the parameter σ_8 . We have modelled the galaxy cluster contribution to the PDF and tested our formalism with simulated Compton parameter maps. We have applied this formalism to fit for σ_8 against the PDF extracted by *Planck* data. We have considered only values for $y \gtrsim 4.5 \times 10^{-6}$ in order to leave out contamination from instrumental noise and other astrophysical foregrounds, and obtained the final estimate $\sigma_8 = 0.77 \pm 0.02$ (68% C.L.). This result is compatible with other cluster-based estimates, and shows a tension with the value obtained from CMB analysis (~ 0.83). This tension may be due to systematics in the modelling or instrumental calibration or it can be the first hint for a necessary extension of the standard cosmological model.

The study related to the CMB presented in this thesis is based on the QUIJOTE experiment, and on the data obtained with the multi-frequency instrument (MFI). We have carried out the pointing calibration of the first QUIJOTE telescope, developing a set of coordinate transformations to correct for the telescope non-idealities: these transformations have been implemented in the MFI data reduction pipeline and are routinely employed to achieve a pointing correction with errors below 1 minute of arc. We have considered observations of the MFI in the galactic regions W49, W51 (molecular clouds) and IC443 (supernova remnant), and assessed the relative contribution of different emission mechanisms. In particular, we have found hints of detection of anomalous microwave emission (AME) in intensity in all regions, with a higher significance in W49. We have also detected synchrotron emission in the regions W49 and IC443. This information is relevant for modelling the synchrotron emission properties in our Galaxy, and this way making the separation of the cosmological B-modes signal easier in future data from this and other experiments.

Este documento incorpora firma electrónica, y es copia auténtica de un documento electrónico archivado por la ULL según la Ley 39/2015. Su autenticidad puede ser contrastada en la siguiente dirección https://sede.ull.es/validacion/	
--	--

Identificador del documento: 973742

Código de verificación: Jfg6xBh0

Fecha: 30/06/2017 15:10:10

Firmado por: DENIS TRAMONTE UNIVERSIDAD DE LA LAGUNA

RAFAEL DELFIN BARRENA DELGADO UNIVERSIDAD DE LA LAGUNA

30/06/2017 15:21:31

JOSE ALBERTO RUBIÑO MARTIN UNIVERSIDAD DE LA LAGUNA
--

30/06/2017 15:34:17

ERNESTO PEREDA DE PABLO UNIVERSIDAD DE LA LAGUNA

06/07/2017 13:51:19

Contents

1	Introduction: cosmological parameters, observables and probes	1
1.1	The homogeneous Universe	1
1.1.1	Cosmic inventory	2
1.1.2	Dynamics	4
1.1.3	Density parameters	4
1.1.4	Redshift evolution	6
1.1.5	The Λ CDM model	7
1.2	Large Scale Structure	9
1.2.1	Statistics of perturbations	10
1.2.2	Primordial perturbations	11
1.2.3	Evolution of perturbations	13
1.2.4	Mapping the Large Scale Structure	14
1.3	The Cosmic Microwave Background	16
1.3.1	CMB anisotropies	17
1.3.2	Cosmological interpretation of the angular power spectrum	20
1.3.3	CMB polarisation	22
1.3.4	Observing the CMB	25
1.4	Clusters of galaxies	33
1.4.1	Clusters in optical light	35
1.4.2	Clusters in X-rays	37
1.4.3	Clusters in radio waves	40
1.4.4	Clusters and gravitational lensing	45
1.4.5	Cosmology with galaxy clusters	46
1.5	Objectives of this work	47
2	The conditional mass function of dark matter halos	49
2.1	The unconditional mass function	50
2.1.1	The Press-Schechter formalism	50

2.1.2	Extensions to the Press-Schechter formalism	52
2.2	The conditional mass function	56
2.2.1	Formalism for the CMF	57
2.2.2	The standard rescaling	58
2.2.3	The local rescaling	59
2.2.4	Examples and comparisons	61
2.3	Mass function normalisation	64
2.4	Test of CMF against numerical simulations	68
2.4.1	The simulations set	68
2.4.2	Testing the UMF	69
2.4.3	Methodology for CMF tests	71
2.4.4	Testing CMF normalisation	75
2.4.5	Testing the CMF in overdense/underdense regions	77
2.5	A fitting formula for the CMF in underdense regions	82
2.6	An alternative approach: rescaling cosmology	86
2.6.1	Defining a local cosmology	86
2.6.2	Application to the mass function	89
2.7	Conclusions	92
3	Cosmology with cluster number counts	95
3.1	Predicting the output of a cluster survey	95
3.1.1	Mass function	96
3.1.2	Comoving volume element	96
3.1.3	Survey selection function	98
3.1.4	Survey simulation	101
3.1.5	Sample bias	103
3.2	Cosmological constraints with cluster abundance	104
3.2.1	Cluster-based likelihood	104
3.2.2	Monte Carlo Markov Chains	105
3.2.3	Results	108
3.2.4	Effect of threshold mass	111
3.3	Application to <i>Planck</i> data	111
3.3.1	<i>Planck</i> SZ catalogues	112
3.3.2	<i>Planck</i> scaling relations	113
3.3.3	<i>Planck</i> selection function	117
3.3.4	<i>Planck</i> cluster survey prediction	117
3.3.5	Parameter estimation with <i>Planck</i> data	120
3.4	Validation of cluster detections	123
3.4.1	Results and future works	125
3.5	Conclusions	126

Este documento incorpora firma electrónica, y es copia auténtica de un documento electrónico archivado por la ULL según la Ley 39/2015.
Su autenticidad puede ser contrastada en la siguiente dirección <https://sede.ull.es/validacion/>

Identificador del documento: 973742	Código de verificación: Jfg6xBh0	Fecha: 30/06/2017 15:10:10
Firmado por: DENIS TRAMONTE UNIVERSIDAD DE LA LAGUNA		
RAFAEL DELFIN BARRENA DELGADO UNIVERSIDAD DE LA LAGUNA		30/06/2017 15:21:31
JOSE ALBERTO RUBIÑO MARTIN UNIVERSIDAD DE LA LAGUNA		30/06/2017 15:34:17
ERNESTO PEREDA DE PABLO UNIVERSIDAD DE LA LAGUNA		06/07/2017 13:51:19

4 Cosmology with the Sunyaev-Zel'dovich effect	131
4.1 The y map	131
4.1.1 The Compton parameter	132
4.1.2 <i>Planck</i> data	132
4.2 The SZ 1D PDF	134
4.2.1 The $P(y)$ from <i>Planck</i> data	134
4.2.2 Physical meaning of the $P(y)$	135
4.2.3 The $P(y)$ as a cosmological tool	137
4.3 Computing the PDF	138
4.3.1 Cluster pressure profile	139
4.3.2 Compton parameter profile and beam smoothing	141
4.3.3 Cluster contribution to the y map	143
4.3.4 Modelling the noise contribution	146
4.4 Testing the formalism	150
4.4.1 Pure cluster tSZ map	150
4.4.2 Including instrumental effects	153
4.4.3 Comparison with predicted PDF	154
4.5 Application to <i>Planck</i> data	156
4.5.1 Methodology	157
4.5.2 Results	158
4.6 Forecasts for the COrE mission	161
4.6.1 The mission	161
4.6.2 Simulated data	161
4.6.3 Results	162
4.7 Conclusions	163
5 The QUIJOTE Experiment	167
5.1 Project overview	167
5.1.1 Scientific goals	171
5.1.2 The Multi Frequency Instrument	174
5.2 Instrumental calibration: the pointing model	177
5.2.1 Formalism for pointing correction	178
5.2.2 Modelling the telescope pointing errors	180
5.2.3 Parameter estimation	189
5.2.4 Conclusions about QUIJOTE pointing model	200
5.3 Study of Galactic foreground emissions with the MFI	201
5.3.1 Galactic regions	201
5.3.2 Data selection	204
5.3.3 Gain calibration	205
5.3.4 Map-making	206

Este documento incorpora firma electrónica, y es copia auténtica de un documento electrónico archivado por la ULL según la Ley 39/2015.
Su autenticidad puede ser contrastada en la siguiente dirección <https://sede.ull.es/validacion/>

Identificador del documento: 973742

Código de verificación: Jfg6xBh0

Fecha: 30/06/2017 15:10:10

Firmado por: DENIS TRAMONTE UNIVERSIDAD DE LA LAGUNA	30/06/2017 15:21:31
RAFAEL DELFIN BARRENA DELGADO UNIVERSIDAD DE LA LAGUNA	30/06/2017 15:34:17
JOSE ALBERTO RUBIÑO MARTIN UNIVERSIDAD DE LA LAGUNA	06/07/2017 13:51:19
ERNESTO PEREDA DE PABLO UNIVERSIDAD DE LA LAGUNA	

5.3.5	Flux extraction	213
5.3.6	Spectral Energy Distributions	216
5.3.7	Multicomponent fit of the intensity SEDs	219
5.3.8	Summary of this analysis	220
6	Conclusions	223
A	Fitting tables and procedures for the halo bias	229
B	Pointing correction for non-perpendicularities	237
	Bibliography	257

Este documento incorpora firma electrónica, y es copia auténtica de un documento electrónico archivado por la ULL según la Ley 39/2015.
Su autenticidad puede ser contrastada en la siguiente dirección <https://sede.ull.es/validacion/>

Identificador del documento: 973742	Código de verificación: Jfg6xBh0
Firmado por: DENIS TRAMONTE UNIVERSIDAD DE LA LAGUNA	Fecha: 30/06/2017 15:10:10
RAFAEL DELFIN BARRENA DELGADO UNIVERSIDAD DE LA LAGUNA	30/06/2017 15:21:31
JOSE ALBERTO RUBIÑO MARTIN UNIVERSIDAD DE LA LAGUNA	30/06/2017 15:34:17
ERNESTO PEREDA DE PABLO UNIVERSIDAD DE LA LAGUNA	06/07/2017 13:51:19

1

Introduction: cosmological parameters, observables and probes

The birth of cosmology as a science can be dated back to the establishment of the theory of General Relativity in the early 1920s. Theoretical works on the subject were benefitted by the continuous improvement in astrophysical observations. However, it was only in the last two decades that the sensitivity achievable by experiments upgraded cosmology to the status of a precision science. The increasing amount of available data contributed to rule out many theoretical proposals, leading to the establishment of a widely accepted standard cosmological model; nowadays, much of the effort in cosmology is dedicated to the improvement of the precision in the estimation of the parameters that define this model. There are still open issues, though, which require even more sensitive observations. With the increasing volume of data that beat down statistical errors, the control of systematics, both in the acquisition and reduction of observational data, and in the underlying theoretical modelling, becomes crucially important to avoid biases in the final parameter estimation.

We dedicate this chapter to a review of the theoretical and experimental frameworks of modern cosmology. We outline the most important parameters that are used to define a cosmological model, and their physical meaning. We describe three important observational probes that can be exploited to constrain cosmological models, namely the large scale structure of the Universe, the Cosmic Microwave Background and the clusters of galaxies. Finally, we introduce the goals of this thesis work.

1.1 The homogeneous Universe

In this first section we remind some basic concepts about the standard cosmological model. For a detailed treatment of the subject we redirect to dedicated texts such as [Weinberg \(1972\)](#), [Padmanabhan \(1993\)](#), [Peebles \(1993\)](#) or [Peacock \(1999\)](#).

Modern cosmology is based on three main pillars:

- The validity of *general relativity*, at least at the scales of length and energy we are concerned about.
- The validity of *Weyl's postulate*, stating that there exists a family of *geodesics* such that one and only one member of this family passes through each point of the spacetime. Any observer whose world line is described by such a geodesic is called a *comoving observer*.
- The validity of the *cosmological principle*, according to which space, on large scales ($\gtrsim 100 \text{ Mpc}$), is *homogeneous* and *isotropic*.

As a consequence of these three assumptions the metric tensor describing the homogeneous Universe takes the following form, known as the *Lemaître-Friedmann-Robertson-Walker metric*:

$$ds^2 = -c^2 dt^2 + a(t)^2 \left[\frac{dr^2}{1 - kr^2} + r^2(d\theta^2 + \sin^2 \theta d\varphi^2) \right], \quad (1.1)$$

with c the speed of light and k is proportional to the space curvature. The spatial part of the metric is multiplied by the scale factor $a(t)$ which accounts for the observed expansion of the Universe. We take the scale factor to be dimensionless and normalised to unity at present time.

1.1.1 Cosmic inventory

In general relativity the geometrical properties of a space are determined by the distribution of the energy density, quantified by the energy-momentum tensor. The relation between the metric tensor and the energy momentum tensor is described by Einstein equation. The isotropy of the cosmic fluid results in its energy-momentum tensor to be specified only by its pressure P and its density ρ . The equation of state connecting the two is usually written in the form:

$$P = w\rho, \quad (1.2)$$

and the value of w depends on the particular component of the cosmic fluid we are considering.

- *Baryonic matter* contributes to only approximately 5% of the total energy-density of the Universe. This component includes all the matter made of protons, neutrons and electrons. In the present Universe baryons are non-relativistic and they are taken to exert null pressure ($w = 0$). Baryonic matter is made chiefly of hydrogen and helium, usually in ionised state; atomic and molecular phases can also be found in some colder galactic regions (Osterbrock & Ferland 2006).

Este documento incorpora firma electrónica, y es copia auténtica de un documento electrónico archivado por la ULL según la Ley 39/2015.
Su autenticidad puede ser contrastada en la siguiente dirección <https://sede.ull.es/validacion/>

Identificador del documento: 973742	Código de verificación: Jfg6xBh0
Firmado por: DENIS TRAMONTE UNIVERSIDAD DE LA LAGUNA	Fecha: 30/06/2017 15:10:10
RAFAEL DELFIN BARRENA DELGADO UNIVERSIDAD DE LA LAGUNA	30/06/2017 15:21:31
JOSE ALBERTO RUBIÑO MARTIN UNIVERSIDAD DE LA LAGUNA	30/06/2017 15:34:17
ERNESTO PEREDA DE PABLO UNIVERSIDAD DE LA LAGUNA	06/07/2017 13:51:19

- *Dark matter* is made of particles that are not included in the Standard Model of particle physics, and whose nature is still under debate. It represents the major fraction of matter present in our Universe, contributing to around the 27% of the total energy density today. Evidence for the existence of dark matter comes from its gravitational effects, like the study of the rotation curves of spiral galaxies (Rubin et al. 1980; Persic et al. 1996), the observation of gravitational lensing phenomena (Massey et al. 2010), or the amplitude of primordial CMB anisotropies (Peebles 1982). Theory of structure evolution suggests that its particles are non-relativistic, and from here it is usually called *cold dark matter* (CDM). By definition CDM is a collisionless system, so it is pressureless and $w = 0$.
- *Electromagnetic radiation*, in the form of the Cosmic Microwave Background (CMB). In the case of radiation we have $w = 1/3$. Its present contribution to the total amount of energy density is very small; however, it is an important cosmological observable to probe the early Universe. We will talk extensively about this in section 1.3.
- *Neutrinos* are the other relativistic component of the cosmic fluid. A background of neutrinos is predicted by theories of the evolution of the Universe, its energy density contribution being lower than the photon one. There is no direct detection of this background, but evidences supporting its existence can be found in other observables, like the CMB or the LSS (Lopez et al. 1999; Planck Collaboration et al. 2016e; Abazajian & Kaplinghat 2016). Possible, more general models of dark radiation (that is, any ingredient contributing to the expansion rate of the Universe in the same way as a radiation background) have also been considered, finding no strong evidence for a departure from the standard neutrino model from CMB data (Audren et al. 2015).
- *Dark energy* is the dominant component of the cosmic fluid at present time, accounting for 68% of its total energy density. It was introduced to explain the observed acceleration in the expansion of the Universe (Riess et al. 1998; Perlmutter et al. 1999; Frieman et al. 2008a). Its simplest model predicts $w = -1$; in this case it is customary to talk about a “cosmological constant” Λ , to be included in Einstein’s equation as an additional term (Peebles & Ratra 2003). More general models allow the equation of state of dark energy to evolve with time (Chevallier & Polarski 2001). Latest experimental results, however, favours the cosmological constant model (Planck Collaboration et al. 2016e).

Este documento incorpora firma electrónica, y es copia auténtica de un documento electrónico archivado por la ULL según la Ley 39/2015.
Su autenticidad puede ser contrastada en la siguiente dirección <https://sede.ull.es/validacion/>

Firmado por:	Identificador del documento:	Código de verificación:	Fecha:
DENIS TRAMONTE UNIVERSIDAD DE LA LAGUNA	973742	Jfg6xBh0	30/06/2017 15:10:10
RAFAEL DELFIN BARRENA DELGADO UNIVERSIDAD DE LA LAGUNA			30/06/2017 15:21:31
JOSE ALBERTO RUBIÑO MARTIN UNIVERSIDAD DE LA LAGUNA			30/06/2017 15:34:17
ERNESTO PEREDA DE PABLO UNIVERSIDAD DE LA LAGUNA			06/07/2017 13:51:19

Component	Energy density	Scale factor
Matter	$\rho \propto a^{-3}$	$a \propto t^{2/3}$
Radiation	$\rho \propto a^{-4}$	$a \propto t^{1/2}$
Dark energy	$\rho = \text{const}$	$a \propto e^{Ht}$

Table 1.1: Evolution of the energy density and of the scale factor, for different components dominating the expansion of the Universe.

The evolution of the Universe as a whole is determined by the relative abundances of the components that constitute the cosmic fluid.

1.1.2 Dynamics

By combining the LFRW metric 1.1 with the energy-momentum tensor of the cosmic fluid via Einstein's equation, the following set of equations describing the dynamics of the Universe can be derived (Lyth & Liddle 2009):

$$\left(\frac{\dot{a}}{a}\right)^2 = \frac{8\pi G}{3}\rho - \frac{k}{a^2} + \frac{\Lambda}{3}, \quad (1.3)$$

$$\frac{\ddot{a}}{a} = -\frac{4\pi G}{3}(\rho + 3P) + \frac{\Lambda}{3}, \quad (1.4)$$

$$\dot{\rho} = -3\frac{\dot{a}}{a}(\rho + P). \quad (1.5)$$

Equations 1.3 to 1.5 determine the temporal evolution of the scale factor depending on the physical properties of the cosmic fluid; by adding the information of the equation of state, we find for the different components described in section 1.1.1 the dependences summarised in table 1.1. The parameter H entering the last expression is the Hubble parameter which is defined in the next section. From the table above it is clear that going back in time the dominant component in the cosmic fluid changes from dark energy to matter to radiation. To a first approximation a can be taken to scale with time as if the Universe was made only of the dominating component.

1.1.3 Density parameters

The Hubble parameter is defined as:

$$H(t) = \frac{\dot{a}(t)}{a(t)}. \quad (1.6)$$

Este documento incorpora firma electrónica, y es copia auténtica de un documento electrónico archivado por la ULL según la Ley 39/2015.
Su autenticidad puede ser contrastada en la siguiente dirección <https://sede.ull.es/validacion/>

Identificador del documento: 973742	Código de verificación: Jfg6xBh0
Firmado por: DENIS TRAMONTE UNIVERSIDAD DE LA LAGUNA	Fecha: 30/06/2017 15:10:10
RAFAEL DELFIN BARRENA DELGADO UNIVERSIDAD DE LA LAGUNA	30/06/2017 15:21:31
JOSE ALBERTO RUBIÑO MARTIN UNIVERSIDAD DE LA LAGUNA	30/06/2017 15:34:17
ERNESTO PEREDA DE PABLO UNIVERSIDAD DE LA LAGUNA	06/07/2017 13:51:19

It represents the expansion rate of the Universe and evolves with time. It is usually considered as a function of redshift, $z \equiv a^{-1} - 1$. Its present value, H_0 , is commonly written as the dimensionless quantity:

$$h \equiv \frac{H_0}{100 \text{ km s}^{-1}\text{Mpc}^{-1}}. \quad (1.7)$$

The parameter h is usually explicitly included when writing numerical quantities (e.g. masses, densities, length scales etc.), thus making them unaffected by the uncertainty on H_0 .

By including the Hubble parameter, equation 1.3 can be recast as:

$$H^2 = \frac{8\pi G}{3}(\rho + \rho_\Lambda) - \frac{k}{a^2}, \quad (1.8)$$

where the cosmological constant was absorbed in the definition of its energy density ρ_Λ , while ρ is the sum of the contributions coming from baryons, CDM and radiation. The *critical energy density* ρ_c is defined as the one required by a flat Universe:

$$\rho_c(z) = \frac{3H(z)^2}{8\pi G}. \quad (1.9)$$

Its present value is:

$$\rho_c = 1.88 h^2 \times 10^{-29} \text{ g/cm}^3 = 2.78 h^2 \times 10^{11} M_\odot/\text{Mpc}^3. \quad (1.10)$$

Now, $10^{11} M_\odot$ is the typical mass of a galaxy, and 1 Mpc^3 is the typical separation between galaxies, so we expect the total density of the Universe to be close to the critical one. Current cosmological constraints actually favour a flat-Universe model (Planck Collaboration et al. 2016e).

For each component of the cosmic fluid its *density parameter* Ω is defined as the energy density in units of the critical energy density:

$$\Omega_i(z) = \frac{\rho_i(z)}{\rho_c(z)}. \quad (1.11)$$

A density parameter for the curvature can be defined as:

$$\Omega_k \equiv -\frac{k}{a^2 H^2}. \quad (1.12)$$

The first Friedmann equation 1.3 can thus be rewritten as:

$$\Omega + \Omega_\Lambda + \Omega_k = 1, \quad (1.13)$$

Este documento incorpora firma electrónica, y es copia auténtica de un documento electrónico archivado por la ULL según la Ley 39/2015.
Su autenticidad puede ser contrastada en la siguiente dirección <https://sede.ull.es/validacion/>

Identificador del documento: 973742

Código de verificación: Jfg6xBh0

Fecha: 30/06/2017 15:10:10

Firmado por: DENIS TRAMONTE
UNIVERSIDAD DE LA LAGUNA

RAFAEL DELFIN BARRENA DELGADO
UNIVERSIDAD DE LA LAGUNA

JOSE ALBERTO RUBIÑO MARTIN
UNIVERSIDAD DE LA LAGUNA

ERNESTO PEREDA DE PABLO
UNIVERSIDAD DE LA LAGUNA

30/06/2017 15:21:31

30/06/2017 15:34:17

06/07/2017 13:51:19

where $\Omega = \Omega_b + \Omega_c + \Omega_r$ comprises the contributions of baryons (Ω_b), CDM (Ω_c) and radiation (Ω_r).

By introducing the time evolutions outlined in table 1.1 in equation 1.8 the redshift dependence of the Hubble parameter can be written as $H(z) = E(z)H_0$, where H_0 is the parameter present value and:

$$E(z) \equiv [\Omega_m(1+z)^3 + \Omega_r(1+z)^4 + \Omega_k(1+z)^2 + \Omega_\Lambda]^{1/2}. \quad (1.14)$$

The redshift evolution of the density parameters then becomes:

$$\Omega_m(z) = \Omega_m \frac{(1+z)^3}{E^2(z)}, \quad \Omega_r(z) = \Omega_r \frac{(1+z)^4}{E^2(z)}, \quad (1.15)$$

$$\Omega_k(z) = \Omega_k \frac{(1+z)^2}{E^2(z)}, \quad \Omega_\Lambda(z) = \Omega_\Lambda \frac{1}{E^2(z)}, \quad (1.16)$$

where $\Omega = \Omega_b + \Omega_c$ is the total matter density parameter (hereafter we will use the symbols Ω_m , Ω_r , Ω_k and Ω_Λ with no explicit redshift dependence to refer to their present values).

As a last remark about the density parameter, from equation 1.11 we see that the density parameters are actually physical densities times a quantity proportional to H^{-2} . It therefore makes sense to define the physical densities as:

$$\omega_i \equiv \Omega_i h^2, \quad (1.17)$$

which are independent of the Hubble constant. These are the values constrained by observations and are often used instead of the density parameters defined in 1.11.

1.1.4 Redshift evolution

From the results of the LFRW models in section 1.1.2 it is clear that going backwards in time the energy density of the cosmic fluid keeps growing, and so does its temperature. Eventually, this leads to a singularity for $a \rightarrow 0$, which is known as the Big Bang. The presence of this singularity is due to the extrapolation of General Relativity to physical conditions in which this theory is no longer applicable. The very first stages of evolution of the Universe are described by quantum field theory, and go beyond the scope of this work; see e.g. Kolb & Turner (1990) for a detailed description. It is worth mentioning, however, that modern cosmological models have introduced an epoch of accelerated expansion in these early stages of the evolution of the Universe, which is called *inflation* (Guth 1981). The inflationary model was proposed to solve some problems in observational cosmology, related to the flatness of

Este documento incorpora firma electrónica, y es copia auténtica de un documento electrónico archivado por la ULL según la Ley 39/2015.
Su autenticidad puede ser contrastada en la siguiente dirección <https://sede.ull.es/validacion/>

Identificador del documento: 973742

Código de verificación: Jfg6xBh0

Fecha: 30/06/2017 15:10:10

Firmado por: DENIS TRAMONTE
UNIVERSIDAD DE LA LAGUNA

RAFAEL DELFIN BARRENA DELGADO
UNIVERSIDAD DE LA LAGUNA

JOSE ALBERTO RUBIÑO MARTIN
UNIVERSIDAD DE LA LAGUNA

ERNESTO PEREDA DE PABLO
UNIVERSIDAD DE LA LAGUNA

30/06/2017 15:21:31

30/06/2017 15:34:17

06/07/2017 13:51:19

the observed Universe, the remarkable isotropy of the CMB radiation and the observed absence of magnetic monopoles (Linde 2008). One of the merits of the inflationary model is that it is capable of producing primordial perturbations over the homogeneous background: these are the initial condition for the formation of structures (from stars to clusters of galaxies) visible nowadays.

When the temperature of the Universe dropped below ~ 1 MeV, approximately 1 second after the Big-Bang, the process of primordial nucleosynthesis took place (Boesgaard & Steigman 1985; Steigman 2004), leaving the cosmic fluid in a state of an ionised plasma made of electron, protons, nuclei of helium and other light elements, photons and neutrinos (which had already decoupled from the other components of the cosmic fluid and followed an independent thermal evolution). When the temperature dropped below ~ 0.3 eV, or ~ 3500 K, the first neutral atoms formed, in a process called recombination. In the plasma state, photons efficiently interacted with free electrons via Compton scattering; but after recombination, given the much lower cross section for the Compton scatter with an atom compared to an electron, the matter-radiation interactions were strongly suppressed determining a decoupling of the radiation from matter. This event occurred at redshift $z \sim 1000$, or around 380 kyr after the Big-Bang. It was the origin of the CMB, which we will consider in detail in section 1.3.

In the meantime, the primordial density perturbation growth led to the formation of the first stars at $z \sim 30$; the high energy radiation emitted by this first generation of stars started a process of reionisation of the interstellar medium (Zaroubi 2013), which was complete by $z \sim 11$. However, at this stage matter was already so diluted in the Universe that Compton interactions with CMB photons are sufficiently rare as to allow the CMB to be observed. The expansion of the Universe after inflation was dominated first by radiation and later on by matter, in both cases being decelerated; at $z \lesssim 2$ dark energy became the dominant component of the cosmic fluid, so that we live today in a second phase of accelerated expansion. Meanwhile, matter kept clustering, finally shaping the large scale structure observable today. A pictorial representation of the evolution of the Universe is shown in figure 1.1.

1.1.5 The Λ CDM model

In general, the observational properties of the Universe are described via a set of cosmological parameters. Such parameters can be classified in three groups, as follows.

- *Composition, evolution and geometry parameters.* In this first category

Este documento incorpora firma electrónica, y es copia auténtica de un documento electrónico archivado por la ULL según la Ley 39/2015.
Su autenticidad puede ser contrastada en la siguiente dirección <https://sede.ull.es/validacion/>

Identificador del documento:	973742	Código de verificación:	Jfg6xBh0
Firmado por:	DENIS TRAMONTE UNIVERSIDAD DE LA LAGUNA	Fecha:	30/06/2017 15:10:10
	RAFAEL DELFIN BARRENA DELGADO UNIVERSIDAD DE LA LAGUNA		30/06/2017 15:21:31
	JOSE ALBERTO RUBIÑO MARTIN UNIVERSIDAD DE LA LAGUNA		30/06/2017 15:34:17
	ERNESTO PEREDA DE PABLO UNIVERSIDAD DE LA LAGUNA		06/07/2017 13:51:19

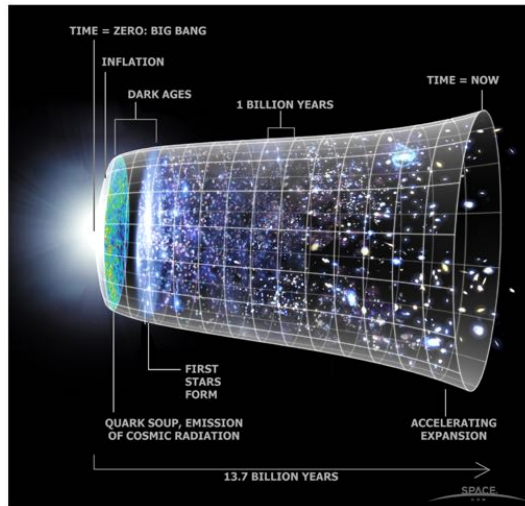


Figure 1.1: Redshift evolution of the Universe, according to the standard cosmological model. Credits:NASA/WMAP Science Team.

we place all parameters that describe the geometrical properties of the Universe, its evolution and the composition of the cosmic fluid. Hence, all the density parameters, Ω_b , Ω_c , Ω_r , Ω_k and Ω_Λ , and the Hubble parameter H_0 . Clearly, not all of these are independent. Current observations agree in a flat universe, so that Ω_k is usually taken to be zero, and the radiation density is usually neglected as well in the local Universe. The remaining densities sum to one, and the set of independent parameters that is usually chosen is $\{\Omega_b, \Omega_c, H_0\}$, or $\{\omega_b, \omega_c, H_0\}$. Another important parameter entering this group is the *angular sound horizon at recombination*, θ_s , which sometimes is taken as an independent parameter instead of H_0 .

- *Initial condition parameters.* These parameters are related to the primordial perturbations of the energy density, whose evolution leads to the formation of structures, which is the topic of the next section. The two main quantities to be included in this category are the *amplitude* A_s and the *spectral index* n_s of the primordial power spectrum of scalar perturbations (we will properly define them in section 1.2.2).

Este documento incorpora firma electrónica, y es copia auténtica de un documento electrónico archivado por la ULL según la Ley 39/2015.
Su autenticidad puede ser contrastada en la siguiente dirección <https://sede.ull.es/validacion/>

Identificador del documento: 973742	Código de verificación: Jfg6xBh0
Firmado por: DENIS TRAMONTE UNIVERSIDAD DE LA LAGUNA	Fecha: 30/06/2017 15:10:10
RAFAEL DELFIN BARRENA DELGADO UNIVERSIDAD DE LA LAGUNA	30/06/2017 15:21:31
JOSE ALBERTO RUBIÑO MARTIN UNIVERSIDAD DE LA LAGUNA	30/06/2017 15:34:17
ERNESTO PEREDA DE PABLO UNIVERSIDAD DE LA LAGUNA	06/07/2017 13:51:19

- *Astrophysical parameters.* They are related to astrophysical processes, like radiation transfer, ionisation or recombination. The most important one is the optical depth of Thomson scattering to recombination, τ , defined as:

$$\tau = \sigma_T \int_0^{z_{\text{rec}}} dz' n_e(z'), \quad (1.18)$$

where σ_T is the Thomson cross section and $n_e(z)$ the electron density at redshift z .

The so-called ΛCDM model is the description of the Universe that we have presented up to now, that is, a flat Universe with cold dark matter and a cosmological constant. After a proper cosmological model has been set, the challenge of observational cosmology is determining the values of the parameters that define it. We are going to consider in this work three main cosmological observables, namely the large scale distribution of matter, the anisotropies of the cosmic microwave background and the abundance and physical properties of clusters of galaxies. The rest of this chapter is dedicated to introducing each one of them.

There exist of course various non-standard cosmological models, but they generally fail when trying to accommodate the full set of observables in their theoretical framework; we will not consider them in the rest of this work. Throughout this chapter we will be using the cosmological model reported in table 1.2.

Ω_b	Ω_m	Ω_Λ	h	A_s	n_s	τ
4.6×10^{-2}	0.3	0.7	0.7	2.5×10^{-9}	0.96	0.09

Table 1.2: Cosmological model used for the examples in this chapter.

1.2 Large Scale Structure

At scales $\lesssim 100$ Mpc the Universe is clearly not homogeneous, observations revealing the existence of a large web in which matter is distributed along filaments and walls, between which lie large cosmic voids. In the nodes of this web we find the largest concentrations of galaxies, often bound into clusters. This framework is known as the Large Scale Structure (LSS) of the Universe.

The existence of structures is included in the cosmological model by decomposing the evolution of the Universe in a homogeneous background plus a set of perturbations. These deviations from homogeneity are the gravitational

Este documento incorpora firma electrónica, y es copia auténtica de un documento electrónico archivado por la ULL según la Ley 39/2015.
Su autenticidad puede ser contrastada en la siguiente dirección <https://sede.ull.es/validacion/>

Identificador del documento: 973742	Código de verificación: Jfg6xBh0	Fecha: 30/06/2017 15:10:10
Firmado por: DENIS TRAMONTE UNIVERSIDAD DE LA LAGUNA		
RAFAEL DELFIN BARRENA DELGADO UNIVERSIDAD DE LA LAGUNA		30/06/2017 15:21:31
JOSE ALBERTO RUBIÑO MARTIN UNIVERSIDAD DE LA LAGUNA		30/06/2017 15:34:17
ERNESTO PEREDA DE PABLO UNIVERSIDAD DE LA LAGUNA		06/07/2017 13:51:19

amplification of small density fluctuations in the early Universe, and they eventually lead to the formation of the structures visible today. We focus in this section on the description of these perturbations; for a more detailed review on the subject we redirect to Peebles (1980), Longair (1998) and Barkana & Loeb (2001).

1.2.1 Statistics of perturbations

The matter density contrast field in the Universe in a generic position \mathbf{r} at redshift z is defined as:

$$\delta(\mathbf{r}, z) \equiv \frac{\rho_m(\mathbf{r}, z) - \bar{\rho}_m(z)}{\bar{\rho}_m(z)}, \quad (1.19)$$

where $\rho_m(\mathbf{r}, z)$ is the matter density field and $\bar{\rho}_m(z)$ the average matter density at time z . The redshift dependence of δ at a fixed position is determined by the physical processes taking place during the evolution of the Universe. However, the dependence on the position at fixed redshift is random. The density contrast is indeed a random field; the one we can observe in our Universe is a particular realisation of an ensemble whose probability distribution is dictated by the underlying cosmology. It is therefore interesting to study the stochastic properties of this random field.

The most important quantity is the matter power spectrum $P(k)$. Given the Fourier components of the density contrast field,

$$\delta_{\mathbf{k}} = \int d^3r \delta(\mathbf{r}) e^{-i\mathbf{k}\cdot\mathbf{r}}, \quad (1.20)$$

the matter power spectrum is defined as:

$$\langle \delta_{\mathbf{k}} \delta_{\mathbf{k}'} \rangle \equiv (2\pi)^3 P(k) \delta^D(\mathbf{k} - \mathbf{k}'), \quad (1.21)$$

where δ^D is the Dirac delta function, and space isotropy results in the spectrum being a function of the modulus of k alone. The brackets “ $\langle \rangle$ ” denote the ensemble average for the perturbation random field. Since the primordial density perturbations are supposed to be a Gaussian random field (see section 1.2.2), in which the phases of the Fourier components $\delta_{\mathbf{k}}$ are uniformly distributed random numbers, equation 1.21 can be simplified to

$$P(k) = \langle |\delta_{\mathbf{k}}|^2 \rangle. \quad (1.22)$$

The power spectrum is the Fourier transform of the two-point correlation function $\xi(x) \equiv \langle \delta(\mathbf{r}) \delta(\mathbf{r} + \mathbf{x}) \rangle$. It can be used to compute the *variance* of the

Este documento incorpora firma electrónica, y es copia auténtica de un documento electrónico archivado por la ULL según la Ley 39/2015.
Su autenticidad puede ser contrastada en la siguiente dirección <https://sede.ull.es/validacion/>

Identificador del documento: 973742

Código de verificación: Jfg6xBh0

Fecha: 30/06/2017 15:10:10

Firmado por: DENIS TRAMONTE UNIVERSIDAD DE LA LAGUNA	30/06/2017 15:21:31
RAFAEL DELFIN BARRENA DELGADO UNIVERSIDAD DE LA LAGUNA	30/06/2017 15:34:17
JOSE ALBERTO RUBIÑO MARTIN UNIVERSIDAD DE LA LAGUNA	06/07/2017 13:51:19
ERNESTO PEREDA DE PABLO UNIVERSIDAD DE LA LAGUNA	

field:

$$\sigma^2 = \langle \delta^2(r) \rangle = \frac{1}{(2\pi)^3} \int P(k) d^3k. \quad (1.23)$$

The previous integral can also be expressed, using spherical coordinates for \mathbf{k} , as:

$$\sigma^2 = \frac{1}{2\pi^2} \int k^3 P(k) d\ln k \equiv \int \Delta^2(k) d\ln k, \quad (1.24)$$

with $\Delta^2(k) \equiv k^3 P(k)/2\pi^2$ a dimensionless power spectrum quantifying the contribution to the variance per logarithmic interval.

It is common in cosmology to consider the perturbation field filtered over a certain scale R , in order to smooth out the contribution from smaller scales. In that case the power spectrum $P(k)$ in 1.23 should be replaced by its smoothed version $P_R(k) = w_R(k)^2 P(k)$, were $w_R(k)$ is called the filter window function. In the most widely used case of a top-hat filter the window function can be computed to give:

$$w_R(k) = \frac{3}{(kR)^3} [\sin(kR) - kR \cos(kR)]. \quad (1.25)$$

Higher-order correlators (like the bi-spectrum or the three-point correlation function) can also be used to investigate the stochastic properties of the perturbation field, in particular the level of non-Gaussianity. This topic goes beyond the scope of this work.

1.2.2 Primordial perturbations

We refer to primordial perturbations as those that were present after the end of the inflationary epoch, and that provide the initial conditions for the subsequent evolution of structures in the Universe. The fluctuation on the matter density that we are considering are due to *scalar* perturbations; the existence of primordial *tensor* perturbations is also allowed. Theory and observations led to the establishment of the following important properties characterising scalar primordial perturbations.

- *Adiabatic.* Adiabatic perturbations have the property that the perturbed field $\rho(\mathbf{r}, t)$ at a position \mathbf{r} and time t has the same value as the unper- turbed field at a different time $\bar{\rho}(t + \delta t)$, with δt dependent on \mathbf{r} . If the cosmic fluid is made of different components, the shift in time $\delta t(\mathbf{r})$ is the same for all the species. Using the continuity equation 1.5 this im- plies that all matter components have the same density contrast δ_m , while radiation perturbations obey $\delta_r = 4/3 \delta_m$. Adiabatic perturbations are

Este documento incorpora firma electrónica, y es copia auténtica de un documento electrónico archivado por la ULL según la Ley 39/2015.
Su autenticidad puede ser contrastada en la siguiente dirección <https://sede.ull.es/validacion/>

Identificador del documento: 973742	Código de verificación: Jfg6xBh0
Firmado por: DENIS TRAMONTE UNIVERSIDAD DE LA LAGUNA	Fecha: 30/06/2017 15:10:10
RAFAEL DELFIN BARRENA DELGADO UNIVERSIDAD DE LA LAGUNA	30/06/2017 15:21:31
JOSE ALBERTO RUBIÑO MARTIN UNIVERSIDAD DE LA LAGUNA	30/06/2017 15:34:17
ERNESTO PEREDA DE PABLO UNIVERSIDAD DE LA LAGUNA	06/07/2017 13:51:19

a fundamental consequence of most inflationary models (Gordon et al. 2001).

- *Gaussian*. This refers to the existence of possible correlations between the Fourier components of the contrast field δ . That is, if measuring one Fourier component $\delta_{\mathbf{k}}$ can give information on the outcome of measuring another one. If the field δ is *Gaussian*, the only existing relation between its Fourier components is the reality condition $\delta_{\mathbf{k}}^* = \delta_{-\mathbf{k}}$. The simplest inflationary models predict Gaussian or nearly Gaussian primordial perturbations (Acquaviva et al. 2003). Within observational uncertainties, the primordial perturbation field is considered Gaussian (Planck Collaboration et al. 2016f).
- *Nearly scale invariant*. This means that there are no privileged scales in the primordial density field. Mathematically, this corresponds to a linear dependence on k of the matter power spectrum; this particular case is known as Harrison-Zel'dovich power spectrum, from the works of Harrison (1970) and Zeldovich (1972). Observationally, the perturbation in the energy density is found to be nearly scale independent, the departure from invariance being quantified by the introduction of a spectral index whose value is close to unity (Planck Collaboration et al. 2016e).

According to the theoretical predictions from inflation, the primordial matter power spectrum $P_{\text{prim}}(k)$ has the following scale dependence:

$$P_{\text{prim}}(k) \propto \left(\frac{k}{k_p}\right)^{n_s}, \quad (1.26)$$

where k_p is an arbitrary pivot scale. The parameter n_s is referred to as the *scalar spectral index*¹. The case $n_s = 1$ corresponds to a Harrison-Zel'dovich spectrum; any other value for n_s quantifies the deviation from scale invariance. As already mentioned in section 1.1.5, the normalisation of the matter power spectrum is set by the amplitude parameter A_s . The quantities A_s and n_s are fundamental cosmological parameters that characterise the initial conditions in the evolution of structures in our Universe.

Note that another parameter that can be used for fixing the normalisation of the matter power spectrum is the amplitude of the density fluctuation at a conventionally chosen scale; historically the scale $8 h^{-1} \text{ Mpc}$ has been chosen,

¹In more general models a dependence on k is included for n_s ; we talk in this case of a *running* of the spectral index.

because with former cosmological models the fluctuation amplitude was very close to unity at this scale. The corresponding parameter, σ_8 , is computed as:

$$\sigma_8 \equiv \sigma(R = 8 h^{-1} \text{ Mpc}) = \int \Delta^2(k) w^2(R = 8 h^{-1} \text{ Mpc}) d \ln k, \quad (1.27)$$

where $w(R = 8 h^{-1} \text{ Mpc})$ is the top-hat window function at the chosen scale. The parameter σ_8 is a fundamental cosmological parameter and is often employed instead of A_s to normalise the spectrum of scalar perturbations.

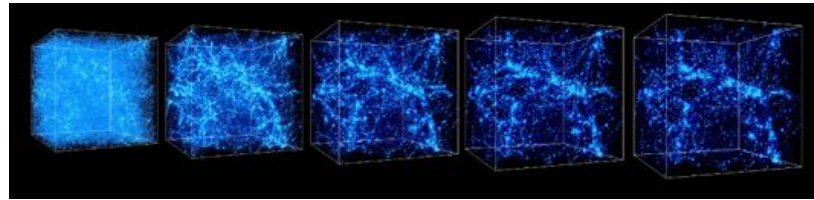


Figure 1.2: Numerical simulations showing the evolution of the LSS, from initial small perturbations on the homogeneous background to the present structures; the figure shows different snapshots from an initial redshift $z = 30$ to the present $z = 0$. Credit: simulations were performed at the National Center for Supercomputer Applications by Andrey Kravtsov (The University of Chicago) and Anatoly Klypin (New Mexico State University). Visualisations by Andrey Kravtsov.

1.2.3 Evolution of perturbations

Primordial perturbations generated at the end of the inflationary epoch undergo an evolution determined by gravitational instability and the effect of pressure and dissipation. The result of this process is an alteration of the shape of the power spectrum, that can be written as:

$$P(k; z) = P_{\text{prim}}(k) T^2(k) G^2(z), \quad (1.28)$$

where $T(k)$ is the *matter transfer function* and $G(z)$ is the *growth factor* of scalar perturbations. The transfer functions accounts for the scale modification of the matter power spectrum; the original (nearly-) scale independence is broken by physical processes imprinting scales on it. The transfer function can be computed with a Boltzmann code, like the Code for Anisotropies in the Microwave Background (CAMB, Lewis et al. 2000), or alternatively fitting formulae can be found in Bond & Efstathiou (1984), Peacock & Dodds (1994) or in Eisenstein & Hu (1998). The inclusion of the transfer function results in the

Este documento incorpora firma electrónica, y es copia auténtica de un documento electrónico archivado por la ULL según la Ley 39/2015.
Su autenticidad puede ser contrastada en la siguiente dirección <https://sede.ull.es/validacion/>

Identificador del documento: 973742

Código de verificación: Jfg6xBh0

Fecha: 30/06/2017 15:10:10

Firmado por: DENIS TRAMONTE
UNIVERSIDAD DE LA LAGUNA

RAFAEL DELFIN BARRENA DELGADO
UNIVERSIDAD DE LA LAGUNA

JOSE ALBERTO RUBIÑO MARTIN
UNIVERSIDAD DE LA LAGUNA

ERNESTO PEREDA DE PABLO
UNIVERSIDAD DE LA LAGUNA

30/06/2017 15:21:31

30/06/2017 15:34:17

06/07/2017 13:51:19

matter power spectrum taking the shape shown in figure 1.3. The plot can be understood qualitatively. The peak in the power spectrum is reached at a scale corresponding to the horizon at the redshift z_{eq} of matter-radiation equality. The loss of power at higher k is due to the fact that in a radiation-dominated Universe perturbations grow slower than in a matter-dominated Universe, due to the effect of the radiation pressure. At lower k we find instead perturbations that entered the horizon during matter domination, and their power depends on the scale (smaller scales enter the horizon earlier and have more time to grow). The wiggles in the power spectrum at scales above the horizon at z_{eq} are due to the oscillations of the plasma of baryons and radiation, that are transmitted to the dark matter by baryons. These features are called Baryon Acoustic Oscillations (BAO, Bassett & Hlozek 2010); they affect the present spatial distribution of galaxies, and are as such a powerful tool in observational cosmology. In general, the mass range in which structures can form is limited at low masses by pressure support and at high masses by the fact that a very large region enters the horizon too late for having the time to collapse; structures are therefore expected to form from the scale of subgalactic objects to the scale of the largest clusters of galaxies.

The second factor entering equation 1.28 accounts for the growth of perturbations with redshift. In linear theory it can be evaluated as:

$$\tilde{G}(a) = H(a) \int_0^a \frac{da'}{[a' H(a')]^3}, \quad (1.29)$$

and the growth factor normalised to unity at present is given by $G(a) = \tilde{G}(a)/\tilde{G}(1)$. A good numerical fit to the integral 1.29 can be found in Lahav et al. (1991).

1.2.4 Mapping the Large Scale Structure

Density fluctuations in the matter field evolve, shaping the present large-scale distribution of matter in the Universe (see figure 1.2). In order to map the LSS we must determine the three-dimensional position of galaxies in space. This implies measuring the redshift of galaxies; for this reason, these observations are usually referred to as galaxy surveys.

Mapping the LSS can provide direct insights into the cosmological model. The clustering of galaxies mathematically translates into a correlation function. More precisely, the expected number of pair of galaxies with one galaxy in a volume element δV_1 and the other in δV_2 , separated by a distance r , is given by (Percival 2013):

$$\langle n_{\text{pair}} \rangle = \bar{n}^2 [1 + \xi(r)] \delta V_1 \delta V_2, \quad (1.30)$$

Este documento incorpora firma electrónica, y es copia auténtica de un documento electrónico archivado por la ULL según la Ley 39/2015.
Su autenticidad puede ser contrastada en la siguiente dirección <https://sede.ull.es/validacion/>

Firmado por:	IDENTIFICADOR DEL DOCUMENTO:	CÓDIGO DE VERIFICACIÓN:	FECHA:
DENIS TRAMONTE UNIVERSIDAD DE LA LAGUNA	973742	Jfg6xBh0	30/06/2017 15:10:10
RAFAEL DELFIN BARRENA DELGADO UNIVERSIDAD DE LA LAGUNA			30/06/2017 15:21:31
JOSE ALBERTO RUBIÑO MARTIN UNIVERSIDAD DE LA LAGUNA			30/06/2017 15:34:17
ERNESTO PEREDA DE PABLO UNIVERSIDAD DE LA LAGUNA			06/07/2017 13:51:19

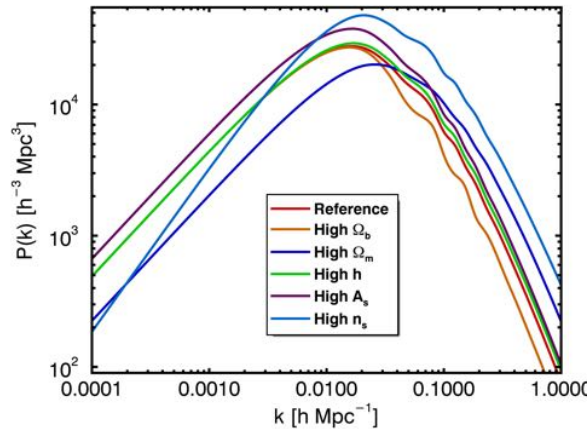


Figure 1.3: Matter power spectrum 1.28 computed at $z = 0$ using the cosmology from table 1.2 (“Reference”). We also show the effect on the spectrum of changing one cosmological parameter at a time. When different from their reference values, cosmological parameters are set to: $\Omega_b = 0.08$, $\Omega_m = 0.45$, $h = 0.75$, $A_s = 3.4 \times 10^9$, $n_s = 1.25$.

where \bar{n} is the mean number density of galaxies and $\xi(r)$ is referred to as the two-point correlation function. It quantifies the excess clustering of galaxies at a separation r (isotropy leaves only the dependence on the modulus of the distance). It can be shown that it is the Fourier transform of the matter power spectrum 1.22. The characterisation of the function $\xi(r)$ can thus give information on $P(k)$, which is the quantity more closely related to theory.

There is another important feature of the function $\xi(r)$. The BAO wiggles visible in the matter power spectrum in 1.3, due to the oscillation of the radiation-baryon plasma, are actually standing sound waves that imprint a scale of compression and rarefaction in the distribution of galaxies at large scales. This feature is visible in the function $\xi(r)$ as a peak (called the BAO peak), and its scale provides a measurement of the sound horizon today. This estimate can be compared with the sound horizon at recombination as extracted from observations of the CMB, thus providing a powerful tool to probe models of the evolution of Universe, particularly on the nature of dark energy that determines its accelerated expansion (Bassett & Hlozek 2010).

From here we understand the importance of observing the large scale distri-

Este documento incorpora firma electrónica, y es copia auténtica de un documento electrónico archivado por la ULL según la Ley 39/2015.
Su autenticidad puede ser contrastada en la siguiente dirección <https://sede.ull.es/validacion/>

Identificador del documento: 973742

Código de verificación: Jfg6xBh0

Fecha: 30/06/2017 15:10:10

Firmado por: DENIS TRAMONTE
UNIVERSIDAD DE LA LAGUNA

RAFAEL DELFIN BARRENA DELGADO
UNIVERSIDAD DE LA LAGUNA

JOSE ALBERTO RUBIÑO MARTIN
UNIVERSIDAD DE LA LAGUNA

ERNESTO PEREDA DE PABLO
UNIVERSIDAD DE LA LAGUNA

30/06/2017 15:21:31

30/06/2017 15:34:17

06/07/2017 13:51:19

bution of matter in order to reconstruct the correlation function and the matter power spectrum. These observations are carried out in optical/IR wavelengths, spectroscopic techniques being used for determining the redshift of galaxies. The first attempts at cataloguing galaxies date back to the 30s with the works of H. Shapley, and later F. Zwicky. For the following two decades we can cite the works of D.C. Shane (e.g., [Shane 1956](#)). However, the first redshift survey is usually taken as the work of [de Vaucouleurs et al. \(1991\)](#). After that, an increasing amount of data resulted from efforts of different surveys; among the most relevant, we can cite the Center for Astrophysics redshift survey (CfA, [Falco et al. 1999](#)), the Las Campanas Redshift Survey (LCRS, [Shectman et al. 1996](#)), the 2dF Galaxy Redshift Survey (2dFGRS, [Colless et al. 2001](#)), the 6dF Galaxy Survey (6dFGS, [Jones et al. 2009](#)), the 2MASS Redshift Survey (2MRS, [Huchra et al. 2012](#)) and the WiggleZ Dark Energy Survey ([Hinton et al. 2017](#)). From space we cite the catalogue built with the Infrared Astronomical Satellite (IRAS, [Saunders et al. 1990, 2000](#)).

We finally cite the Sloan Digital Sky Survey (SDSS), an important multi-wavelength experiment employing a dedicated 2.5 m telescope at the Apache Point Observatory (US), and which began observations in 1998. The experiment history is divided into four phases. SDSS I ([York et al. 2000a](#)) was carried out from 2000 to 2005. SDSS II, from 2005 to 2008, was dedicated to a survey of supernovae ([Frieman et al. 2008b](#)) and to an extension of the previous phase with the SEGUE survey ([Yanny et al. 2009](#)). SDSS III lasted from 2008 to 2014 and comprised four main surveys: BOSS, designed to detect the BAO signature ([Dawson et al. 2013](#)); APOGEE, for the study of galactic evolution ([Majewski et al. 2015](#)); SEGUE-2, improving stellar observations from the first survey ([Rockosi 2012](#)); and MARVELS, dedicated to exoplanetary science ([Ge et al. 2008](#)). The last phase of the project, SDSS IV, began in 2014 and is ongoing; it comprises a stellar survey in the Milky Way with APOGEE-2 ([Majewski et al. 2016](#)), a galaxy and quasar survey with eBOSS ([Dawson et al. 2016](#)) and a survey of nearby galaxies with MaNGA ([Bundy et al. 2015](#)). Data from SDSS have been and are currently largely used in cosmological studies of the LSS.

1.3 The Cosmic Microwave Background

As anticipated in section [1.1.4](#), when the temperature in the Universe was low enough to allow for the formation of neutral hydrogen atoms, the photons decoupled from the baryons leading to the creation of the Cosmic Microwave Background (CMB). From that moment on radiation could propagate freely in the cosmic fluid. The expansion of the Universe resulted in its temperature

Este documento incorpora firma electrónica, y es copia auténtica de un documento electrónico archivado por la ULL según la Ley 39/2015.
Su autenticidad puede ser contrastada en la siguiente dirección <https://sede.ull.es/validacion/>

Identificador del documento:	973742	Código de verificación:	Jfg6xBh0
Firmado por:	DENIS TRAMONTE UNIVERSIDAD DE LA LAGUNA	Fecha:	30/06/2017 15:10:10
	RAFAEL DELFIN BARRENA DELGADO UNIVERSIDAD DE LA LAGUNA		30/06/2017 15:21:31
	JOSE ALBERTO RUBIÑO MARTIN UNIVERSIDAD DE LA LAGUNA		30/06/2017 15:34:17
	ERNESTO PEREDA DE PABLO UNIVERSIDAD DE LA LAGUNA		06/07/2017 13:51:19

lowering to $\sim 2.7\text{K}$ today. For a fixed observer, the CMB is detected as if it were emitted isotropically from a projected sphere that is called the last scattering surface; the last scattering redshift z_{ls} has been estimated in Spergel et al. (2003) as:

$$z_{\text{ls}} = 1088 \pm 97, \quad (1.31)$$

with a finite redshift width that accounts for the process not being instantaneous.

The CMB was serendipitously discovered in 1964 by A. Penzias and B. Wilson while calibrating a sensitive microwave antenna designed for satellite communications at Bell Laboratories in New Jersey (Penzias & Wilson 1965). Their discovery was recognised in Dicke et al. (1965) as a cosmological signal. From then on, increasing efforts have been undertaken to improve CMB observations and to characterise its properties, soon making it a fundamental tool in modern cosmology. This radiation shows two important features.

- It has a blackbody spectrum with a measured temperature of (Fixsen et al. 1996; Fixsen & Mather 2002):

$$T_{\text{CMB}} = 2.725 \pm 0.001 \text{ K}. \quad (1.32)$$

The intensity peaks at a frequency $\nu \simeq 160\text{ GHz}$ (or equivalently at $\lambda \simeq 1\text{ mm}$), in the microwave region of the spectrum. By integrating the blackbody spectrum with the temperature 1.32 we find that the density parameter for the CMB radiation today is $\Omega_{\text{CMB}} \simeq 2.5 h^{-2} \times 10^{-5}$.

- It shows a remarkable isotropy over the sky. Deviations from isotropy were measured only several years after the CMB discovery, first at the level of one part in 10^3 (the CMB dipole, Corey & Wilkinson 1976; Lubin et al. 1983), and later at the level of one part in 10^5 (Smoot et al. 1992). CMB anisotropies are the topic of section 1.3.1.

The discovery of the CMB was a fundamental milestone in the history of cosmology: this radiation is a relic of a hotter phase in the history of the Universe, and was the evidence that ruled out the steady-state theories (Hoyle 1954; Bondi 1990).

1.3.1 CMB anisotropies

Despite the CMB isotropy, the greatest amount of information from this probe is encoded in its anisotropies (White et al. 1994). We consider now the CMB temperature as a scalar field defined over the sphere, $T(\mathbf{r}_0, \hat{\mathbf{n}})$, where \mathbf{r}_0 denotes

Este documento incorpora firma electrónica, y es copia auténtica de un documento electrónico archivado por la ULL según la Ley 39/2015.
Su autenticidad puede ser contrastada en la siguiente dirección <https://sede.ull.es/validacion/>

Identificador del documento: 973742	Código de verificación: Jfg6xBh0	Fecha: 30/06/2017 15:10:10
Firmado por: DENIS TRAMONTE UNIVERSIDAD DE LA LAGUNA		
RAFAEL DELFIN BARRENA DELGADO UNIVERSIDAD DE LA LAGUNA		30/06/2017 15:21:31
JOSE ALBERTO RUBIÑO MARTIN UNIVERSIDAD DE LA LAGUNA		30/06/2017 15:34:17
ERNESTO PEREDA DE PABLO UNIVERSIDAD DE LA LAGUNA		06/07/2017 13:51:19

the position of the observer with respect to a proper reference frame ², and \mathbf{n} is the observing direction. We define the fractional anisotropies as the scalar field:

$$\Theta(\mathbf{r}_0, \hat{\mathbf{n}}) \equiv \frac{T(\mathbf{r}_0, \hat{\mathbf{n}}) - T_0(\mathbf{r}_0)}{T_0(\mathbf{r}_0)}. \quad (1.33)$$

where T_0 is the average CMB temperature from 1.32. As a scalar function defined over a sphere, the temperature anisotropies can be written as a superposition of spherical harmonics (Abramowitz & Stegun 1972), yielding:

$$\Theta(\mathbf{r}_0, \hat{\mathbf{n}}) = \sum_{\ell>0} \sum_{m=-\ell}^{+\ell} a_{\ell m}(\mathbf{r}_0) Y_\ell^m(\hat{\mathbf{n}}). \quad (1.34)$$

In this decomposition, the $\ell = 0$ component is the monopole term corresponding to the average temperature T_0 and does not appear according to definition 1.33. The first term is the dipole corresponding to $\ell = 1$, with a contribution around 10^{-3} to the fractional temperature anisotropies. Most of it, however, comes from the Doppler shift of the CMB due to the motion of the Solar System (Bennett et al. 2003): the analysis shows that our Galaxy has a peculiar velocity of ~ 600 km/s relative to the CMB, which reflects the motion of the Local Group of Galaxies towards the Great Attractor. The CMB then defines a comoving rest frame in which this contribution to the dipole is null. Higher orders contributes with fractional anisotropies of order $\sim 10^{-5}$; these anisotropies are found over angles $\theta \sim 180^\circ/\ell$, with ℓ the multipole order.

The different angular contributions are weighted by the coefficients $a_{\ell m}$, which contain the CMB spatial information. Just as in the case of the matter density contrast defined in 1.19, the temperature anisotropy Θ is a random field, and due to the assumed homogeneity and isotropy of the Universe we expect the ensemble average of the coefficients $a_{\ell m}$ to be null, $\langle a_{\ell m}(\mathbf{r}) \rangle = 0$. In the same way, it is possible to define an angular power spectrum for the anisotropies, as:

$$\langle |a_{\ell m}(\mathbf{r})|^2 \rangle = \langle a_{\ell m}(\mathbf{r}) a_{\ell' m'}^*(\mathbf{r}) \rangle \equiv \delta_{\ell \ell'} \delta_{mm'} C_l, \quad (1.35)$$

where $\delta_{\ell \ell'}$ is the Kronecker delta; the dependence on \mathbf{r} vanishes when performing the ensemble average, and the dependence on m also vanishes thanks to isotropy.

The temperature anisotropies are the imprint on the radiation field of the matter density perturbations; since inflation predicts the latter to be a Gaussian

²This dependence must be included because, in principle, observers in different positions could observe different temperature patterns in the CMB.

random field, and given that the dominant processes producing temperature anisotropy involve linear physics, gaussianity is also expected for the Θ field. The study of CMB anisotropies is indeed one of the most important test benches for the gaussianity of primordial perturbations, which up to date is basically confirmed (Planck Collaboration et al. 2016f).

The angular power spectrum can be rewritten in the following way:

$$C_\ell \equiv \langle |a_{\ell m}(\mathbf{r})|^2 \rangle = \langle |a_{\ell m}(\mathbf{r})|^2 \rangle_{\text{space}} = \frac{1}{2\ell + 1} \sum_m \langle |a_{\ell m}(\mathbf{r})|^2 \rangle, \quad (1.36)$$

where in the second equality we used the ergodic property to change the ensemble average into a spatial average, and in the third one we took advantage of the field isotropy. This relation provides a direct way to compute the temperature power spectrum starting from the coefficients $a_{\ell m}$. However, since we can observe only one realisation of the anisotropy field, the one corresponding to our position \mathbf{r}_0 and to our Universe, the quantity that we can actually compute is:

$$\hat{C}_\ell = \frac{1}{2\ell + 1} \sum_m |a_{\ell m}(\mathbf{r}_0)|^2. \quad (1.37)$$

The estimator \hat{C}_ℓ is an estimator of the CMB power spectrum, which is unbiased, $\langle \hat{C}_\ell \rangle = C_\ell$, with an expected scatter quantified by (Abbott & Wise 1984):

$$\sigma^2(\hat{C}_\ell) = \frac{2C_\ell^2}{2\ell + 1}. \quad (1.38)$$

Since C_ℓ does not grow with ℓ , from 1.38 it is clear that the spectrum reconstructed from observations is a good estimator of the underlying “true” spectrum at high multipoles, while the error grows larger at low ℓ . The fact that $C_\ell \neq 0$ is referred to as *cosmic variance*. This effect cannot be reduced by improving the sensitivity of our observations, it is a limit set by the fact that we can observe only one realisation of the ensamble of possible fields of CMB anisotropies.

To close this section, we remind that additional issues affect the power spectrum extracted from a CMB map, namely the smoothing due to the map pixelisation and the instrumental beam. In both cases, the effect can be modelled via a convolution between the original signal and the beam or pixel; in Fourier space, this results in the product between the C_ℓ and the corresponding window functions. In formulae, it is possible to predict the CMB spectrum measured from a real map, C_ℓ^{obs} , as:

$$C_\ell^{\text{obs}} = C_\ell^{\text{theo}} B_\ell w_\ell, \quad (1.39)$$

Este documento incorpora firma electrónica, y es copia auténtica de un documento electrónico archivado por la ULL según la Ley 39/2015.
Su autenticidad puede ser contrastada en la siguiente dirección <https://sede.ull.es/validacion/>

Identificador del documento: 973742	Código de verificación: Jfg6xBh0	Fecha: 30/06/2017 15:10:10
Firmado por: DENIS TRAMONTE UNIVERSIDAD DE LA LAGUNA		
RAFAEL DELFIN BARRENA DELGADO UNIVERSIDAD DE LA LAGUNA		30/06/2017 15:21:31
JOSE ALBERTO RUBIÑO MARTIN UNIVERSIDAD DE LA LAGUNA		30/06/2017 15:34:17
ERNESTO PEREDA DE PABLO UNIVERSIDAD DE LA LAGUNA		06/07/2017 13:51:19

with C_ℓ^{theo} the original spectrum and B_ℓ and w_ℓ the beam and the pixel window functions, respectively.

1.3.2 Cosmological interpretation of the angular power spectrum

We explain now the relation between the CMB angular power spectrum and the values of the cosmological parameters. A detailed description can be found in Hu et al. (1998), Hu et al. (2001), Scott & Smoot (2006) and in Bucher (2015). In order to visualise the impact of the cosmology on the C_ℓ coefficients, in figure 1.4 we plot the power spectrum corresponding to the baseline cosmology of table 1.2, together with the spectrum resulting from changing the value of one cosmological parameter at a time.

First of all, the overall amplitude of the power spectrum depends crucially on the dark matter content of the Universe, Ω_{DM} . To understand why, one has to remember that the observed temperature anisotropies are a memory of the (baryonic) matter perturbations imprinted on the radiation field before recombination; to account for the observed current value of density perturbation, linear perturbation theory predicts a value of the matter perturbations at recombination such that the consequent temperature fluctuations would be of order $\Delta T/T \approx 10^{-3}$, a value that is not observed. The introduction of dark matter can solve the contradiction (Peebles 1982): the interaction between baryonic matter and radiation prevents baryon density perturbations to grow; density perturbations in dark matter, instead, are free to grow, since this kind of matter does not interact with the photons. Once recombination occurs, the baryons are not coupled to photons anymore, and they are free to fall into the potential wells previously generated by the growth of dark matter perturbations; this process is capable of generating the observed present density contrast even with the observed temperature anisotropies of $\Delta T/T \approx 10^{-5}$.

More specific features of the power spectrum, for a given multipole range, reflect the physical processes occurring over the corresponding scale. A fundamental length is the angular size of the causal horizon at the last scattering surface, which is around 2 degrees or $\ell \simeq 100$. At scales larger than that, $\ell \lesssim 100$, what we see is the primordial power spectrum generated by inflation, unaffected by the physical processes that take place at recombination. From figure 1.4 we see that the spectrum at low ℓ is quite flat. The shape of the low ℓ power spectrum is sensitive to the scalar spectral index n_s (a spectral index close to unity results in a nearly flat power spectrum at low ℓ , as observed).

For $\ell \gtrsim 100$ the shape of the power spectrum is determined by the physical processes that take place at recombination, which produce the *primary anisotropies* of the CMB. Before recombination, the coupling between matter

Este documento incorpora firma electrónica, y es copia auténtica de un documento electrónico archivado por la ULL según la Ley 39/2015.
Su autenticidad puede ser contrastada en la siguiente dirección <https://sede.ull.es/validacion/>

Identificador del documento:	973742	Código de verificación:	Jfg6xBh0
Firmado por:	DENIS TRAMONTE UNIVERSIDAD DE LA LAGUNA	Fecha:	30/06/2017 15:10:10
	RAFAEL DELFIN BARRENA DELGADO UNIVERSIDAD DE LA LAGUNA		30/06/2017 15:21:31
	JOSE ALBERTO RUBIÑO MARTIN UNIVERSIDAD DE LA LAGUNA		30/06/2017 15:34:17
	ERNESTO PEREDA DE PABLO UNIVERSIDAD DE LA LAGUNA		06/07/2017 13:51:19

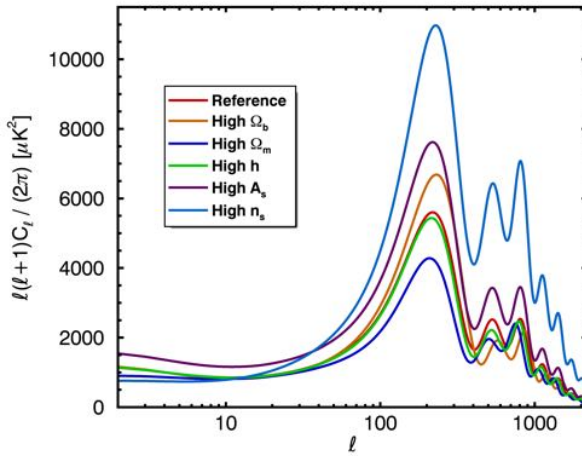


Figure 1.4: Effect of changing one cosmological parameter at a time on the CMB angular power spectrum. When different from their reference values, cosmological parameters are set to: $\Omega_b = 0.08$, $\Omega_m = 0.45$, $h = 0.75$, $A_s = 3.4 \times 10^9$, $n_s = 1.25$, as in figure 1.3.

and radiation implied that any bulk motion of the photons had to be shared by the baryons. The whole system underwent acoustic oscillations, driven by the contrast between the gravitational attraction of matter and the radiation pressure. As a result, the spectrum shows a series of peaks, which are the CMB equivalent of the BAO wiggles that we saw in the matter power spectrum (figure 1.3). This region of the power spectrum can therefore provide a vast amount of information about physical parameters of the cosmic fluid (Hu & Dodelson 2002). For instance, the first peak is particularly important in constraining the total energy density of the Universe, while the relative amplitude of the first peak to the plateau amplitude depends on the ratio $\Omega_b/\Omega_{\text{DM}}$.

The CMB power spectrum also shows the effect of *secondary anisotropies*, imprinted on the CMB after recombination. Among the most relevant sources of secondary anisotropies, we can cite the *Sunyaev-Zel'dovich effect* (Sunyaev & Zeldovich 1970), the *Integrated Sachs-Wolfe effect* (Sachs & Wolfe 1967), the *Rees-Sciama effect* (Rees & Sciama 1968), the *Ostriker-Vishniac effect* (Ostriker & Vishniac 1986), the interaction with ionised baryons after reionisation, and gravitational lensing by large scale structures. A complete description of

Este documento incorpora firma electrónica, y es copia auténtica de un documento electrónico archivado por la ULL según la Ley 39/2015.
Su autenticidad puede ser contrastada en la siguiente dirección <https://sede.ull.es/validacion/>

Identificador del documento: 973742

Código de verificación: Jfg6xBh0

Fecha: 30/06/2017 15:10:10

Firmado por: DENIS TRAMONTE
UNIVERSIDAD DE LA LAGUNA

RAFAEL DELFIN BARRENA DELGADO
UNIVERSIDAD DE LA LAGUNA

JOSE ALBERTO RUBIÑO MARTIN
UNIVERSIDAD DE LA LAGUNA

ERNESTO PEREDA DE PABLO
UNIVERSIDAD DE LA LAGUNA

30/06/2017 15:21:31

30/06/2017 15:34:17

06/07/2017 13:51:19

these effects is beyond the scope of this work, with the exception of the Sunyaev-Zel'dovich effect, which will be extensively considered in the following. For a review on secondary anisotropies see e.g. Refregier (1999) or Aghanim et al. (2008). Finally, the loss of power at high values of ℓ is called *Silk damping* (Silk 1968); it is due to photon diffusion from higher to lower density regions, resulting in a reduction of the fluctuations amplitude due to the coupling between matter and radiation.

1.3.3 CMB polarisation

The cosmic microwave background radiation is polarised, the mechanism responsible being Thomson scattering of photons by electrons at the last scattering surface (Zaldarriaga & Seljak 1997; Seljak & Zaldarriaga 1997; Kamionkowski et al. 1997). The presence of a quadrupole pattern in the CMB temperature (that is, in term of the anisotropies, the $l = 2$ component) results in the generation of a linear polarisation of the CMB after the Thomson scattering. More precisely, for a single scattering process, if the incident radiation is unpolarised, the scattered one is linearly polarised as a result of the angular dependence of the differential cross section of Thomson scattering, $d\sigma/d\Omega \propto 1 + \cos^2 \theta$, with θ the angle between the incident and scattered directions. However, if the incoming radiation field were isotropic, the contributions from orthogonal polarisation states (associated with orthogonal incident directions) would cancel out; instead, if the incoming radiation field possesses a quadrupolar variation in intensity, the scattered radiation emerges with a non-null linear polarisation (Hu & White 1997). This means that the Stokes parameter V is null, and the polarisation can be described as a combination of the parameters Q and U .

It is therefore possible to build CMB polarisation maps, as it was done for the intensity, and analyse their spectral properties. Since Q and U are not scalar fields, it is not possible to write for them a decomposition equivalent to equation 1.34 for the temperature. However, the combinations $Q \pm iU$ are quantities of spin ± 2 , and as such they can be decomposed in terms of a set of spin-weighted harmonics ${}_{\pm 2}Y_{\ell}^m$ as (Goldberg et al. 1967):

$$(U + iQ)(\hat{\mathbf{n}}) = \sum_{\ell>0} \sum_{m=-\ell}^{+\ell} a_{2,\ell m} {}_2Y_{\ell}^m(\hat{\mathbf{n}}), \quad (1.40)$$

$$(U - iQ)(\hat{\mathbf{n}}) = \sum_{\ell>0} \sum_{m=-\ell}^{+\ell} a_{-2,\ell m} {}_{-2}Y_{\ell}^m(\hat{\mathbf{n}}). \quad (1.41)$$

The Stokes parameters are quantities that depend on the reference frame in which they are defined. We follow here the convention adopted by the software

Este documento incorpora firma electrónica, y es copia auténtica de un documento electrónico archivado por la ULL según la Ley 39/2015.
Su autenticidad puede ser contrastada en la siguiente dirección <https://sede.ull.es/validacion/>

Identificador del documento: 973742

Código de verificación: Jfg6xBh0

Fecha: 30/06/2017 15:10:10

Firmado por: DENIS TRAMONTE
UNIVERSIDAD DE LA LAGUNA

RAFAEL DELFIN BARRENA DELGADO
UNIVERSIDAD DE LA LAGUNA

JOSE ALBERTO RUBIÑO MARTIN
UNIVERSIDAD DE LA LAGUNA

ERNESTO PEREDA DE PABLO
UNIVERSIDAD DE LA LAGUNA

30/06/2017 15:21:31

30/06/2017 15:34:17

06/07/2017 13:51:19

HEALPix (Górski & Hivon 2011), and consider an orthonormal base $(\mathbf{e}_1, \mathbf{e}_2, \mathbf{n})$, where the \mathbf{n} versor points towards the considered sky position, \mathbf{e}_1 points towards the local south and \mathbf{e}_2 points east to complete the right-handed frame. These versors define the sign of the Stokes parameter, the \mathbf{e}_1 (\mathbf{e}_2) being the direction for $Q > 0$ ($Q < 0$) and the bisector of \mathbf{e}_1 and \mathbf{e}_2 (\mathbf{e}_1 and $-\mathbf{e}_2$) being the direction for $U > 0$ ($U < 0$).

Now, the coefficients $a_{\pm 2, \ell m}$ are the actual observable quantities, like the $a_{T, \ell m}$ for temperature³. However, polarisation maps are usually decomposed in terms of the linear combinations (see e.g. Zaldarriaga & Seljak 1997; Kamionkowski et al. 1997; Zaldarriaga 1998):

$$\begin{aligned} a_{E, \ell m} &\equiv -\frac{a_{2, \ell m} + a_{-2, \ell m}}{2}, \\ a_{B, \ell m} &\equiv -\frac{a_{2, \ell m} - a_{-2, \ell m}}{2i}. \end{aligned} \quad (1.42)$$

These are scalar quantities, and are called *E-field* (or *gradient field*) and *B-field* (or *rotational field*). They allow for the following decompositions of the Stokes parameter (which are nothing more than a re-writing of equations 1.40 and 1.41):

$$\begin{aligned} Q(\hat{\mathbf{n}}) &= -\sum_{\ell m} a_{E, \ell m} X_{1, \ell m}(\hat{\mathbf{n}}) + i a_{B, \ell m} X_{2, \ell m}(\hat{\mathbf{n}}), \\ U(\hat{\mathbf{n}}) &= -\sum_{\ell m} a_{B, \ell m} X_{1, \ell m}(\hat{\mathbf{n}}) - i a_{E, \ell m} X_{2, \ell m}(\hat{\mathbf{n}}), \end{aligned} \quad (1.43)$$

where $X_{1, \ell m} \equiv ({}^2 Y_\ell^m + {}^{-2} Y_\ell^m)/2$ and $X_{2, \ell m} \equiv ({}^2 Y_\ell^m - {}^{-2} Y_\ell^m)/2i$. By proceeding as we did with the intensity field, we can define the power spectrum for each of the polarisation parameters as:

$$\langle a_{E, \ell m}^* a_{E, \ell' m'} \rangle \equiv \delta_{\ell \ell'} \delta_{mm'} C_{E\ell}, \quad \langle a_{B, \ell m}^* a_{B, \ell' m'} \rangle \equiv \delta_{\ell \ell'} \delta_{mm'} C_{B\ell}. \quad (1.44)$$

The existence of more than one random field also offers the possibility to define *cross-correlations*, so that one can write, more generally:

$$\langle a_{X, \ell m}^* a_{Y, \ell' m'} \rangle \equiv \delta_{\ell \ell'} \delta_{mm'} C_{\ell}^{XY}, \quad (1.45)$$

where $X, Y = T, E$ or B . When the two quantities are the same, one talks about *auto-correlations* and we recover the definition of the power spectra. In

³In this section we slightly change the notation from $a_{\ell m}$ to $a_{T, \ell m}$ to make the reference to the temperature field more clear.

analogy with equation (1.37), the last relation leads to the definition:

$$\hat{C}_\ell^{XY} \equiv \frac{1}{2\ell+1} \sum_{m=-\ell}^{+\ell} a_{X,\ell m}^* a_{Y,\ell m}. \quad (1.46)$$

The \hat{C}_ℓ^{XY} are the estimators for the quantities C_ℓ^{XY} .

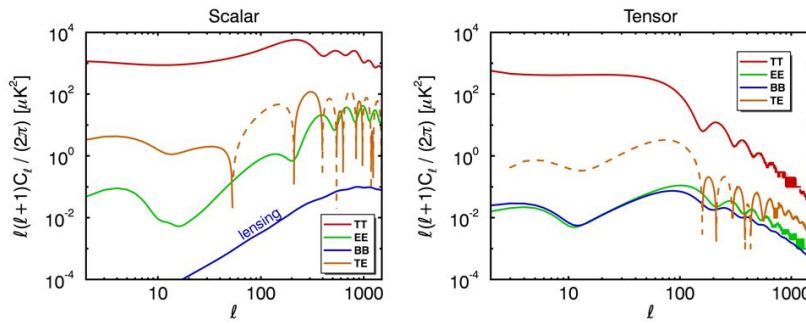


Figure 1.5: Auto-correlation power spectra C_ℓ^{TT} , C_ℓ^{EE} , C_ℓ^{BB} and cross-correlation power spectrum C_ℓ^{TE} , computed for our reference cosmology from table 1.2, in the case of purely scalar (left) and purely tensor (right) primordial perturbations. Discontinuous line means the cross-correlation C_ℓ^{TE} becomes negative.

Note that the cross-correlations C_l^{TB} and C_l^{EB} are expected to be null. Indeed, the coefficients $a_{E,\ell m}$ and $a_{B,\ell m}$ defined in 1.42 behave differently under a parity transformation: the $a_{E,\ell m}$ are scalars and are invariant, while the $a_{B,\ell m}$ are pseudo-scalars and they change the sign. As a result, when computing the cross-correlation C_l^{EB} , the average 1.45 vanishes for statistical isotropy. For the same reason the cross-correlation C_l^{TB} is also null. To sum up, CMB anisotropies are statistically characterised by a set of four functions: the auto-correlations C_l^{TT} , C_l^{EE} and C_l^{BB} (the power spectra), and the cross-correlation C_l^{TE} . Each of these quantities is related to a different physical mechanism of anisotropy generation at the last scattering surface.

We said that the CMB polarisation arises from the existence of a quadrupolar moment in the temperature field; the quadrupole is described by the spherical harmonics with $l = 2$ and $m = 0, \pm 1$ and ± 2 . These values of m correspond to three different sources of temperature anisotropies: the *scalar* (or *compressional*) perturbations, corresponding to $m = 0$; the *vector* (or *vortical*) perturbations, corresponding to $m = \pm 1$; and the *tensor* (or *gravita-*

Este documento incorpora firma electrónica, y es copia auténtica de un documento electrónico archivado por la ULL según la Ley 39/2015.
Su autenticidad puede ser contrastada en la siguiente dirección <https://sede.ull.es/validacion/>

Identificador del documento: 973742

Código de verificación: Jfg6xBh0

Fecha: 30/06/2017 15:10:10

Firmado por: DENIS TRAMONTE
UNIVERSIDAD DE LA LAGUNA

RAFAEL DELFIN BARRENA DELGADO
UNIVERSIDAD DE LA LAGUNA

JOSE ALBERTO RUBIÑO MARTIN
UNIVERSIDAD DE LA LAGUNA

ERNESTO PEREDA DE PABLO
UNIVERSIDAD DE LA LAGUNA

30/06/2017 15:21:31

30/06/2017 15:34:17

06/07/2017 13:51:19

tional wave) perturbations, corresponding to $m = \pm 2$. Vector modes generates time-decaying perturbations and are usually not considered. Scalar perturbations, due to fluctuations in density alone, can generate primordial E-modes in the CMB polarisation. Tensor perturbations, instead, can generate primordial B-modes, and are due to gravitational waves in the primordial Universe. A background of primordial gravitational waves is expected to be generated by inflation (Guzzetti et al. 2016). Hence, the detection of B-modes would be a very important evidence in favour of inflationary models. A commonly used quantity is the *tensor-to-scalar ratio* r , which is the relative amplitude of the tensor to the scalar primordial power spectra. The energy scale V at which inflation occurred is related to r through (Rubio-Martin et al. 2009; Planck Collaboration et al. 2016g):

$$r = 0.001 \left(\frac{V}{10^{16} \text{ GeV}} \right)^4, \quad (1.47)$$

so that the detection of B-modes and the determination of r would provide important insights into the physics of inflation.

In fig. 1.5 we show the different contributions of the C_ℓ^{XX} quantities, in the case of pure scalar and pure tensor primordial perturbations. We see that the polarisation angular power spectra are subdominant with respect to the pure temperature signal, meaning their detection is rather challenging. The B-modes signal visible in the scalar case is originated by gravitational lensing of E-modes by LSS in the path of the CMB photons from the last-scattering surface; this signal appears only at small scales. The lensed B-modes have been observed: the first (indirect) detection was achieved with the SPT experiment (Hanson et al. 2013), while the POLARBEAR experiment provided for the first time a direct detection (The Polarbear Collaboration: P. A. R. Ade et al. 2014). The next observational challenge is to detect the primordial large scale B-modes, for which only upper limits are currently available: $r \lesssim 0.11$ (at a scale $k = 0.002 h \text{ Mpc}^{-1}$, Planck Collaboration et al. 2016g). We will provide further information about experimental results in this field in section 1.3.4.

1.3.4 Observing the CMB

In this section we provide some information about the main experimental results in CMB research. Improvements in our knowledge of the CMB radiation have often been achieved thanks to an interplay between ground-based experiments and space-satellite experiments, which complemented each other in terms of spectral and spatial coverage. The main issue here is that we cannot observe directly the simple cosmic radiation field as coming from the surface of last

Este documento incorpora firma electrónica, y es copia auténtica de un documento electrónico archivado por la ULL según la Ley 39/2015.
Su autenticidad puede ser contrastada en la siguiente dirección <https://sede.ull.es/validacion/>

Identificador del documento:	973742	Código de verificación:	Jfg6xBh0
Firmado por:	DENIS TRAMONTE UNIVERSIDAD DE LA LAGUNA	Fecha:	30/06/2017 15:10:10
	RAFAEL DELFIN BARRENA DELGADO UNIVERSIDAD DE LA LAGUNA		30/06/2017 15:21:31
	JOSE ALBERTO RUBIÑO MARTIN UNIVERSIDAD DE LA LAGUNA		30/06/2017 15:34:17
	ERNESTO PEREDA DE PABLO UNIVERSIDAD DE LA LAGUNA		06/07/2017 13:51:19

scattering, but we have to face a lot of different sources of foreground radiation which actually constitute a contamination of the cosmic signal. Therefore, it is of fundamental importance to characterise and understand each type of foreground, in order to be able to remove it from the acquired data during the analysis process.

Observational issues

There are basically three sources of contamination affecting CMB observations.

- *Earth's atmosphere.* This contamination clearly affects only ground-based observations. The main problem regarding the atmosphere is that it is *turbulent* (Hinder 1970); as a result, apart from contributing with *white noise*, it contributes with a noise component that increases at large scales (*pink noise* or *1/f noise*, due to its frequency dependence). An absolutely homogeneous, plane-parallel symmetric atmosphere could be taken into account with a simple law like $\sec^{-1} \theta$ (with θ the angle from the zenith) and it would cancel out when considering two observations at the same elevation. However, its turbulence introduces large scale fluctuations that make observations of CMB at $l \lesssim 300$ very difficult from Earth. Besides, in the radio range our atmosphere is characterised by strong emission lines of oxygen (at 60 and 119 GHz) and water vapour (22 and 183 GHz), so that ground observations are usually carried on at frequencies below 22 GHz or in the bands within the lines, near 30 or 90 GHz (Danese & Partridge 1989).

In conclusion, the presence of the atmosphere limits CMB temperature observations from Earth to low frequencies and small angular scales. The atmospheric emission is not polarised, though, meaning that polarisation observations do not have this angular scale restriction. In general, the effect of the atmosphere is usually mitigated working at high-altitude, cold and dry sites (for telescopes) or by placing the instrumentation on balloons.

- *Galactic emission.* The Galactic emission comes through four basic different mechanisms, having each of them a specific frequency spectrum.

The *free-free emission*, or *bremsstrahlung*, is the radiation emitted by accelerated electrons in ionised gas regions (mainly HII regions); the temperature dependence on the frequency follows a power law of the form $T(\nu) \propto \nu^{-2.1}$, at least at sufficiently high frequency (usually greater than ~ 1 GHz). The relative contribution from this kind of emission falls

Este documento incorpora firma electrónica, y es copia auténtica de un documento electrónico archivado por la ULL según la Ley 39/2015.
Su autenticidad puede ser contrastada en la siguiente dirección <https://sede.ull.es/validacion/>

Firmado por:	Identificador del documento:	Código de verificación:	Fecha:
DENIS TRAMONTE UNIVERSIDAD DE LA LAGUNA	973742	Jfg6xBh0	30/06/2017 15:10:10
RAFAEL DELFIN BARRENA DELGADO UNIVERSIDAD DE LA LAGUNA			30/06/2017 15:21:31
JOSE ALBERTO RUBIÑO MARTIN UNIVERSIDAD DE LA LAGUNA			30/06/2017 15:34:17
ERNESTO PEREDA DE PABLO UNIVERSIDAD DE LA LAGUNA			06/07/2017 13:51:19

down at high frequency. However, it is dominated at $\nu \lesssim 50$ GHz by synchrotron emission, and at $\nu \gtrsim 150$ GHz by thermal dust emission, so that its subtraction is difficult. The characterisation of its spatial distribution take advantage of its correlation with the H α line emission (Smoot 1998; Gaustad et al. 2001; Haffner et al. 2003). The free-free emission is intrinsically unpolarised, due to the isotropy and randomness of the directions of scattered electrons; observationally, an upper limit of 1% has been set for the free-free polarisation fraction averaged over the sky (Macellari et al. 2011).

The second type of Galactic foreground is the *synchrotron emission*, which is the radiation emitted by electrons (or other charged particles) spiralling in a magnetic field at relativistic velocities. These relativistic electrons are the electron component of the cosmic rays that pervade our Galaxy and are produced in supernova explosions; the magnetic field is the galactic magnetic field. This emission is characterised by a power-law dependence $T(\nu) \propto \nu^\beta$ with $\beta \simeq -2.7$ (Bennett et al. 2013), although β can change from place to place; anyway, its contribution falls off with frequency more rapidly than the free-free emission. For this reason it is typically important for frequencies below 100 GHz (Haslam et al. 1982). Synchrotron radiation is highly polarised, due to the directional pattern of this emission (the energy is radiated mainly in the plane of the electron motion). Data from the *Planck* satellite (see section 1.3.4) enabled to build a synchrotron polarisation map (Planck Collaboration et al. 2016j), with values for the polarisation fraction up to 50%.

Another contribution is the *thermal emission of dust grains*. Dust constitutes the 1% in mass of the interstellar matter and is made of solid particles of sizes in the range $0.01 - 1 \mu\text{m}$; despite this small contribution, it is very effective in altering starlight through extinction and reddening (Schlegel et al. 1998). Besides, it is responsible for a continuous emission in the infrared and millimetric region of the spectrum, in the form of a modified blackbody spectrum with a frequency dependence $T(\nu) \propto \nu^{2+\beta}$, with β typically between 1 and 2 (Planck Collaboration et al. 2014c). It is the dominant contribution for frequencies above 150 GHz. Dust grains responsible for this radiation are usually non-spherical, and tend to be oriented according to the direction of the local magnetic field; this alignment results in the thermal dust emission being polarised, with a polarisation fraction up to 20% (Planck Collaboration et al. 2015b).

Finally, the *anomalous microwave emission* (AME), which does not follow a power law, but peaks at frequencies around 20 – 30 GHz; it has

Este documento incorpora firma electrónica, y es copia auténtica de un documento electrónico archivado por la ULL según la Ley 39/2015.
Su autenticidad puede ser contrastada en la siguiente dirección <https://sede.ull.es/validacion/>

Identificador del documento:	973742	Código de verificación:	Jfg6xBh0
Firmado por:	DENIS TRAMONTE UNIVERSIDAD DE LA LAGUNA	Fecha:	30/06/2017 15:10:10
	RAFAEL DELFIN BARRENA DELGADO UNIVERSIDAD DE LA LAGUNA		30/06/2017 15:21:31
	JOSE ALBERTO RUBIÑO MARTIN UNIVERSIDAD DE LA LAGUNA		30/06/2017 15:34:17
	ERNESTO PEREDA DE PABLO UNIVERSIDAD DE LA LAGUNA		06/07/2017 13:51:19

been interpreted as an electro-dipole radiation from small spinning dust grains (Draine & Lazarian 1998; Bonaldi et al. 2007; Rubiño-Martín et al. 2012a). Despite theoretical models normally predict non-null AME polarisation, usually at a level below 10%, observations have only provided upper limits on the AME polarisation fraction, the most stringent being below 1% (Rubiño-Martín et al. 2012a; Génova-Santos et al. 2017).

To the above list it is possible to add the *zodiacal light*, even if its origin is more local than Galactic. It is due to the Sun light reflected by small dust particles in the Solar System (interplanetary dust particles). It peaks at submillimetre wavelengths (e.g., Leinert et al. 1997) and as such it affects mainly radio observations at high frequencies. Spatial and frequency models of the zodiacal light emission are used in radio surveys to characterise its contribution to the resulting sky maps (Planck Collaboration et al. 2014e).

We see that, talking about frequency, there is not a preferred observational strategy to follow when dealing with the Galactic foregrounds. One can perform observations at the frequency region where the total galactic contribution has its minimum, but in this case there are at least two mechanisms contributing in a comparable way to the contamination; or one can observe in frequency ranges where a singular process dominates over the others, but paying the price of a higher contamination (see figure 1.6). Instead, when talking about the preferred angular size, the Galactic foreground generally favours observations at large l (or small angular size).

- *Extragalactic emission.* The extragalactic radio sources are typically synchrotron emitters⁴; depending on the case, they can be seen as individual objects or they contribute with a noise-like foreground without the possibility of being identified individually (Sadler et al. 2006). In both cases, the contamination becomes a major problem at large l , or at small angular scales (the opposite behaviour with respect to the atmospheric and galactic foregrounds). They can be treated in different ways, by studying their properties observationally, through radio surveys; or by directly masking out their contribution, as is usually done when they can be identified individually.

Another important extragalactic contribution comes from the *cosmic infrared background* (CIB, Wright & Reese 2000; Hauser & Dwek 2001; Dole

⁴They also contribute with free-free emission, but at low frequencies sources with a strong synchrotron component are the ones that are most easily identified.

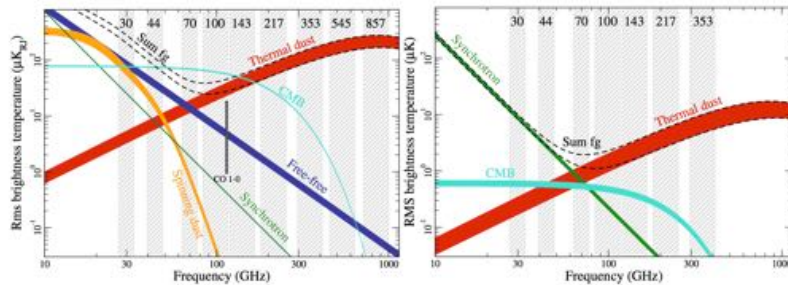


Figure 1.6: Brightness of foregrounds contribution compared to the CMB signal, in the case of intensity (left) and polarisation (right). We see that in intensity there is a frequency window in which the CMB is dominant, while it is always subdominant in polarisation. Figure taken from Planck Collaboration et al. (2016a).

et al. 2006). This foreground peaks at submillimetre wavelengths, so it can affect highest frequency radio observations; it is produced by the photons released by the processes of structure formation that have taken place since recombination. As a consequence, it also shows anisotropies that trace the clustering of galaxies, which can be studied in relation with the underlying dark matter distribution (Planck Collaboration et al. 2011d).

It is clear that a large variety of experimental techniques is required to face all these contributions; from here we understand the importance of the complementarity between experiments on Earth and in space.

CMB Experiments

The milestones in the process of detecting CMB anisotropies were three satellite missions (see figure 1.7):

- The NASA COBE (*COsmic Background Explorer*) satellite was launched in November 1989 (Mather et al. 1990). COBE carried three instruments: the *Far Infrared Absolute Spectrometer* (FIRAS, Mather et al. 1994), for measuring the CMB spectrum; the *Differential Microwave Radiometer* (DMR, Smoot et al. 1992), to map the anisotropies of the CMB temperature field; and the *Diffuse InfraRed Background Experiment* (DIRBE, Kashlinsky et al. 1996), an infrared detector for the study of dust emission. The FIRAS instrument confirmed the blackbody shape of the CMB

Este documento incorpora firma electrónica, y es copia auténtica de un documento electrónico archivado por la ULL según la Ley 39/2015.
Su autenticidad puede ser contrastada en la siguiente dirección <https://sede.ull.es/validacion/>

Identificador del documento: 973742	Código de verificación: Jfg6xBh0	Fecha: 30/06/2017 15:10:10
Firmado por: DENIS TRAMONTE UNIVERSIDAD DE LA LAGUNA		
RAFAEL DELFIN BARRENA DELGADO UNIVERSIDAD DE LA LAGUNA		30/06/2017 15:21:31
JOSE ALBERTO RUBIÑO MARTIN UNIVERSIDAD DE LA LAGUNA		30/06/2017 15:34:17
ERNESTO PEREDA DE PABLO UNIVERSIDAD DE LA LAGUNA		06/07/2017 13:51:19

spectrum, allowing the temperature estimate in 1.32, while the DMR instrument provided a first sky map of temperature anisotropies. The instrument beam was about 7 degrees in size, so that the information on the power spectrum could be recovered only up to $l \approx 25$.

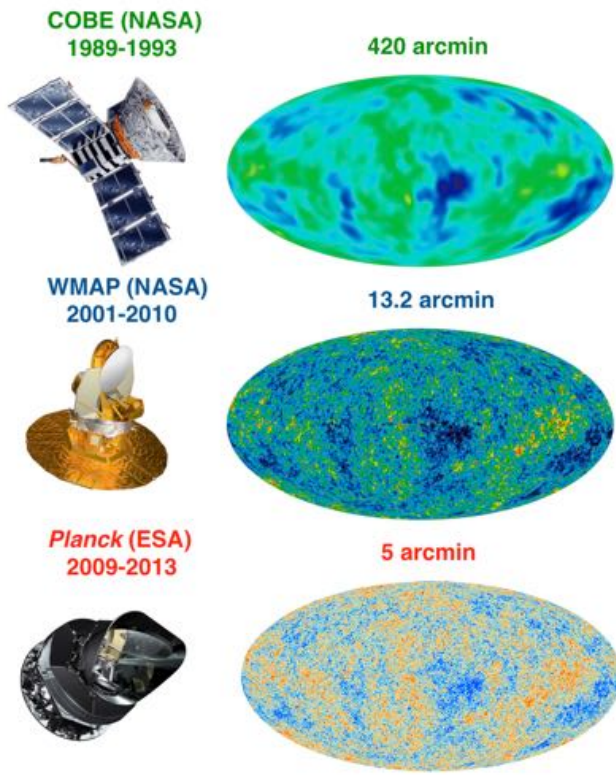


Figure 1.7: Summary of CMB space missions.

- The following NASA satellite for the study of the CMB, WMAP, (*Wilkinson Microwave Anisotropy Probe*), was launched in June 2001 and it greatly improved the results obtained with COBE (Bennett et al. 2013; Hinshaw et al. 2013). It measured the CMB temperature at five different frequencies, at 23, 33, 41, 61 and 94 GHz, with a maximum resolution at

Este documento incorpora firma electrónica, y es copia auténtica de un documento electrónico archivado por la ULL según la Ley 39/2015.
Su autenticidad puede ser contrastada en la siguiente dirección <https://sede.ull.es/validacion/>

Identificador del documento:	973742	Código de verificación:	Jfg6xBh0
Firmado por:	DENIS TRAMONTE UNIVERSIDAD DE LA LAGUNA	Fecha:	30/06/2017 15:10:10
	RAFAEL DELFIN BARRENA DELGADO UNIVERSIDAD DE LA LAGUNA		30/06/2017 15:21:31
	JOSE ALBERTO RUBIÑO MARTIN UNIVERSIDAD DE LA LAGUNA		30/06/2017 15:34:17
	ERNESTO PEREDA DE PABLO UNIVERSIDAD DE LA LAGUNA		06/07/2017 13:51:19

the highest frequency of 13.2 arcminutes FWHM. This resolution enabled the study of the angular power spectrum up to $l \approx 1000$ (but with increasing errors for the highest values of l). The WMAP results have played a fundamental role in establishing the standard cosmological model, and in refining important cosmological parameters; it marked the beginning of the era of “precision cosmology”.

- The WMAP successor is the ESA *Planck* satellite, launched in May 2009 ([Planck Collaboration et al. 2016a](#)). *Planck*’s observations improved and extended WMAP’s results. The spacecraft carried two instruments: the *Low Frequency Instrument* (LFI, [Planck Collaboration et al. 2014a](#)), observing at 30, 44 and 70 GHz, and the *High Frequency Instrument* (HFI, [Planck Collaboration et al. 2014b](#)), observing at 100, 143, 217, 353, 545 and 857 GHz; the resolution depends on the frequency, but in the best cases it is as small as 5’, and this enabled to push the power spectrum analyses up to $l \simeq 2500$. The multipole range covered by *Planck* is actually the broadest to date, and this gave the opportunity to study a very extended region of the spectrum with data coming from a single instrument, thus avoiding possible systematic errors that can arise when combining data from two different experiments. *Planck*’s cosmological results on CMB anisotropies have been published in two releases, the first in 2013 [Planck Collaboration et al. \(2014f\)](#) and the second in [Planck Collaboration et al. \(2016e\)](#). The mission has confirmed the flat Universe cosmological model and refined the values of cosmological parameters.

In the meantime, other experiments were being carried on from Earth to target more specific observational purposes and to complete the satellite data sets with the study of the CMB radiation at smaller angular scales. The BOOMERanG experiment ([de Bernardis et al. 2001](#)) provided the first consistent detection of the first and second acoustic peaks, thus setting an important constraint over the total energy density of the Universe ([Masi 2002](#)). DASI detected the first peak in agreement with the other experiments, and it also detected the second and third acoustic peaks, showing consistency with the adiabatic inflationary cosmological models; finally, it provided a first detection of CMB E-mode polarisation ([Leitch et al. 2005](#)). The CBI experiment ([Padin et al. 2001](#)) detected the Silk damping of the spectrum and an excess of power at scales $\ell \gtrsim 2500$, which was later ascribed to the contribution of point radio sources; it also obtained the first detailed E-mode polarisation spectrum. MAXIMA ([Rabii et al. 2006](#)) was a balloon-borne experiment; it also enabled the detection of the first three acoustic peaks, providing estimates on the geometry of the Universe and the baryon density in agreement with the standard

Este documento incorpora firma electrónica, y es copia auténtica de un documento electrónico archivado por la ULL según la Ley 39/2015.
Su autenticidad puede ser contrastada en la siguiente dirección <https://sede.ull.es/validacion/>

Identificador del documento:	973742	Código de verificación:	Jfg6xBh0
Firmado por:	DENIS TRAMONTE UNIVERSIDAD DE LA LAGUNA	Fecha:	30/06/2017 15:10:10
	RAFAEL DELFIN BARRENA DELGADO UNIVERSIDAD DE LA LAGUNA		30/06/2017 15:21:31
	JOSE ALBERTO RUBIÑO MARTIN UNIVERSIDAD DE LA LAGUNA		30/06/2017 15:34:17
	ERNESTO PEREDA DE PABLO UNIVERSIDAD DE LA LAGUNA		06/07/2017 13:51:19

cosmological model (Stompor et al. 2003). *Archeops* (Benoit et al. 2004) was another balloon-borne experiment that, for the first time and before WMAP, joined in a single observation the large angular scales already sampled by COBE satellite and the first acoustic peak region, confirming the flatness of the Universe. ACBAR (Reichardt et al. 2009) provided the most precise high- ℓ CMB spectral data to that date.

At the Teide Observatory in Tenerife (Rebolo et al. 2000) CMB studies began with the *Tenerife CMB Experiment* (Davies et al. 1987), that provided an independent confirmation of CMB anisotropies discovered by COBE. The IAC-Bartol Experiment (Femenia et al. 1998) and the JBO-IAC interferometer (Harrison et al. 2000) both measured the CMB anisotropies with an angular resolution of 2° and 1° respectively. VSA (Dickinson et al. 2004; Rebolo et al. 2004) was the first experiment to clearly measure the third acoustic peak (Grainge et al. 2003) and contributed to constraining cosmological parameters like the total energy density or the baryonic energy density. COSMOSMAS (Galegos et al. 2001) gave an important contribution to the characterisation of the anomalous microwave emission (Watson et al. 2005). The latest CMB experiment at Teide Observatory is QUIJOTE, to which we will dedicate chapter 5 of this work.



Figure 1.8: Pictures of ACT, SPT, BICEP2 and the two C-BASS telescopes.

Este documento incorpora firma electrónica, y es copia auténtica de un documento electrónico archivado por la ULL según la Ley 39/2015.
Su autenticidad puede ser contrastada en la siguiente dirección <https://sede.ull.es/validacion/>

Identificador del documento: 973742	Código de verificación: Jfg6xBh0
Firmado por: DENIS TRAMONTE UNIVERSIDAD DE LA LAGUNA	Fecha: 30/06/2017 15:10:10
RAFAEL DELFIN BARRENA DELGADO UNIVERSIDAD DE LA LAGUNA	30/06/2017 15:21:31
JOSE ALBERTO RUBIÑO MARTIN UNIVERSIDAD DE LA LAGUNA	30/06/2017 15:34:17
ERNESTO PEREDA DE PABLO UNIVERSIDAD DE LA LAGUNA	06/07/2017 13:51:19

More recent experiments were specifically dedicated to the observation of CMB polarisation. QUIET (Bischoff et al. 2013) detected the E-mode and contributed to the constraint on the level of B-mode (QUIET Collaboration et al. 2011, 2012). POLARBEAR provided a measurement of the secondary B-modes anisotropy generated by lensing (The Polarbear Collaboration; P. A. R. Ade et al. 2014). The *Atacama Cosmology Telescope* (ACT, figure 1.8), in a first phase provided CMB-based cosmological constraints in Das et al. (2011), Sherwin et al. (2011) and Sievers et al. (2013), and played a major role in the detection of clusters of galaxies (Hasselfield et al. 2013), as we will see better in the next section. The second phase of the experiment, ACTpol, began in 2013 and consisted in the deployment of a polarisation sensitive receiver; the main scientific highlights can be found in Naess et al. (2014) and van Engelen et al. (2015). The *South Pole Telescope* (SPT, figure 1.8) mapped a large sky area at three frequency bands and high resolution (Story et al. 2013; George et al. 2015), giving also important contributions to the detection of clusters of galaxies (Reichardt et al. 2013; Bleem et al. 2015). The second phase of the experiment is dedicated to the measurement of the CMB polarisation (Crites et al. 2015; Keisler et al. 2015). Another series of CMB polarisation experiments in the South Pole began with BICEP1 (Barkats et al. 2014), later replaced by BICEP2 (figure 1.8), which claimed the detection of primordial B-modes at a level corresponding to $r \simeq 0.2$ (BICEP2 Collaboration et al. 2014); this result, however, was lately proven wrong, the detected B-modes signal coming from a residual dust contribution (Ade et al. 2015). The experiment continues with its latest phase (the Keck Array, BICEP2 Collaboration et al. 2016). Finally, the C-BASS experiment (C-Band All Sky Survey, King et al. 2010, figure 1.8) is dedicated to synchrotron characterisation in temperature and polarisation at low frequencies; preliminary results can be found in Irfan et al. (2015).

The detailed characterisation of the polarisation anisotropies is the new frontier in CMB cosmology. As already mentioned, in chapter 5 we will consider in detail the QUIJOTE experiment, which is specifically designed for observing the polarisation of the CMB and other galactic and extragalactic foregrounds.

1.4 Clusters of galaxies

As we saw in section 1.2, the growth of structures in a Universe dominated by cold dark matter follows a bottom-up scenario. Overdense regions eventually decouple from the background expansion and collapse upon themselves reaching virial equilibrium. This process first happens for smaller scale perturbations, which have the greater amplitude, so that the first object to collapse are subgalactic. These objects, in turn, once virialised, under the mutual gravitational

Este documento incorpora firma electrónica, y es copia auténtica de un documento electrónico archivado por la ULL según la Ley 39/2015.
Su autenticidad puede ser contrastada en la siguiente dirección <https://sede.ull.es/validacion/>

Identificador del documento:	973742	Código de verificación:	Jfg6xBh0
Firmado por:	DENIS TRAMONTE UNIVERSIDAD DE LA LAGUNA	Fecha:	30/06/2017 15:10:10
	RAFAEL DELFIN BARRENA DELGADO UNIVERSIDAD DE LA LAGUNA		30/06/2017 15:21:31
	JOSE ALBERTO RUBIÑO MARTIN UNIVERSIDAD DE LA LAGUNA		30/06/2017 15:34:17
	ERNESTO PEREDA DE PABLO UNIVERSIDAD DE LA LAGUNA		06/07/2017 13:51:19

interaction, group into larger structures.

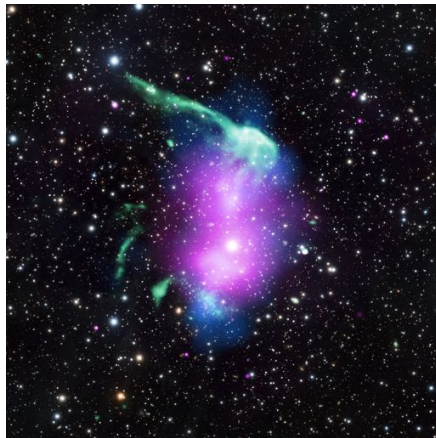


Figure 1.9: A composite, multi-wavelength image of the Toothbrush Cluster. Image credit: X-ray: NASA/CXC/SAO/R. van Weeren et al; Radio: LOFAR/ASTRON; Optical: NAOJ/Subaru.

Galaxy clusters lie at the top of the structure hierarchy: they are the biggest objects that have reached virial equilibrium, and the last ones to form (Voit 2005; Allen et al. 2011). We do not expect to observe clusters at redshift $z \gtrsim 2$. For the sake of comparison, the first generation of stars formed at $z \sim 30$, and the first generation of galaxies at $z \sim 10$, at the end of the reionisation era. Clusters contain typically 100 to 1000 luminous galaxies, and have a characteristic scale of ~ 1 Mpc, resulting in angular extents on the sky from one arcminute to one degree for the lowest redshift clusters. We know cluster masses to span the range from 10^{13} to $10^{15} M_{\odot}$.

Despite their name, clusters do not contain only galaxies. Actually, they are complex multi-component systems made of dark matter and baryonic matter in several phases. They form at the positions of the peaks of the large scale matter distribution, i.e. the largest dark matter halos. Even though they were first identified thanks to the visible light coming from stars and galaxies, the total stellar mass is just a small fraction of the total cluster mass; in a cluster we can also find cold, molecular gas, warm and hot gas and nonthermal plasma. The strong potential well generated by the halo gravitational pull heats up the intracluster medium (ICM), resulting in cluster cores filled with hot plasma with electron temperatures around $T_e \sim 5 - 10$ keV on average.

Este documento incorpora firma electrónica, y es copia auténtica de un documento electrónico archivado por la ULL según la Ley 39/2015.
Su autenticidad puede ser contrastada en la siguiente dirección <https://sede.ull.es/validacion/>

Identificador del documento: 973742

Código de verificación: Jfg6xBh0

Fecha: 30/06/2017 15:10:10

Firmado por: DENIS TRAMONTE
UNIVERSIDAD DE LA LAGUNA

RAFAEL DELFIN BARRENA DELGADO
UNIVERSIDAD DE LA LAGUNA

JOSE ALBERTO RUBIÑO MARTIN
UNIVERSIDAD DE LA LAGUNA

ERNESTO PEREDA DE PABLO
UNIVERSIDAD DE LA LAGUNA

30/06/2017 15:21:31

30/06/2017 15:34:17

06/07/2017 13:51:19

This complex composition is actually an advantage, in the sense that clusters can be observed in different wavelengths according to the component we are observing. In fact, the observation of clusters in a specific spectral range is sensitive to a physical process rather than others, and the combination of different observational data can provide a better understanding of the cluster properties. This is particularly important given that the cluster mass, which is the quantity most easily related to theory, is not directly observable. Different types of observations can provide different methods for computing the mass, which are usually referred to as *mass proxies*.

In the following, we describe the three main spectral ranges in which cluster emission can be observed, optical, X-rays and radio, adding also some information on the possibility of detecting clusters with gravitational lensing effects.

1.4.1 Clusters in optical light

Optical and near infrared emission from galaxy clusters is almost exclusively light emitted from stars. Indeed, in this spectral range the hot gas is not visible and clusters appear as groups of individual galaxies. Clusters members are mainly elliptical and lenticular galaxies (more generally, *early-type galaxies*), especially in the central region, where the largest and brightest ones lie.

Optical observation of galaxy clusters is now a well established field (Biviano 2000). By the end of the eighteenth century, C. Messier and W. Herschel had already identified concentrations of galaxies in the constellations of Virgo and Coma Berenices, which are known today indeed as the Virgo cluster and the Coma cluster. The constant improvement in cluster optical observations with time led to the remarkable result of Abell's catalogs (Abell 1958; Abell et al. 1989). His detection method was based on the magnitude of member galaxies. The cluster distance was estimated from the apparent magnitude of its tenth brightest member galaxy. Then, all the galaxies lying within a fixed projected radius (which could be determined from the distance evaluation) and brighter than a magnitude threshold set at two magnitudes below the brightest cluster galaxy, were considered members. After correcting for projection effects, only those candidates with at least 50 galaxies brighter than the threshold were taken as effective galaxy clusters.

Current cluster identification techniques extend and refine the method introduced by Abell (e.g., Lumsden et al. 1992; Dalton et al. 1997). A useful additional information is the color of galaxies, which can help identifying distant clusters, for which the contrast with respect to the background is less evident. An interesting property of many clusters is that their bulk of early-type galaxies are redder than other galaxies at the same redshift, due to their

Este documento incorpora firma electrónica, y es copia auténtica de un documento electrónico archivado por la ULL según la Ley 39/2015.
Su autenticidad puede ser contrastada en la siguiente dirección <https://sede.ull.es/validacion/>

Identificador del documento:	973742	Código de verificación:	Jfg6xBh0
Firmado por:	DENIS TRAMONTE UNIVERSIDAD DE LA LAGUNA	Fecha:	30/06/2017 15:10:10
	RAFAEL DELFIN BARRENA DELGADO UNIVERSIDAD DE LA LAGUNA		30/06/2017 15:21:31
	JOSE ALBERTO RUBIÑO MARTIN UNIVERSIDAD DE LA LAGUNA		30/06/2017 15:34:17
	ERNESTO PEREDA DE PABLO UNIVERSIDAD DE LA LAGUNA		06/07/2017 13:51:19

lack of ongoing star formation. As a result, these galaxies lie in a specific region of the color-magnitude diagram, which is known as the *red sequence* (Gladders & Yee 2000). New search methods exploit this strong empirical property and use the red sequence as a direct indicator of overdensities where clusters can be found.

Once a cluster has been identified, its mass must be estimated. In principle, this could be inferred from its total luminosity, but the determination of the latter by adding the luminosities of individual galaxies is not feasible, especially for farther clusters in which only the brightest members can be detected. However, the luminosity function of member galaxies (i.e., the number of galaxies per luminosity interval) shows a substantial homogeneity among clusters (Schechter 1976); this implies that it is possible to use the luminosity information from the nearest clusters to fit for the low luminosity tail of the distribution in case of distant ones, and to get an estimate of their total luminosity, and the corresponding mass. Another important way of estimat-



Figure 1.10: The Abell cluster in optical light, observed by the Hubble Space Telescope. The effect of gravitational lensing of background light is also visible. Credit: NASA, ESA, Hubble Heritage Team (STScI/AURA), and J. Blakeslee (NRC Herzberg, DAO) & H. Ford (JHU).

ing the mass of a cluster from optical observations is to measure the velocity dispersion of its galaxies. This also provides a tool for better identifying a cluster: since such distribution is expected to be gaussian, galaxies whose velocity falls outside the gaussian best fit are unlikely member galaxies, and they can

Este documento incorpora firma electrónica, y es copia auténtica de un documento electrónico archivado por la ULL según la Ley 39/2015.
Su autenticidad puede ser contrastada en la siguiente dirección <https://sede.ull.es/validacion/>

Identificador del documento: 973742

Código de verificación: Jfg6xBh0

Fecha: 30/06/2017 15:10:10

Firmado por: DENIS TRAMONTE
UNIVERSIDAD DE LA LAGUNA

RAFAEL DELFIN BARRENA DELGADO
UNIVERSIDAD DE LA LAGUNA

JOSE ALBERTO RUBIÑO MARTIN
UNIVERSIDAD DE LA LAGUNA

ERNESTO PEREDA DE PABLO
UNIVERSIDAD DE LA LAGUNA

30/06/2017 15:21:31

30/06/2017 15:34:17

06/07/2017 13:51:19

be discarded. Also, if the velocity distribution is far from being a gaussian, then the candidate is not a cluster, being more probably a superposition of smaller independent structures. The gaussianity of the distribution is expected since clusters are relaxed, virialised objects; a straight application of the virial theorem also allows the estimation of the total mass ([Voit 2005](#)).

We conclude this section by listing the most recent optical surveys of galaxy clusters. We already referred to the work of Abell, that was based on visual inspection of photographic plates from the Palomar Observatory Sky Survey. The confirmed candidates were further characterised in classes of richness (the number of member galaxies) and distance. The catalog was updated and extended to the southern sky in ([Abell et al. 1989](#)). More recently, the Red Sequence Cluster Survey (using the Canada France-Hawaii 3.6 m telescope for the northern hemisphere, and the Cerro Tololo Inter-American Observatory 4 m telescope for the southern hemisphere), began in mid-1999, and observations were finished by late 2000. It made use of the red sequence imprint of clusters for their identification ([Gladders & Yee 2005](#)). Latest optical surveys employ multicolor photometry, the most important being the Sloan Digital Sky Survey (SDSS, [Koester et al. 2007](#); [Wen et al. 2012](#); [Rykoff et al. 2014](#)), a large imaging and spectroscopic survey employing a dedicated 2.5 m telescope at Apache Point Observatory.

1.4.2 Clusters in X-rays

We direct now our attention to the intracluster medium (ICM). The inefficiency of the star and galaxy formation processes results in most of the baryonic matter in a cluster (a fraction up to 90%) to be free in the form of intergalactic gas. The deep potential well of a galaxy cluster compresses the gas and heats it up to X-ray emitting temperatures. The process responsible for the emission is the *thermal bremsstrahlung*, or *free-free emission*, that is the radiation emitted by accelerated charged particles ([Sarazin 1988](#)). X-ray emission is usually quantified by a spectral emissivity function $\Lambda(\nu, T_e)$, which depends on the observed frequency ν and the electron temperature T_e . These quantities are not uniform across the cluster surface; in [Birkinshaw \(1999\)](#) the X-ray spectral surface brightness is defined at each position as:

$$b_X(\nu) = \frac{1}{4\pi(1+z)^3} \int_{\text{LOS}} dl n_e(\mathbf{r})^2 \Lambda(\nu, T_e(\mathbf{r})), \quad (1.48)$$

where the density profile is expressed in terms of the electron number density $n_e(\mathbf{r})$.

Este documento incorpora firma electrónica, y es copia auténtica de un documento electrónico archivado por la ULL según la Ley 39/2015.
Su autenticidad puede ser contrastada en la siguiente dirección <https://sede.ull.es/validacion/>

Identificador del documento: 973742	Código de verificación: Jfg6xBh0
Firmado por: DENIS TRAMONTE UNIVERSIDAD DE LA LAGUNA	Fecha: 30/06/2017 15:10:10
RAFAEL DELFIN BARRENA DELGADO UNIVERSIDAD DE LA LAGUNA	30/06/2017 15:21:31
JOSE ALBERTO RUBIÑO MARTIN UNIVERSIDAD DE LA LAGUNA	30/06/2017 15:34:17
ERNESTO PEREDA DE PABLO UNIVERSIDAD DE LA LAGUNA	06/07/2017 13:51:19

Equation 1.48 cannot be uniquely inverted to give the temperature and density profile of the intercluster medium. It is then customary to introduce suitable parametrisations for the radial dependence of these quantities. The simplest model assumes that the gas is in hydrostatic equilibrium, isothermal and spherically distributed inside the cluster (*isothermal beta model*, Cavaliere & Fusco-Femiano 1976, 1978). More accurate parametrisations relax the isothermal hypothesis (Hughes et al. 1988) or the assumption of spherical symmetry (Hughes & Birkinshaw 1998). These parametrisations are used to get an estimate of the plasma temperature, which is closely related to the overall mass. Indeed, it is the cluster gravitational potential the responsible for the gas heating. The estimation is complicated by the non-isothermality of the gas and the fact that it can contain different temperature components. Usually in the literature values are reported for global spectral-fit temperatures, which in turn give an estimate for the dispersion velocity of member galaxies (Lubin & Bahcall 1993; Xue & Wu 2000).

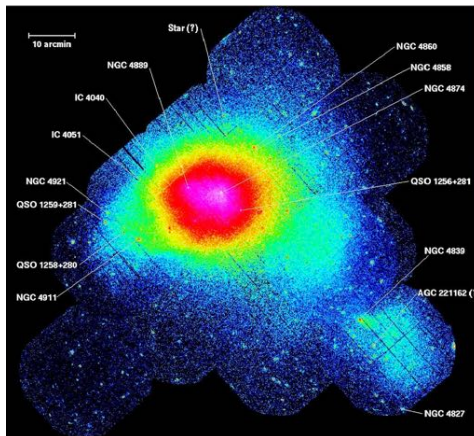


Figure 1.11: X-ray image of the Coma cluster, observed with XMM-Newton. Credit: ESA/XMM-Newton; image courtesy of U. Briel, MPE Garching.

In X-rays, clusters are easily observed and distinguished from the foreground. This is due to the centrally-concentrated emission profile: galaxy clusters are the only X-ray luminous, continuous and spatially extended extragalactic sources. Besides, from equation 1.48 we see that the surface brightness is dependent on the density squared, which enhances the contrast with respect to the less dense background. Unfortunately, the same relation shows that X-

Este documento incorpora firma electrónica, y es copia auténtica de un documento electrónico archivado por la ULL según la Ley 39/2015.
Su autenticidad puede ser contrastada en la siguiente dirección <https://sede.ull.es/validacion/>

Identificador del documento: 973742

Código de verificación: Jfg6xBh0

Firmado por: DENIS TRAMONTE
UNIVERSIDAD DE LA LAGUNA

Fecha: 30/06/2017 15:10:10

RAFAEL DELFIN BARRENA DELGADO
UNIVERSIDAD DE LA LAGUNA

30/06/2017 15:21:31

JOSE ALBERTO RUBIÑO MARTIN
UNIVERSIDAD DE LA LAGUNA

30/06/2017 15:34:17

ERNESTO PEREDA DE PABLO
UNIVERSIDAD DE LA LAGUNA

06/07/2017 13:51:19

ray brightness suffers from redshift dimming, which sets a limit distance for a cluster of a given size to be observed, according to the detector sensitivity. In addition, since our atmosphere blocks X-rays, these observations must be carried out from space, which considerably increases their cost.

First detections of X-ray emission from clusters are dated to the early seventies (Gursky et al. 1971; Forman et al. 1972). Later on, efforts were spent to design X-ray surveys. The most important one was the Rosat All-Sky Survey (RASS, Voges et al. 1999) by the *ROSAT* satellite, launched in June 1990. Such survey allowed the preparation of several X-ray based catalogues: the ROSAT Brightest Cluster Sample (BCS, Ebeling et al. 1998), covering the northern sky; the ROSAT-ESO Flux-Limited X-ray Galaxy Cluster Survey (REFLEX, Böhringer et al. 2004), covering the southern sky, the HIghest X-ray FLUX Galaxy Cluster Sample (HIFLUGCS Reiprich & Böhringer 2002) with the brightest clusters at high galactic latitude; and the MAssive Cluster Survey (MACS, Ebeling et al. 2010), extending HIFLUGCS to higher redshift and fainter fluxes. The ROSAT satellite also performed pointed observations, with which the catalogues RDCS (Rosat Deep Cluster Survey (RDCS, Rosati et al. 1998), and 400 Square Degree ROSAT PSPC Galaxy Cluster Survey (400d, Burenin et al. 2007), were built.

Observations from ROSAT were the starting point for higher precision observations conducted by the next generation of X-ray observatories, especially by *Chandra* and *XMM-Newton*. *Chandra* is a NASA satellite launched in 1999; among others, it was also dedicated to observations of galaxy clusters (Hicks et al. 2008), providing data at the basis of subsequent cosmological analysis (Allen et al. 2004, 2008a) also in combination with other data sets (Bonamente et al. 2008). The *XMM-Newton* satellite is the *Chandra* counterpart from ESA: it was also launched in 1999, and has delivered different cluster catalogues, like the XMM Cluster Survey (XCS Mehrtens et al. 2012), the 2XMMi/SDSS catalogue (Takey et al. 2011), the XMM Large Scale Structure survey (XMM-LSS Pacaud et al. 2007) and the XMM-Newton Distant Cluster Project (XDCP, Fassbender et al. 2011).

One last remark. X-ray emission from clusters is not limited to thermal bremsstrahlung; it also enters in line emission, made of photons released in the process of de-excitation of ions previously excited by collision (collisional de-excitation is unlikely because of the low plasma density). Free-free emission dominates over line emission for temperatures above $T \simeq 2$ keV (which is the most common situation for clusters), the opposite occurring at lower temperatures. If line emission can be detected, it gives information on the abundance of elements like iron, oxygen and silicon in the ICM, and conclusions on the star formation history in the cluster can be drawn. This topic goes beyond the

Este documento incorpora firma electrónica, y es copia auténtica de un documento electrónico archivado por la ULL según la Ley 39/2015.
Su autenticidad puede ser contrastada en la siguiente dirección <https://sede.ull.es/validacion/>

Identificador del documento:	973742	Código de verificación:	Jfg6xBh0
Firmado por:	DENIS TRAMONTE UNIVERSIDAD DE LA LAGUNA	Fecha:	30/06/2017 15:10:10
	RAFAEL DELFIN BARRENA DELGADO UNIVERSIDAD DE LA LAGUNA		30/06/2017 15:21:31
	JOSE ALBERTO RUBIÑO MARTIN UNIVERSIDAD DE LA LAGUNA		30/06/2017 15:34:17
	ERNESTO PEREDA DE PABLO UNIVERSIDAD DE LA LAGUNA		06/07/2017 13:51:19

scope of this work.

1.4.3 Clusters in radio waves

Observations of clusters in radio waves are not sensitive to a proper radio emission from the cluster itself; rather, they take advantage of the distortion, produced by clusters, of the Cosmic Microwave Background radiation. We first describe the underlying physical process, turning later to its use as a tool for the detection of galaxy clusters.

The Sunyaev-Zel'dovich effect

The *Sunyaev-Zel'dovich (SZ) effect* (Sunyaev & Zeldovich 1970, 1972) is a small spectral distortion of the Cosmic Microwave Background radiation spectrum caused by the scattering of CMB photons off a distribution of high energy electrons. A CMB photon passing through a cluster can indeed interact with a high energy electron of the ICM via inverse Compton scattering: as a result, the photon energy is boosted by a quantity $k_B T_e / m_e c^2$, with k_B being the Boltzmann constant, T_e the electron temperature and m_e the electron mass. The detailed calculation can be found in Birkinshaw (1999).

Things are complicated by the fact that we are dealing with a population of photons distributed as a blackbody. The overall result of the inverse Compton scattering on the population of CMB photons is a peculiar spectral distortion quantified by a temperature variation around $T \lesssim 1$ mK; considered as a function of the frequency, the SZE causes the CMB intensity to increase at high frequencies and to decrease at low frequencies, the zero point being around $\nu_0 \simeq 218$ GHz. The temperature distortion is expressed as (Carlstrom et al. 2002):

$$\frac{\Delta T_{\text{SZ}}}{T_0} = y f(x). \quad (1.49)$$

The first factor is the *Compton y-parameter*:

$$y = \int_{\text{LOS}} dl n_e \frac{k_B T_e}{m_e c^2} \sigma_T, \quad (1.50)$$

where the integration is performed along the line of sight, and where σ_T is the Thomson cross section. This term quantifies the total energy transfer from the electron plasma to the CMB, being the product of the energy boost per collision and the integrated probability of scattering. The second factor in 1.49

Este documento incorpora firma electrónica, y es copia auténtica de un documento electrónico archivado por la ULL según la Ley 39/2015.
Su autenticidad puede ser contrastada en la siguiente dirección <https://sede.ull.es/validacion/>

Identificador del documento: 973742	Código de verificación: Jfg6xBh0
Firmado por: DENIS TRAMONTE UNIVERSIDAD DE LA LAGUNA	Fecha: 30/06/2017 15:10:10
RAFAEL DELFIN BARRENA DELGADO UNIVERSIDAD DE LA LAGUNA	30/06/2017 15:21:31
JOSE ALBERTO RUBIÑO MARTIN UNIVERSIDAD DE LA LAGUNA	30/06/2017 15:34:17
ERNESTO PEREDA DE PABLO UNIVERSIDAD DE LA LAGUNA	06/07/2017 13:51:19

represents the frequency modulation of the transfer; as a function of the dimensionless photon frequency, $x = h\nu/k_{\text{B}}T_{\text{CMB}}$, it is given by:

$$f(x) = \left(x \frac{e^x + 1}{e^x - 1} - 4 \right) (1 + \delta_{\text{SZ}}(x, T_e)), \quad (1.51)$$

with $\delta_{\text{SZ}}(x, T_e)$ a relativistic correction term. Equation 1.49 can be expressed in terms of the specific intensity rather than temperature. For a blackbody, we know that

$$I(\nu, T) = \frac{2h}{c^2} \frac{\nu^3}{e^{h\nu/k_{\text{B}}T} - 1}. \quad (1.52)$$

By differentiating with respect to the temperature we can write the explicit variation of the intensity,

$$\frac{\Delta I}{I_0} = g(x)y, \quad (1.53)$$

where y retains the same meaning as before, $I_0 = 2(k_{\text{B}}T)^3/(hc)^2$ and the frequency dependence is now:

$$g(x) = \frac{x^4 e^x}{(e^x - 1)^2} f(x). \quad (1.54)$$

A very important feature of relations 1.49 and 1.53 is that they are *independent*

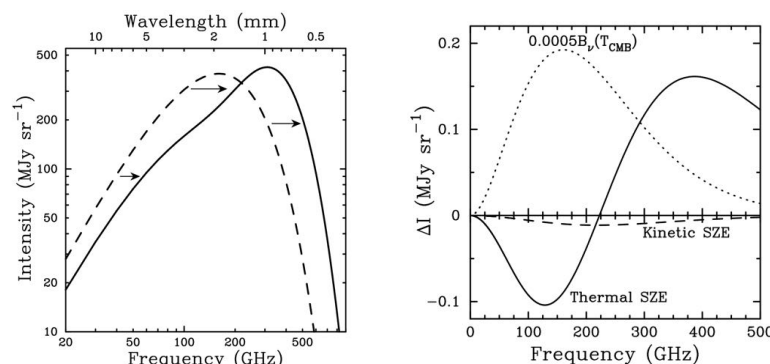


Figure 1.12: Left: shift of the CMB spectrum produced by the tSZ. Right: spectral distortions produced by the thermal and kinetic SZ effects, together with the rescaled CMB spectrum (dotted line). Figures from Carlstrom et al. (2002).

of redshift: this makes the SZE an extremely powerful tool for detecting high-redshift clusters, since it does not suffer redshift dimming, as it was the case for the X-ray emission.

The effect described so far is usually referred to as *thermal* SZE. If the cluster is not at rest in the CMB frame (that is, if it is not comoving with the expansion of the Universe), a further spectral distortion has to be included, due to the Doppler effect of the moving cluster. This additional spectral distortion is called *kinetic* SZE, and can be observed if the cluster peculiar velocity has a component v_{pec} along the line of sight, yielding (Sunyaev & Zeldovich 1970, 1972; Planck Collaboration et al. 2016m):

$$\frac{\Delta T_{\text{kSZ}}}{T_{\text{CMB}}} = \int_{\text{LOS}} dl \sigma_T n_e \left(\frac{\mathbf{v}}{c} \cdot \hat{\mathbf{n}} \right) \simeq -\tau_e \left(\frac{v_{\text{pec}}}{c} \right), \quad (1.55)$$

with τ_e the cluster optical depth. Unlike the thermal SZE, the kinetic SZE results in an absolute temperature shift of the CMB spectrum, which is actually indistinguishable from the primordial CMB anisotropies using spectral information only; the shift can be towards higher or lower temperatures according to the peculiar velocity component being negative or positive, respectively (Phillips 1995; Birkinshaw 1999). However, in galaxy clusters the kinetic effect is a second-order effect with respect to the thermal one: for $T_e \sim 10$ keV the kSZE is usually a factor ~ 0.1 of the tSZE. The difference between the two contributions decreases for lower values of the electron temperature.

Since the SZE lies in the radio section of the spectrum, its detection requires the use of radio (or millimetre) telescopes; the resolution of a radio telescope is set by the FWHM of its beam *point spread function* (PSF)⁵, which implies that the SZE signal gets *integrated* over the region subtended by the beam. This integration is carried out over the solid angle in the sky; since the Compton parameter of 1.50 is a pressure integrated over the line of sight, the resulting quantity is a pressure integrated over a volume, that is, the product of the total number of electrons in the cluster and the temperature (in other words, the total thermal energy of the cluster). The total number of electrons is proportional to the overall mass of the cluster⁶, so that:

$$\int d\Omega \Delta T_{\text{SZ}} \propto \frac{N_e \langle T_e \rangle}{D_A^2} \propto \frac{M \langle T_e \rangle}{D_A^2}, \quad (1.56)$$

⁵As a reference for the concepts of radio astronomy used throughout this chapter, see Wilson et al. (2009).

⁶To be precise, the total electron number is directly related to the cluster gas fraction; this, in turn, gives an estimate of the total mass of the cluster as $M_{\text{gas}} = f_g M_{\text{tot}}$, where f_g is the gas mass fraction.

where we used the relation 3.3 between the area element, the infinitesimal solid angle and the angular diameter distance D_A . As we discuss in section 3.1.2, the angular diameter distance is nearly flat at redshift $z \sim 1.5$; since at high redshift the matter density is higher, a cluster of a given mass will be denser and therefore hotter, compensating for the slowly growing term D_A . As a result, the limit of a SZE survey, for high z and provided that the angular resolution is comparable to the cluster size, will be just a mass threshold, with little dependence on redshift.

To sum up, we can list the following important features of the (thermal) Sunyaev-Zel'dovich effect:

- it is a small spectral distortion of the CMB of order $\lesssim 1$ mK, due to the inverse Compton scattering of photons over a population of high energy electrons;
- it is proportional to the cluster pressure integrated along the line of sight;
- its surface brightness is independent of redshift;
- it has a peculiar spectral dependence, with a decrease in intensity for $\nu \lesssim 218$ GHz and an increase at higher frequencies;
- the integrated SZE (i.e. the quantity we can observe) is proportional to the temperature weighted mass of the cluster.

Observing clusters in radio

As already stated, the Sunyaev-Zel'dovich effect was first proposed in the 70's, but its detection did not follow immediately (Birkinshaw 1991). Instrumentation and techniques to observe clusters have been dramatically improved during the last decades. The main issue is the presence of sources of contamination. First of all the anisotropies in the CMB, especially for low-redshift clusters that have an angular extent comparable to the characteristic scales of CMB temperature fluctuations; if the thermal SZE can be distinguished thanks to its spectral signature, this is not true for the kinetic SZE. In this case the two effects are usually disentangled by considering spatial information or using other techniques, as pairwise velocity analyses (Hand et al. 2012; Mueller et al. 2015; Hernández-Monteagudo et al. 2015). Another source of contamination are point radio sources located along the line of sight (LaRoque et al. 2002); these sources usually have a spectral flux with a frequency dependence $S_\nu \propto \nu^{-0.7}$ (synchrotron emission), while the SZE spectrum goes as $S_\nu \propto \nu^2$ in the Rayleigh-Jeans limit (which is usually the case in radio astronomy) so that

Este documento incorpora firma electrónica, y es copia auténtica de un documento electrónico archivado por la ULL según la Ley 39/2015.
Su autenticidad puede ser contrastada en la siguiente dirección <https://sede.ull.es/validacion/>

Identificador del documento: 973742	Código de verificación: Jfg6xBh0	Fecha: 30/06/2017 15:10:10
Firmado por: DENIS TRAMONTE UNIVERSIDAD DE LA LAGUNA		
RAFAEL DELFIN BARRENA DELGADO UNIVERSIDAD DE LA LAGUNA		30/06/2017 15:21:31
JOSE ALBERTO RUBIÑO MARTIN UNIVERSIDAD DE LA LAGUNA		30/06/2017 15:34:17
ERNESTO PEREDA DE PABLO UNIVERSIDAD DE LA LAGUNA		06/07/2017 13:51:19

point sources are a minor problem at higher frequency. Finally, dust emission from both our Galaxy and extragalactic sources must be taken into account at frequencies down to the null of the thermal SZE, the dust flux increasing at higher frequencies. Apart from the presence of these foreground sources, another important issue when performing SZE observations is the control of instrumental systematics, which requires accurate observational strategies.

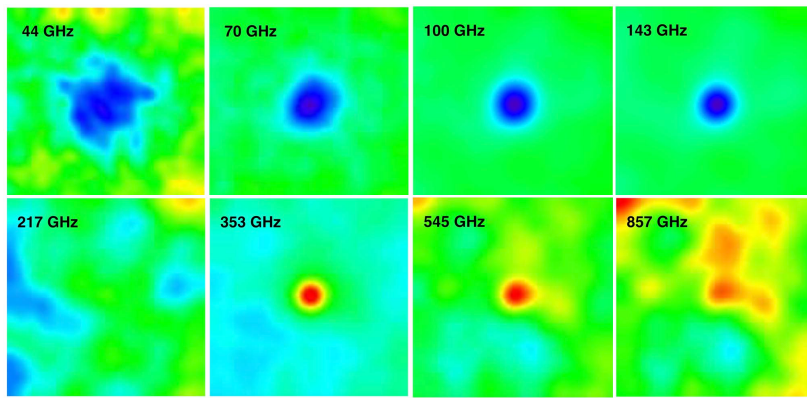


Figure 1.13: The typical tSZ spectral signature in a galaxy cluster observed by *Planck*. Each panel shows a CLASS 1 cluster candidate (see section 3.4.1) for an individual *Planck* frequency channel, over a $\sim 2.5 \times 2.5$ square degrees area. The spectral distortion plotted in figure 1.12 can easily be traced. Plots are taken from [Planck Collaboration et al. \(2014i\)](#).

In the beginning, observations of the SZE were performed with single-dish radio telescope. Among the first detections we cite the work of Birkinshaw and collaborators with the OVRO 40 m telescope ([Birkinshaw et al. 1978a,b](#)). However, better results in radio observations of SZE can be obtained with interferometers; the first interferometric observation of the SZE was performed with the Ryle Telescope and is described in [Jones et al. \(1993\)](#). A remarkable property of interferometric observations is that only signals that correlate between the array elements will contribute to the response of the interferometer. Interferometric observations achieve an angular resolution of $\sim \lambda/B$, with B the baseline (separation between antennae) and λ the observing wavelength; as a result, the interferometer is not sensitive to gradients in the atmospheric emission or other large-scale emissions. What is usually done is to employ simultaneously long baselines to observe and monitor point sources (which will be later subtracted) and shorter baselines to observe the SZE (this is quite important since point sources are usually variable, thus requiring a continuous

Este documento incorpora firma electrónica, y es copia auténtica de un documento electrónico archivado por la ULL según la Ley 39/2015.
Su autenticidad puede ser contrastada en la siguiente dirección <https://sede.ull.es/validacion/>

Identificador del documento: 973742

Código de verificación: Jfg6xBh0

Fecha: 30/06/2017 15:10:10

Firmado por: DENIS TRAMONTE
UNIVERSIDAD DE LA LAGUNA

RAFAEL DELFIN BARRENA DELGADO
UNIVERSIDAD DE LA LAGUNA

JOSE ALBERTO RUBIÑO MARTIN
UNIVERSIDAD DE LA LAGUNA

ERNESTO PEREDA DE PABLO
UNIVERSIDAD DE LA LAGUNA

30/06/2017 15:21:31

30/06/2017 15:34:17

06/07/2017 13:51:19

monitoring).

The use of interferometric SZE instruments has opened the possibility of performing deep SZE surveys and building large SZ catalogues. The use of SZ cluster samples in cosmology was proposed already in [Barbosa et al. \(1996\)](#) and [Aghanim et al. \(1997\)](#), but it was only during the last decade that SZ catalogues reached a significant size. These data come from both ground-based and space observations.

The first large SZE catalogs are currently under construction. Data come from ground-based observations, like the ones from the SPT (South Pole Telescope (SPT, [Reichardt et al. 2013](#)) and the Atacama Cosmology Telescope (ACT, [Hasselfield et al. 2013](#)), but also from space missions like *Planck*. *Planck* is the benchmark experiment for this work, so we will extensively talk about it in the next sections.

1.4.4 Clusters and gravitational lensing

One last possibility for finding clusters rely on the gravitational effect they produce on light passing through them ([Bartelmann & Schneider 2001](#)). Radiation coming from galaxies placed beyond the cluster with respect to our line of sight undergoes a deflection when passing through the cluster gravitational potential; the result is that images of background galaxies are *lensed*. Since the original shape of a single background galaxy is usually unknown, the lensing effect is observed for an entire field of such galaxies, considering the orientation of the shape alteration common to all of them.

Lensing depends on the cluster mass enclosed within a certain projected radius r_{\perp} , which we call M_r . More precisely, the deflection angle is sensitive to the gradient of the gravitational potential inside r_{\perp} . In the case of a spherical symmetrical distribution of matter, the resulting deflection angle is expected to be $4GM_r/c^2r_{\perp}$. So, the measure of weak lensing allows us to derive the mass M_r , but in order to recover the real cluster mass, information is needed on how matter is distributed within the column bounded by r_{\perp} . To this aim, models of mass and temperature distribution like the ones we mentioned in section [1.4.2](#) are employed.

Weak lensing masses are expected to correlate quite well with cluster richness, thus representing another good mass proxy. However, lensing estimations are limited by the possible superposition of other mass structures along the line of sight.

Este documento incorpora firma electrónica, y es copia auténtica de un documento electrónico archivado por la ULL según la Ley 39/2015.
Su autenticidad puede ser contrastada en la siguiente dirección <https://sede.ull.es/validacion/>

Identificador del documento:	973742	Código de verificación:	Jfg6xBh0
Firmado por:	DENIS TRAMONTE UNIVERSIDAD DE LA LAGUNA	Fecha:	30/06/2017 15:10:10
	RAFAEL DELFIN BARRENA DELGADO UNIVERSIDAD DE LA LAGUNA		30/06/2017 15:21:31
	JOSE ALBERTO RUBIÑO MARTIN UNIVERSIDAD DE LA LAGUNA		30/06/2017 15:34:17
	ERNESTO PEREDA DE PABLO UNIVERSIDAD DE LA LAGUNA		06/07/2017 13:51:19

1.4.5 Cosmology with galaxy clusters

Observing galaxy clusters and characterising their properties is important because it allows to constrain the values of cosmological parameters. In particular, great advantage can be taken by the combination of cluster data in different wavelengths. The combination of data from X-ray and SZE can give an estimate of the Hubble constant (Birkinshaw & Hughes 1994; Reese 2000). If we compare equations 1.48 and 1.50 we see that, while the X-ray surface brightness is proportional to the electron density squared, the SZE signal is proportional to the density alone. This allows to solve the system for the angular diameter distance, which combined with the redshift of the cluster can provide an estimate of the Hubble parameter. This method, however, assumes that the cluster is spherically symmetric and that, over the line of sight, the root mean square of the electron density equals its simple average, $\langle n_e^2 \rangle^{1/2} = \langle n_e \rangle$. More generally, there could be local overdense structures inside the clusters, resulting in an overestimate of H_0 . Correction for this systematics can be addressed with the new generation of X-ray and SZE sky surveys (Grainge et al. 2002; Schmidt et al. 2004; Bonamente et al. 2006).

A second parameter that can be estimated from observations of galaxy clusters is the matter density parameter Ω_m . This is done at first as an estimation of the baryon fraction, $f_b = \Omega_b/\Omega_m$, which is reasonably approximated by the gas mass fraction f_g in the cluster. The gas mass is estimated from SZE or X-ray data, provided that the cluster is in hydrostatic equilibrium and the density and temperature profiles are known; the total mass of the cluster is obtained from gravitational lensing measurements or optical analyses of the velocity dispersion. If the baryon density parameter Ω_b is known (i.e. from observations of the CMB, or from models of the Big Bang nucleosynthesis), the total matter density parameter can be obtained. This way one would likely get an overestimation of Ω_m , due to the fact that the gas fraction is a lower limit for the baryon fraction, $f_g \leq f_b$. Indeed, some baryons are lost during the gravitational collapse that leads to the formation of clusters, and some of the remaining ones are trapped in galaxies. This systematic effect is usually handled by assuming the fraction of baryons trapped in galaxies to be a constant ratio, fitted to the lowest redshift clusters. For more information we redirect to Allen et al. (2008b) and LaRoque et al. (2006).

Another way in which clusters can give information on the large-scale Universe is through the local velocity field (Strauss & Willick 1995); peculiar velocities of galaxy clusters can be obtained by kinetic SZE measurements (Kashlinsky & Atrio-Barandela 2000). Besides, cluster statistics can be used to constrain the equation of state of dark energy. The simplest extension of a pure

Este documento incorpora firma electrónica, y es copia auténtica de un documento electrónico archivado por la ULL según la Ley 39/2015.
Su autenticidad puede ser contrastada en la siguiente dirección <https://sede.ull.es/validacion/>

Identificador del documento:	973742	Código de verificación:	Jfg6xBh0
Firmado por:	DENIS TRAMONTE UNIVERSIDAD DE LA LAGUNA	Fecha:	30/06/2017 15:10:10
	RAFAEL DELFIN BARRENA DELGADO UNIVERSIDAD DE LA LAGUNA		30/06/2017 15:21:31
	JOSE ALBERTO RUBIÑO MARTIN UNIVERSIDAD DE LA LAGUNA		30/06/2017 15:34:17
	ERNESTO PEREDA DE PABLO UNIVERSIDAD DE LA LAGUNA		06/07/2017 13:51:19

cosmological constant model is to expand it to first order as a function of the scale factor:

$$w(a) = w_0 + w_a(1 - a), \quad (1.57)$$

so that the equation of state takes the value w_0 at $z = 0$ and approaches $w_0 + w_a$ at high redshift. High-redshift cluster surveys can help constraining this model; see [Vikhlinin et al. \(2009\)](#).

Another important observational property which can provide information on cosmology, particularly on the matter density parameter and the normalisation of the matter power spectrum, is the *number counts* of clusters. This will be the subject of chapter 3.

1.5 Objectives of this work

This thesis work aims at contributing to the cosmological exploitation of the three cosmological probes we have described in this chapter. The main goal is not only providing estimates for the values of cosmological parameters, but also contributing to improve the numerical and analytical tools employed for this kind of analysis. Therefore, this requires the combination of analytical models, numerical simulations and instrumental data, depending on the case. More specifically, the scientific objectives tackled in each of the chapters of this thesis work are the following.

- *Study of the conditional mass function of dark matter halos.* In chapter 2 we study the abundance of dark matter halos inside regions with a definite density contrast with respect to the background, quantified by the conditional mass function (CMF). In the literature, possible parametrisations for the CMF have been proposed, but there are not many dedicated works. Our aim is to test thoroughly the conditional mass function against N-body simulations, and check its normalisation at different scales, in order to point out which parametrisation for the CMF works the best and under what assumptions it can be applied. We also want to derive a fitting function to quickly compute the halo bias inside underdense regions, which is a fundamental ingredient to test cosmological models on the basis of the abundance of large scale voids.
- *Use of halo abundance as a cosmological probe.* In chapter 3 we consider how the redshift distribution of the number of galaxy clusters can be used to constrain cosmological parameters. We want to implement the computation of the cluster redshift distribution corresponding to a given

Este documento incorpora firma electrónica, y es copia auténtica de un documento electrónico archivado por la ULL según la Ley 39/2015.
Su autenticidad puede ser contrastada en la siguiente dirección <https://sede.ull.es/validacion/>

Identificador del documento: 973742	Código de verificación: Jfg6xBh0	Fecha: 30/06/2017 15:10:10
Firmado por: DENIS TRAMONTE UNIVERSIDAD DE LA LAGUNA		
RAFAEL DELFIN BARRENA DELGADO UNIVERSIDAD DE LA LAGUNA		30/06/2017 15:21:31
JOSE ALBERTO RUBIÑO MARTIN UNIVERSIDAD DE LA LAGUNA		30/06/2017 15:34:17
ERNESTO PEREDA DE PABLO UNIVERSIDAD DE LA LAGUNA		06/07/2017 13:51:19

cosmological model, and to develop a statistical tool for the inverse problem of reconstructing the original cosmological model starting from the simulated abundance of clusters. Our final goal is to apply these tools to the catalogue of galaxy clusters detected by the *Planck* satellite by means of the SZ effect, and to obtain constraints on the parameters Ω_m and σ_8 .

- *Use of the Sunyaev-Zel'dovich effect as a cosmological probe.* Chapter 4 is dedicated to the study of the thermal Sunyaev-Zel'dovich effect in terms of all-sky maps of the Compton parameter y . In particular, we consider the corresponding 1-dimensional probability distribution function (PDF) for the Compton parameter, which carries a wealth of information on the different astrophysical emissions entering the reconstructed y -map, and which is particularly sensitive to the parameter σ_8 . We want to model the galaxy clusters contribution to the PDF and to test our formalism against simulated Compton parameter maps. Our aim is to apply this formalism to the Compton parameter maps provided by the *Planck* satellite, with the aim of constraining the parameter σ_8 .
- *Contribution to the calibration and data analysis of the QUIJOTE experiment.* We consider in chapter 5 the QUIJOTE experiment, dedicated to the observation of CMB polarisation. First of all, we want to carry out the calibration of the pointing model of the first QUIJOTE telescope. Our goal is to provide a set of pointing corrections to be implemented in the experiment pipeline for data reduction. Finally, we focus on the scientific exploitation of QUIJOTE data. We consider observations of the galactic regions IC443 (a supernova remnant), W49 and W51 (supernova remnants within molecular clouds), with the aim of assessing the contribution of the anomalous microwave emission in supernova remnants, and of characterising the level of their polarised emission.

Este documento incorpora firma electrónica, y es copia auténtica de un documento electrónico archivado por la ULL según la Ley 39/2015.
Su autenticidad puede ser contrastada en la siguiente dirección <https://sede.ull.es/validacion/>

Identificador del documento:	973742	Código de verificación:	Jfg6xBh0
Firmado por:	DENIS TRAMONTE UNIVERSIDAD DE LA LAGUNA	Fecha:	30/06/2017 15:10:10
	RAFAEL DELFIN BARRENA DELGADO UNIVERSIDAD DE LA LAGUNA		30/06/2017 15:21:31
	JOSE ALBERTO RUBIÑO MARTIN UNIVERSIDAD DE LA LAGUNA		30/06/2017 15:34:17
	ERNESTO PEREDA DE PABLO UNIVERSIDAD DE LA LAGUNA		06/07/2017 13:51:19

2

The conditional mass function of dark matter halos

In this chapter we focus on the study of the halo mass function, i.e. the mass distribution of comoving halo density. We introduce the basic formalism used to derive an analytic expression for the mass function and present its subsequent improvements. We then turn into the problem of determining the halo density distribution inside regions with a definite density contrast with respect to the background, which is quantified by the conditional mass function (CMF). We consider in particular two recipes already described in the literature, compare their prediction, and check that none of them is properly normalised. We explicitly modify their analytical expressions in order to satisfy normalisation at different scales. We then test the CMFs prediction against halo abundances extracted from numerical simulations, and prove that after this modification the CMF provides a better description of numerical results. We provide a fitting formula for computing the CMF in underdense regions, in terms of the matter-to-halo bias function. Finally, we describe different recipes for computing the CMF, based on the assumption that the conditioning region can be treated as an independent universe with a locally-defined cosmology. The results of the work presented in this chapter are published in Tramonte et al. (2017), with the exception of section 2.6, which is the subject of a paper in preparation (Betancort-Rijo et al. in prep.).

2.1 The unconditional mass function

As pointed out in chapter 1, perturbations in the matter density of the Universe grow during its redshift evolution, eventually decoupling from the background expansion and leading to the formation of collapsed objects, in the form of dark matter halos. The abundance of collapsed dark matter halos as a function of mass, and its dependence on redshift, is one of the basic tools in modern cosmology, and is quantified by the so-called *halo mass function*. More precisely, we define the mass function $dn/dm(m, z)$ as the distribution of the comoving number density of halos in such a way that the quantity $dn/dm(m, z) dm$ is the number of halos with masses in the range $[m, m + dm]$ per unit comoving volume at redshift z .

2.1.1 The Press-Schechter formalism

The halo mass function was first estimated analytically in [Press & Schechter \(1974\)](#), hereafter PS74). This formalism constitutes the basis for any later analytic development; it is based on the assumption that initial fluctuations are drawn from a Gaussian distribution, and on the physics of spherical collapse. Indeed, when an overdense region finally collapses the linear theory becomes inadequate; but if the collapse maintains spherical symmetry, then the process can be treated analytically.

Let us consider an overdense sphere of radius R , in a spatially-flat matter-dominated Universe; according to Birkhoff's theorem, the whole Universe outside the sphere continues evolving as if $k = 0$, while the sphere evolves independently of the rest of the space, behaving as an independent closed universe with $k > 0$. In this universe we can define a local scale factor \tilde{a} . The evolution of the scale factor in a closed universe is not as straightforward to derive as in the flat case, because the curvature term in Friedmann's equation prevents us from expressing a as function of t . However, both the scale factor and the time can be written as functions of a parameter θ defined in $[0, 2\pi[$, yielding:

$$\frac{\tilde{a}}{\tilde{a}_{\max}} = \frac{1}{2}(1 - \cos \theta) \quad \frac{t}{t_{\max}} = \frac{1}{\pi}(\theta - \sin \theta). \quad (2.1)$$

Hence, the local scale factor grows at the beginning, it has a turnaround when $t = t_{\max}$ when it reaches its maximum value \tilde{a}_{\max} and then drops to zero at $t = 2t_{\max}$. Physically, this corresponds to the overdensity initially taking part to the expansion of the background Universe, and later decoupling to collapse into a bound object.

Este documento incorpora firma electrónica, y es copia auténtica de un documento electrónico archivado por la ULL según la Ley 39/2015.
Su autenticidad puede ser contrastada en la siguiente dirección <https://sede.ull.es/validacion/>

Identificador del documento: 973742

Código de verificación: Jfg6xBh0

Fecha: 30/06/2017 15:10:10

Firmado por: DENIS TRAMONTE
UNIVERSIDAD DE LA LAGUNA

RAFAEL DELFIN BARRENA DELGADO
UNIVERSIDAD DE LA LAGUNA

JOSE ALBERTO RUBIÑO MARTIN
UNIVERSIDAD DE LA LAGUNA

ERNESTO PEREDA DE PABLO
UNIVERSIDAD DE LA LAGUNA

30/06/2017 15:21:31

30/06/2017 15:34:17

06/07/2017 13:51:19

Since we are assuming matter domination, $\rho \propto a^{-3}$, and the (linear) density contrast evolves as:

$$1 + \delta_l = \frac{a^3}{\tilde{a}^3}, \quad (2.2)$$

with a the scale factor for the background Universe. By combining equations 2.1 with equation 2.2, we find, at first order:

$$\delta_l = \frac{3}{20} \left(6\pi \frac{t}{t_{\max}} \right)^{2/3}, \quad (2.3)$$

from which we see that at turnaround, when the structure begins to collapse, the density contrast is roughly equal to unity. The value of the linear overdensity by the time the collapse is complete can be found by setting $t = 2t_{\max}$:

$$\delta_c \equiv \delta_l(t = 2t_{\max}) \simeq 1.686. \quad (2.4)$$

This is an important value that sets the limit for the density contrast above which an overdensity region is to be considered collapsed, and is usually referred to as the *critical density* (Peebles 1980). Notice that, even though this value has been derived in the particular case of a pure Einstein-de Sitter cosmology, it can be safely applied to more general models, given it has a weak dependence on cosmological parameters (Navarro et al. 1997).

In the Press-Schechter formalism, the linear density contrast follows a Gaussian distribution, i.e. the probability for a randomly chosen region of radius R to have a density contrast δ_l at redshift z is given by:

$$P(\delta_l, R, z) = \frac{1}{\sqrt{2\pi}\sigma(R, z)} \exp\left(-\frac{\delta_l^2}{2\sigma^2(R, z)}\right), \quad (2.5)$$

with $\sigma^2(R, z)$ the variance of the contrast density field at scale R . The fractional volume of the Universe with $\delta_l(R, z) > \delta_c$ gives an estimate of the fractional mass $f(m > m(R), z)$ that ends up into collapsed objects of mass $m(R)$ at redshift z . By integrating 2.5 we find:

$$f(m > m(R), z) = \frac{1}{2} \operatorname{erfc}\left(\frac{\delta_c}{\sqrt{2}\sigma(R, z)}\right), \quad (2.6)$$

where erfc denotes the complementary error function. By taking the derivative of 2.6 with respect to the mass we find the fractional change in the collapsed volume per dm variation; by multiplying by the matter density at redshift z

Este documento incorpora firma electrónica, y es copia auténtica de un documento electrónico archivado por la ULL según la Ley 39/2015.
Su autenticidad puede ser contrastada en la siguiente dirección <https://sede.ull.es/validacion/>

Identificador del documento: 973742

Código de verificación: Jfg6xBh0

Fecha: 30/06/2017 15:10:10

Firmado por: DENIS TRAMONTE UNIVERSIDAD DE LA LAGUNA	30/06/2017 15:21:31
RAFAEL DELFIN BARRENA DELGADO UNIVERSIDAD DE LA LAGUNA	30/06/2017 15:34:17
JOSE ALBERTO RUBIÑO MARTIN UNIVERSIDAD DE LA LAGUNA	06/07/2017 13:51:19
ERNESTO PEREDA DE PABLO UNIVERSIDAD DE LA LAGUNA	

this quantity turns into fractional mass, and dividing by m yields the mass distribution of the number density of collapsed objects, that is, the mass function:

$$\frac{dn}{dm}(m, z) = -\sqrt{\frac{2}{\pi}} \frac{\rho_m}{m} \frac{\delta_c}{\sigma^2(m, z)} \frac{d\sigma(m, z)}{dm} \exp\left(-\frac{\delta_c^2}{2\sigma^2}\right). \quad (2.7)$$

Notice that the final expression 2.7 gets rid of the factor 1/2 appearing in equation 2.6 in order to ensure that the associated probability distribution is properly normalised. That 1/2 factor is actually an artefact deriving from this simple derivation. The final mass function results naturally normalised following the more complete derivation in [Betancort-Rijo & Montero-Dorta \(2006a\)](#).

The quantity in equation 2.7 is referred to as the *Press-Schechter* mass function. Following [Jenkins et al. \(2001, J01 from now on\)](#), equation 2.7 can be more conveniently rewritten as:

$$\frac{dn}{dm}(m, z) \equiv \frac{\rho_m}{m} \frac{d \ln \sigma^{-1}(m, z)}{dm} f(\sigma, \delta_c, z), \quad (2.8)$$

where all the information on the mass function is contained in $f(\sigma, \delta_c, z)$, that is the mass fraction contained in collapsed objects per unit $\ln \sigma^{-1}$ (this last quantity is often employed as an alias for the mass). In the case of the Press-Schechter formalism:

$$f_{\text{PS}}(\sigma, \delta_c) = \sqrt{\frac{2}{\pi}} \left(\frac{\delta_c}{\sigma} \right) e^{-\delta_c^2/2\sigma^2}. \quad (2.9)$$

The Press-Schechter mass function is reasonably accurate despite this simple derivation; however, it is known to underestimate the abundance of high mass objects and to overestimate the abundance of low mass halos (see Figure 2.1, and J01 for a discussion). A more accurate modelling of the function f is therefore required for cosmological applications.

2.1.2 Extensions to the Press-Schechter formalism

There were subsequent works aimed at improving the analytical expression of the mass function. [Bond et al. \(1991\)](#) developed the so-called ‘excursion set formalism’, in whose framework the [PS74](#) mass function can be derived from the barrier-crossing statistics of many independent, uncorrelated random walks. However, this recipe underestimates the abundance of high mass collapsed objects ([Efstathiou et al. 1988](#)) due to the fact that in deriving the analytical expression, all mass elements are assumed to be at the centre of the object

Este documento incorpora firma electrónica, y es copia auténtica de un documento electrónico archivado por la ULL según la Ley 39/2015.
Su autenticidad puede ser contrastada en la siguiente dirección <https://sede.ull.es/validacion/>

Identificador del documento: 973742	Código de verificación: Jfg6xBh0
Firmado por: DENIS TRAMONTE UNIVERSIDAD DE LA LAGUNA	Fecha: 30/06/2017 15:10:10
RAFAEL DELFIN BARRENA DELGADO UNIVERSIDAD DE LA LAGUNA	30/06/2017 15:21:31
JOSE ALBERTO RUBIÑO MARTIN UNIVERSIDAD DE LA LAGUNA	30/06/2017 15:34:17
ERNESTO PEREDA DE PABLO UNIVERSIDAD DE LA LAGUNA	06/07/2017 13:51:19

they belong to (Betancort-Rijo & Montero-Dorta 2006a). As a consequence of this, the accumulated mass fraction is not a universal function of the linear variance of the density contrast but depends on the shape of the power spectrum (Betancort-Rijo & Montero-Dorta 2006b).

The treatment of the ellipsoidal collapse was incorporated into the formalism in several works (Bond & Myers 1996; Sheth et al. 2001; Sheth & Tormen 2002) by using a moving barrier. Those studies provided an approximated analytical expression for the distribution of first crossings of the moving barrier, which was used in Sheth & Tormen (1999, ST99, from now on) to provide a new parametrisation of the mass function:

$$f_{\text{ST}}(\sigma, \delta_c) = A \sqrt{\frac{2a}{\pi}} \left[1 + \left(\frac{\sigma^2}{a\delta_c^2} \right)^p \right] \frac{\delta_c}{\sigma} \exp \left(\frac{a\delta_c^2}{2\sigma^2} \right), \quad (2.10)$$

with $A = 0.3222$, $a = 0.707$ and $p = 0.3$. Comparisons with N-body simulations show that this new formalism significantly improves the PS74 mass function in predicting the halo mass distribution. The ST99 parametrisation has been tested against N-body simulations in J01, providing a very good agreement. In the same reference an alternative fitting formula was proposed:

$$f_{\text{J01}}(\sigma) = 0.315 \exp \left[- |\ln \sigma^{-1} + 0.61|^{3.8} \right]. \quad (2.11)$$

This functional form for the mass function is capable of achieving agreements with numerical simulations with an error below $\sim 10\text{--}30\%$ at all masses, and is said to be universal, in the sense that it can be applied to different cosmological models and different redshifts. However, the fit cannot be extrapolated beyond the mass range employed in that work. Warren et al. (2006, W06 from now on) improved the fit providing a mass function parametrisation in the form:

$$f_{\text{W06}}(\sigma) = A (\sigma^{-a} + b) e^{-c/\sigma^2}, \quad (2.12)$$

The right-hand-side of equation 2.12 is explicitly written as the product of a power-law factor, reproducing the mass function behaviour at small scales, and an exponential factor that fits for the high-mass cut-off. This function is capable of reproducing the halo abundance with an error $\sim 5\%$ at redshift $z = 0$ and for a fixed cosmology. The work of Reed et al. (2007), instead, provides a good fit for the mass function at redshifts 10–30, obtained by extending the ST99 parametrisation 2.10.

Notice that in the works cited so far the fit of the mass function parametric form is done against catalogues obtained using friends-of-friends (FoF) defined halos (Davis et al. 1985). The FoF algorithm is computationally efficient and

Este documento incorpora firma electrónica, y es copia auténtica de un documento electrónico archivado por la ULL según la Ley 39/2015.
Su autenticidad puede ser contrastada en la siguiente dirección <https://sede.ull.es/validacion/>

Identificador del documento: 973742	Código de verificación: Jfg6xBh0	Fecha: 30/06/2017 15:10:10
Firmado por: DENIS TRAMONTE UNIVERSIDAD DE LA LAGUNA		
RAFAEL DELFIN BARRENA DELGADO UNIVERSIDAD DE LA LAGUNA		30/06/2017 15:21:31
JOSE ALBERTO RUBIÑO MARTIN UNIVERSIDAD DE LA LAGUNA		30/06/2017 15:34:17
ERNESTO PEREDA DE PABLO UNIVERSIDAD DE LA LAGUNA		06/07/2017 13:51:19

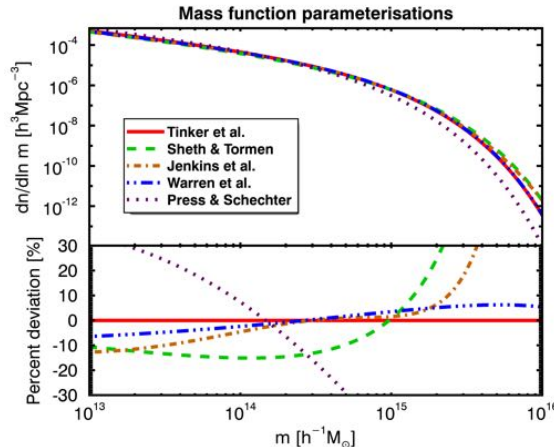


Figure 2.1: Comparison between different mass functions parametrisations, computed using the cosmological parameters from table 2.1: PS74, ST99, J01, W06 and T08 with $\Delta = 200$ (see the text for details). Lower panel shows percent difference with respect to the T08 mass function, which is the reference parametrisation used in this work. The PS74 function is indeed the most inaccurate, clearly underestimating the abundance of most massive halos. The W06 function is the closest to the T08 one, sharing the same functional form.

has the advantage that it does not assume any a-priori halo shape. However, a major issue concerning masses obtained with FoF finders is that they are not easily accommodated within the theoretical formalism, which is usually based on spherical overdensity (SO) mass. The corresponding SO algorithm (Lacey & Cole 1994) identifies objects as spherical regions enclosing a certain overdensity around density peaks. More precisely, a sphere of radius R_Δ and mass M_Δ has an overdensity Δ if the following relation holds:

$$\Delta = \frac{M_\Delta}{(4/3)\pi\rho_m(z)R_\Delta^3}, \quad (2.13)$$

with $\rho_m(z)$ the mean matter density of the Universe at redshift z . In this case the overdensity Δ is referred to as *mean*, because it is defined with respect to the matter density (in other applications the overdensity is defined with respect to the critical density of the Universe $\rho_c(z)$).

The task of fitting the mass function against SO-defined halo catalogues has been addressed in Tinker et al. (2008, T08 from now on). The proposed function has the form:

$$f_{\text{T08}}(\sigma) = A \left[\left(\frac{\sigma}{b} \right)^{-a} + 1 \right] e^{-c/\sigma^2}, \quad (2.14)$$

Este documento incorpora firma electrónica, y es copia auténtica de un documento electrónico archivado por la ULL según la Ley 39/2015.
Su autenticidad puede ser contrastada en la siguiente dirección <https://sede.ull.es/validacion/>

Identificador del documento: 973742

Código de verificación: Jfg6xBh0

Fecha: 30/06/2017 15:10:10

Firmado por: DENIS TRAMONTE
UNIVERSIDAD DE LA LAGUNA

RAFAEL DELFIN BARRENA DELGADO
UNIVERSIDAD DE LA LAGUNA

JOSE ALBERTO RUBIÑO MARTIN
UNIVERSIDAD DE LA LAGUNA

ERNESTO PEREDA DE PABLO
UNIVERSIDAD DE LA LAGUNA

30/06/2017 15:21:31

30/06/2017 15:34:17

06/07/2017 13:51:19

which is the same as the W06 fit with a re-definition of the fitting parameters. This mass function is capable of reproducing the halo abundance from numerical simulations with an accuracy $\lesssim 5\%$, at $z = 0$ and in the mass range $10^{11} h^{-1} M_\odot < M < 10^{15} h^{-1} M_\odot$. The improvement of this fit compared to other parametrisations comes from the fitting parameters being allowed to depend on redshift and on the value of overdensity Δ employed by the halo finder. In that work, the halo mass function is claimed not to be universal at this level of accuracy; the dependence of the fitting parameters on redshift is explored up to $z = 2.5$, and their dependence on the mean overdensity is considered for Δ in the range 200 to 3200. In T08, tables are provided for computing the fitting parameters at different values of Δ and z . This mass function is the standard reference used in most cluster cosmology analyses, and is the one we shall take as reference throughout the present work as well.

There have been subsequent attempts at improving Tinker's fit. The impact of the initial conditions for the simulations used to fit the mass function can be found in Crocce et al. (2006). In Crocce et al. (2010), the halo abundance is fitted over five orders of magnitude in mass, and its redshift evolution explored up to $z = 2$; the fitting formula is the same as in W06, but with different parameters in order to correct for the underestimation of the most massive halo abundance. The resulting fit reproduces the simulated halo abundance with a $\sim 2\%$ accuracy. The cosmology and redshift dependence of the mass function is also explored in Courtin et al. (2011), showing the universality is not verified in absolute terms, holding true only for $z = 0$ and for a limited set of cosmologies; this is due to some cosmology-dependent features in the mass function, like the value of the threshold density for collapse, whose value depends on cosmological parameters. In Angulo et al. (2012) an accurate fit with errors within 5 % is provided over eight orders of magnitude for the halo mass, extending Tinker's fitting range; a discussion on how different halo definitions affect the mass function is also provided. Watson et al. (2013) explore in detail the difference between FoF and SO-defined mass functions; they find agreement below 5 % error with Tinker's fit, with major differences in the high-mass end, and extend the result to higher mass values. Finally, Despali et al. (2016) provide a fit with 5–8 % error for different redshifts and cosmologies, provided the mass function is defined in terms of the virial overdensity halo mass; in the same work, scaling relations for the fitting parameters are provided in order to compute the mass function for different redshifts and halo-mass definitions.

The inclusion of baryon physics in the simulations may also impact the fits of the halo mass function. For instance, Bocquet et al. (2016) shows how the inclusion of baryonic feedback leads to a decrease in the halo masses, which in turn leads to a decrease of the halo abundance at a given mass; the effect is

Este documento incorpora firma electrónica, y es copia auténtica de un documento electrónico archivado por la ULL según la Ley 39/2015.
Su autenticidad puede ser contrastada en la siguiente dirección <https://sede.ull.es/validacion/>

Identificador del documento:	973742	Código de verificación:	Jfg6xBh0
Firmado por:	DENIS TRAMONTE UNIVERSIDAD DE LA LAGUNA	Fecha:	30/06/2017 15:10:10
	RAFAEL DELFIN BARRENA DELGADO UNIVERSIDAD DE LA LAGUNA		30/06/2017 15:21:31
	JOSE ALBERTO RUBIÑO MARTIN UNIVERSIDAD DE LA LAGUNA		30/06/2017 15:34:17
	ERNESTO PEREDA DE PABLO UNIVERSIDAD DE LA LAGUNA		06/07/2017 13:51:19

more important at low redshifts and low masses, where differences with respect to dark matter-only fits can grow up to $\sim 15\%$. The study of baryonic effects on the mass function in other halo mass ranges has been tackled in [Velliscig et al. \(2014\)](#) and [Martizzi et al. \(2014\)](#).

2.2 The conditional mass function

All the works on the mass function described so far consider perturbations in the matter distribution defined with respect to a background which is considered homogeneous. Such a mass function is usually referred to as *unconditional* (UMF). We address now the study of the *conditional mass function* (CMF), meaning the function describing the abundance of objects inside an environment (the *condition*) with a definite density contrast with respect to the background, where the predictions from the UMF are no longer adequate. Locally underdense or overdense regions do alter the mass distribution of collapsed halos (e.g., [Sheth & Lemson 1999](#)); this applies, for instance, when studying the halo abundance inside a supercluster or a cosmic void.

Despite all the effort that has been undertaken to provide an accurate parametrisation of the unconditional mass function (UMF), the conditional mass function (CMF) has not been so thoroughly studied and not a definite recipe can be found in the literature. Existing work on the subject usually take the UMF as a starting point and try to adapt it to the conditioned environment.

In [Cole & Kaiser \(1989\)](#) the abundance of collapsed halos in perturbed regions is computed starting from the [PS74](#) UMF and using the ‘peak-background split’ formalism; their work is particularly focused on the application of the halo bias to astronomical objects like clusters of galaxies, quasars or the study of the diffuse X-ray background. The spatial distribution of dark matter halos and its relation to the underlying mass distribution has also been studied in [Mo & White \(1996\)](#): the authors develop an analytical model, based on the extended Press-Schechter formalism and the spherical collapse assumption, to describe the halo bias function defined as the ratio between the overdensity of halos in a conditioning region and its matter density contrast. Comparison with N-body simulations confirms the accuracy of this model in the case of an Einstein-de-Sitter universe. Other attempts were based on the framework of the spherical collapse, and extended the [PS74](#) mass function, in the excursion set formalism ([Bond et al. 1991](#); [Lacey & Cole 1993](#)). This approach, however, is not adequate to reproduce results from N-body simulations (e.g., [Tormen 1998](#); [Betancort-Rijo & Montero-Dorta 2006a](#); [Neyrinck et al. 2014](#)). The work in [Sheth & Tormen \(2002\)](#) extends the excursion set formalism by including the physics of ellipsoidal collapse. Their results reasonably agree with N-body

Este documento incorpora firma electrónica, y es copia auténtica de un documento electrónico archivado por la ULL según la Ley 39/2015.
Su autenticidad puede ser contrastada en la siguiente dirección <https://sede.ull.es/validacion/>

Identificador del documento:	973742	Código de verificación:	Jfg6xBh0
Firmado por:	DENIS TRAMONTE UNIVERSIDAD DE LA LAGUNA	Fecha:	30/06/2017 15:10:10
	RAFAEL DELFIN BARRENA DELGADO UNIVERSIDAD DE LA LAGUNA		30/06/2017 15:21:31
	JOSE ALBERTO RUBIÑO MARTIN UNIVERSIDAD DE LA LAGUNA		30/06/2017 15:34:17
	ERNESTO PEREDA DE PABLO UNIVERSIDAD DE LA LAGUNA		06/07/2017 13:51:19

simulations; this formalism, however, is used to quantify the difference in halo abundance when considering the mass function evolution from one redshift to another, and cannot be used for computing the CMF at fixed redshift z , which is the problem we address in this work. An extension of the work on the CMF can be found in Rubiño-Martín et al. (2008, hereafter RBP08): among the major changes with respect to previous studies, it introduces the dependence of the CMF on the radial position inside the condition (assumed spherical), and explicitly implements the UMF scaling in such a way that the corresponding CMF is properly normalised over the possible values of the density contrast. The resulting CMF shows good agreement with numerical simulations for the conditions explored in that work.

2.2.1 Formalism for the CMF

From now on we will label the UMF with dn_u/dm . The conditional mass function (CMF), which we label with dn_c/dm , also carries information on the region in which it is defined, namely its size and density contrast. We will always consider spherical regions with matter density contrast δ_m , defined as:

$$\delta_m = \frac{\tilde{\rho}_m - \rho_m}{\rho_m}, \quad (2.15)$$

where ρ_m is the average background matter density and $\tilde{\rho}_m$ the matter density inside the condition. The corresponding linear density contrast δ_l can be computed as (Sheth & Tormen 2002):

$$\delta_l(\delta_m) = \frac{\delta_c}{1.68647} \left[1.68647 - \frac{1.35}{(1 + \delta_m)^{2/3}} - \frac{1.12431}{(1 + \delta_m)^{1/2}} + \frac{0.78785}{(1 + \delta_m)^{0.58661}} \right]. \quad (2.16)$$

In the framework of the CMF it is useful to employ (comoving) Lagrangian coordinates rather than (comoving) Eulerian coordinates. In fact, an overdense (underdense) region does not follow the Hubble flow and it actually shrinks (dilates) during the evolution of the Universe, meaning its Eulerian size changes (the Lagrangian one is constant by construction). Hereafter, we will use the variables R and Q to denote the condition Eulerian and Lagrangian radius, respectively. The two are related by:

$$Q = R(1 + \delta_m)^{1/3}. \quad (2.17)$$

This relation shows that Q is the radius used to define the condition mass in the background cosmology. Hence, the Eulerian and Lagrangian radius are

Este documento incorpora firma electrónica, y es copia auténtica de un documento electrónico archivado por la ULL según la Ley 39/2015.
Su autenticidad puede ser contrastada en la siguiente dirección <https://sede.ull.es/validacion/>

Identificador del documento: 973742	Código de verificación: Jfg6xBh0	Fecha: 30/06/2017 15:10:10
Firmado por: DENIS TRAMONTE UNIVERSIDAD DE LA LAGUNA		
RAFAEL DELFIN BARRENA DELGADO UNIVERSIDAD DE LA LAGUNA		30/06/2017 15:21:31
JOSE ALBERTO RUBIÑO MARTIN UNIVERSIDAD DE LA LAGUNA		30/06/2017 15:34:17
ERNESTO PEREDA DE PABLO UNIVERSIDAD DE LA LAGUNA		06/07/2017 13:51:19

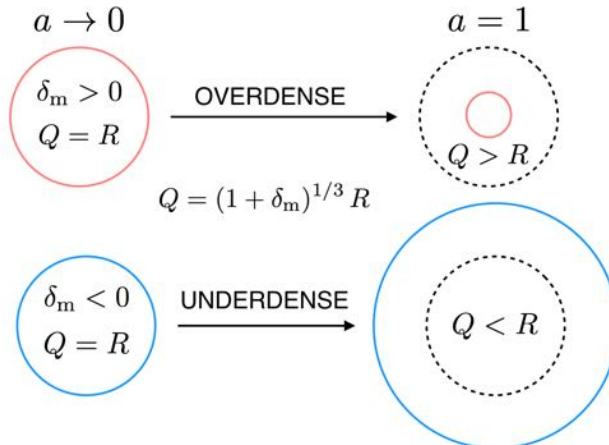


Figure 2.2: Graphic representation of the difference between the Eulerian radius R and the Lagrangian radius Q . While the former evolves according to the local density contrast, the latter remains invariant throughout all redshifts.

expected to coincide before the evolution of matter perturbation, when $a \rightarrow 0$ and $\delta_1 \ll 1$ (see Figure 2.2). The use of Lagrangian coordinates ensures we can talk about a unique value of Q which is valid at all redshifts.

Apart from mass and redshift, the conditional mass function also depends on the condition radius and density contrast, $d\eta_c/dm(m, z; Q, \delta_1)$. There exist different approaches in the literature to derive analytically an expression for the CMF, usually based on the rescaling of some quantities entering the definition of the UMF. We will concentrate in particular on two methods, namely the standard rescaling and one that is implemented locally.

2.2.2 The standard rescaling

The most straightforward way to obtain the conditional mass function is by taking the same analytical expression for the UMF and rewriting it in terms of the rescaled variables:

$$\begin{aligned}\delta_c &\longrightarrow \delta'_c = \delta_c - \delta_1 \\ \sigma^2 &\longrightarrow \sigma'^2 = \sigma^2 - \sigma_1^2,\end{aligned}\tag{2.18}$$

where δ_1 is the condition linear density contrast and $\sigma_1^2 \equiv \sigma^2(R)$ is the variance of the matter field at the condition scale. We refer hereafter to equations 2.18

Este documento incorpora firma electrónica, y es copia auténtica de un documento electrónico archivado por la ULL según la Ley 39/2015.
Su autenticidad puede ser contrastada en la siguiente dirección <https://sede.ull.es/validacion/>

Identificador del documento: 973742

Código de verificación: Jfg6xBh0

Fecha: 30/06/2017 15:10:10

Firmado por: DENIS TRAMONTE
UNIVERSIDAD DE LA LAGUNA

RAFAEL DELFIN BARRENA DELGADO
UNIVERSIDAD DE LA LAGUNA

JOSE ALBERTO RUBIÑO MARTIN
UNIVERSIDAD DE LA LAGUNA

ERNESTO PEREDA DE PABLO
UNIVERSIDAD DE LA LAGUNA

30/06/2017 15:21:31

30/06/2017 15:34:17

06/07/2017 13:51:19

as the *standard rescaling*. The first equation in 2.18 is a threshold offset, taking into account perturbations form in a background whose density is closer to or farther from the critical density. The second equation accounts for the fact that we are considering perturbations inside a finite-size condition: the contribution to the matter variance coming from density perturbations on scales greater than the condition should not be taken into account.

This recipe is the basis for a number of works on the CMF. For instance, the so-called excursion set formalism, also known as extended Press-Schechter (Bond et al. 1991; Lacey & Cole 1993), which is based on the hypothesis of spherical collapse. An extension to this work, including the ellipsoidal collapse, can be found in Sheth & Tormen (2002).

This rescaling can be applied to any UMF parametrisations. However, care must be taken when rescaling mass function parametrisations like T08, W06 or J01, which do not show any explicit dependence on the critical density δ_c . The parameter can be introduced by taking into account that in ST99 or in the Press-Schechter formalism the function f depends on δ_c only via the ratio $\nu \equiv (\delta_c/\sigma)^2$. In the case of the aforementioned UMFs, following RBP08, we can rewrite the variance as $\sigma^2 = \delta_c^2/\nu$, and apply the scaling 2.18 to the variable ν . This yields:

$$\sigma'^2 = [\sigma^2 - \sigma_1^2] \left[\frac{\delta_c}{\delta_c - \delta_1} \right]^2, \quad (2.19)$$

which can be applied to equation 2.14.

2.2.3 The local rescaling

The *local rescaling* is an attempt at improving the standard rescaling by introducing in the CMF a dependence on the position inside the condition; it was first presented in RBP08. In the unconditional framework for the mass function halos form in correspondence to regions with linear overdensity δ_1 , which eventually collapse to form an object of mass m ; over the scale of the corresponding radius R_1 , the density field has variance σ_1^2 . Since density perturbation is a Gaussian random field, the probability for the perturbation δ_1 over a scale R_1 is given by:

$$P(\delta_1|R_1) = \frac{1}{\sqrt{2\pi}\sigma_1} \exp\left(-\frac{\delta_1^2}{2\sigma_1^2}\right). \quad (2.20)$$

Now let us consider a conditioning region in the Universe, characterised by a Lagrangian radius Q_1 and a linear overdensity δ_1 . The probability of having a region of size $Q_2 < Q_1$ with an overdensity $\delta_2 > \delta_1$ at a distance q from the

Este documento incorpora firma electrónica, y es copia auténtica de un documento electrónico archivado por la ULL según la Ley 39/2015.
Su autenticidad puede ser contrastada en la siguiente dirección <https://sede.ull.es/validacion/>

Identificador del documento: 973742

Código de verificación: Jfg6xBh0

Fecha: 30/06/2017 15:10:10

Firmado por: DENIS TRAMONTE
UNIVERSIDAD DE LA LAGUNA

RAFAEL DELFIN BARRENA DELGADO
UNIVERSIDAD DE LA LAGUNA

JOSE ALBERTO RUBIÑO MARTIN
UNIVERSIDAD DE LA LAGUNA

ERNESTO PEREDA DE PABLO
UNIVERSIDAD DE LA LAGUNA

30/06/2017 15:21:31

30/06/2017 15:34:17

06/07/2017 13:51:19

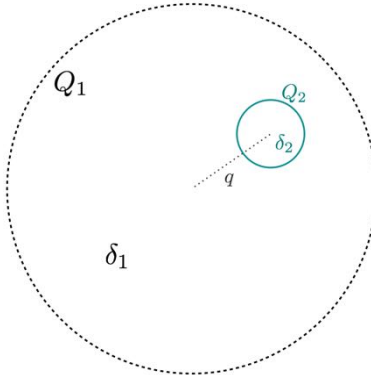


Figure 2.3: Representation of the basic framework for developing the formalism of the local CMF. The condition is represented as a sphere with Lagrangian radius Q_1 and density contrast δ_1 . At a distance q from its centre, we consider another region, with Lagrangian radius $Q_2 < Q_1$, and density contrast $\delta_2 > \delta_1$: such region encloses a total mass m , which is going to be the collapsed halo.

centre of the condition (Figure 2.3) is given by:

$$P(\delta_2|\delta_1, q, Q_1) = \frac{P(\delta_1, \delta_2|q, Q_1)}{P(\delta_1)}, \quad (2.21)$$

where $P(\delta_1)$ has the same form as 2.20 and the joint probability distribution is given by a multivariate Gaussian:

$$P(\delta_1, \delta_2|q, Q_1) = \frac{1}{2\pi |\det(C)|^{1/2}} \exp\left(-\frac{1}{2} \boldsymbol{\delta}^T C^{-1} \boldsymbol{\delta}\right). \quad (2.22)$$

In the relation above $\boldsymbol{\delta}^T = (\delta_1, \delta_2)$ and C denotes the covariance matrix:

$$C = \begin{pmatrix} \sigma_1^2 & \sigma_{12} \\ \sigma_{12} & \sigma_2^2 \end{pmatrix}. \quad (2.23)$$

The diagonal terms are the variances $\sigma_1^2 \equiv \sigma^2(Q_1)$, $\sigma_2^2 \equiv \sigma^2(Q_2)$, while the covariance is given by:

$$\begin{aligned} \sigma_{12} &= \sigma_{12}(q, Q_1, Q_2) = \\ &= \frac{b(z)^2}{2\pi} \int_0^\infty dk k^2 P(k) w(kQ_1) w(kQ_2) \frac{\sin(kq)}{kq}. \end{aligned} \quad (2.24)$$

Este documento incorpora firma electrónica, y es copia auténtica de un documento electrónico archivado por la ULL según la Ley 39/2015.
Su autenticidad puede ser contrastada en la siguiente dirección <https://sede.ull.es/validacion/>

Identificador del documento: 973742

Código de verificación: Jfg6xBh0

Fecha: 30/06/2017 15:10:10

Firmado por: DENIS TRAMONTE
UNIVERSIDAD DE LA LAGUNA

RAFAEL DELFIN BARRENA DELGADO
UNIVERSIDAD DE LA LAGUNA

JOSE ALBERTO RUBIÑO MARTIN
UNIVERSIDAD DE LA LAGUNA

ERNESTO PEREDA DE PABLO
UNIVERSIDAD DE LA LAGUNA

30/06/2017 15:21:31

30/06/2017 15:34:17

06/07/2017 13:51:19

Explicit computation of equation 2.21 yields:

$$\begin{aligned} P(\delta_2|\delta_1, q, Q_1) = & (2\pi)^{-1/2} \left(\sigma_2^2 - \frac{\sigma_{12}^2}{\sigma_1^2} \right)^{-1/2} \\ & \times \exp \left[-\frac{1}{2} \frac{(\delta_2 - \delta_1 \sigma_{12}/\sigma_1^2)^2}{\sigma_2^2 - \sigma_{12}^2/\sigma_1^2} \right]. \end{aligned} \quad (2.25)$$

If we compare equation 2.25 with equation 2.20 we see that it is natural to adopt as rescaled variables the quantities:

$$\begin{aligned} \delta'_c &= \delta_c - D(q, \delta_1, \delta_2)\delta_1 \\ \sigma'^2_2 &= \sigma_2^2 - D^2(q, \delta_1, \delta_2)\sigma_1^2, \end{aligned} \quad (2.26)$$

in which we defined

$$D(q, Q_1, Q_2) = \frac{\sigma_{12}(q, Q_1, Q_2)}{\sigma_1^2(Q_1)}. \quad (2.27)$$

We refer to the equations 2.26 as the local rescaling; it is the recipe for scaling the variables to obtain the CMF from the UMF.

Again, this rescaling can be applied to any UMF parametrisation, but if the critical density does not appear explicitly the rescaling has to be applied to the variable $\nu = (\delta_c/\sigma)^2$, yielding:

$$\sigma'^2_2 = [\sigma_2^2 - D(q, \delta_1, \delta_2)^2 \sigma_1^2] \left[\frac{\delta_c}{\delta_c - D(q, \delta_1, \delta_2)\delta_1} \right]^2, \quad (2.28)$$

which can be used for the T08 UMF. The σ term appearing in the derivative of equation 2.8, instead, should be always rescaled using 2.26 only.

In RBP08 it is said that the quantity defined in equation 2.27, for $Q_2 \ll Q_1$, is practically independent of Q_2 , a property that can be exploited to speed up the computation. In particular, this allowed computing the mass derivative of the variance appearing in equation 2.8 without the need of applying each time the rescaling. However, we found that this approximation is not so good in most of the mass range we employ. In this work we therefore always applied the full computation with no approximations.

2.2.4 Examples and comparisons

We show in Figure 2.4 some comparisons between the UMF and the CMF rescalings. We consider the T08 mass function computed with a mean overdensity $\Delta = 200$ at redshift $z = 0$, and as the underlying cosmology the

Este documento incorpora firma electrónica, y es copia auténtica de un documento electrónico archivado por la ULL según la Ley 39/2015.
Su autenticidad puede ser contrastada en la siguiente dirección <https://sede.ull.es/validacion/>

Identificador del documento: 973742	Código de verificación: Jfg6xBh0
Firmado por: DENIS TRAMONTE UNIVERSIDAD DE LA LAGUNA	Fecha: 30/06/2017 15:10:10
RAFAEL DELFIN BARRENA DELGADO UNIVERSIDAD DE LA LAGUNA	30/06/2017 15:21:31
JOSE ALBERTO RUBIÑO MARTIN UNIVERSIDAD DE LA LAGUNA	30/06/2017 15:34:17
ERNESTO PEREDA DE PABLO UNIVERSIDAD DE LA LAGUNA	06/07/2017 13:51:19

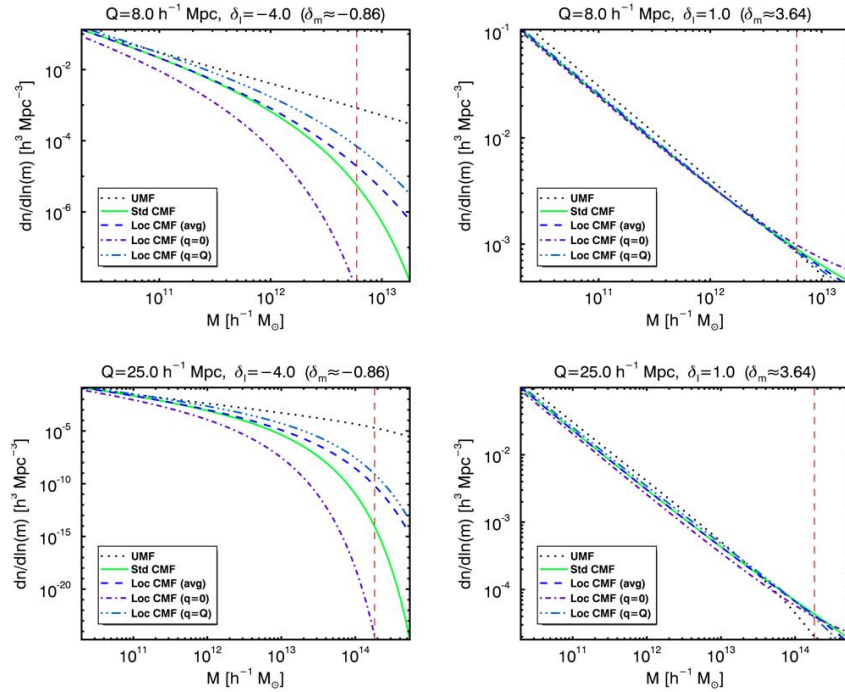


Figure 2.4: Comparison between the UMF and different CMF rescalings computed using the T08 parametrisation, in small-scale regions (upper panels), large scale regions (lower panels), underdensities (left panels) and overdensities (right panels). We consider the CMF computed with the standard rescaling and three cases of the locally rescaled CMF, namely the CMF evaluated in the centre of the condition ($q = 0$), at the condition border ($q = Q$) and its volume average inside the condition computed with equation 2.29. The vertical dashed line marks the fraction 1/30 of the condition mass, above which the formalism for computing the CMF is no longer reliable.

set of parameters listed in table 2.1. We considered a small scale region, $Q = 8 h^{-1} \text{Mpc}$, and a larger one, $Q = 25 h^{-1} \text{Mpc}$, both in the case of an underdensity, $\delta_l = -4.0$ ($\delta_m \approx -0.86$), and of an overdensity, $\delta_l = 1.0$ ($\delta_m \approx 3.64$). For each case, we plot the unconditional mass function, the standard CMF with the rescaling 2.19 and the local CMF with the rescaling 2.28. The local rescaling leaves a dependence on the radial distance q from the centre of the condition; we include both the case of the CMF evaluated in the centre of the

Este documento incorpora firma electrónica, y es copia auténtica de un documento electrónico archivado por la ULL según la Ley 39/2015.
Su autenticidad puede ser contrastada en la siguiente dirección <https://sede.ull.es/validacion/>

Identificador del documento: 973742

Código de verificación: Jfg6xBh0

Fecha: 30/06/2017 15:10:10

Firmado por: DENIS TRAMONTE
UNIVERSIDAD DE LA LAGUNA

RAFAEL DELFIN BARRENA DELGADO
UNIVERSIDAD DE LA LAGUNA

JOSE ALBERTO RUBIÑO MARTIN
UNIVERSIDAD DE LA LAGUNA

ERNESTO PEREDA DE PABLO
UNIVERSIDAD DE LA LAGUNA

30/06/2017 15:21:31

30/06/2017 15:34:17

06/07/2017 13:51:19

Table 2.1: Values of cosmological parameters for our reference model.

Ω_m	Ω_b	Ω_Λ	h	n_s	σ_8
0.3	4.6×10^{-2}	0.7	0.7	0.96	0.8

condition, $q = 0$, and at its boundary, $q = Q$. Besides, we consider the volume average of the local CMF inside the condition, defined as:

$$\frac{dn_c^{\text{avg}}}{dm}(m, z; q, \delta_l) = \frac{3}{q^3} \int_0^q dq q^2 \frac{dn_c}{dm}(m, z; q, \delta_l, q), \quad (2.29)$$

which is no longer dependent on the radius q . In the plots of figure 2.4 we also add a vertical dashed line which marks a mass equal to a fraction 1/30 of the mass of the condition. In RBP08, this value is taken as a limit threshold over which the formalism for computing the CMF is no longer applicable, given we are considering scales too close to the condition mass.

From figure 2.4 we see that, for a fixed condition radius, underdensities are much more affected in the mass distribution of halos, compared to overdensities. Indeed, by looking at the values of the halo density, values in the case of $\delta_l = -4.0$ are strongly reduced compared to the case of $\delta_l = 1.0$. The presence of high-mass collapsed objects in such an underdense region is strongly suppressed, and this is well reproduced by all parametrisations of the CMF, which consistently lie below the reference UMF. Since we are considering the abundance of rare objects, in the case of underdensities we are fully in the exponential cut-off of the mass function, which enhances the differences between the parametrisations. In the case of overdensities, instead, we are considering the mass distribution of relatively abundant objects, so we are exploring the power-law regime of the mass functions and differences are less visible. In this case, the CMFs predict a higher abundance of high-mass objects compared to the UMF, while the abundance of low mass halos slightly decreases. Differences are larger in the case of higher values of the condition radius, given this allows us to explore the mass function behavior up to higher masses; however, for a fixed halo mass, differences between the CMFs are larger in the case of smaller conditions.

From now on, when talking about the local rescaling, we will usually refer to its average in the condition as computed with equation 2.29. We see that this CMF shows reasonable agreement with the standard rescaling; this is clear in the overdense regions, and also in the underdense regions as long as we are not considering the high-mass tail. The local CMF computed in the centre of the condition or in its boundary shows less agreement with the standard CMF; these are rather extreme cases that we are not going to consider in the

Este documento incorpora firma electrónica, y es copia auténtica de un documento electrónico archivado por la ULL según la Ley 39/2015.
Su autenticidad puede ser contrastada en la siguiente dirección <https://sede.ull.es/validacion/>

Identificador del documento: 973742

Código de verificación: Jfg6xBh0

Fecha: 30/06/2017 15:10:10

Firmado por: DENIS TRAMONTE UNIVERSIDAD DE LA LAGUNA	30/06/2017 15:21:31
RAFAEL DELFIN BARRENA DELGADO UNIVERSIDAD DE LA LAGUNA	30/06/2017 15:34:17
JOSE ALBERTO RUBIÑO MARTIN UNIVERSIDAD DE LA LAGUNA	06/07/2017 13:51:19
ERNESTO PEREDA DE PABLO UNIVERSIDAD DE LA LAGUNA	

following. Notice that, even though we are only showing the case of the T08 mass functions, these conclusions apply to any other UMF parametrisation.

2.3 Mass function normalisation

In RBP08 it is stressed that the conditional mass function should satisfy a normalisation condition: by integrating the CMF over the possible values of the linear overdensity inside a condition Q , each weighted by its probability distribution, the unconditional mass function must be recovered. In formulae:

$$\frac{dn_u}{dm}(m) = \int_{-\infty}^X d\delta_l \frac{dn_c}{dm}(m; Q, \delta_l) G(\delta_l; \sigma_l), \quad m < m(Q), \quad (2.30)$$

where $G(\delta_l; \sigma_l)$ stands for a Gaussian with zero mean and variance σ_l , which by hypothesis is the probability distribution for the density contrast field, and the CMF dn_c/dm can be either the standard CMF or the local CMF averaged inside the condition. Equation 2.30 is an application of the law of total probability, in which the conditional mass function is indeed the conditioned probability for halo of a given mass, given a conditioning δ_l . Note that by construction, the expression must be evaluated at masses no larger than the condition mass $m(Q)$. The upper integration limit X is equal to the critical density δ_c for mass functions based on the physics of spherical collapse (Press & Schechter 1974), and to the value of the moving barrier shape when the ellipsoidal collapse is allowed (Sheth & Tormen 2002). In our case we are considering the T08 mass function, so we take as limit $X = \delta_c$.

We note that this normalisation condition has been previously discussed in the literature, mainly in connection to the PS mass function. For example, several authors (Sheth & Lemson 1999; Musso et al. 2012; Neyrinck et al. 2014) have shown that for the (unphysical) case of an unbound upper limit of the integral (i.e. $X = +\infty$), the normalisation is satisfied for the PS mass function. Therefore, when the integration is truncated to the corresponding upper limit, a modification of the normalisation is required in order to verify the equation.

In RBP08, this condition was applied to different prescriptions for the unconditional mass function. In particular, they show that, for the case of the ST99 and the W06 mass functions, the local rescaling as defined in equation 2.26 does not satisfy the condition 2.30. The method proposed in RBP08 to solve the normalisation problem is the introduction of a normalisation parameter α , which we shall refer to as the *normalisation parameter*, in the rescaling for the

Este documento incorpora firma electrónica, y es copia auténtica de un documento electrónico archivado por la ULL según la Ley 39/2015.
Su autenticidad puede ser contrastada en la siguiente dirección <https://sede.ull.es/validacion/>

Firmado por:	Identificador del documento:	Código de verificación:	Fecha:
DENIS TRAMONTE UNIVERSIDAD DE LA LAGUNA	973742	Jfg6xBh0	30/06/2017 15:10:10
RAFAEL DELFIN BARRENA DELGADO UNIVERSIDAD DE LA LAGUNA			30/06/2017 15:21:31
JOSE ALBERTO RUBIÑO MARTIN UNIVERSIDAD DE LA LAGUNA			30/06/2017 15:34:17
ERNESTO PEREDA DE PABLO UNIVERSIDAD DE LA LAGUNA			06/07/2017 13:51:19

critical density:

$$\delta_c \rightarrow \delta'_c = \delta_c \left[1 - D(q, Q_1, Q_2) \frac{\delta_1}{\alpha} \right]. \quad (2.31)$$

For the mass function parametrisations of J01, W06 and T08, in which δ_c does not appear explicitly, the new rescaling is to be applied in the form:

$$\sigma'^2_2 = [\sigma^2_2 - D(q, Q_1, Q_2)^2 \sigma^2_1] \left[\frac{\alpha}{\alpha - D(q, Q_1, Q_2) \delta_1} \right]^2, \quad (2.32)$$

which should be used instead of equation 2.28.

A proper value for α should yield a normalised CMF over all the mass range we are using. In RBP08 the normalisation parameter was estimated for the ST99 and W06 mass functions, for one particular value of the condition Lagrangian radius. In this work we repeated the same analysis for the T08 mass function; in addition, we studied the dependence of α on the size of the condition, both for the standard and the local rescaling. In the case of the standard CMF, the normalised rescaling reads:

$$\delta'_c = \delta_c \left(1 - \frac{\delta_1}{\alpha} \right), \quad (2.33)$$

for the mass function parametrisations where δ_c appears explicitly; otherwise, the rescaling takes the form:

$$\sigma'^2_2 = (\sigma^2_2 - \sigma^2_1) \left(\frac{\alpha}{\alpha - \delta_1} \right)^2. \quad (2.34)$$

We followed the same method described in RBP08. In order to determine the precision with which the normalisation is satisfied by the CMF we computed the ratio:

$$R(m, Q) \equiv \left[\frac{dn_u}{dm}(m) \right]^{-1} \int_{-\infty}^X d\delta_1 \frac{dn_c}{dm}(m; Q, \delta_1) G(\delta_1; \sigma_1), \quad (2.35)$$

that quantifies the error in the normalisation (how much the integrated conditional mass function differs from the expected unconditional one). In equation 2.35 the CMF is to be computed with the new rescaling 2.31 or 2.32, depending on the chosen parametrisation for the initial UMF. By varying the parameter α we end up with a three-variable function $R(m, Q, \alpha)$. We considered different values for the condition Lagrangian radius, in the range [5, 30] h^{-1} Mpc. For each case, we computed the quantity $(1 - R(m, Q, \alpha)) \times 100$ and considered the regions in the (m, α) plane where it is at most 10 %, 5 %

Este documento incorpora firma electrónica, y es copia auténtica de un documento electrónico archivado por la ULL según la Ley 39/2015.
Su autenticidad puede ser contrastada en la siguiente dirección <https://sede.ull.es/validacion/>

Identificador del documento: 973742

Código de verificación: Jfg6xBh0

Fecha: 30/06/2017 15:10:10

Firmado por: DENIS TRAMONTE
UNIVERSIDAD DE LA LAGUNA

RAFAEL DELFIN BARRENA DELGADO
UNIVERSIDAD DE LA LAGUNA

JOSE ALBERTO RUBIÑO MARTIN
UNIVERSIDAD DE LA LAGUNA

ERNESTO PEREDA DE PABLO
UNIVERSIDAD DE LA LAGUNA

30/06/2017 15:21:31

30/06/2017 15:34:17

06/07/2017 13:51:19

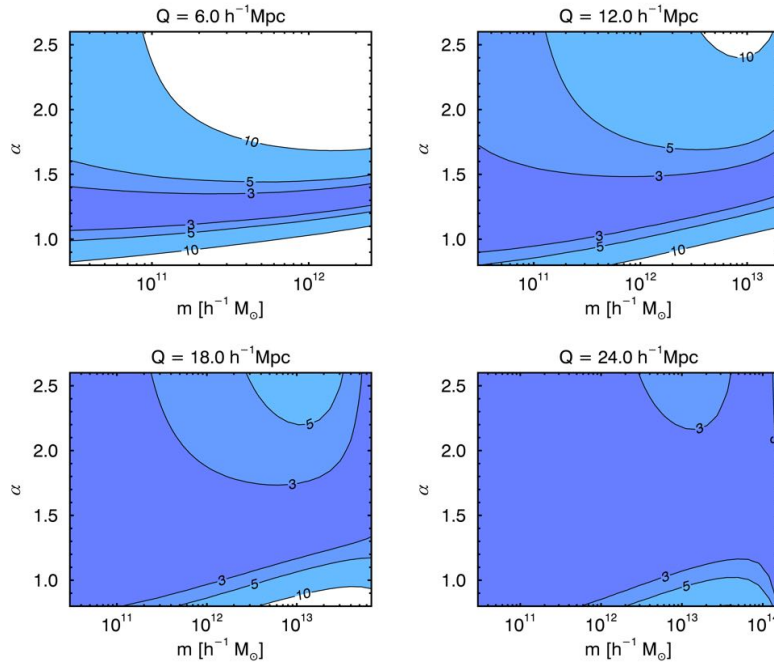


Figure 2.5: Regions showing the allowed values for the normalisation parameter α , as a function of the mass, in order to have the normalisation condition satisfied with 10%, 5% and 3% accuracy, respectively. The conditional mass function is computed using the T08 parametrisation with the local rescaling. The plots show how the contours evolve when the condition size increases: larger conditions are less effective in determining a unique value for the normalisation parameter, ultimately leaving α unconstrained.

and 3 %. The results are plotted in figure 2.5 for the case of local rescaling, and in figure 2.6 for the standard rescaling.

We see that it is indeed possible to choose a unique α satisfying the normalisation condition with a $\sim 3\%$ accuracy for all masses; in the case of $Q = 6 \text{ } h^{-1} \text{ Mpc}$, the normalisation parameter is quite well constrained as:

$$\alpha = 1.25 \quad (2.36)$$

However, the precision contours largely widens when the condition becomes larger, meaning that larger conditions are not effective in constraining the normalisation problem. In fact, we see that for $Q \gtrsim 20 \text{ } h^{-1} \text{ Mpc}$ the usual value

Este documento incorpora firma electrónica, y es copia auténtica de un documento electrónico archivado por la ULL según la Ley 39/2015.
Su autenticidad puede ser contrastada en la siguiente dirección <https://sede.ull.es/validacion/>

Identificador del documento: 973742

Código de verificación: Jfg6xBh0

Firmado por: DENIS TRAMONTE
UNIVERSIDAD DE LA LAGUNA

Fecha: 30/06/2017 15:10:10

RAFAEL DELFIN BARRENA DELGADO
UNIVERSIDAD DE LA LAGUNA

30/06/2017 15:21:31

JOSE ALBERTO RUBIÑO MARTIN
UNIVERSIDAD DE LA LAGUNA

30/06/2017 15:34:17

ERNESTO PEREDA DE PABLO
UNIVERSIDAD DE LA LAGUNA

06/07/2017 13:51:19

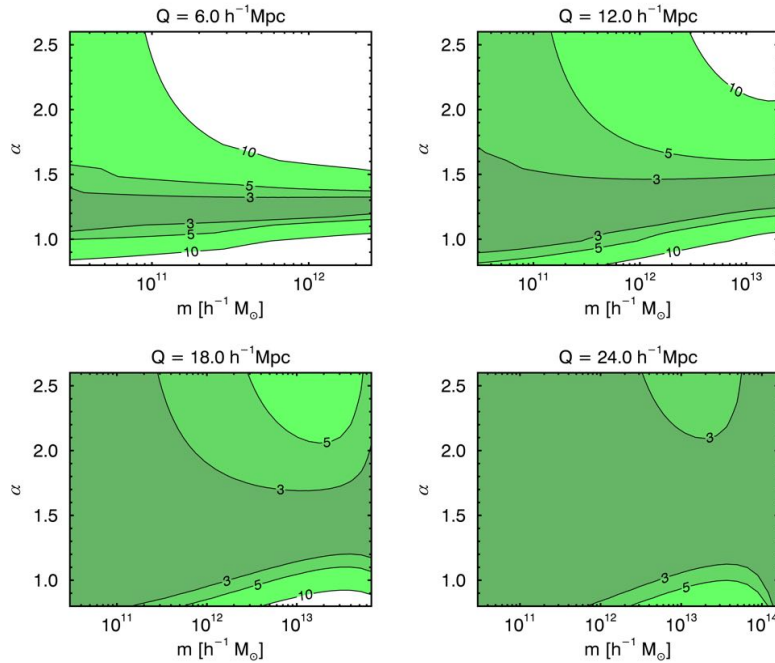


Figure 2.6: Same as Figure 2.5, but computing the mass function with the standard rescaling.

$\delta_c = 1.686$ is allowed for the whole mass range (notice that setting $\alpha = \delta_c$ is equivalent to using the original form of the local rescaling, equations 2.26 and 2.28). The same conclusion apply for the case of the standard rescaling, constraining the value $\alpha = 1.25$ in the smaller conditions, but leaving it unconstrained when the radius is larger.

To sum up, both the local and the standard rescalings need the introduction of the α parameter for satisfying the normalisation condition 2.30. Small scale conditions are quite effective in constraining its value to $\alpha = 1.25$, which we shall adopt in the following for the normalised local and standard rescaling of the T08 mass function. This result is consistent with the one found in RBP08 for the ST99 mass function in conditions of similar size. The normalisation parameter is instead unconstrained by larger conditions; requiring a normalised CMF is thus not enough for constraining the value of α at scales $Q \gtrsim 20 h^{-1} \text{ Mpc}$. In order to test whether the same normalisation parameter

can be used also for large scales, we have to compare the CMF with numerical simulations, which is the subject of section 2.4.

2.4 Test of CMF against numerical simulations

In this section we test the validity of the CMF prescriptions by comparing the predicted abundance of halos with numerical simulations. We want to extend the work in RBP08 by employing a considerably larger number of conditions, in order to reduce the statistical uncertainties associated with the particular condition choice. We will test the CMFs against counts extracted from simulations at different scales, and both in overdense and underdense regions. We will also explore the effect of employing different values for the normalisation parameter α entering the computation of the locally-rescaled CMF.

We present in the following the simulation set we considered, the algorithm we employed to identify regions with a given density contrast and to build the halo mass distribution, and the results we obtained when comparing such a distribution with the theoretical recipe for the conditional mass function.

Table 2.2: Table summarising the properties of the two simulations used in this work.

Name	Size (h^{-1} Mpc)	Particle mass ($h^{-1} M_{\odot}$)	Softening (h^{-1} kpc)
LSS	1500	2.7×10^{11}	60
SSS	250	1.2×10^9	10

2.4.1 The simulations set

We considered two N-body dark matter-only simulations. Each simulation contains 10^9 particles in a cubic box with periodic conditions at the boundary, in one case of size $250 h^{-1}$ Mpc, and in the other of size $1500 h^{-1}$ Mpc. We shall refer to these simulations as the Small Scale Simulation (SSS) and the Large Scale Simulation (LSS), respectively. The basic information on these simulations is summarised in table 2.2. The LSS was selected among the Minerva sample of 100 realisations of the same volume size (Grieb et al. 2016); the SSS, instead, was performed in order to extend the lower halo mass range. Initial conditions were generated starting from an initial glass configuration, and using the 2LPT code implementing the method described in Crocce et al. (2006). We adopted a flat Λ CDM model with parameters: $h = 0.695$, $\Omega_b = 0$, $\Omega_m = 0.285$, $n_s = 0.9632$ and $\sigma_8 = 0.828$ (Sánchez et al. (2013), Table I), and computed the input linear power spectrum with CAMB (Lewis et al. 2000). The initial

Este documento incorpora firma electrónica, y es copia auténtica de un documento electrónico archivado por la ULL según la Ley 39/2015.
Su autenticidad puede ser contrastada en la siguiente dirección <https://sede.ull.es/validacion/>

Identificador del documento: 973742	Código de verificación: Jfg6xBh0
Firmado por: DENIS TRAMONTE UNIVERSIDAD DE LA LAGUNA	Fecha: 30/06/2017 15:10:10
RAFAEL DELFIN BARRENA DELGADO UNIVERSIDAD DE LA LAGUNA	30/06/2017 15:21:31
JOSE ALBERTO RUBIÑO MARTIN UNIVERSIDAD DE LA LAGUNA	30/06/2017 15:34:17
ERNESTO PEREDA DE PABLO UNIVERSIDAD DE LA LAGUNA	06/07/2017 13:51:19

conditions were evolved from $z = 63$ to $z = 0$ using GADGET (last described in Springel et al. 2005).

On the simulation snapshot we ran a FoF halo finder with linking length $\ell = 0.1$. This approximately corresponds to a spherical overdensity $\Delta = 1600$, and is used to separate density peaks that would be taken as a single halo by a lower overdensity finder. Then, around each identified peak, halos were searched with a spherical overdensity $\Delta = 200$, after processing the FoF output with the SUBFIND code (Springel et al. 2001).

2.4.2 Testing the UMF

In Figure 2.7 we show the comparison between the T08 mass function, computed with an overdensity parameter $\Delta = 200$, and the halo counts extracted from the simulations. Error bars associated with the simulation data points were computed assuming poissonian statistics inside each mass bin. To avoid boundary effects or resolution effects, the safe mass range we can use for each simulation is $[10^{10.5}, 10^{14.5}] h^{-1} \text{ Mpc}$ with the SSS, and $[10^{13}, 10^{15.5}] h^{-1} \text{ Mpc}$ with the LSS. By joining the two simulations we are capable of exploring a range of masses extending over five orders of magnitude. For both simulations, the lower mass limit is a resolution limit: below that scale, the halo finder is no longer able to converge in computing the halo mass with overdensity 200, and all the substructures around the previously identified density peaks are lost. When determining the theoretical UMF, we checked that the finite-box effect has a negligible impact on the computation of the variance, remaining below one part in 10^3 also in the SSS.

The first plot in Figure 2.7 shows that the number density of halos extracted from both simulations is capable of reproducing the overall shape of the T08 mass function, showing the same dependence on mass over the whole range we are exploring. However, the residual plot in the lower panel shows that there are still some differences with respect to the theoretical prediction, mostly at the level of 10 %. This is a systematic effect which is due to the use of only one simulation for each box; for instance, the excess of halo abundance for the LSS visible in the high-mass end can be removed by averaging many realisations of the same simulation (see Figure 1 of Grieb et al. 2016); this deviation however concerns very high masses where errors become large and are not useful for the following analysis.

Besides, a numerical resolution effect is visible in both simulations: it can be recognised as a change in the mass dependence of the residual halo abundance at masses $\sim 2 \times 10^{11} h^{-1} \text{ Mpc}$ in the SSS and $\sim 5 \times 10^{13} h^{-1} \text{ Mpc}$ in the LSS. Given the individual particle masses reported in table 2.2, these values correspond in

Este documento incorpora firma electrónica, y es copia auténtica de un documento electrónico archivado por la ULL según la Ley 39/2015.
Su autenticidad puede ser contrastada en la siguiente dirección <https://sede.ull.es/validacion/>

Identificador del documento:	973742	Código de verificación:	Jfg6xBh0
Firmado por:	DENIS TRAMONTE UNIVERSIDAD DE LA LAGUNA	Fecha:	30/06/2017 15:10:10
	RAFAEL DELFIN BARRENA DELGADO UNIVERSIDAD DE LA LAGUNA		30/06/2017 15:21:31
	JOSE ALBERTO RUBIÑO MARTIN UNIVERSIDAD DE LA LAGUNA		30/06/2017 15:34:17
	ERNESTO PEREDA DE PABLO UNIVERSIDAD DE LA LAGUNA		06/07/2017 13:51:19

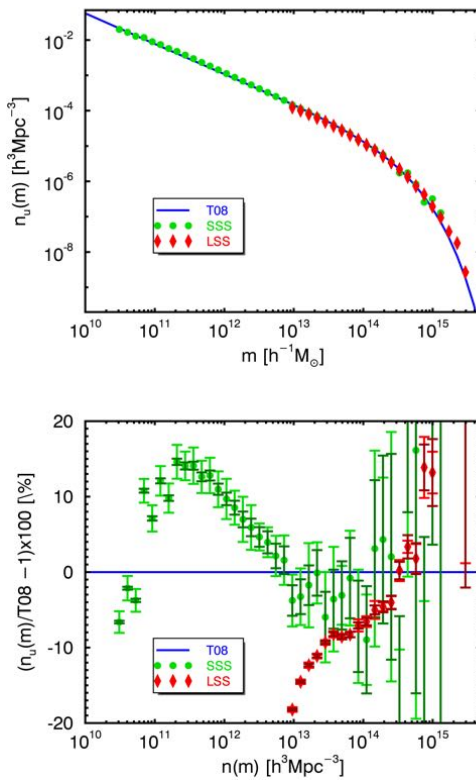


Figure 2.7: Unconditional mass function test for the simulation set. Upper panel: points mark the halo number density as a function of mass, obtained from the Small Scale Simulation (circles) and the Large Scale Simulation (diamonds); the line shows the abundance predicted by the T08 UMF computed with the same underlying cosmology and an overdensity parameter $\Delta = 200$. Lower panel: same as the upper panel but showing the percent residuals with respect to the theoretical UMF. Poissonian errors are overplotted (darker error bars), together with numerical errors computed dividing each box into eight subsets of equal volume (lighter error bars). Although the abundances extracted from simulations reproduce the overall shape of the T08 UMF, they are affected by systematics that can produce deviations at the level of $\sim 10\%$. These offsets, which could in principle be strongly reduced by averaging over a large number of simulations, must be accounted for in the subsequent analysis.

Este documento incorpora firma electrónica, y es copia auténtica de un documento electrónico archivado por la ULL según la Ley 39/2015.
Su autenticidad puede ser contrastada en la siguiente dirección <https://sede.ull.es/validacion/>

Identificador del documento: 973742

Código de verificación: Jfg6xBh0

Fecha: 30/06/2017 15:10:10

Firmado por: DENIS TRAMONTE
UNIVERSIDAD DE LA LAGUNA

RAFAEL DELFIN BARRENA DELGADO
UNIVERSIDAD DE LA LAGUNA

JOSE ALBERTO RUBIÑO MARTIN
UNIVERSIDAD DE LA LAGUNA

ERNESTO PEREDA DE PABLO
UNIVERSIDAD DE LA LAGUNA

30/06/2017 15:21:31

30/06/2017 15:34:17

06/07/2017 13:51:19

both cases to halos containing around 200 particles. We actually considered such halos in LSS when performing the analysis described in section 2.4.3. In order to test to what extent this numerical issue can affect our results, we explicitly computed the bias as the ratio of the variance of halo number density to the variance of matter, as a function of mass. We found that numerical resolution effects in the LSS only show up below masses $\sim 6 \times 10^{12} h^{-1}$ Mpc, corresponding to halos made of around 20 particles, which are not considered in our analysis. These resolution effects are therefore not a significant issue.

In order to achieve a better agreement with the theoretical mass function, the average of many simulations in each box should be used. This goes beyond the scope of this work. Here, in order to account for possible systematics in the following analyses, when considering comparisons between simulated and predicted halo abundances in conditioned environments, we will always be comparing the ratios of each CMF to the corresponding UMF, i.e. directly comparing the halo bias function.

2.4.3 Methodology for CMF tests

Testing the CMF requires comparing the theoretical abundance of halos with the actual counts extracted from regions of the simulation with a definite density contrast. In order to identify such regions we placed a large number of spheres on the simulation snapshot, storing the total number of particles inside each one of them; this allowed us to determine the number density of particles inside each sphere. By knowing the average particle density, the sphere density contrast could be computed using the expression 2.15. The sphere positions were generated randomly with a uniform distribution inside the simulation box; taking advantage of the periodic boundary conditions, any point of the box was a possible sphere centre. The sphere radii were also generated randomly; in the case of the SSS, which we employed for the smaller conditions, the values for the Eulerian radius R were drawn from a uniform distribution in the interval $[5, 15] h^{-1}$ Mpc. The largest conditions were instead placed over the LSS, with radii drawn from a uniform distribution in the interval $[20, 30] h^{-1}$ Mpc. We employed a total of 4.4×10^5 spheres for the LSS, and of 6×10^4 spheres for the SSS: the smaller simulation volume ensures that the same spatial coverage can be obtained with a lower number of spheres. In both cases the spheres are allowed to overlap; in fact, this is not an issue when building the final halo distributions. In figures 2.8 and 2.9 we show two sample slices of the SSS and LSS, respectively, showing the simulation particles, the identified halos and the spheres whose centres lie inside the slices.

Note that the aforementioned radii are the Eulerian quantities R ; once the

Este documento incorpora firma electrónica, y es copia auténtica de un documento electrónico archivado por la ULL según la Ley 39/2015.
Su autenticidad puede ser contrastada en la siguiente dirección <https://sede.ull.es/validacion/>

Identificador del documento:	973742	Código de verificación:	Jfg6xBh0
Firmado por:	DENIS TRAMONTE UNIVERSIDAD DE LA LAGUNA	Fecha:	30/06/2017 15:10:10
	RAFAEL DELFIN BARRENA DELGADO UNIVERSIDAD DE LA LAGUNA		30/06/2017 15:21:31
	JOSE ALBERTO RUBIÑO MARTIN UNIVERSIDAD DE LA LAGUNA		30/06/2017 15:34:17
	ERNESTO PEREDA DE PABLO UNIVERSIDAD DE LA LAGUNA		06/07/2017 13:51:19

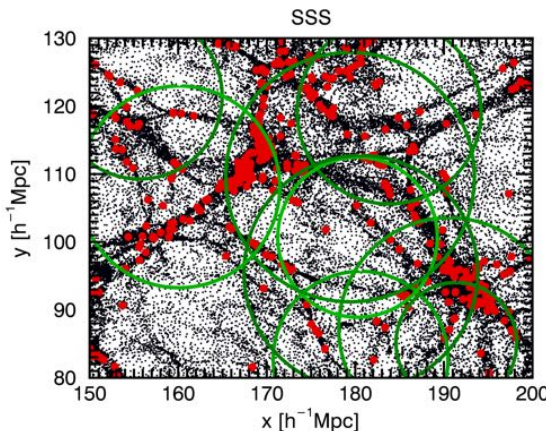


Figure 2.8: Examples of a snapshot slice from the SSS box, showing a $50 \times 50 h^{-2} \text{Mpc}^2$ area with a $1 h^{-1} \text{Mpc}$ depth. Simulation particles are shown as black dots, while red spots represent identified halos. Green circles show the randomly placed spheres. The abundance of particles inside each sphere defines its density contrast, while the mass distribution of the encompassed halos is the simulated CMF.

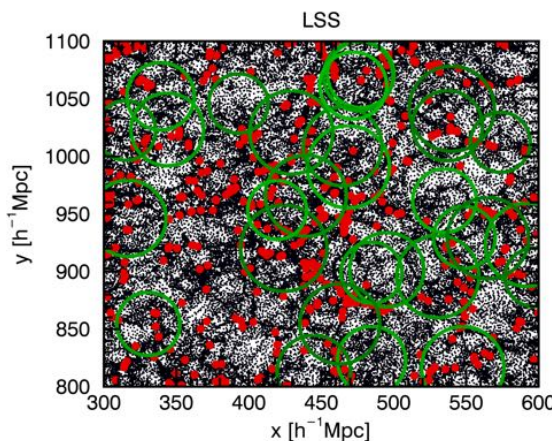


Figure 2.9: Same as figure 2.8, this time showing a $300 \times 300 h^{-2} \text{Mpc}^2$ area slice from the LSS, with a $3 h^{-1} \text{Mpc}$ depth.

Este documento incorpora firma electrónica, y es copia auténtica de un documento electrónico archivado por la ULL según la Ley 39/2015.
Su autenticidad puede ser contrastada en la siguiente dirección <https://sede.ull.es/validacion/>

Identificador del documento: 973742

Código de verificación: Jfg6xBh0

Firmado por: DENIS TRAMONTE
UNIVERSIDAD DE LA LAGUNA

Fecha: 30/06/2017 15:10:10

RAFAEL DELFIN BARRENA DELGADO
UNIVERSIDAD DE LA LAGUNA

30/06/2017 15:21:31

JOSE ALBERTO RUBIÑO MARTIN
UNIVERSIDAD DE LA LAGUNA

30/06/2017 15:34:17

ERNESTO PEREDA DE PABLO
UNIVERSIDAD DE LA LAGUNA

06/07/2017 13:51:19

physical overdensity δ_m inside each sphere is computed, its Lagrangian radius can be determined with 2.17. The corresponding linear overdensity δ_l can be obtained via equation 2.16, and this is the last quantity needed to completely characterise each sphere. In Figure 2.10 we show the final normalised distributions for the quantities Q , δ_m and δ_l , in both simulations. We see that in the case of the SSS, a consequence of using smaller spheres is that the density contrast is peaked at more negative values compared to the LSS case, and as a result the distribution of Lagrangian radii is rather asymmetric. With the LSS spheres the density contrast distribution peak lies closer to zero, and the Lagrangian radius distribution has a more symmetric shape around the interval allowed by the prior Eulerian radius distribution.

This set of characterised conditions can be used to test the theoretical predictions of the CMF. The comparison between theory and simulation was performed at the level of the halo density as a function of mass, computed as a histogram over a specified set of mass bins. In principle, this comparison could be performed for each of the spheres we placed over the simulations. Typically, a single sphere contains around $\sim 10^2\text{--}10^3$ halos in the SSS and $\sim 10\text{--}10^2$ in the LSS. However, given the high number of spheres we employed, it was convenient to group them into bins of Eulerian radius and linear density contrast, and consider the comparison between the simulated and theoretical histograms averaged inside each (R, δ_l) bin. This way we could take advantage of the higher statistics resulting from averaging the halo mass distribution from many conditions with common size and density contrast.

We obtained the simulated histograms as follows. For each sphere, using the information of its position and Eulerian radius, we recorded all collapsed objects retrieved by the halo finder that lie inside the sphere. Let us fix a (R, δ_l) bin and let N_s be the total number of spheres whose size and density contrast fall in this bin; we joined in a single set all the halos contained inside these N_s spheres, and binned these halos over a specified set of mass bins $(m)_j$. We represent by N_j the number of halos whose masses enter the j -th mass bin. We defined our halo density histogram extracted from the simulation by the quantity:

$$n_c^{\text{sim}}(m_j; R, \delta_l) = \frac{N_j}{N_s V_R}, \quad (2.37)$$

where V_R is the average Eulerian volume of the spheres belonging to the (R, δ_l) bin, $V_R = 4\pi R^3/3$. We chose a sufficiently small step $\Delta R = 0.5 h^{-1}$ Mpc between radius bins, in order to ensure the central value R was representative of the size of all spheres in the bin. We then computed the theoretical prediction for the halo density in the bin (R, δ_l) . For each sphere in this bin, we computed the theoretical CMF $dn_{c,i}/dm(m; Q, \delta_l)$ using the exact values of δ_l

Este documento incorpora firma electrónica, y es copia auténtica de un documento electrónico archivado por la ULL según la Ley 39/2015.
Su autenticidad puede ser contrastada en la siguiente dirección <https://sede.ull.es/validacion/>

Identificador del documento: 973742	Código de verificación: Jfg6xBh0	Fecha: 30/06/2017 15:10:10
Firmado por: DENIS TRAMONTE UNIVERSIDAD DE LA LAGUNA		
RAFAEL DELFIN BARRENA DELGADO UNIVERSIDAD DE LA LAGUNA		30/06/2017 15:21:31
JOSE ALBERTO RUBIÑO MARTIN UNIVERSIDAD DE LA LAGUNA		30/06/2017 15:34:17
ERNESTO PEREDA DE PABLO UNIVERSIDAD DE LA LAGUNA		06/07/2017 13:51:19

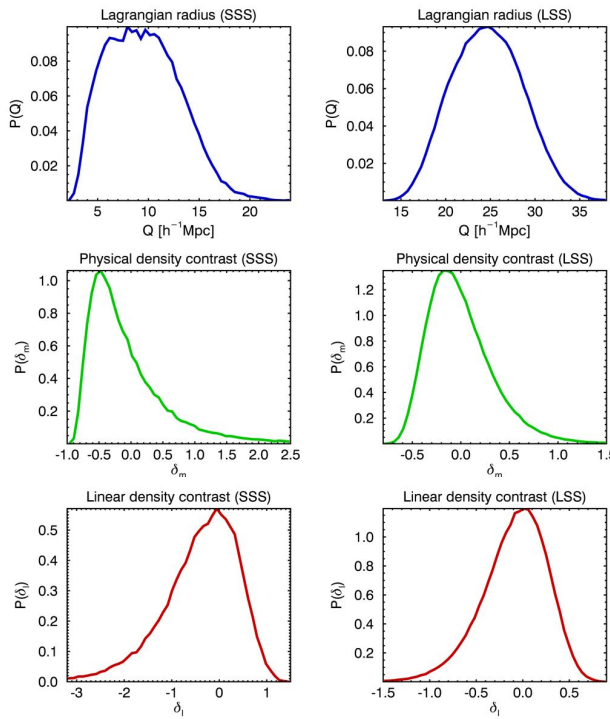


Figure 2.10: Posterior distributions for the quantities characterising the conditions, resulting from randomly placed spheres over the simulations with a top-hat prior for their Eulerian radius (see the text for details). From top to bottom: normalised distribution for the Lagrangian radius Q , the physical density contrast δ_m and the linear density contrast δ_l . Left column: Small Scale Simulation, with a total 6×10^4 spheres; right column: Large Scale Simulation, with a total 4.4×10^5 spheres.

and Q of the sphere; we integrated the CMF over the same mass bins $(m)_j$ considered earlier, to transform the distribution into a density as a function of mass, $n_i(m_j; Q, \delta_l)$. Here the subscript j runs over the mass bins, the subscript i over the different spheres contained inside the (R, δ_l) bin, $i = 1, \dots, N_s$. The N_s histograms obtained this way, one for each sphere, had to be combined to get an average estimate for the (R, δ_l) bin. Note that the density of objects extracted from the simulation is Eulerian, while the formalism for the CMF

Este documento incorpora firma electrónica, y es copia auténtica de un documento electrónico archivado por la ULL según la Ley 39/2015.
Su autenticidad puede ser contrastada en la siguiente dirección <https://sede.ull.es/validacion/>

Identificador del documento: 973742

Código de verificación: Jfg6xBh0

Fecha: 30/06/2017 15:10:10

Firmado por: DENIS TRAMONTE UNIVERSIDAD DE LA LAGUNA	30/06/2017 15:21:31
RAFAEL DELFIN BARRENA DELGADO UNIVERSIDAD DE LA LAGUNA	30/06/2017 15:34:17
JOSE ALBERTO RUBIÑO MARTIN UNIVERSIDAD DE LA LAGUNA	06/07/2017 13:51:19
ERNESTO PEREDA DE PABLO UNIVERSIDAD DE LA LAGUNA	

described so far yields the Lagrangian density. So, the theoretical histograms were combined by first multiplying each one by the sphere Lagrangian volume $V_{Q,i} = 4\pi Q_i^3/3$, by summing the corresponding halo numbers, and by translating to final Eulerian density dividing by the mean Eulerian volume of the bin V_R . In formulae:

$$n_c^{\text{theo}}(m_j; R, \delta_l) = \frac{1}{N_s V_R} \sum_{i=1}^{N_s} n_i(m_j; Q, \delta_l) V_{Q,i} \quad (2.38)$$

The theoretical histograms were generated using both the CMF from the standard rescaling and from the local rescaling. We also explored the effect of the normalisation parameter α in changing the agreement between the CMF and the simulation; we considered in particular the value $\alpha = 1.25$, which is the one required for normalising the T08 mass function, and also an intermediate value $\alpha = 1.5$, which lies between 1.25 and δ_c . Notice that, although the CMF is naturally expressed in Lagrangian density, we could not bin the spheres in Q and δ_l because these quantities are not independent.

2.4.4 Testing CMF normalisation

The first consistency test to be applied to any analytical prescription to compute the CMF is the normalisation condition. The conditional halo mass function must recover the unconditional one when averaged over all possible values of the density contrast. In practice, this is done by evaluating the analytical CMF for all the set of possible conditions (R, δ_l) that we have obtained with the spheres described in the previous subsection, and averaging over all of them.

Note that this test is independent and complementary to the analysis performed in section 2.3. There are two main differences: first, we are using here, by construction, the true probability distribution of δ_l as derived from our simulations (see Figure 2.10); and second, we are integrating for a fixed Eulerian R value, instead of for a fixed Lagrangian Q value.

The normalisation condition must hold true for each value of the radius, that is, for all bins in R . We show in Figure 2.11 the results for one radius bin, for both simulations, plotted in terms of the halo density. We plot the analytical predictions from equation 2.38 obtained using the two different recipes for the CMFs, namely the local and the standard rescalings of the T08 function, both with no explicit normalisation and with normalisation parameter $\alpha = 1.25$.

Middle panels in figure 2.11 show the residuals for the points obtained from the simulation using equation 2.37 (averaged over all the values of δ_l for the particular bin of R we are considering) with respect to the global simulation

Este documento incorpora firma electrónica, y es copia auténtica de un documento electrónico archivado por la ULL según la Ley 39/2015.
Su autenticidad puede ser contrastada en la siguiente dirección <https://sede.ull.es/validacion/>

Identificador del documento: 973742	Código de verificación: Jfg6xBh0	Fecha: 30/06/2017 15:10:10
Firmado por: DENIS TRAMONTE UNIVERSIDAD DE LA LAGUNA		
RAFAEL DELFIN BARRENA DELGADO UNIVERSIDAD DE LA LAGUNA		30/06/2017 15:21:31
JOSE ALBERTO RUBIÑO MARTIN UNIVERSIDAD DE LA LAGUNA		30/06/2017 15:34:17
ERNESTO PEREDA DE PABLO UNIVERSIDAD DE LA LAGUNA		06/07/2017 13:51:19

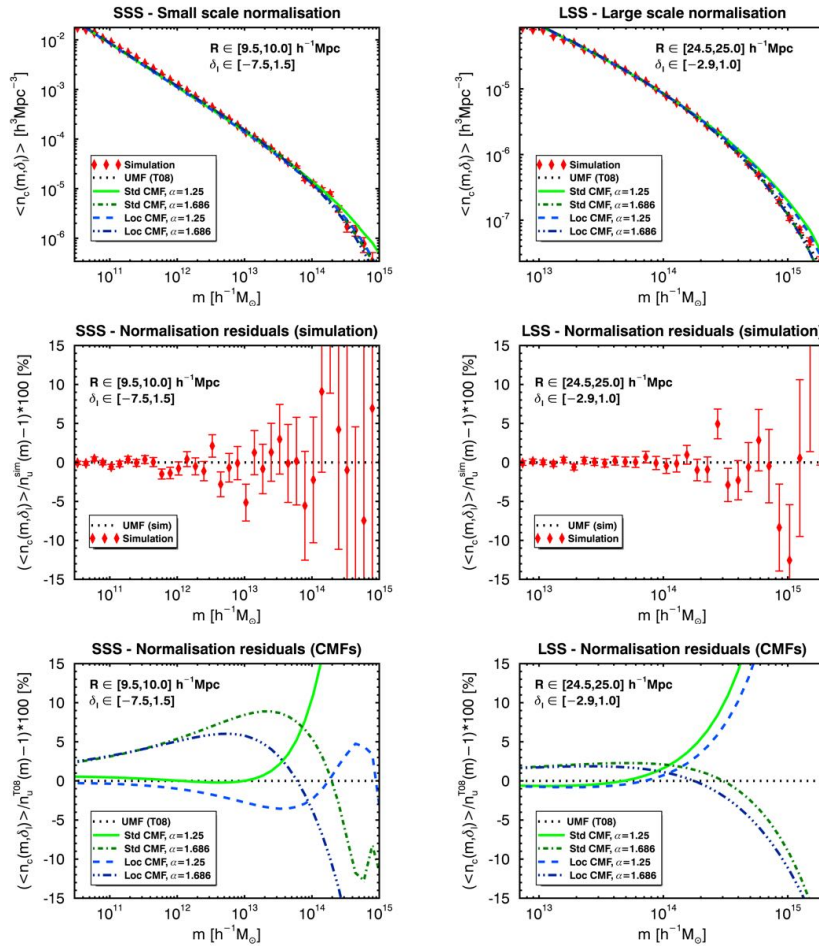


Figure 2.11: Normalisation test for the CMF, for both the SSS (left column) and the LSS (right column). Points are halo abundances from simulation with Poissonian errors; we also plot the standard and the local CMF, both with no explicit normalisation and normalised with $\alpha = 1.25$. Middle panels show the residual of the simulated abundances with respect to the simulated UMF plotted with points in figure 2.7. Lower panels show the residuals of the analytical CMFs with respect to the T08 UMF.

Este documento incorpora firma electrónica, y es copia auténtica de un documento electrónico archivado por la ULL según la Ley 39/2015.
Su autenticidad puede ser contrastada en la siguiente dirección <https://sede.ull.es/validacion/>

Identificador del documento: 973742

Código de verificación: Jfg6xBh0

Fecha: 30/06/2017 15:10:10

Firmado por: DENIS TRAMONTE
UNIVERSIDAD DE LA LAGUNA

RAFAEL DELFIN BARRENA DELGADO
UNIVERSIDAD DE LA LAGUNA

JOSE ALBERTO RUBIÑO MARTIN
UNIVERSIDAD DE LA LAGUNA

ERNESTO PEREDA DE PABLO
UNIVERSIDAD DE LA LAGUNA

30/06/2017 15:21:31

30/06/2017 15:34:17

06/07/2017 13:51:19

UMF, plotted with points in figure 2.7. The averaged abundances are capable of recovering the prediction from the box UMF (in both cases) within a few percent accuracy (this also applies to all the other radius bins). This result proves the consistency of our algorithm in placing random spheres and averaging their content. Note that errors become larger in the high mass end where the box finite-size effect becomes important and the statistics of collapsed objects is poorer.

The lower panels of figure 2.11 show the residuals for the different CMF recipes, computed as percent deviations with respect to the T08 UMF. Residuals from the analytical determinations of the CMF give us information about the accuracy at which the normalisation condition is satisfied. These residuals are clearly reduced when introducing the normalisation parameter $\alpha = 1.25$ in the UMF rescalings, resulting in a final $\sim 1\%$ error with respect to the T08 mass function. This confirms that the modification of the rescaling introduced to accomplish the normalisation condition also works when using the proper δ_1 distribution from numerical simulation, and for a fixed Eulerian condition radius. These conclusions are the same for both the CMF computed with the standard rescaling and the CMF computed with the local rescaling. Residuals from all theoretical CMFs are larger than 10 % above a certain mass threshold, around $\sim 10^{14} h^{-1} M_\odot$ for the SSS, and $\sim 4 \times 10^{14} h^{-1} M_\odot$ for the LSS. Now, in RBP08 it is underlined that the formalism for computing the CMF is expected to fail when approaching the mass of the condition; in the same reference, a fraction of 1/30 of the condition mass is chosen as an upper limit, setting the mass range where the CMF formalism is valid. According to this prescription, the mass values above which our residuals become very large correspond to the limiting top masses for conditions of size $Q \sim 20 h^{-1} \text{Mpc}$ for the SSS, and $Q \sim 35 h^{-1} \text{Mpc}$ for the LSS. By looking at the Q probability distributions in Figure 2.10, we found these radii to fall in the very high tail of the distributions. Errors in normalisations therefore arise in a mass interval dominated by rare massive objects that are found in highly overdense regions, which we are not going to consider in the following analysis.

2.4.5 Testing the CMF in overdense/underdense regions

We then checked the predictions of the CMF recipes for individual density contrast bins. Note that results from equation 2.38, in this case, are not the quantity that can be compared to the simulation results from equation 2.37; indeed, according to the discussion in section 2.4.2, the abundances extracted from simulations are affected by systematics due to cosmic variance. So, let n_u^{theo} and n_u^{sim} be the halo abundances computed using the unconditional mass

Este documento incorpora firma electrónica, y es copia auténtica de un documento electrónico archivado por la ULL según la Ley 39/2015.
Su autenticidad puede ser contrastada en la siguiente dirección <https://sede.ull.es/validacion/>

Identificador del documento:	973742	Código de verificación:	Jfg6xBh0
Firmado por:	DENIS TRAMONTE UNIVERSIDAD DE LA LAGUNA	Fecha:	30/06/2017 15:10:10
	RAFAEL DELFIN BARRENA DELGADO UNIVERSIDAD DE LA LAGUNA		30/06/2017 15:21:31
	JOSE ALBERTO RUBIÑO MARTIN UNIVERSIDAD DE LA LAGUNA		30/06/2017 15:34:17
	ERNESTO PEREDA DE PABLO UNIVERSIDAD DE LA LAGUNA		06/07/2017 13:51:19

functions from theory (T08) and simulations, respectively; both are plotted in Figure 2.7. In order to take the aforementioned systematics into account, the theoretical prediction can be rescaled as:

$$\tilde{n}_c^{\text{theo}}(m_j; R, \delta_l) = n_c^{\text{theo}}(m_j; R, \delta_l) \frac{n_u^{\text{sim}}(m_j)}{n_u^{\text{theo}}(m_j)}. \quad (2.39)$$

The prediction \tilde{n}^{theo} is the one we finally compared with the simulation counts n^{sim} for testing the CMFs recipes. In practice, this is equivalent to directly compare the so-called matter-to-halo bias function (Sheth & Lemson 1999), both from the simulations and the from theoretical predictions.

In Figure 2.12 we show the comparison between the simulations and the CMFs computed using the standard rescaling and the local rescaling, both without normalisation, in the case of strongly underdense, underdense and overdense regions. In all plots, a vertical line shows the mass corresponding to 1/30 of the condition mass. We see that, in overdense regions, both the standard and the local CMF provide a very similar prediction, and in good agreement with the counts from simulations. In underdense regions, however, the agreement with simulations gets poorer, and it becomes even worse in the case of strongly underdense regions. Note that the oscillations of the theoretical predictions at low masses is simply a consequence of the normalisation performed with equation 2.39.

In Figures 2.13 we consider the same radius and density contrast bins, but now we show the comparison between counts from simulations and the prediction from the local rescaling with explicit normalisation. We employed the value $\alpha = 1.25$ as required by the T08 mass function normalisation; we also show, as a reference, the locally rescaled CMF without normalisation and normalised with an intermediate choice of the normalisation parameter, $\alpha = 1.5$. In case of underdense regions, the explicit normalisation of the CMF implies a clear improvement when reproducing the counts from simulations, particularly when the density contrast is higher. For the most underdense bin we show, when changing from the not normalised CMF to the one using $\alpha = 1.25$, the reduced χ^2 changes from 9.7 to 2.4 in the SSS, and from 22.6 to 0.7 in the LSS. These results suggest that normalising the local CMF with $\alpha = 1.25$ provides a more accurate recipe in underdense regions, both at small and large scales; this is in agreement with the results in RBP08, where the same value for α is employed for normalising the ST99 mass function. In the case of overdense regions, the use of the same value of α does not always produce an improvement in the agreement with simulated counts. When introducing the 1.25 normalisation parameter, the reduced χ^2 changes from 1.8 to 42.7 in the

Este documento incorpora firma electrónica, y es copia auténtica de un documento electrónico archivado por la ULL según la Ley 39/2015.
Su autenticidad puede ser contrastada en la siguiente dirección <https://sede.ull.es/validacion/>

Identificador del documento: 973742

Código de verificación: Jfg6xBh0

Fecha: 30/06/2017 15:10:10

Firmado por: DENIS TRAMONTE UNIVERSIDAD DE LA LAGUNA	30/06/2017 15:21:31
RAFAEL DELFIN BARRENA DELGADO UNIVERSIDAD DE LA LAGUNA	30/06/2017 15:34:17
JOSE ALBERTO RUBIÑO MARTIN UNIVERSIDAD DE LA LAGUNA	06/07/2017 13:51:19
ERNESTO PEREDA DE PABLO UNIVERSIDAD DE LA LAGUNA	

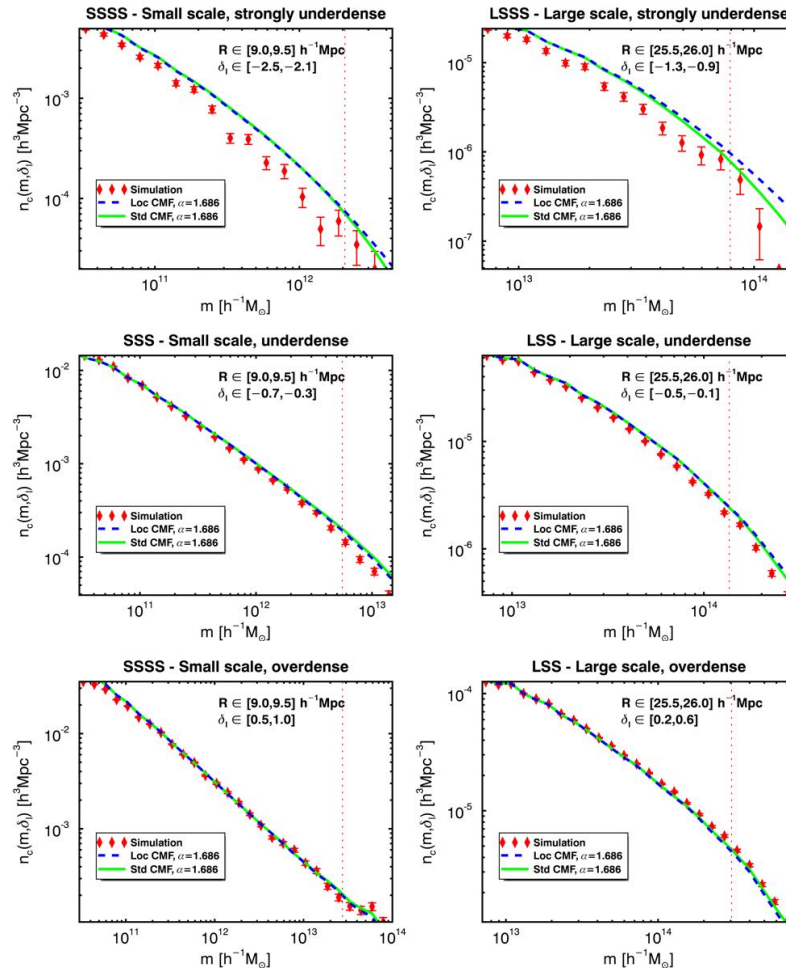


Figure 2.12: Comparison between simulation and theoretical CMFs, in the case of the SSS (left column) and the LSS (right column). From top to bottom we show a strongly underdense region, a region with moderate underdensity and an overdense region. We plot the simulation points with Poissonian errors and both the standard and the local rescaling, without explicit normalisation. The vertical dotted line represents a fraction 1/30 of the average condition mass.

Este documento incorpora firma electrónica, y es copia auténtica de un documento electrónico archivado por la ULL según la Ley 39/2015.
Su autenticidad puede ser contrastada en la siguiente dirección <https://sede.ull.es/validacion/>

Identificador del documento: 973742

Código de verificación: Jfg6xBh0

Fecha: 30/06/2017 15:10:10

Firmado por: DENIS TRAMONTE
UNIVERSIDAD DE LA LAGUNA

RAFAEL DELFIN BARRENA DELGADO
UNIVERSIDAD DE LA LAGUNA

JOSE ALBERTO RUBIÑO MARTIN
UNIVERSIDAD DE LA LAGUNA

ERNESTO PEREDA DE PABLO
UNIVERSIDAD DE LA LAGUNA

30/06/2017 15:21:31

30/06/2017 15:34:17

06/07/2017 13:51:19

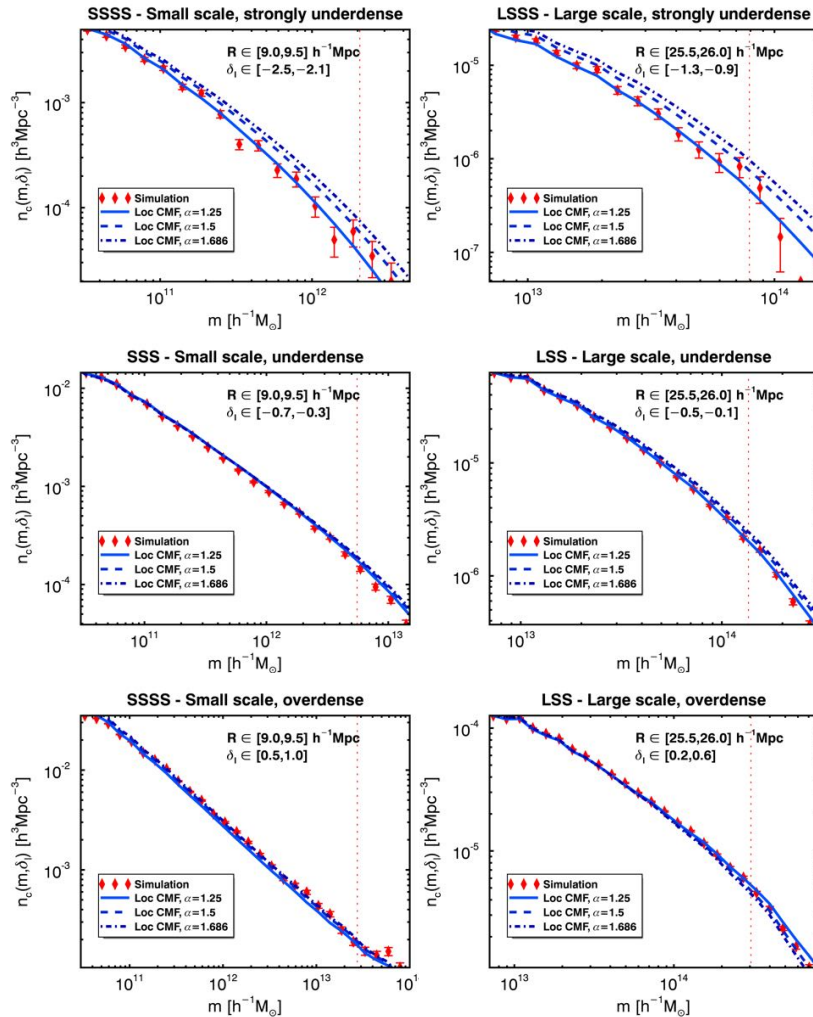


Figure 2.13: Same plot as in figure 2.12, but showing the effect of the normalisation parameter on the local CMF. We plot the CMF with no explicit normalisation, with normalisation parameter $\alpha = 1.25$, and with a more conservative value $\alpha = 1.5$.

Este documento incorpora firma electrónica, y es copia auténtica de un documento electrónico archivado por la ULL según la Ley 39/2015.
Su autenticidad puede ser contrastada en la siguiente dirección <https://sede.ull.es/validacion/>

Identificador del documento: 973742

Código de verificación: Jfg6xBh0

Fecha: 30/06/2017 15:10:10

Firmado por: DENIS TRAMONTE
UNIVERSIDAD DE LA LAGUNA

RAFAEL DELFIN BARRENA DELGADO
UNIVERSIDAD DE LA LAGUNA

JOSE ALBERTO RUBIÑO MARTIN
UNIVERSIDAD DE LA LAGUNA

ERNESTO PEREDA DE PABLO
UNIVERSIDAD DE LA LAGUNA

30/06/2017 15:21:31

30/06/2017 15:34:17

06/07/2017 13:51:19

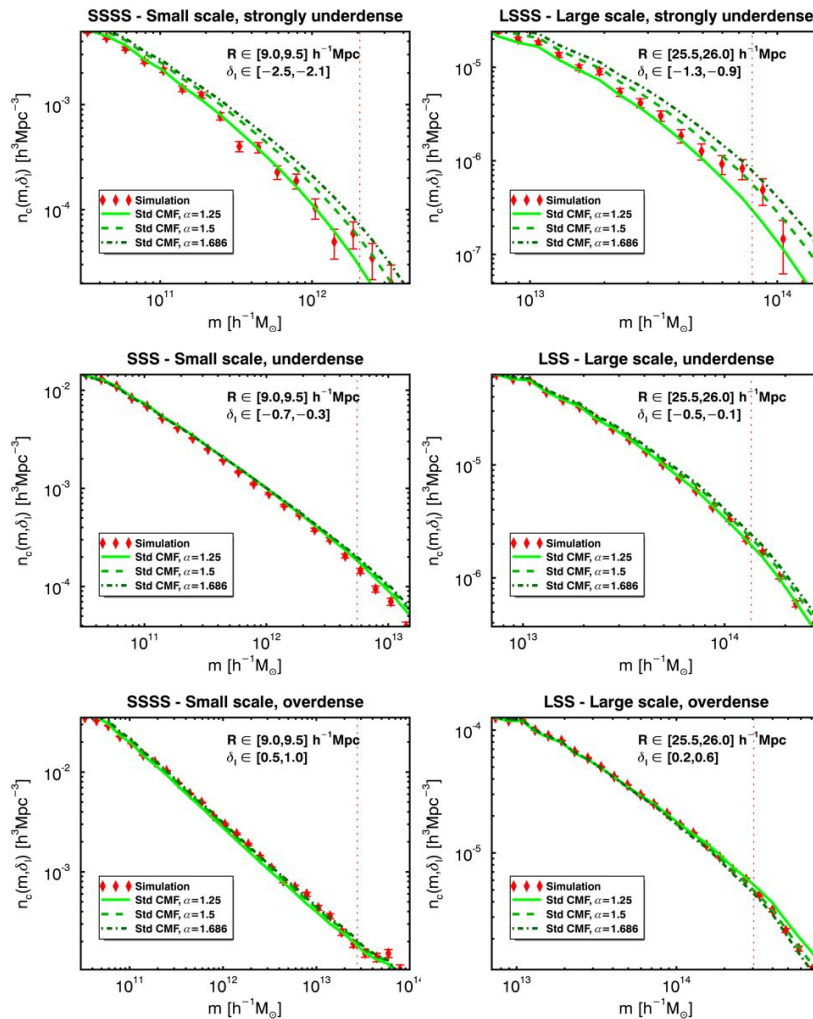


Figure 2.14: Same plot as in figure 2.13, but considering this time the effect of the normalisation parameter on the standard rescaling.

Este documento incorpora firma electrónica, y es copia auténtica de un documento electrónico archivado por la ULL según la Ley 39/2015.
Su autenticidad puede ser contrastada en la siguiente dirección <https://sede.ull.es/validacion/>

Identificador del documento: 973742

Código de verificación: Jfg6xBh0

Fecha: 30/06/2017 15:10:10

Firmado por: DENIS TRAMONTE
UNIVERSIDAD DE LA LAGUNA

RAFAEL DELFIN BARRENA DELGADO
UNIVERSIDAD DE LA LAGUNA

JOSE ALBERTO RUBIÑO MARTIN
UNIVERSIDAD DE LA LAGUNA

ERNESTO PEREDA DE PABLO
UNIVERSIDAD DE LA LAGUNA

30/06/2017 15:21:31

30/06/2017 15:34:17

06/07/2017 13:51:19

SSS, actually worsening the fit, while in the LSS we have again improvement with the reduced χ^2 changing from 16.5 to 3.3.

We repeated the same comparisons using the standard CMF, computed with explicit normalisation parameters $\alpha = 1.25$ and $\alpha = 1.5$. The resulting plots comparing the theoretical prediction with the simulation counts, for the same set of radius and overdensity bins considered so far, are shown in figure 2.14. The results are much alike the ones obtained with the local rescaling, with the explicit normalisation substantially improving the agreement with simulation in underdense regions but not always in overdensities. In this case, for the most underdense bin, when introducing the $\alpha = 1.25$ parameter the reduced χ^2 changes from 10.3 to 2.4 in the SSS and from 18.0 to 2.0 in the LSS. In the positive δ_1 bin, instead, the reduced χ^2 changes from 1.7 to 40.5 in the SSS, and from 11.4 to 2.9 in the LSS.

When comparing these χ^2 with the ones quoted above, and for all possible cases, we find that the agreement with simulation is basically the same when using the local CMF or the standard CMF (see e.g., figure 2.12), although the local rescaling provides a better description in underdense and intermediate regions than the standard rescaling. In overdense regions, however, the standard rescaling seems slightly better for this particular simulation.

In conclusion, when trying to reproduce the abundance of halos inside conditioning regions, the best recipe for computing the CMF, in either the standard or the local rescaling, requires the use of the α parameter. When using $\alpha = 1.25$, for underdense regions we clearly improve the agreement with numerical simulations, while for the case of overdensities, although there is still an improvement for large scales, we have an overcorrection for small regions. We checked that these conclusions still hold when changing the mass range over which we computed the χ^2 . The large values for the χ^2 obtained with the explicit normalisation in the SSS may be due to an underestimation of the errors; what matters here is that in this case the normalised CMF worsens the agreement with simulated abundances. It is not clear whether this issue is due to the particular simulation we are using. The same comparison could be repeated by combining results from many N-body simulations; this goes beyond the scope of this work. In any case, we conclude that the normalised CMF with $\alpha = 1.25$ is the one that works better in the majority of the cases.

2.5 A fitting formula for the CMF in underdense regions

As discussed in RBP08, one of the main driving goals for developing a proper parametrisation of the conditional mass function is the theoretical study of void statistics. A void can be considered, within our framework, as a locally

Este documento incorpora firma electrónica, y es copia auténtica de un documento electrónico archivado por la ULL según la Ley 39/2015.
Su autenticidad puede ser contrastada en la siguiente dirección <https://sede.ull.es/validacion/>

Identificador del documento:	973742	Código de verificación:	Jfg6xBh0
Firmado por:	DENIS TRAMONTE UNIVERSIDAD DE LA LAGUNA	Fecha:	30/06/2017 15:10:10
	RAFAEL DELFIN BARRENA DELGADO UNIVERSIDAD DE LA LAGUNA		30/06/2017 15:21:31
	JOSE ALBERTO RUBIÑO MARTIN UNIVERSIDAD DE LA LAGUNA		30/06/2017 15:34:17
	ERNESTO PEREDA DE PABLO UNIVERSIDAD DE LA LAGUNA		06/07/2017 13:51:19

underdense region, and the distribution of collapsed objects within it can be described by the CMF. The formalism for computing the number density of voids is discussed in Patiri et al. (2006); voids can be used as a tool to constrain cosmological parameters, as it is shown in Betancort-Rijo et al. (2009).

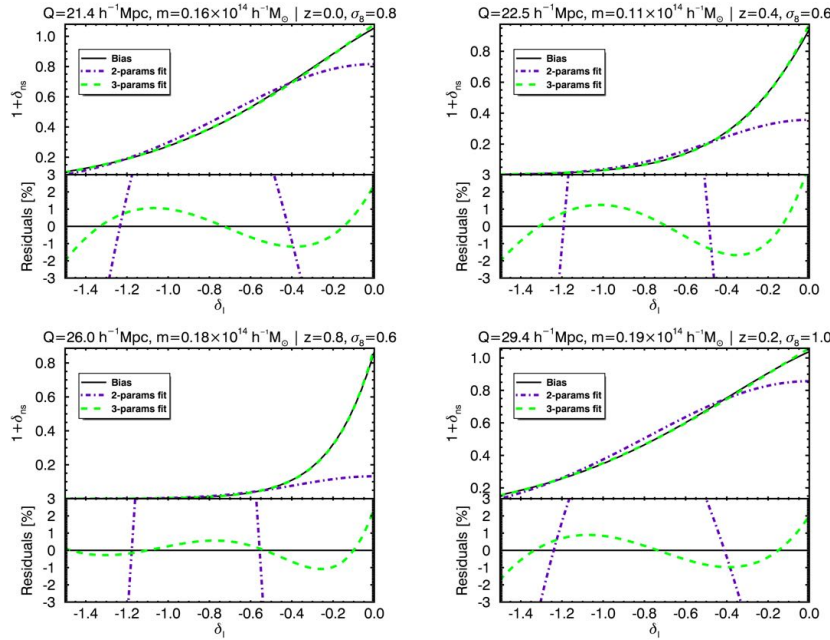


Figure 2.15: Bias between the integrated CMF and UMF plotted as a function of the linear density contrast. We compare the prediction from the two-parameter fit 2.44 and the three-parameter fit 2.45, together with the theoretical bias computed with 2.41, for different values of condition radius, mass, redshift and σ_8 (the case is made explicit in the title).

In those works the probability of finding a void of a given radius requires the computation of the quantity:

$$1 + \delta_N(m, z; Q, \delta_l) = [1 + \delta_m(\delta_l)][1 + \delta_{ns}(m, z; Q, \delta_l)], \quad (2.40)$$

where we made the dependence on the objects mass, on redshift and on the void radius explicit. We can call the first factor a *systematic bias*, which is due to the different expansion rate of the void compared to the background. The second factor in equation 2.40 is the *statistical bias* (or simply the bias),

accounting for the clustering of the protohaloes within the condition before it expands in comoving coordinates. This is usually referred to in the literature as the (matter-to-)halo bias function (Sheth & van de Weygaert 2004; Furlanetto & Piran 2006; Paranjape et al. 2012; Jennings et al. 2013). Again in Patiri et al. (2006), it is shown that the relation between the bias and the CMF is given by:

$$1 + \delta_{\text{ns}}(m, z; Q, \delta_l) = \frac{1}{N_u(m, z)} \left[\frac{3}{Q^3} \int_0^Q dq q^2 N_c(m, z; q, Q, \delta_l) \right]. \quad (2.41)$$

Here $N_u(m)$ is simply the cumulative mass function for collapsed objects of mass greater than m , in the unconditional case:

$$N_u(m, z) = \int_m^{+\infty} dm' \frac{dn_u}{dm'}(m', z), \quad (2.42)$$

and $N_c(m; q, Q, \delta_l)$ is the equivalent for the conditional mass function:

$$N_c(m, z; q, Q, \delta_l) = \int_m^M dm' \frac{dn_c}{dm'}(m', z; q, Q, \delta_l). \quad (2.43)$$

In this case the mass range over which the mass function has to be integrated is limited by the mass of the condition; the upper integration extrema should therefore be a proper fraction M of the condition mass $m(Q)$. In our computations we always used $M = m(Q)/30$. Notice that the mass function we use in equations 2.41 and 2.43 is the locally-rescaled CMF with normalisation parameter $\alpha = 1.25$. Indeed, the voids that are best suited for constraining cosmological models are the largest ones, and according to the discussion in section 2.4.5 this is the best CMF recipe in the case of underdensities and large conditions.

Equation 2.41 gives the ratio of the total density of collapsed objects above a given mass in the conditioned environment with respect to the unconditional one. It contains all the information on the conditional mass function, and is the starting point for the study of void statistics. Given all the dependences that show up in equation 2.41, the full numerical computation of the bias is very time-consuming. Therefore, efforts have been made to find a numerical fit for the bias, which allows us to avoid heavy numerical computations. In RBP08 a fitting formula in the form:

$$1 + \delta_{\text{ns}}(m, z; Q, \delta_l) = A(m, z, Q) e^{-b(m, z, Q)\delta_l^2}, \quad (2.44)$$

is discussed, and a procedure for computing the fitting parameters A and b is provided. The fit 2.44 is a good approximation for the bias at the scales discussed in RBP08 (around $Q = 9 h^{-1}$ Mpc) and for strongly underdense regions.

Este documento incorpora firma electrónica, y es copia auténtica de un documento electrónico archivado por la ULL según la Ley 39/2015.
Su autenticidad puede ser contrastada en la siguiente dirección <https://sede.ull.es/validacion/>

Identificador del documento: 973742	Código de verificación: Jfg6xBh0	Fecha: 30/06/2017 15:10:10
Firmado por: DENIS TRAMONTE UNIVERSIDAD DE LA LAGUNA		
RAFAEL DELFIN BARRENA DELGADO UNIVERSIDAD DE LA LAGUNA		30/06/2017 15:21:31
JOSE ALBERTO RUBIÑO MARTIN UNIVERSIDAD DE LA LAGUNA		30/06/2017 15:34:17
ERNESTO PEREDA DE PABLO UNIVERSIDAD DE LA LAGUNA		06/07/2017 13:51:19

However, as already stated, when dealing with void statistics the largest voids are the ones that best constrain cosmological parameters, on scales around $Q = 20 h^{-1}$ Mpc. The fit 2.44 cannot be applied to those scales, nor when the density contrast approaches zero. In this work, we consider an extension of the fitting formula 2.44, which can be applied to a broader range of condition sizes and overdensities; the function we propose has the form:

$$1 + \delta_{\text{ns}}(m, z; Q, \delta_l) = A(m, z, Q) e^{-b(m, z, Q)\delta_l^2 + c(m, z, Q)\delta_l}, \quad (2.45)$$

which differs from 2.44 in the addition of the extra parameter c . This equation guarantees that the limit for small δ_l of this bias is linear in δ_l , and not quadratic.

We wanted to check the goodness of this fit at reproducing the bias. To this aim, we implemented the full computation given in equation 2.41, using the reference cosmology from table 2.1, for different values of the condition radius in the range $Q \in [18, 28] h^{-1}$ Mpc. The linear density contrasts we considered span the range¹ $[-1.5, 0.0]$. We also considered the dependence on redshift, which we moved in the range $[0, 1]$, and on the parameter σ_8 , which we allowed to vary in the range $[0.6, 1.0]$. According to the results described in section 2.4.5, since we are considering underdense regions, we computed the UMF employing the normalised local rescaling 2.32, with normalisation parameter $\alpha = 1.25$. For every case, we fitted both functions 2.44 and 2.45 against the bias, as a function of δ_l . We show some examples in figure 2.15; the use of the additional parameter clearly improves the goodness of the fit, which is capable of reproducing the bias with a relative error of only $\sim 1\text{-}2\%$ (the two-parameter fit errors can grow as large as 80% for values of δ_l close to zero). This result is useful for computing the halo abundance as a function of mass in underdense regions, without implementing the full computation of the local CMF rescaling: by computing the bias with 2.45 and the integrated UMF with 2.42, their product already yields the integrated CMF, which can be derived to obtain the proper conditional mass function.

The fitting parameters A , b and c inherit the dependence on redshift, on the condition size and on the object mass; in addition, they are dependent on the underlying cosmology. Our goal was to give a fitting formula which is capable of reproducing the bias computed with any chosen cosmology, and any scale and redshift. To this aim, we further fitted the dependence of the parameters on these quantities; the full procedure is described in appendix A. As a final result, for the reference cosmology it is possible to vary the redshift and σ_8

¹Since this fit is intended as a tool for the study of void statistics, we considered only underdense regions.

obtaining final errors in the fit below $\sim 8.5\%$, but in most cases around a few percent. When changing also the values for the cosmological parameters h and Ω_m the quality of the fit degrades and the relative error can get as large as $\sim 40\%$ in the worst cases.

2.6 An alternative approach: rescaling cosmology

Apart from the rescaling of the critical density contrast and of the perturbation variance, other approaches are possible to determine the abundance of halos inside a conditioning region. We already commented in section 2.1.1 that the condition can be treated as an independent universe with a locally defined cosmology. The basic idea of this section is that the conditional mass function for the abundance of halos inside the condition can be estimated as the unconditional mass function computed using the values of the parameters that characterise the condition local cosmology. The problem then turns into the determination of the proper values for the local cosmological parameters; we show in the following different ways to perform such a computation and assess the agreement of the resulting mass function with the rescalings we have used so far.

There have been attempts in the literature to compute the mass function using a locally defined cosmology. For instance, Gottlöber et al. (2003) stress the efficiency of computing the halo abundance in voids by rescaling the matter power spectrum via a redefinition of the parameter σ_8 ; a prescription for computing the local cosmological parameters in voids is derived also in Goldberg & Vogeley (2004), with the aim of improving the efficiency of specialised void numerical simulations. Here we want to consider a more general way of rescaling cosmology that can be applied also for overdense regions. Most of the information we will discuss in the following is going to be part of a work in preparation (Betancort-Rijo et al. in prep.).

2.6.1 Defining a local cosmology

First we present the detailed derivation of the parameter rescalings that are needed for defining the cosmology inside the conditioning region; the application to the halo mass function will be discussed afterwards. As a convention, from now on we will always mark with a tilde sign the quantities that are defined or computed in the local universe.

Este documento incorpora firma electrónica, y es copia auténtica de un documento electrónico archivado por la ULL según la Ley 39/2015.
Su autenticidad puede ser contrastada en la siguiente dirección <https://sede.ull.es/validacion/>

Identificador del documento:	973742	Código de verificación:	Jfg6xBh0
Firmado por:	DENIS TRAMONTE UNIVERSIDAD DE LA LAGUNA	Fecha:	30/06/2017 15:10:10
	RAFAEL DELFIN BARRENA DELGADO UNIVERSIDAD DE LA LAGUNA		30/06/2017 15:21:31
	JOSE ALBERTO RUBIÑO MARTIN UNIVERSIDAD DE LA LAGUNA		30/06/2017 15:34:17
	ERNESTO PEREDA DE PABLO UNIVERSIDAD DE LA LAGUNA		06/07/2017 13:51:19

Local linear density contrast

The local universe is a region with density contrast δ_m and linear density contrast δ_l (we write these quantities without the tilde sign because, even though they refer to the local universe, they are computed in the global Universe). In turn, we can consider the global universe as a fluctuation with respect to the condition, with density contrasts $\tilde{\delta}_m$ and $\tilde{\delta}_l$. Since the physical density contrast is just the ratio between the two matter densities, we have

$$1 + \tilde{\delta}_m = \frac{1}{1 + \delta_m}. \quad (2.46)$$

When the scale factor was very small, $a_{\text{in}} \ll 1$, the perturbation was also small, $\delta_l \ll 1$ and its evolution was linear; hence, $\tilde{\delta}_l(a_{\text{in}}) = -\delta_l(a_{\text{in}})$. Now, the evolution of the linear value of the density contrast can be written, in the global Universe, as:

$$\delta_l = \frac{D(a=1)}{D(a_{\text{in}})} \delta_l(a_{\text{in}}), \quad (2.47)$$

where $D(a)$ is the growth factor of linear perturbations,

$$D(a) = \frac{1}{2af(a)} \int_0^a da' f^3(a'), \quad (2.48)$$

$$f(a) = \left[1 + \Omega_m \left(\frac{1}{a} - 1 \right) + \Omega_\Lambda (a^2 - 1) \right]^{-1/2}. \quad (2.49)$$

A similar expression can be written for the perturbation defined in the local universe:

$$\tilde{\delta}_l = \frac{\tilde{D}(1)}{\tilde{D}(a_{\text{in}}(1 + \delta_m)^{1/3})}, \quad (2.50)$$

where \tilde{D} is the growth factor computed according to the local cosmology. Now, we saw in section 2.1.1 that the conditioning region has a locally-defined scale factor \tilde{a} . The factor $(1 + \delta_m)^{1/3}$ in equation 2.50 comes from the fact that we are normalising both the global Universe a and the local universe \tilde{a} to be equal to unity at present time; but since at present time the local universe scale factor has expanded by an extra $(1 + \delta_m)^{-1/3}$, its initial value must be $(1 + \delta_m)^{1/3}$ times the value of the scale factor in the global universe. We can now combine equations 2.46 and 2.50 to relate the linear density contrast in the two universes; in order to make the equality exact we have to take the limit $a_{\text{in}} \rightarrow 0$:

$$\tilde{\delta}_l = - \left[\frac{\tilde{D}(1)}{D(1)} \frac{(1 + \delta_m)^{1/3}}{\mu} \right] \delta_l, \quad (2.51)$$

Este documento incorpora firma electrónica, y es copia auténtica de un documento electrónico archivado por la ULL según la Ley 39/2015.
Su autenticidad puede ser contrastada en la siguiente dirección <https://sede.ull.es/validacion/>

Identificador del documento: 973742

Código de verificación: Jfg6xBh0

Fecha: 30/06/2017 15:10:10

Firmado por: DENIS TRAMONTE
UNIVERSIDAD DE LA LAGUNA

RAFAEL DELFIN BARRENA DELGADO
UNIVERSIDAD DE LA LAGUNA

JOSE ALBERTO RUBIÑO MARTIN
UNIVERSIDAD DE LA LAGUNA

ERNESTO PEREDA DE PABLO
UNIVERSIDAD DE LA LAGUNA

30/06/2017 15:21:31

30/06/2017 15:34:17

06/07/2017 13:51:19

where

$$\mu = \lim_{a \rightarrow 0} \frac{\tilde{D}(a)}{D(a)}. \quad (2.52)$$

In deriving equation 2.51 we made use of the fact that for $a \ll 1$, $\tilde{D}(a) \sim D(a) \sim a$, which allowed us to take the $(1 + \delta_m)^{1/3}$ factor out of the limit 2.52.

Local parameters

The change in the Hubble parameter can be computed exploiting its meaning of expansion rate; in Betancort-Rijo et al. (2006) a recipe is provided to compute the local deviation from the Hubble flow for a spherical cloud with overdensity δ_m :

$$\mathcal{V}(\delta_m) = -\frac{1}{3} \frac{\delta_1(\delta_m)}{1 + \delta_m} \left[\frac{d\delta_1(\delta_m)}{d\delta_m} \right]^{-1} \left[\frac{d \ln D(a)}{da} \right]_{a=1}. \quad (2.53)$$

Equation 2.53 allows us to compute the rescaled Hubble parameter as:

$$\tilde{H}_0 = [1 + \mathcal{V}(\delta_m)] H_0. \quad (2.54)$$

The local Hubble parameters defines a local critical density $\tilde{\rho}_c$. Accordingly, the rescaling for the other parameters reads:

$$\tilde{\Omega}_m = \frac{1 + \delta_m}{[1 + \mathcal{V}(\delta_m)]^2} \Omega_m, \quad (2.55)$$

$$\tilde{\Omega}_\Lambda = \frac{1}{[1 + \mathcal{V}(\delta_m)]^2} \Omega_\Lambda, \quad (2.56)$$

$$\tilde{\Omega}_k = 1 - \tilde{\Omega}_\Lambda - \tilde{\Omega}_m. \quad (2.57)$$

The CMB temperature also changes given the different expansion rate of the condition with respect to the background. Given that for radiation $T \propto a^{-1}$, we have:

$$\tilde{T}_{CMB} = (1 + \delta_m)^{1/3} T_{CMB}. \quad (2.58)$$

Finally, the power spectrum normalisation changes. If the normalisation in the global Universe is set by the parameter σ_8 , then the corresponding local parameter can be obtained as:

$$\tilde{\sigma}_8 = \left[\frac{\tilde{D}(1)}{D(1)} \frac{(1 + \delta_m)^{1/3}}{\mu} \right] \left(\frac{\sigma(\tilde{R}_8)}{\sigma(R_8)} \right) \sigma_8, \quad (2.59)$$

where μ is defined in equation 2.52, $R_8 = 8 h^{-1} \text{ Mpc}$ and

$$\tilde{R}_8 = 8 \frac{(1 + \delta_m)^{1/3}}{[1 + \mathcal{V}(\delta_m)]} h^{-1} \text{ Mpc}. \quad (2.60)$$

Este documento incorpora firma electrónica, y es copia auténtica de un documento electrónico archivado por la ULL según la Ley 39/2015.
Su autenticidad puede ser contrastada en la siguiente dirección <https://sede.ull.es/validacion/>

Identificador del documento: 973742

Código de verificación: Jfg6xBh0

Fecha: 30/06/2017 15:10:10

Firmado por: DENIS TRAMONTE
UNIVERSIDAD DE LA LAGUNA

RAFAEL DELFIN BARRENA DELGADO
UNIVERSIDAD DE LA LAGUNA

JOSE ALBERTO RUBIÑO MARTIN
UNIVERSIDAD DE LA LAGUNA

ERNESTO PEREDA DE PABLO
UNIVERSIDAD DE LA LAGUNA

30/06/2017 15:21:31

30/06/2017 15:34:17

06/07/2017 13:51:19

The term in square brackets in equation 2.59 accounts for the change of power in the local universe with respect to the global one. Indeed, it is the ratio between the local and global linear perturbations 2.51. The factor in round brackets in equation 2.59 takes into account the change of the pivot scale for the normalisation of the power spectrum; this scale is set to $8 h^{-1}$ Mpc, but in the local universe both the scale and the implicit h units change; these changes are accounted for in equation 2.60.

The last step is relating the critical density for the local universe $\tilde{\delta}_c$ to its corresponding value in the global Universe δ_c . According to equation 2.16, the transformation between physical and linear density contrast can be written in the form $\delta_l = \delta_c f(\delta_m)$, where the function f only depends on δ_m ; hence it is possible to write for the local universe the corresponding relation $\tilde{\delta}_l = \tilde{\delta}_c f(\tilde{\delta}_m)$. Using the relations described in section 2.6.1, it is possible to write:

$$\tilde{\delta}_c = \frac{\tilde{\delta}_l}{f(\tilde{\delta}_m)} = \frac{\tilde{\delta}_l}{f((1 + \delta_m)^{-1} - 1)} = \delta_c \left[\frac{\tilde{\delta}_l}{\delta_l((1 + \delta_m)^{-1} - 1)} \right], \quad (2.61)$$

where $\tilde{\delta}_l$ is given by equation 2.51.

2.6.2 Application to the mass function

The locally-defined parameters, computed using the equations in section 2.6.1, can be used to compute the local power spectrum and from there the mass function, using the expression for the unconditional one 2.8. However, a rescaling for the variance is still needed:

$$\tilde{\sigma}' = (\tilde{\sigma}^2 - \tilde{\sigma}_1^2)^{1/2} \frac{\delta_c}{\delta'_c}, \quad (2.62)$$

where $\tilde{\sigma}_1$ is the variance at a scale corresponding to the mass of the condition, computed in the local universe. Indeed, since we are considering perturbations inside the condition, the contribution to the variance from all perturbations at scales larger than Q must be removed. The last factor in equation 2.62 takes into account the change in the critical density for collapse due to the different cosmology (keep in mind that the UMF is more properly a function of the combination δ_c/σ). Clearly, the matter density ρ_m in equation 2.8 must be replaced by the local value $\tilde{\rho}_m$. However, since we want to compare the resulting mass function with the CMF computed in the global Universe, an extra factor $(1 + \delta_m)^{-1}$ is required to convert the Eulerian number density to Lagrangian. This is equivalent to maintaining the global matter density ρ_m as

Este documento incorpora firma electrónica, y es copia auténtica de un documento electrónico archivado por la ULL según la Ley 39/2015.
Su autenticidad puede ser contrastada en la siguiente dirección <https://sede.ull.es/validacion/>

Identificador del documento: 973742	Código de verificación: Jfg6xBh0
Firmado por: DENIS TRAMONTE UNIVERSIDAD DE LA LAGUNA	Fecha: 30/06/2017 15:10:10
RAFAEL DELFIN BARRENA DELGADO UNIVERSIDAD DE LA LAGUNA	30/06/2017 15:21:31
JOSE ALBERTO RUBIÑO MARTIN UNIVERSIDAD DE LA LAGUNA	30/06/2017 15:34:17
ERNESTO PEREDA DE PABLO UNIVERSIDAD DE LA LAGUNA	06/07/2017 13:51:19

a factor in the UMF expression. We shall refer to this way of computing the mass function as the *cosmological parameter rescaling* (CPR).

We considered also an alternative recipe, which we call the *power spectrum rescaling* (PSR), in which the condition is still considered as a local universe, but the change in cosmology is applied at the level of the power spectrum. If we know the $P(k)$ computed in the global Universe, the local one can be computed as:

$$\tilde{P}(k) = \left[\frac{\tilde{D}(1)}{D(1)} \frac{(1 + \delta_m)^{1/3}}{\mu} \right]^2 (1 + \delta_m)^{-1} P(k(1 + \delta_m)^{-1/3}). \quad (2.63)$$

In this case the factor multiplying k in the argument of the power spectrum takes into account the change of scales in the local universe, which is the inverse of the length transformation. The $(1 + \delta_m)^{-1}$ factor is the Jacobian of the variable change applied to the power spectrum, which is in fact a power distribution. The expression in square brackets scales the amplitude of the perturbations in the local Universe; its derivation is needed for the rescaling of the power spectrum normalisation, as in equation 2.59. By computing the variance using the power spectrum 2.63 we find that the power spectrum rescaling is equivalent to this new variance rescaling:

$$\sigma'^2 = (\sigma^2 - \sigma_1^2)^{1/2} \left[\frac{\tilde{D}(1)}{D(1)} \frac{(1 + \delta_m)^{-1/3}}{\mu} \right] \frac{\delta_c}{\bar{\delta}_c}, \quad (2.64)$$

which is a way of computing the mass function similar to the standard and local rescalings. Notice that in the case of equations 2.63 and 2.64 all quantities with no explicit tilde sign should be computed in the global Universe, as well as all other quantities entering the mass function expression 2.8. An advantage of using 2.64 instead of 2.63 is that it does not require to compute the matter power spectrum for the local cosmology.

We show in figure 2.16 the comparison between these new rescalings, the CPR and the PSR, together with the old standard CMF rescaling (SR). We also tested an alternative way of rescaling cosmological parameters, as described in Chiang (2015): according to this formalism, local parameters are computed at a redshift in which the local matter density is equal to the matter density of the global Universe today. In this case the simple use of rescaling 2.62 yields the proper mass function, provided the power spectrum computed with the local parameters is normalised according to the amplitude $\bar{\sigma}_8$ defined in 2.59.

Note that we decided to compare the new rescalings with the other recipes for the CMF, and not with the numerical simulations from section 2.4. This test

Este documento incorpora firma electrónica, y es copia auténtica de un documento electrónico archivado por la ULL según la Ley 39/2015.
Su autenticidad puede ser contrastada en la siguiente dirección <https://sede.ull.es/validacion/>

Identificador del documento: 973742

Código de verificación: Jfg6xBh0

Fecha: 30/06/2017 15:10:10

Firmado por: DENIS TRAMONTE
UNIVERSIDAD DE LA LAGUNA

RAFAEL DELFIN BARRENA DELGADO
UNIVERSIDAD DE LA LAGUNA

JOSE ALBERTO RUBIÑO MARTIN
UNIVERSIDAD DE LA LAGUNA

ERNESTO PEREDA DE PABLO
UNIVERSIDAD DE LA LAGUNA

30/06/2017 15:21:31

30/06/2017 15:34:17

06/07/2017 13:51:19

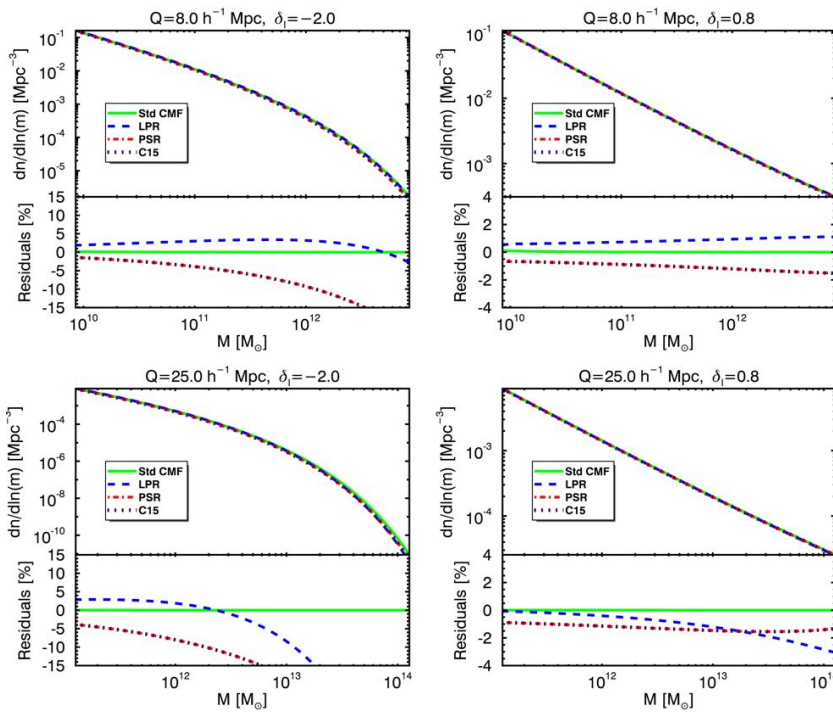


Figure 2.16: Comparison between the standard CMF and the mass function computations based on a locally defined cosmology: we consider the local parameter rescaling (CPR), the power spectrum rescaling (PSR), and the rescaling defined in Chiang (2015). Residuals are computed with respect to the standard CMF. We show results for underdensities and overdensities at both small and large scale.

indeed aims at checking the consistency of two different theoretical prescriptions for computing the CMF. If we compared the new rescalings with our numerical simulations, we should also take into account the systematic effects described in section 2.4.2. The comparison with the old recipes, instead, is unaffected by those systematics and can give a clearer indication of the actual goodness of the rescalings described in this section.

From figure 2.16 we see that in the case of overdensities the agreement between the new parametrisations and the standard CMF is very good over all mass range. In the case of underdense regions, difference can grow up to

$\sim 20\%$ at high masses. The residual plots show that the PSR and the Chiang (2015) rescaling are basically the same. The LPR instead show some difference due to some approximations implicit in its derivation.

2.7 Conclusions

We have compared the predicted CMF of dark matter halos from two theoretical prescriptions against numerical N-body simulations: the standard rescaling of the UMF, and a rescaling locally defined inside the condition (RBP08). Both prescriptions use as a reference the T08 parametrisation for the UMF. Drawing from the results of RBP08, the locally-rescaled mass function requires the introduction of an additional parameter α in order to satisfy the normalisation condition, i.e., the integral of the CMF over the weighted density contrast should yield the initial UMF. The problem of normalisation thus turns into the problem of determining a proper value for α that satisfies the normalisation condition over the whole mass range in which the mass function is to be computed. We repeated the analysis described in RBP08, and found that the standard rescaling also requires the normalisation to be implemented explicitly via the parameter α . For the first time, we obtained the value of α needed to normalise the T08 mass function, and studied its dependence on the size of the condition. We found that this parameter is well constrained by small regions ($Q \sim 8 h^{-1} \text{ Mpc}$), yielding the estimate $\alpha = 1.25$ for both the standard and the local rescalings; large conditions ($Q \sim 25 h^{-1} \text{ Mpc}$), instead, are much less effective in constraining its value, leaving α undetermined.

In order to test the validity of these CMFs in predicting the abundance of collapsed objects inside conditions, we tested the results from the theoretical rescalings against halo counts extracted from numerical simulations. We employed two different dark matter-only simulations, one at relatively small scales ($250 h^{-1} \text{ Mpc}$ box size), the other at larger scales ($1500 h^{-1} \text{ Mpc}$ box size). Jointly, the two simulations allowed us to explore the mass range $[10^{10.5}, 10^{15.5}] h^{-1} \text{ Mpc}$. The corresponding halo catalogues were obtained using a FoF algorithm with $b = 0.2$, which corresponds to the $\Delta = 200$ spherical overdensity mass function definition used in T08. As a preliminary check, we compared the halo densities as a function of mass, extracted from both simulations, with the prediction computed using the T08 UMF. We found that the simulated counts reproduce the mass dependence of the theoretical halo abundances but are affected by systematic effects at the level of $\sim 10\%$ relative error. These offsets are due to the use of a single simulation for each box and have been accounted for in our analyses.

We then placed a large number of spheres over the simulations, with random

Este documento incorpora firma electrónica, y es copia auténtica de un documento electrónico archivado por la ULL según la Ley 39/2015.
Su autenticidad puede ser contrastada en la siguiente dirección <https://sede.ull.es/validacion/>

Identificador del documento:	973742	Código de verificación:	Jfg6xBh0
Firmado por:	DENIS TRAMONTE UNIVERSIDAD DE LA LAGUNA	Fecha:	30/06/2017 15:10:10
	RAFAEL DELFIN BARRENA DELGADO UNIVERSIDAD DE LA LAGUNA		30/06/2017 15:21:31
	JOSE ALBERTO RUBIÑO MARTIN UNIVERSIDAD DE LA LAGUNA		30/06/2017 15:34:17
	ERNESTO PEREDA DE PABLO UNIVERSIDAD DE LA LAGUNA		06/07/2017 13:51:19

positions and radii, in order to simulate the conditioning regions. We grouped the spheres in bins of size and density contrast, and obtained the corresponding conditioned halo density as a function of mass. These distributions were then compared with the predictions from the different CMF recipes. For every radius bin, we joined together all spheres with common size and all possible density contrasts, in order to test a new normalisation condition. This is an important test since by construction we are using the exact probability distribution of δ_l when averaging over different spheres. We found that the new normalisation condition is satisfied within a few percent accuracy by the abundances from simulations, when compared to the UMF from the complete halo catalogue. The theoretical recipes for computing the CMF also achieve that precision in the normalisation when compared to the T08 UMF prediction, provided the normalisation is explicitly applied with the parameter $\alpha = 1.25$. Normalisation is no longer achieved in the high mass end, where errors from the simulation grow large and the formalism for computing the CMF begins to fail for getting too close to the condition mass.

The following test was to check the CMF prediction for the halo abundance inside regions with a definite density contrast. We found that the explicitly normalised CMF with $\alpha = 1.25$ is the most accurate recipe in reproducing simulated halo counts inside underdense regions, both at small and large scales; the CMF can be computed either with the standard or the local rescalings, both providing very similar results, although the latter provides a slightly better fit. In the case of overdense regions, the use of the same normalisation parameter results in an improvement of the agreement with simulations at large scales, but in a slight overcorrection at small scales. Apart from this case, the use of the locally rescaled CMF normalised with $\alpha = 1.25$ is the recipe that best works in most cases.

We presented an analytical fit for computing the CMF in underdense regions, in terms of the bias with respect to the UMF. By multiplying the fitting function times the integrated UMF, the integrated CMF can be obtained, avoiding the time-consuming computation required to implement the normalised local rescaling in underdense regions. In RBP08, a possible analytical expression for this fitting function was proposed, which could be applied to extremely underdense regions (voids); we checked that such a fit is actually inadequate at reproducing the bias dependence on the density contrast when δ_l gets closer to zero. We proposed a different fitting function by adding an additional parameter, that clearly improves the agreement with the CMF bias, yielding final errors below $\sim 2\%$. The dependence of the fitting parameters on the condition size, the halo mass and the cosmology has also been fitted; it is possible to use the same fitting parameters for computing the bias with different values of

Este documento incorpora firma electrónica, y es copia auténtica de un documento electrónico archivado por la ULL según la Ley 39/2015.
Su autenticidad puede ser contrastada en la siguiente dirección <https://sede.ull.es/validacion/>

Identificador del documento:	973742	Código de verificación:	Jfg6xBh0
Firmado por:	DENIS TRAMONTE UNIVERSIDAD DE LA LAGUNA	Fecha:	30/06/2017 15:10:10
	RAFAEL DELFIN BARRENA DELGADO UNIVERSIDAD DE LA LAGUNA		30/06/2017 15:21:31
	JOSE ALBERTO RUBIÑO MARTIN UNIVERSIDAD DE LA LAGUNA		30/06/2017 15:34:17
	ERNESTO PEREDA DE PABLO UNIVERSIDAD DE LA LAGUNA		06/07/2017 13:51:19

the mass, the condition radius, the redshift and σ_8 , with a relative error below $\sim 8\%$. It is also possible to apply the same fitting parameters moving h and Ω_m from their reference values, computing the bias within a 40% error.

Finally, we considered a different approach for determining the halo abundance in conditioning regions, based on the assumption that the region itself can be treated as an independent universe in which the UMF yields the CMF for the global Universe. We described the way cosmological parameters need to be rescaled for defining the local cosmology, and how the power spectrum is to be re-normalised. We considered different ways of implementing these changes into the mass function: results are in good agreement with the standard CMF, except for very large scales where errors gets larger than $\sim 20\%$.

Este documento incorpora firma electrónica, y es copia auténtica de un documento electrónico archivado por la ULL según la Ley 39/2015.
Su autenticidad puede ser contrastada en la siguiente dirección <https://sede.ull.es/validacion/>

Identificador del documento: 973742

Código de verificación: Jfg6xBh0

Firmado por: DENIS TRAMONTE <i>UNIVERSIDAD DE LA LAGUNA</i>	Fecha: 30/06/2017 15:10:10
RAFAEL DELFIN BARRENA DELGADO <i>UNIVERSIDAD DE LA LAGUNA</i>	30/06/2017 15:21:31
JOSE ALBERTO RUBIÑO MARTIN <i>UNIVERSIDAD DE LA LAGUNA</i>	30/06/2017 15:34:17
ERNESTO PEREDA DE PABLO <i>UNIVERSIDAD DE LA LAGUNA</i>	06/07/2017 13:51:19

3

Cosmology with cluster number counts

The study of galaxy clusters is a fundamental tool in modern cosmology. Galaxy clusters form in correspondence to the most massive halos, thus tracing the distribution of matter at large scales: their abundance is therefore sensitive to the underlying cosmology, particularly to the total amount of matter in the Universe and to the amplitude of density perturbations. From here the interest in the observation of clusters, and in the construction of large cluster catalogues. In this chapter we detail how it is possible to extract cosmological constraints from the analysis of the cluster abundance. After showing how to compute the cluster abundance according to a specified cosmological model, we implement a proper statistical tool that we test over simulated cluster surveys, in order to assess its accuracy in the recovery of cosmological parameters. We stress in particular the importance of the observational selection function in determining the survey outcome and the precision in the final parameter estimates. Then, we apply the same methodology on real data from the *Planck* satellite, reproducing the preliminary results obtained by the Planck Collaboration. Finally, we discuss how these estimates can be improved with future observations and data analysis, both by using a larger data set, and by reducing the systematics affecting the underlying modelling.

3.1 Predicting the output of a cluster survey

We discussed in section 1.4.5 how different observation of galaxy clusters can be combined to provide cosmological estimates. Throughout this chapter we

will consider the abundance of clusters as a function of redshift as a cosmological tool. In this section, in particular, we focus on the forward problem of predicting the cluster redshift distribution starting from a given cosmological model. More specifically, we are interested in simulating the output of a cluster survey, which also requires assessing how instrumental issues affect the cluster observations. We will take as a reference the cosmological model from table 3.1.

The computation requires three main elements, namely:

- a proper mass function for computing the cluster density distribution as a function of mass;
- a comoving volume element, for translating the cluster number density into cluster number in the FRW geometry;
- a selection function to model the effect of instrumentation when performing a cluster survey.

We discuss each point in the following.

Ω_m	Ω_b	H_0	σ_8	n_s	τ
0.316	4.91×10^{-2}	67.1	0.847	0.968	0.0925

Table 3.1: Fiducial cosmology used for simulating a cluster survey.

3.1.1 Mass function

We know that clusters of galaxies form in correspondence to the dark matter halos. We can model their abundance, therefore, using the unconditional halo mass function (UMF). We extensively discussed the UMF in the previous chapter. We employed equation 2.8 to compute the UMF, and adopted the Tinker et al. (2008) parametrization (equation 2.14). The Tinker mass function is based on a fit over a set of numerical N-body simulations where halos are identified with a spherical overdensity (SO) algorithm. The fitting parameters in 2.14 depend therefore on the value of the overdensity employed by the halo finder, and can be found in the reference work. A common choice is to use the mass function defined with overdensity $\Delta = 200$; we adopted this choice as well.

3.1.2 Comoving volume element

The comoving volume element is required to transform the density of objects predicted by the mass function into a number. Its definition relies on the use

Este documento incorpora firma electrónica, y es copia auténtica de un documento electrónico archivado por la ULL según la Ley 39/2015.
Su autenticidad puede ser contrastada en la siguiente dirección <https://sede.ull.es/validacion/>

Identificador del documento: 973742	Código de verificación: Jfg6xBh0	Fecha: 30/06/2017 15:10:10
Firmado por: DENIS TRAMONTE UNIVERSIDAD DE LA LAGUNA		
RAFAEL DELFIN BARRENA DELGADO UNIVERSIDAD DE LA LAGUNA		30/06/2017 15:21:31
JOSE ALBERTO RUBIÑO MARTIN UNIVERSIDAD DE LA LAGUNA		30/06/2017 15:34:17
ERNESTO PEREDA DE PABLO UNIVERSIDAD DE LA LAGUNA		06/07/2017 13:51:19

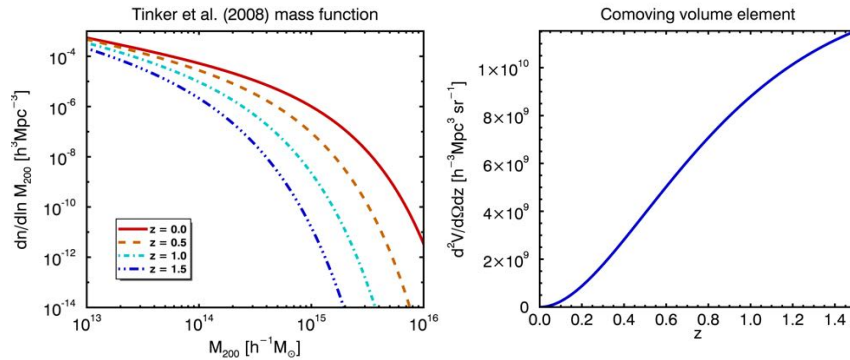


Figure 3.1: *Left:* mass function from Tinker et al. (2008) computed at different redshifts as a function of M_{200} . *Right:* comoving volume element, as a function of redshift.

of the angular diameter distance, which in the case of a flat Universe can be written as (Hogg 1999):

$$D_A(z) = \frac{1}{1+z} \int_0^z dz' \frac{dz'}{H(z')}. \quad (3.1)$$

The angular diameter distance is the ratio of the transversal physical dimension of an object to its angular size. It is one of the most important definitions of distances in cosmology, because it allows to compute physical lengths from an observable, that is the angular size. Notice that with the definition 3.1 the result is a physical distance, not comoving. The redshift dependence in 3.1 has the consequence that the angular diameter distance does not increase indefinitely with redshift; instead, it reaches a maximum at a redshift around ~ 1.5 and then it slowly decreases. This feature, which is due to the expansion of space, has the effect of enhancing the apparent size of high-redshift objects.

The comoving volume element can be obtained as the product of a comoving area element dA and a comoving angular diameter distance element. We know that the angular diameter distance converts angles into physical transverse distances, so that the square of the angular diameter distance times a solid angle element $d\Omega$ gives a physical infinitesimal area; a factor $(1+z)^2$ is enough to make it comoving. So:

$$dA = (1+z)^2 D_A^2 d\Omega. \quad (3.2)$$

From equation 3.1 we see that the expression for the comoving angular distance element is $dz/H(z)$. By putting all together, we get the final expression for the

comoving volume element:

$$dV = \frac{(1+z)^2 D_A^2(z)}{H^2(z)} d\Omega dz, \quad (3.3)$$

which is the volume enclosed in a solid angle element $d\Omega$ and a redshift infinitesimal interval dz .

3.1.3 Survey selection function

The concept of selection function was originally introduced in the context of optical surveys, where objects become increasingly more difficult to detect the fainter and the farther they are (Martínez & Saar 2002). The selection function $S(x)$ gives an estimate of the probability that a galaxy more brilliant than a particular cutoff, at distance x , is detected by the survey (x being any distance measure, such as luminosity distance, angular diameter distance, redshift, etc.). If up to a certain distance the condition $S(x) = 1$ is fulfilled, the survey is said to be *complete* up to that distance¹.

To better understand the meaning of the selection function, we give an indication of how it can be evaluated in the case of an optical survey. The computation starts from the *luminosity function* $\phi(L)dL$, that expresses the number density of objects whose luminosity falls between L and $L + dL$ (this concept is quite similar to the mass function, replacing the mass with luminosity). For instance, Schechter's parametrisation yields:

$$\phi(L)dL = \phi_* \left(\frac{L}{L_*} \right)^\alpha \exp \left(-\frac{L}{L_*} \right) d \left(\frac{L}{L_*} \right), \quad (3.4)$$

where the parameters ϕ_* , L_* and α are fitted to observations (Schechter 1976). The same expression, rewritten in terms of the *absolute magnitude*² M , takes the form:

$$\phi(M)dM = 0.4 \ln(10) \phi_* \left[10^{0.4(M_*-M)} \right]^{\alpha+1} \exp \left[-10^{0.4(M_*-M)} \right] dM, \quad (3.5)$$

¹More generally, the completeness of a survey is defined as the fraction of objects with properties above some observable limit that are identified.

²The *apparent magnitude* m of a celestial object is defined as $m = m_0 - 2.5 \log_{10}(L/L_0)$, where m_0 and L_0 are some reference values of apparent magnitude and luminosity. The absolute magnitude is defined as the hypothetical apparent brightness of an object if placed at a luminosity distance of 10 pc. Apparent and absolute magnitudes are the most common quantities astronomers use to quantify the brightness of sky objects.

Este documento incorpora firma electrónica, y es copia auténtica de un documento electrónico archivado por la ULL según la Ley 39/2015.
Su autenticidad puede ser contrastada en la siguiente dirección <https://sede.ull.es/validacion/>

Identificador del documento: 973742

Código de verificación: Jfg6xBh0

Fecha: 30/06/2017 15:10:10

Firmado por: DENIS TRAMONTE UNIVERSIDAD DE LA LAGUNA	30/06/2017 15:21:31
RAFAEL DELFIN BARRENA DELGADO UNIVERSIDAD DE LA LAGUNA	30/06/2017 15:34:17
JOSE ALBERTO RUBIÑO MARTIN UNIVERSIDAD DE LA LAGUNA	06/07/2017 13:51:19
ERNESTO PEREDA DE PABLO UNIVERSIDAD DE LA LAGUNA	

with M_* the magnitude corresponding to the luminosity L_* . The selection function is then computed as the ratio:

$$S(x) = \frac{\int_{-\infty}^{M(x)} dM \phi(M)}{\int_{-\infty}^{M_{\max}} dM \phi(M)}. \quad (3.6)$$

To understand this expression, we remind that an optical survey has a brightness threshold below which an object cannot be detected; such lower limit in luminosity translates into an upper limit in apparent magnitude m_{lim} . Then, $M(x)$ is defined as the corresponding absolute magnitude, and gets a dependence on distance: indeed, farther objects need to be brighter to be detected, so we expect $M(x)$ to decrease with distance. The magnitude M_{\max} is defined as $M_{\max} = \max(M(x), M_{\text{com}})$, and M_{com} is the maximum magnitude for which the survey is complete. This definition ensures that the ratio is equal to unity up to the largest distance x such that $M(x) > M_{\text{com}}$; then, the absolute magnitude threshold will fall below the completeness magnitude, so that the ratio will be less than unity and not all objects with $M > M(x)$ will be detected.

Eventually the selection function drops to zero at distances such that objects would need to be extremely bright to be detected. So, when observing beyond the completeness limit the selection function must be taken into account to handle the fraction of objects that is missed by the survey; otherwise, all estimates coming from survey data would bear an important systematic error.

Selection in mass and redshift

In order to compute the abundance of clusters as a function of redshift, the ideal situation would be to have a selection function written in terms of the cluster redshift and mass, $S(M, z)$. However, the cluster mass is not directly observable. The selection function will be written in terms of the cluster observables, and will need to be translated into a function of M and z . We will deal with this problem in section 3.3.3. For the moment, let us suppose we can write the selection as a function of mass and redshift.

In this case the aforementioned luminosity limit is replaced by a threshold mass, which is usually dependent on redshift. However, as we saw, a clear advantage of SZ surveys is that their threshold mass is nearly independent of z . The simplest case would be therefore to fix a threshold mass above which the survey is complete and below which no object can be detected. However, in order to make our survey simulation more realistic, we should employ a selection function that maintains some dependence on z , and that does not behave like a step function when crossing the threshold mass. We chose for this purpose the

Este documento incorpora firma electrónica, y es copia auténtica de un documento electrónico archivado por la ULL según la Ley 39/2015.
Su autenticidad puede ser contrastada en la siguiente dirección <https://sede.ull.es/validacion/>

Identificador del documento: 973742	Código de verificación: Jfg6xBh0
Firmado por: DENIS TRAMONTE UNIVERSIDAD DE LA LAGUNA	Fecha: 30/06/2017 15:10:10
RAFAEL DELFIN BARRENA DELGADO UNIVERSIDAD DE LA LAGUNA	30/06/2017 15:21:31
JOSE ALBERTO RUBIÑO MARTIN UNIVERSIDAD DE LA LAGUNA	30/06/2017 15:34:17
ERNESTO PEREDA DE PABLO UNIVERSIDAD DE LA LAGUNA	06/07/2017 13:51:19

selection function from Albrecht et al. (2006). Their parameterization reads:

$$S(M, z) = \frac{1}{2} \operatorname{erfc} \left[\frac{\ln M_{\text{th}} - \ln M}{\sqrt{2\sigma_{\ln M}(z)^2}} \right]. \quad (3.7)$$

In this formula M_{th} is the threshold mass, which they take as constant. However, they allow a redshift dependence for the scatter $\sigma_{\ln M}$, which is supposed to grow with z given that at high redshift mass measurements get less precise. In order to build a selection function similar to the one considered in Albrecht et al. (2006), we considered a linear growth of the scatter from $\sigma_{\ln M}(z=0) = 0.25$ to $\sigma_{\ln M}(z=2) = 0.40$. The resulting selection function falls to zero for low masses and high redshifts; however, the most dramatic dependence is on the threshold mass. In figure 3.2 we plot the selection function at three different redshifts, showing that for higher values of z the change from zero to unity becomes less sharp. In the same figure we also see the effect of changing the threshold mass for a fixed z , which results in a shift of the selection function along the mass axis, enlarging or shortening the effective range of mass detectable by the survey.

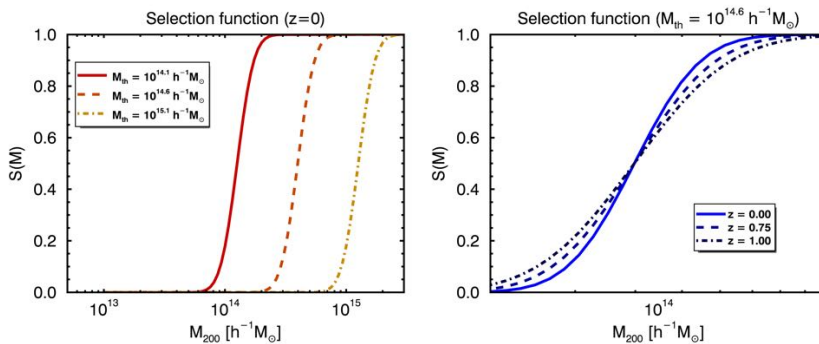


Figure 3.2: Left: Albrecht et al. (2006) selection function computed at $z = 0$ for three different values of the threshold mass. Right: selection function at three different redshift, in the case of a $10^{14.6} h^{-1} M_\odot$ threshold mass.

As we will see in the following, the choice of a different threshold mass affects dramatically both the total number of clusters that can be detected, and the size of the final error bars in the estimation of cosmological parameters. For this simulation, we will take as a reference the value $M_{\text{th}} = 10^{15.1} h^{-1} M_\odot$, which results in a total number of observed clusters of the same order of the size of

Planck PSZ1 catalogue (Planck Collaboration et al. 2014i, see section 3.3.1). Just to have a reference, a lower threshold mass $M_{\text{th}} = 10^{14.2} h^{-1} M_{\odot}$ would yield a number of clusters similar to what will be detected by future surveys like *Euclid* (Laureijs et al. 2011).

3.1.4 Survey simulation

We can now put everything together to compute the cluster redshift distribution. The mass function provides the number density distribution of clusters, which integrated over mass yields a finite density. Multiplication by the comoving volume element converts the density into a number (we shall use the capital N for numbers and the lowercase n for densities); this quantity should be integrated over the whole solid angle to leave only the dependence on redshift. Finally, the selection function should be introduced to determine which range of the mass can effectively contribute to the total number of clusters observed by the survey. In formulae:

$$\frac{dN}{dz}(z) = \int_{4\pi} d\Omega \frac{dV}{dz d\Omega}(z) \int_0^\infty dM \frac{dn}{dM}(M, z) S(M, z) \quad (3.8)$$

$$= 4\pi \frac{dV}{dz d\Omega}(z) \int_0^\infty dM \frac{dn}{dM}(M, z) S(M, z), \quad (3.9)$$

where in the last equality we took advantage of the selection function being independent of the position on the sky. Notice that the integral over mass can be extended over the whole range without producing divergences: indeed, down to very low masses, the growth of the mass function is compensated by the selection function dropping to zero. In the case of a simple redshift-independent step-function selection, this would be equivalent to integrate from the threshold mass M_{th} up to infinity.

The cluster redshift distributions corresponding to different threshold masses for the selection function are plotted in figure 3.3. We see that if the threshold mass grows not only does the distribution falls in absolute value, but also shrinks towards lower values of redshift, that is, we observe less clusters, and the ones we observe are closer to us.

The distribution 3.3 is not yet the quantity we can compare to the output of a survey. What we can measure is the number of clusters inside a definite range of redshift. It is then convenient to divide the redshift range into a set of N_b bins, each of size Δz , and to determine the number of clusters inside each of them. We shall refer to this quantity as the *cluster number count*, which can

Este documento incorpora firma electrónica, y es copia auténtica de un documento electrónico archivado por la ULL según la Ley 39/2015.
Su autenticidad puede ser contrastada en la siguiente dirección <https://sede.ull.es/validacion/>

Identificador del documento: 973742

Código de verificación: Jfg6xBh0

Fecha: 30/06/2017 15:10:10

Firmado por: DENIS TRAMONTE UNIVERSIDAD DE LA LAGUNA	30/06/2017 15:21:31
RAFAEL DELFIN BARRENA DELGADO UNIVERSIDAD DE LA LAGUNA	30/06/2017 15:34:17
JOSE ALBERTO RUBIÑO MARTIN UNIVERSIDAD DE LA LAGUNA	06/07/2017 13:51:19
ERNESTO PEREDA DE PABLO UNIVERSIDAD DE LA LAGUNA	

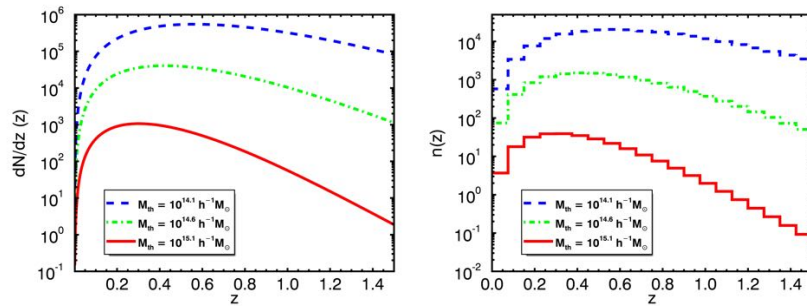


Figure 3.3: *Left:* redshift distribution of the cluster number density, for three simulated surveys with different selection thresholds. *Right:* corresponding number counts over a set of redshift bins.

be computed as:

$$n_i \equiv n(z_i) = \int_{z_i - \Delta z/2}^{z_i + \Delta z/2} dz' \frac{dN}{dz'}(z'). \quad (3.10)$$

In figure 3.3 we also show the resulting number counts computed with 3.10. The binned counts n_i are the quantities that can actually be compared to the result of a cluster survey for testing cosmological models, and represent the final goal of our simulation. As a final remark, notice that the sum of the quantities n_i over all bins, or equivalently the integral of 3.9 over the full redshift range, yields the total cluster number N_c :

$$N_c = \int_0^\infty dz \frac{dN}{dz}(z) = \sum_{i=1}^{N_b} n_i. \quad (3.11)$$

The total number of clusters observed with our reference cosmology and using the three threshold masses considered above is reported in table 3.2.

$M_{\text{th}} (h^{-1} M_{\odot})$	$10^{14.1}$	$10^{14.6}$	$10^{15.1}$
N_c	468030	27235	527

Table 3.2: Total number of clusters observed depending on the threshold mass used for the selection function.

Este documento incorpora firma electrónica, y es copia auténtica de un documento electrónico archivado por la ULL según la Ley 39/2015. Su autenticidad puede ser contrastada en la siguiente dirección https://sede.ull.es/validacion/			
Identificador del documento:	973742	Código de verificación:	Jfg6xBh0
Firmado por:	DENIS TRAMONTE UNIVERSIDAD DE LA LAGUNA	Fecha:	30/06/2017 15:10:10
	RAFAEL DELFIN BARRENA DELGADO UNIVERSIDAD DE LA LAGUNA		30/06/2017 15:21:31
	JOSE ALBERTO RUBIÑO MARTIN UNIVERSIDAD DE LA LAGUNA		30/06/2017 15:34:17
	ERNESTO PEREDA DE PABLO UNIVERSIDAD DE LA LAGUNA		06/07/2017 13:51:19

3.1.5 Sample bias

Before closing this section we should take into account that in general an experiment will not be able to scan the whole sky, and the observations will cover only a definite fraction of the total solid angle. For ground-based observations, clearly only half of the sky is observable (at most), but also detectors on satellites will not be able to observe the region corresponding to the Galactic plane or in the direction of other bright sources. This means that each survey has associated an effective covered sky fraction f_{sky} .

We also wanted to introduce a limited observed region in our survey simulation. Let us suppose that our survey only covers the northern galactic hemisphere. We know the total number of clusters N_c observed by the survey. For each one of them, we generated their galactic coordinates as random numbers from a uniform distribution over the sphere, and kept only those clusters whose galactic latitude was positive.

This procedure actually introduces a systematic effect, which we can call *sample bias*. Taking only the clusters lying above the galactic plane is quite not the same as just dividing the total number of simulated clusters by two (for each redshift bin). Indeed, galactic coordinates are generated randomly, so that the clusters with latitude $l > 0$ will not be exactly half of the total. Depending on the simulation, an excess or a deficit of clusters is expected in the northern hemisphere. As far as the estimation of parameters is concerned, simulations with an excess of clusters will be interpreted as universes with a higher content of matter and a higher *rms* of density perturbations, the opposite happening with simulations with a deficit of clusters, even though they were all generated starting from the same fiducial cosmology. This concept is similar to the cosmic variance we discussed in chapter 1.

In the case of simulations, the sample bias can be accounted for by combining the results from many realisations. To this aim, we performed many simulations with the same fiducial cosmology and averaged the counts corresponding to each redshift bin. Indeed, we know the population of the simulations to be distributed around the one that gives half clusters in the northern and half in the southern hemisphere, with no bias. This way we ensure that the estimation of parameters from the counts in the northern hemisphere is unbiased, and any possible difference of the recovered parameters with respect to the fiducial ones will be due exclusively to errors in the numerical implementation of the estimator.

In the case of real surveys, however, this procedure is not possible. The sample bias is quite a serious issue, which affects indeed any sky survey and is to be added to the cosmic variance as a source of systematics in the parameter

Este documento incorpora firma electrónica, y es copia auténtica de un documento electrónico archivado por la ULL según la Ley 39/2015.
Su autenticidad puede ser contrastada en la siguiente dirección <https://sede.ull.es/validacion/>

Identificador del documento:	973742	Código de verificación:	Jfg6xBh0
Firmado por:	DENIS TRAMONTE UNIVERSIDAD DE LA LAGUNA	Fecha:	30/06/2017 15:10:10
	RAFAEL DELFIN BARRENA DELGADO UNIVERSIDAD DE LA LAGUNA		30/06/2017 15:21:31
	JOSE ALBERTO RUBIÑO MARTIN UNIVERSIDAD DE LA LAGUNA		30/06/2017 15:34:17
	ERNESTO PEREDA DE PABLO UNIVERSIDAD DE LA LAGUNA		06/07/2017 13:51:19

estimation. The only solution is to try and observe the largest sky fraction possible.

3.2 Cosmological constraints with cluster abundance

In this section we show how the observed abundance of clusters of galaxies can be used as a tool for estimating cosmological parameters. We will focus in particular on estimates of the parameters Ω_m and σ_8 . This requires the use of statistical techniques to extract the best-fit parameters from the survey we simulated; if the final estimates are compatible with the original ones, then our method is consistent and unbiased and can be applied for estimating cosmological parameters from real data.

3.2.1 Cluster-based likelihood

Let us consider a set of cluster counts \tilde{n}_i , which are the output of a cluster survey (real or simulated), to which a set of errors ϵ_i is associated. Let $\boldsymbol{\theta}$ be a vector of cosmological parameters, taking values in a proper parameter space Ω . For each particular value of the parameter vector we can compute the corresponding cluster counts $n_i(\boldsymbol{\theta})$ using the procedure described in the previous section. The likelihood function $\mathcal{L}(\boldsymbol{\theta})$ is the probability of getting the fiducial counts \tilde{n}_i starting from the cosmological model $\boldsymbol{\theta}$. The set of parameters $\hat{\boldsymbol{\theta}}$ that gives the highest likelihood is the one we take as our best-fit estimate.

The main issue is how to compute the likelihood. This implies a comparison between the fiducial counts \tilde{n}_i and the counts n_i corresponding to the particular model. In most situations it is fine to assume a Gaussian distribution for the outcomes of the simulation (relying on the central limit theorem). The likelihood is then simply expressed by:

$$\mathcal{L} = e^{-\chi^2(\boldsymbol{\theta})/2}, \quad (3.12)$$

where the *chi-square* in this case reads:

$$\chi^2 \equiv \sum_{i=1}^{N_b} \frac{(\tilde{n}_i(\boldsymbol{\theta}) - n_i)^2}{\epsilon_i^2}, \quad (3.13)$$

where N_b is the total number of redshift bins. In other words, the most likely model is the one giving the lowest chi-square.

In this case, however, the count of clusters in each bin follows a Poissonian distribution, and the probability for the outcome $n_i(\boldsymbol{\theta})$ should be computed,

Este documento incorpora firma electrónica, y es copia auténtica de un documento electrónico archivado por la ULL según la Ley 39/2015.
Su autenticidad puede ser contrastada en la siguiente dirección <https://sede.ull.es/validacion/>

Identificador del documento: 973742

Código de verificación: Jfg6xBh0

Fecha: 30/06/2017 15:10:10

Firmado por: DENIS TRAMONTE
UNIVERSIDAD DE LA LAGUNA

RAFAEL DELFIN BARRENA DELGADO
UNIVERSIDAD DE LA LAGUNA

JOSE ALBERTO RUBIÑO MARTIN
UNIVERSIDAD DE LA LAGUNA

ERNESTO PEREDA DE PABLO
UNIVERSIDAD DE LA LAGUNA

30/06/2017 15:21:31

30/06/2017 15:34:17

06/07/2017 13:51:19

accordingly, as:

$$\mathcal{L} = \prod_{i=1}^{N_b} \frac{n_i^{\tilde{n}_i} e^{-n_i}}{\tilde{n}_i!}. \quad (3.14)$$

In this case, we can take the logarithm of the likelihood to define the quantity χ_p^2 , that is an “effective” chi-square corresponding to the Poissonian distribution:

$$\chi_p^2 = \sum_{i=1}^{N_b} (\tilde{n}_i \ln n_i - n_i - \ln \tilde{n}_i!). \quad (3.15)$$

The advantage of employing expression 3.15 is that the last term $\sum_i \ln \tilde{n}_i!$ is the same for all the different models we test, since it only depends on the initial simulation, and therefore is just a constant quantity that we can ignore (the numerical computation of a factorial, apart from being rather time-consuming, implies the generation of large numbers that can lead to overflow errors). This simplification only alters the absolute value of the likelihood, but does not alter its position in terms of the parameters $\boldsymbol{\theta}$ nor the shape of the final likelihood distribution. In fact, it is customary to define a slightly modified chi-square as $\hat{\chi}_p^2 \equiv \chi_p^2 - \max(\chi_p^2)$, so that the final likelihood $\mathcal{L} = \exp(\hat{\chi}_p^2)$ is normalised to one at the maximum. The statistics encoded in eqs. 3.14 and 3.15 is usually referred to as *Cash statistics*, from Cash (1979).

The Cash statistics reduces to the Gaussian one in the case of very large counts. So, in our case of the cluster-based likelihood, one could think of using expression 3.13 instead of 3.14, substituting ϵ_i with $\sqrt{\tilde{n}_i}$ (which is the definition of rms for a Poissonian distribution). However, some of the redshift bins are expected to have cluster counts up to just a few, and in this case the Gaussian approximation is not valid. In the following we will always compute our likelihood by making use of the proper Cash statistics 3.14.

3.2.2 Monte Carlo Markov Chains

In cosmology, parameter estimation is usually performed employing a Bayesian analysis. Given a set of cosmological parameters $\boldsymbol{\theta}$ and a set of cluster number counts \mathbf{n} , the following relation holds:

$$P(\boldsymbol{\theta}|\mathbf{n}) = \frac{P(\mathbf{n}|\boldsymbol{\theta})P(\boldsymbol{\theta})}{P(\mathbf{n})}, \quad (3.16)$$

which is the Bayes’ theorem. The terms appearing in the relation are:

- $P(\boldsymbol{\theta}|\mathbf{n})$ is called the *posterior distribution*; it is the conditional probability of the cosmological model given the set of data \mathbf{n} . This is the quantity

Este documento incorpora firma electrónica, y es copia auténtica de un documento electrónico archivado por la ULL según la Ley 39/2015.
Su autenticidad puede ser contrastada en la siguiente dirección <https://sede.ull.es/validacion/>

Identificador del documento: 973742

Código de verificación: Jfg6xBh0

Fecha: 30/06/2017 15:10:10

Firmado por: DENIS TRAMONTE
UNIVERSIDAD DE LA LAGUNA

RAFAEL DELFIN BARRENA DELGADO
UNIVERSIDAD DE LA LAGUNA

JOSE ALBERTO RUBIÑO MARTIN
UNIVERSIDAD DE LA LAGUNA

ERNESTO PEREDA DE PABLO
UNIVERSIDAD DE LA LAGUNA

30/06/2017 15:21:31

30/06/2017 15:34:17

06/07/2017 13:51:19

we actually want to determine, since our best fit model is the one that maximises this probability.

- $P(\mathbf{n}|\boldsymbol{\theta})$ is the probability of obtaining the set of counts \mathbf{n} starting from the cosmological model $\boldsymbol{\theta}$. This is the *likelihood* that we described in the previous section.
- $P(\boldsymbol{\theta})$ is the probability of the model, independently of the data. It is called the *prior distribution* and it contains our initial knowledge of the most likely values the parameters can take.
- $P(\mathbf{n})$ is the probability of the data, independently of the model. This factor is not as relevant as the others and can usually be set equal to one in the moment data are provided. Alternatively, it can be regarded as a normalisation factor for the posterior distribution.

Notice that if we take flat priors on the parameters, meaning we only set limits for the range in which they can take values, then the posterior distribution is simply equal to the likelihood. The best-fit parameters will then be the ones providing the highest likelihood. However, if the priors on the parameters are non-trivial then the final posterior distribution can be quite different both from the likelihood and from the prior.

It is usually not practical to determine the posterior analytically using 3.16. It is more efficient to reconstruct the posterior distribution by sampling values from a set distributed according to it. A common way to generate a set of values for the parameters distributed according to the posterior is the use of Markov Chains Monte Carlo (MCMC). The Monte Carlo methods constitute a broad class of computational algorithms that are based on the simulations of random numbers to obtain numerical results. A Markov process (or Markov chain) is a memoryless stochastic process, in which the probability for the system to make a transition to any of the possible states depends only on its current state, and not on the previous ones. We can think of a Markov chain in the space of cosmological parameters as a family of parameter vectors $\boldsymbol{\theta}(t)$, where the variable t is discrete and at each value t_1, t_2, \dots, t_i the parameter variable takes values $\boldsymbol{\theta}_1, \boldsymbol{\theta}_2, \dots, \boldsymbol{\theta}_i$. This way the chain wanders in the parameter space changing the value of $\boldsymbol{\theta}$ at each step according to some transition rule; the transition rule gives the probability for the system to jump from an initial state $\boldsymbol{\theta}_i$ to a final state $\boldsymbol{\theta}_j$. At each time t it is possible to define the probability distribution of the system in the state $\boldsymbol{\theta}_i$, as the probability for the system to be in the state $\boldsymbol{\theta}_i$ at time t . This probability distribution initially changes with time. However, under very general assumptions, the system eventually

Este documento incorpora firma electrónica, y es copia auténtica de un documento electrónico archivado por la ULL según la Ley 39/2015.
Su autenticidad puede ser contrastada en la siguiente dirección <https://sede.ull.es/validacion/>

Identificador del documento:	973742	Código de verificación:	Jfg6xBh0
Firmado por:	DENIS TRAMONTE UNIVERSIDAD DE LA LAGUNA	Fecha:	30/06/2017 15:10:10
	RAFAEL DELFIN BARRENA DELGADO UNIVERSIDAD DE LA LAGUNA		30/06/2017 15:21:31
	JOSE ALBERTO RUBIÑO MARTIN UNIVERSIDAD DE LA LAGUNA		30/06/2017 15:34:17
	ERNESTO PEREDA DE PABLO UNIVERSIDAD DE LA LAGUNA		06/07/2017 13:51:19

reaches a stationary probability distribution, meaning that the probability for the transition from θ_i to θ_j at time t is equal to the probability for the opposite transition. When a chain reaches a stationary distribution, the values taken by the variable θ are sampled according to that distribution.

The Metropolis-Hastings algorithm (Metropolis et al. 1953; Hastings 1970) allows to build a transition rule for the system such that the final stationary distribution is the posterior $P(\theta|\mathbf{n})$ we want to sample from. The transition rule in this case is based on the computation of the likelihood for the system states, which favours or disfavours a given value θ as the new state for the chain. This way, the chain becomes a set of random number distributed according to the posterior distribution, enabling its reconstruction and the determination of the best-fit cosmological model.

There are some issues, however, that must be taken into account. The Markov chain, indeed, will take some time before reaching the final posterior as its stationary distribution. This initial stage is called *burn-in*, and should be removed from the final chain. It is not possible to know *a priori* what fraction of the chain has to be removed; this depends also on the initial points chosen for the chain, and has to be assessed for each case. Another issue is the fact that the samples coming from a Markov chain are strongly correlated, while a proper reconstruction of the posterior requires to employ individual samples. The solution is to perform an operation of *thinning* of the chain, that is, to keep only one state out of n from the initial chain, thus building a thinned (shorter) chain whose values are nearly uncorrelated. The small residual correlations are usually unimportant. Again, there is not a unique prescription for the thinning factor n to be employed.

One last issue when dealing with MCMC is that a chain cannot explore the whole parameter space. It would do so if it could run for an infinite time, but clearly in the finite time of a simulation there are areas of the parameter space that are not reached by the chain. When a chain manages to perform a good exploration of the state space it is said that it achieves good mixing. A poor mixing of the chain, that is, a poor exploration of state space, leads ultimately to wrong results in parameter estimation. A solution is usually to launch several chains, with the same transition rule, but starting from different initial points in the parameter space. The final MCMC can be obtained by merging all chains.

CosmoMC

CosmoMC (Lewis & Bridle 2002) is a FORTRAN 2003/2008 MCMC engine for exploring the cosmological parameter space, that also includes codes for analysing

Este documento incorpora firma electrónica, y es copia auténtica de un documento electrónico archivado por la ULL según la Ley 39/2015.
Su autenticidad puede ser contrastada en la siguiente dirección <https://sede.ull.es/validacion/>

Identificador del documento:	973742	Código de verificación:	Jfg6xBh0
Firmado por:	DENIS TRAMONTE UNIVERSIDAD DE LA LAGUNA	Fecha:	30/06/2017 15:10:10
	RAFAEL DELFIN BARRENA DELGADO UNIVERSIDAD DE LA LAGUNA		30/06/2017 15:21:31
	JOSE ALBERTO RUBIÑO MARTIN UNIVERSIDAD DE LA LAGUNA		30/06/2017 15:34:17
	ERNESTO PEREDA DE PABLO UNIVERSIDAD DE LA LAGUNA		06/07/2017 13:51:19

Monte-Carlo samples and for performing importance sampling³. `CosmoMC` allows to run chains in cosmological parameter space according to the characteristics we specify as input: which parameters we want to vary, the priors on those parameters, the kind of likelihood we want to employ, or the sampling method. The facility `getdist`, that is included in the package, can be used to produce one-dimensional and two-dimensional plots of the posterior distribution of the parameters.

The full package also contains the Boltzmann code `CAMB` (Lewis et al. 2000) for computing the power spectra of matter or CMB. `CosmoMC` is indeed a quite complex code, and just as `CAMB`, it can be used as a closed box by changing the input parameters and getting the output. However, since we wanted to include our likelihood for the abundance of galaxy clusters, we modified one of the `CosmoMC` source codes and included a call to our subroutines. By passing the cosmological parameters and the power spectrum to our code we could compute the corresponding value of the likelihood and pass it back to `CosmoMC`, which uses it to determine the next step of the Markov chain.

3.2.3 Results

In order to test the modified `CosmoMC`, we considered the simulated survey with a threshold mass $M_{\text{th}} = 10^{15.1} h^{-1} M_{\odot}$, and took the corresponding counts \mathbf{n} as our reference data set. We wanted to fit for the value of Ω_m and σ_8 , fixing the values of the other cosmological parameters to the fiducial values from table 3.1. The parameter space to be explored by the chains is therefore two-dimensional. Notice, however, that Ω_m is not handled by `CosmoMC` as a fundamental parameter; the base parameters are the physical densities of baryonic and dark matter, ω_b and ω_c . Now, the simplest bypass would be to fix the value of the Hubble parameter H_0 and to leave ω_c free, which is equivalent to change only Ω_c ; by fixing also the value of ω_b (so that the shape of the matter power spectrum at high k is not altered), this is equivalent to vary only the parameter Ω_m . However, H_0 is not a basic parameter in `CosmoMC` either; the code rather uses the angular size of the sound horizon at recombination, θ_s (more precisely, the `CosmoMC` fundamental parameter is $100 \theta_s$). It is not possible to simply fix the parameter θ_s as if it was equivalent to H_0 , because it also depends on Ω_c . If we fixed θ_s and let ω_c free, then Ω_c and H_0 would both vary, and in such a way as to maintain θ_s constant. Therefore, we also made θ_s free. Similarly, σ_8 is a derived parameter, and `CosmoMC` rather handles the more fundamental parameter A_s , i.e., the amplitude of the scalar perturbations

³The code, developed by A. Lewis, is public and can be downloaded from <http://cosmologist.info/cosmomc/>.

Este documento incorpora firma electrónica, y es copia auténtica de un documento electrónico archivado por la ULL según la Ley 39/2015. Su autenticidad puede ser contrastada en la siguiente dirección https://sede.ull.es/validacion/		
--	--	--

Identificador del documento: 973742

Código de verificación: Jfg6xBh0

Fecha: 30/06/2017 15:10:10

Firmado por: DENIS TRAMONTE UNIVERSIDAD DE LA LAGUNA	30/06/2017 15:21:31
RAFAEL DELFIN BARRENA DELGADO UNIVERSIDAD DE LA LAGUNA	30/06/2017 15:34:17
JOSE ALBERTO RUBIÑO MARTIN UNIVERSIDAD DE LA LAGUNA	06/07/2017 13:51:19
ERNESTO PEREDA DE PABLO UNIVERSIDAD DE LA LAGUNA	

(more precisely, the `CosmoMC` fundamental parameter is $\ln(10^{10} A_s)$). To sum up, the parameters we let free to vary were ω_c in the range $[0.01, 0.30]$, $100 \theta_s$ in $[0.9, 1.2]$ and $\ln(10^{10} A_s)$ in $[2.7, 4.0]$, all of them with a flat prior; to have a reference, the values corresponding to the fiducial cosmology of table 3.1 are $\omega_c = 0.12$, $100 \theta_s = 1.04$ and $\ln(10^{10} A_s) = 3.11$.

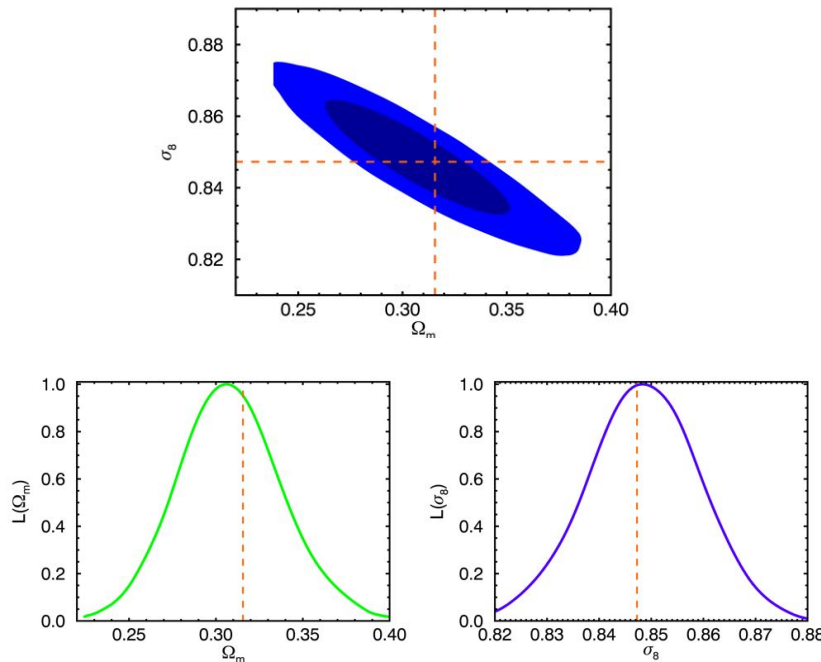


Figure 3.4: Posterior probability distributions obtained with the modified `CosmoMC`. Fiducial values for the cosmological parameter are marked with dashed line. *Upper panel:* correlation plot between Ω_m and σ_8 . *Lower panel:* marginalised probability distributions for the individual parameters.

We launched nine different chains with different starting points in order to achieve a better exploration of the (ω_c, A_s) space. We employed the `getdist` facility to merge the chains and to extract the posterior probability distribution, and concentrated on the derived parameters Ω_m and σ_8 . We show the results in figure 3.4.

Este documento incorpora firma electrónica, y es copia auténtica de un documento electrónico archivado por la ULL según la Ley 39/2015.
Su autenticidad puede ser contrastada en la siguiente dirección <https://sede.ull.es/validacion/>

Identificador del documento: 973742

Código de verificación: Jfg6xBh0

Fecha: 30/06/2017 15:10:10

Firmado por: DENIS TRAMONTE
UNIVERSIDAD DE LA LAGUNA

RAFAEL DELFIN BARRENA DELGADO
UNIVERSIDAD DE LA LAGUNA

JOSE ALBERTO RUBIÑO MARTIN
UNIVERSIDAD DE LA LAGUNA

ERNESTO PEREDA DE PABLO
UNIVERSIDAD DE LA LAGUNA

30/06/2017 15:21:31

30/06/2017 15:34:17

06/07/2017 13:51:19

When different parameters are changed at the same time, it is interesting to study the possible degeneracies between them. For this case, we show in figure 3.4 a correlation plot for the parameters Ω_m and σ_8 : this is a two-dimensional area reporting for each point the posterior probability for the two parameters to take simultaneously the corresponding values on the plot axes. We show two regions limited by the contours corresponding to the confidence levels 68.5% and 95.0%. If there are no degeneracies between two parameters, their correlation plot should appear rather circular. In our case the probability contours are clearly elongated, indicating that the two parameters are correlated. The tilt of the degeneracy direction actually suggests that the two parameters are anti-correlated. This can be understood, since the same number of clusters can be expected in a Universe with higher matter content and less density fluctuations, and vice versa.

In the lower panel we show the results for the marginalised probability distribution for each of the parameters; we also overplot the fiducial values employed for simulating the cluster survey (table 3.1). Our estimation with `CosmoMC` clearly recovers their values, the final estimates being:

$$\Omega_m = 0.307_{-0.029}^{+0.031} \quad \sigma_8 = 0.848 \pm 0.011, \quad (3.17)$$

(errors at 68% C.L.). This can also be seen in the correlation plot, the contours being reasonably centred at the cross defined by the fiducial values. This result proves that our code for estimating cosmological parameters based on cluster abundance is not biased, and can be applied to real data. We will turn to this task in section 3.3

Before closing this section we detail the convention we employed for computing the results in 3.17. In order to obtain the best-fit estimate and the error for a generic parameter x , we considered its cumulative probability distribution $F(x)$, obtained integrating the posterior $f(x)$ as:

$$F(x) = \int_{-\infty}^x dx' f(x'). \quad (3.18)$$

The final estimate is taken as the value x_c such that $F(x_c) = 0.5$ (i.e. the median). The errors are computed at the 68% C.L.: we considered the values x_{inf} and x_{sup} such that $F(x_{\text{inf}}) = 0.16$ and $F(x_{\text{sup}}) = 0.84$. The lower and upper errors are then computed as $\sigma_- = x_c - x_{\text{inf}}$ and $\sigma_+ = x_{\text{sup}} - x_c$, respectively. This is the convention that we adopt throughout this chapter for the computation of the best-fit parameters and their error bars.

Este documento incorpora firma electrónica, y es copia auténtica de un documento electrónico archivado por la ULL según la Ley 39/2015.
Su autenticidad puede ser contrastada en la siguiente dirección <https://sede.ull.es/validacion/>

Identificador del documento: 973742	Código de verificación: Jfg6xBh0
Firmado por: DENIS TRAMONTE UNIVERSIDAD DE LA LAGUNA	Fecha: 30/06/2017 15:10:10
RAFAEL DELFIN BARRENA DELGADO UNIVERSIDAD DE LA LAGUNA	30/06/2017 15:21:31
JOSE ALBERTO RUBIÑO MARTIN UNIVERSIDAD DE LA LAGUNA	30/06/2017 15:34:17
ERNESTO PEREDA DE PABLO UNIVERSIDAD DE LA LAGUNA	06/07/2017 13:51:19

3.2.4 Effect of threshold mass

Before concluding this section we want to show the effect of the threshold mass in the final estimates of cosmological parameters. This time we will consider a different approach for retrieving the cosmological parameters. Instead of reconstructing the posterior distribution on Ω_m and σ_8 , we will consider the effect of changing one parameter at a time. For instance, we can fix σ_8 and change Ω_m in a proper range, and for each value compute the likelihood using 3.14. This way the likelihood becomes a one-dimensional distribution of Ω_m , and since we are considering a flat prior, the value $\tilde{\Omega}_m$ that provides the maximum for the likelihood can be taken as the best-fit value for this parameter. The same can be done by fixing Ω_m and moving σ_8 . The results are plotted in figure 3.5.

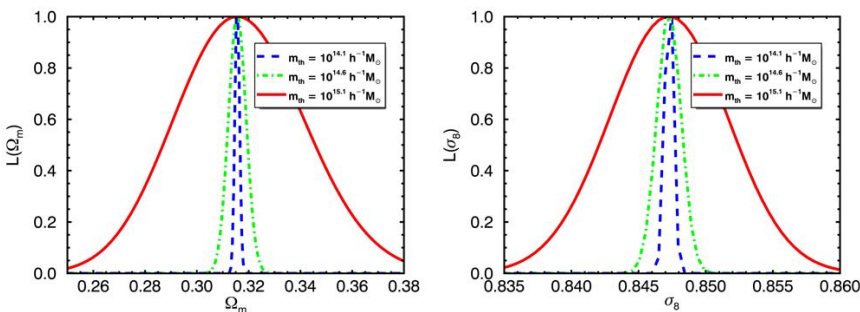


Figure 3.5: Effect of the threshold mass on the estimation of the cosmological parameters Ω_m and σ_8 . The higher number of clusters detectable with a lower threshold mass results in a dramatic improvement of the precision in the final parameter estimates.

We performed such an estimation for three different survey simulations, each computed with a different value for the threshold mass entering the survey selection function. We already know that this results in a dramatic change in the total number of clusters that the survey can detect. This, in turn, determines a strong variation in the size of the error bar that is finally associated with the estimate. The results are detailed in table 3.3.

3.3 Application to *Planck* data

In the following we apply the methodology described in the previous section to real data from the *Planck* satellite. The most important difference here is that we do not have a selection function expressed in terms of the mass and redshift

Este documento incorpora firma electrónica, y es copia auténtica de un documento electrónico archivado por la ULL según la Ley 39/2015.
Su autenticidad puede ser contrastada en la siguiente dirección <https://sede.ull.es/validacion/>

Identificador del documento: 973742

Código de verificación: Jfg6xBh0

Fecha: 30/06/2017 15:10:10

Firmado por: DENIS TRAMONTE
UNIVERSIDAD DE LA LAGUNA

RAFAEL DELFIN BARRENA DELGADO
UNIVERSIDAD DE LA LAGUNA

JOSE ALBERTO RUBIÑO MARTIN
UNIVERSIDAD DE LA LAGUNA

ERNESTO PEREDA DE PABLO
UNIVERSIDAD DE LA LAGUNA

30/06/2017 15:21:31

30/06/2017 15:34:17

06/07/2017 13:51:19

$M_{\text{th}} (h^{-1} M_{\odot})$	10 ^{14.1}	10 ^{14.6}	10 ^{15.1}
N_c	234014	13618	264
Ω_m	0.3156 ± 0.0009	0.316 ± 0.004	0.32 ± 0.02
σ_8	$0.8474^{+0.0008}_{-0.0004}$	0.847 ± 0.001	0.847 ± 0.004

Table 3.3: Total number of clusters and final parameter estimates depending on the selected threshold mass.

of the cluster. We will then introduce the way *Planck* selection function is written in terms of the observables, and the necessary scaling relations used to translate the observables into the cluster redshift and mass. This transformation, as we shall see, is the greatest source of systematics in the final parameter estimates.

3.3.1 Planck SZ catalogues

We already introduced the *Planck* satellite in section 1.3.4. It is a third-generation CMB mission from ESA and it was operative from 2009 to 2013. Its frequency coverage from 30 GHz to 857 GHz made it ideal for detecting galaxy clusters via their tSZ spectral signature on the CMB. This way, *Planck* has delivered the largest SZ cluster catalogue to date. After 10 months of survey data, it delivered an *early Sunyaev-Zel'dovich* (ESZ) catalogue, made of 189 members (Planck Collaboration et al. 2011c). The first *Planck Sunyaev-Zel'dovich* catalogue (PSZ1) counted 1227 detections and was built with data coming from the first 15.5 months of observations (Planck Collaboration et al. 2014i). Finally, the second Planck SZ catalogue (PSZ2) was based on data from the whole 29-month mission and is made of 1653 cluster candidates (Planck Collaboration et al. 2016k).

For this work, we take as a reference the PSZ1 catalogue (by the time we carried out this analysis, the PSZ2 catalogue had not been delivered yet). Before entering into the details of our analysis, it is worth giving some information about the way the catalogue was built.

The search for clusters is done at the map level. Data coming from *Planck* channels are first stacked into individual frequency maps, to which a proper mask is applied in order to remove the Galactic plane region and bright point

Este documento incorpora firma electrónica, y es copia auténtica de un documento electrónico archivado por la ULL según la Ley 39/2015.
Su autenticidad puede ser contrastada en la siguiente dirección <https://sede.ull.es/validacion/>

Identificador del documento: 973742 Código de verificación: Jfg6xBh0

Firmado por: DENIS TRAMONTE UNIVERSIDAD DE LA LAGUNA	Fecha: 30/06/2017 15:10:10
RAFAEL DELFIN BARRENA DELGADO UNIVERSIDAD DE LA LAGUNA	30/06/2017 15:21:31
JOSE ALBERTO RUBIÑO MARTIN UNIVERSIDAD DE LA LAGUNA	30/06/2017 15:34:17
ERNESTO PEREDA DE PABLO UNIVERSIDAD DE LA LAGUNA	06/07/2017 13:51:19

sources (PS); the PS mask was built using the *Planck* Catalogue of Compact Sources (PCCS, [Planck Collaboration et al. 2014j](#)). This union PS-Galactic mask covers 16.3% of the sky. The maps are then employed for a cluster blind search, meaning that no previous information on known clusters is provided as input.

Clusters are identified using three different methods. Two of them are different implementations of the *Matched Multi Filter* (MMF) algorithm ([Herranz et al. 2002](#); [Melin et al. 2006](#)), that searches for clusters via a linear combination of the individual frequency maps plus a spatial filtering to suppress foreground and noise. The two implementations of this method, MMF1 and MMF3, differ in the way they divide the sky in patches where the noise can be considered homogeneous. The PowellSnakes (PwS) method ([Carvalho et al. 2012](#)), instead, is a Bayesian algorithm for detecting compact objects embedded in a diffuse background. Each method yields a list of detections together with their signal-to-noise ratio (S/N). Only detections with S/N above 4.5 are considered. These raw catalogues are first cleaned from spurious detections due to residuals PCCS and CGS (cold galactic sources, [Planck Collaboration et al. 2011f,e](#)). The detection algorithms also assign to each detected SZ candidate a position and an angular size θ_{500} with their uncertainties⁴. The total extension of each cluster is considered to be out to $5\theta_{500}$; the integrated Compton parameter inside that area, i.e. the cluster total flux, is found to be strongly correlated with the cluster size, so that neither the size nor the flux are quoted in the final output catalogue; instead, the flux-size probability contours are provided for each detection.

The different detections methods generally agree in the resulting catalogues; in order to better study the statistics of these catalogues in the recovered quantities, the Planck Collaboration has also considered two extreme cases: a *union* catalogue, made of clusters that are detected by at least one method, and an *intersection* catalogue, made of clusters that are detected by all three algorithms. The statistical characterisation of the catalogue is necessary to obtain information on the accuracy of cluster parameters, and on the catalogue completeness. This characterisation is performed by injecting clusters in simulated data maps, and by comparing the corresponding extracted catalogue with the input one. More details can be found in [Planck Collaboration et al. \(2014i\)](#).

3.3.2 *Planck* scaling relations

The usefulness of a cluster survey for cosmological analyses depends on our ability to transform the cluster observables into quantities that are easily used

⁴For a definition of the angular size θ_{500} see section 3.3.2.

in theoretical predictions, like the cluster mass. In this case, we want to express the cluster mass M_{500} as a function of the observed SZ flux Y_{500} , or, in other words, to derive a proper scaling relation between the two quantities. The way such a relation is determined is detailed in Planck Collaboration et al. (2014g). The main point here is that the scaling relation cannot be determined with SZ data alone; instead, it requires the use of external X-ray data.

- The X-ray flux Y_X , defined as the product of the X-ray temperature T_X and gas mass within R_{500} , $M_{g,500}$, is related to the total thermal energy of the ICM and has been proven to be tightly correlated with the true cluster mass (Kravtsov et al. 2006). In Arnaud et al. (2010), a relation between Y_X and the X-ray hydrostatic mass M_{500}^{HE} is established for a subset of clusters observed with *XMM-Newton*, in the form

$$E^{-2/3}(z) Y_X = 10^{A \pm \sigma_A} [M_{500}^{\text{HE}}]^{\alpha \pm \sigma_\alpha}, \quad (3.19)$$

where $E(z) = H(z)/H_0$ and the numerical value for the parameters A and α are quoted in the reference. Now, the hydrostatic mass is expected to be a biased estimator of the true cluster mass; we will discuss this issue later. For the moment, we can express this bias in terms of an unknown parameter b , such that:

$$M_{500}^{\text{HE}} = (1 - b) M_{500}. \quad (3.20)$$

- Equation 3.19 can be rewritten as:

$$E^{-2/3}(z) Y_X = 10^A [M_{500}^{Y_X}]^\alpha, \quad (3.21)$$

where the uncertainties on the fitting parameters have been absorbed in a re-definition of the mass. This is the baseline mass-proxy relation, where the mass proxy is given by:

$$M_{500}^{Y_X} = 10^{\pm \sigma_A/\alpha} [(1 - b) M_{500}]^{1 \pm \sigma_\alpha/\alpha}. \quad (3.22)$$

- For a set of 71 *Planck* detections, for which good *XMM-Newton* data are available, equation 3.21 can be translated into a relation between the measured SZ flux Y_{500} and the mass proxy $M_{500}^{Y_X}$. The mass proxy indeed defines a radius $R_{500}^{Y_X}$; the SZ flux can be estimated inside a sphere centred at the peak of the X-ray emission, and with radius equal to $R_{500}^{Y_X}$. After correcting for the Malmquist bias, the resulting relation from these 71 clusters is reported in Planck Collaboration et al. (2014g) as:

$$E^{-2/3}(z) D_A^2(z) Y_{500} = 10^{A \pm \sigma_A} [M_{500}^{Y_X}]^{\alpha \pm \sigma_\alpha}, \quad (3.23)$$

Este documento incorpora firma electrónica, y es copia auténtica de un documento electrónico archivado por la ULL según la Ley 39/2015.
Su autenticidad puede ser contrastada en la siguiente dirección <https://sede.ull.es/validacion/>

Identificador del documento: 973742	Código de verificación: Jfg6xBh0	Fecha: 30/06/2017 15:10:10
Firmado por: DENIS TRAMONTE UNIVERSIDAD DE LA LAGUNA		
RAFAEL DELFIN BARRENA DELGADO UNIVERSIDAD DE LA LAGUNA		30/06/2017 15:21:31
JOSE ALBERTO RUBIÑO MARTIN UNIVERSIDAD DE LA LAGUNA		30/06/2017 15:34:17
ERNESTO PEREDA DE PABLO UNIVERSIDAD DE LA LAGUNA		06/07/2017 13:51:19

where D_A is the angular diameter distance accounting for the integration over the cluster solid angle and the values for the parameters A , α and their errors are no longer the same as in equation 3.19 (we continued using the same symbols with a slight abuse of notation).

- The final step consists in introducing the definition of the mass proxy 3.20 into 3.24. This yields the final scaling relation, which including the fitting results, reads:

$$E^{-2/3}(z) \left[\frac{D_A^2(z) Y_{500}}{10^{-4} \text{ Mpc}^2} \right] = 10^{-0.19 \pm 0.02} \left[\frac{(1-b) M_{500}}{6 \times 10^{14} \text{ M}_\odot} \right]^{1.79 \pm 0.08}. \quad (3.24)$$

The mass bias

The mass bias parameter b introduced in equation 3.20 is a consequence of the fact that true mass is not directly measurable, and in order to relate the cluster flux to a mass we have to make some assumptions on its properties. The existence of a bias is inherent to all indirect mass estimations, whatever the proxy employed for its determination. In the case of X-ray mass estimates, the bias has two main contributions. First of all, the X-ray mass estimate relies on the hypothesis that the cluster is in a state of hydrostatic equilibrium; this neglects any additional pressure support from turbulence and bulk motions in the ICM, thus leading to a lower mass estimate (Nagai et al. 2007). The second issue is the determination of the cluster temperature in X-rays, which is assumed as homogeneous; the presence of cooler gas in the ICM would lead, in a single temperature fit, to a lower estimation of the cluster temperature and hence of its mass (Mazzotta et al. 2004). Apart from these, there are other sources of mass bias that are related to instrumental calibration and to the object selection process (X-ray surveys are particularly affected by Malmquist and Eddington biases, Allen et al. 2011; Angulo et al. 2012).

In Planck Collaboration et al. (2014g) the determination of the bias is tackled by comparing the derived flux-mass relation with the one obtained directly from numerical simulations. Predictions from the various simulation sets show a large dispersion, resulting in a large uncertainty on b . However, the results do not suggest any relevant scaling of the bias parameter with mass or redshift. A final, baseline value of $(1-b) = 0.8$ is adopted, with the parameter $(1-b)$ taking values in an accepted larger range of $[0.7, 1.0]$. This result is in agreement with the expected systematics errors in the determination of mass from X-ray observations.

Este documento incorpora firma electrónica, y es copia auténtica de un documento electrónico archivado por la ULL según la Ley 39/2015.
Su autenticidad puede ser contrastada en la siguiente dirección <https://sede.ull.es/validacion/>

Identificador del documento: 973742	Código de verificación: Jfg6xBh0
Firmado por: DENIS TRAMONTE UNIVERSIDAD DE LA LAGUNA	Fecha: 30/06/2017 15:10:10
RAFAEL DELFIN BARRENA DELGADO UNIVERSIDAD DE LA LAGUNA	30/06/2017 15:21:31
JOSE ALBERTO RUBIÑO MARTIN UNIVERSIDAD DE LA LAGUNA	30/06/2017 15:34:17
ERNESTO PEREDA DE PABLO UNIVERSIDAD DE LA LAGUNA	06/07/2017 13:51:19

Scatter

The scaling relation 3.24 works fine as an average relation, but clusters flux densities and masses are actually scattered around this baseline. This scatter has to be taken into account when translating the observational properties of its clusters into its mass. In the following, when predicting the abundance of clusters in a *Planck*-like survey, we will have to translate the basic properties of each cluster, namely its mass and redshift, into the quantities that are directly observables, i.e. its flux and angular size. The flux is computed with a slight generalisation of equation 3.24. Given the derived scaling relation is only an average, we call \bar{Y}_{500} the integrated flux that is related to the cluster mass:

$$\bar{Y}_{500}(M_{500}, z) = Y_* h_{70}^{-2+\alpha} E^{2/3}(z) \left[\frac{D_A(z)}{10^{-2} \text{Mpc}} \right]^{-2} \left[\frac{(1-b)M_{500}}{6 \times 10^4 M_\odot} \right]^\alpha, \quad (3.25)$$

where $h_{70} \equiv h/0.7$, $\alpha = 1.79 \pm 0.08$ and $Y_* = 10^{-0.19 \pm 0.02}$. In order to take into account the scatter of the cluster properties around the average scaling relation 3.25, once the mean flux \bar{Y}_{500} has been computed, the true flux Y_{500} can be determined by sampling from a log-normal distribution:

$$P(\log(Y_{500})|M_{500}, z) = \frac{1}{\sqrt{2\pi\sigma_{\log Y}^2}} \exp \left[-\frac{\log^2[Y_{500}/\bar{Y}_{500}(M_{500}, z)]}{2\pi\sigma_{\log Y}^2} \right] \quad (3.26)$$

(notice that log is base 10). The average of the distribution is indeed the mean flux computed with 3.25, and the rms is estimated in [Planck Collaboration et al. \(2014g\)](#) as $\sigma_{\log Y} = 0.075 \pm 0.010$.

Another important observational quantity is the cluster angular radius θ_{500} . It is defined as $\theta_{500} = R_{500}/D_A$, and can be computed by using $M_{500} = 4/3\pi(500\rho_c)R_{500}^3$. This yields:

$$\bar{\theta}_{500}(M_{500}, z) = \theta_* h_{70}^{-2/3} E^{-2/3}(z) \left[\frac{D_A(z)}{500 \text{Mpc}} \right]^{-1} \left[\frac{(1-b)M_{500}}{3 \times 10^4 M_\odot} \right]^{1/3}, \quad (3.27)$$

where $\theta_* = 6.997 \text{ arcmin}$, and again we stressed that it is the mean baseline relation by using the symbol $\bar{\theta}_{500}$. However, since this relation is analytic, it also yields the true value of the cluster angular extension, $\theta_{500} = \bar{\theta}_{500}$.

The scaling relations 3.25 and 3.27, together with the flux scatter quantified by 3.26, are the fundamental tools we need to translate the clusters mass and redshift into observable properties that can be used to compute the *Planck* selection function.

Este documento incorpora firma electrónica, y es copia auténtica de un documento electrónico archivado por la ULL según la Ley 39/2015.
Su autenticidad puede ser contrastada en la siguiente dirección <https://sede.ull.es/validacion/>

Identificador del documento: 973742

Código de verificación: Jfg6xBh0

Fecha: 30/06/2017 15:10:10

Firmado por: DENIS TRAMONTE
UNIVERSIDAD DE LA LAGUNA

RAFAEL DELFIN BARRENA DELGADO
UNIVERSIDAD DE LA LAGUNA

JOSE ALBERTO RUBIÑO MARTIN
UNIVERSIDAD DE LA LAGUNA

ERNESTO PEREDA DE PABLO
UNIVERSIDAD DE LA LAGUNA

30/06/2017 15:21:31

30/06/2017 15:34:17

06/07/2017 13:51:19

3.3.3 *Planck* selection function

As anticipated, in this case the selection function (also referred to as the *completeness*), is written in terms of the cluster observables, namely its flux Y_{500} and its size θ_{500} . The completeness $\chi(Y_{500}, \theta_{500}; l, b)$ is the probability that a cluster with flux Y_{500} and size θ_{500} is detected at the position of the sky given by its Galactic coordinates (l, b) . It can be estimated by assuming that the probability of the measured value Y_{500} is Gaussian distributed with a standard deviation equal to the noise $\sigma_{Y_{500}}$:

$$\chi(Y_{500}, \theta_{500}; l, b) = \frac{1}{2} \left[1 + \operatorname{erf} \left(\frac{Y_{500} - q \sigma_{Y_{500}}(\theta_{500}; l, b)}{\sqrt{2} \sigma_{Y_{500}}(\theta_{500}; l, b)} \right) \right], \quad (3.28)$$

where q is the selected signal-to-noise ratio and erf is the error function. Notice that the noise $\sigma_{Y_{500}}(\theta_{500}; l, b)$ depends not only on the position on the sky we are considering, but also on the cluster size: indeed it is a by-product of the cluster detection algorithm, and it is determined by the MMF filter that is used for the detection. In the case of the MMF3, noise maps are divided in a set of 504 sky patches, each with a definite value for the noise; the Planck Collaboration provided 32 noise maps corresponding to different values of θ_{500} in the range [0.9, 35.3] arcmin. In order to find the noise corresponding to a given position and to an arbitrary value of θ_{500} , it is possible to interpolate between the maps that are already provided. In figure 3.6 we show two noise maps corresponding to different values of θ_{500} , and the corresponding completenesses as a function of the cluster flux. We see that to a higher θ_{500} it corresponds a lower completeness. Basically, this is because in order to measure the same SZ flux Y_{500} , in the case of higher θ_{500} the signal is to be integrated over a larger area, which enhances the contribution of noise; therefore, if θ_{500} gets higher low-flux clusters can no longer be detected and the completeness worsens.

3.3.4 *Planck* cluster survey prediction

We describe now the way the cluster redshift distribution in a *Planck*-like survey can be computed. Drawing on the results of section 3.1.4, we can write:

$$\frac{dN}{dz}(z) = \int_{4\pi} d\Omega \frac{dV}{dz d\Omega}(z) \int_0^\infty dM_{500} \frac{dn}{dM_{500}}(M_{500}, z) \hat{\chi}(M_{500}, z; l, b). \quad (3.29)$$

The form of 3.29 resembles the one of 3.9; there are, however, some important differences. First of all, the selection function is characterised in terms of the mass M_{500} , so the Tinker's mass function should be accordingly parametrised in terms of the same mass. Up to now we have always considered the UMF as

Este documento incorpora firma electrónica, y es copia auténtica de un documento electrónico archivado por la ULL según la Ley 39/2015.
Su autenticidad puede ser contrastada en la siguiente dirección <https://sede.ull.es/validacion/>

Identificador del documento: 973742	Código de verificación: Jfg6xBh0
Firmado por: DENIS TRAMONTE UNIVERSIDAD DE LA LAGUNA	Fecha: 30/06/2017 15:10:10
RAFAEL DELFIN BARRENA DELGADO UNIVERSIDAD DE LA LAGUNA	30/06/2017 15:21:31
JOSE ALBERTO RUBIÑO MARTIN UNIVERSIDAD DE LA LAGUNA	30/06/2017 15:34:17
ERNESTO PEREDA DE PABLO UNIVERSIDAD DE LA LAGUNA	06/07/2017 13:51:19

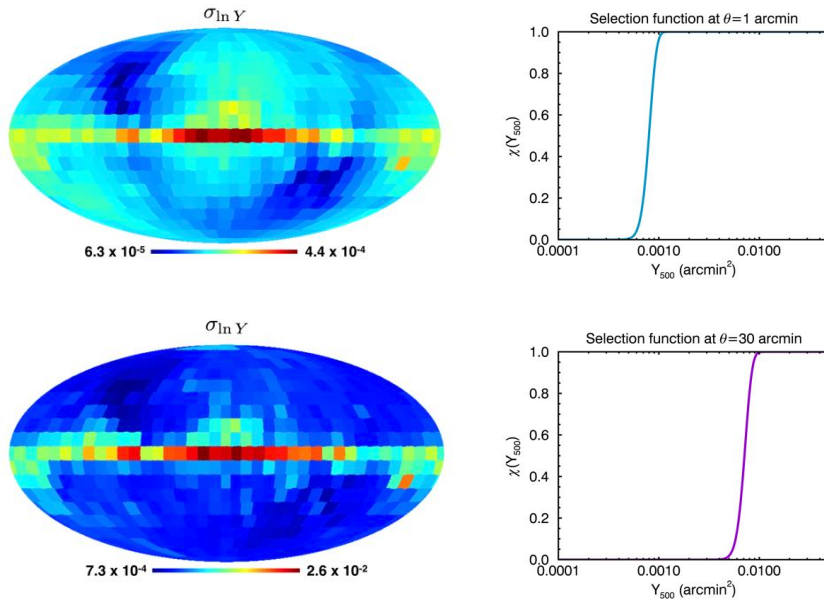


Figure 3.6: Noise maps (*left*) with corresponding completeness functions (*right*), for an angular size of $\theta_{500} = 1'$ (*top*) and $\theta_{500} = 30'$ (*bottom*).

a function of M_{200} , that is, halos defined with an overdensity $\Delta_m = 200$ with respect to the mean matter density. Now we are considering an overdensity $\Delta_c = 500$ defined with respect to the critical density. Notice that, for any redshift z , a mean overdensity can be re-written as a critical overdensity in this way:

$$\Delta_m \rho_m(z) = \Delta_m \Omega_m(z) \rho_c(z) \equiv \Delta_c \rho_c(z), \quad (3.30)$$

so that the relation between the two overdensities is $\Delta_m = \Delta_c / \Omega_m(z)$. In our case, then, we can compute the HMF as a function of M_{500} by considering the equivalent mean overdensity $\Delta_m = 500 / \Omega_m(z)$ and using the values tabulated in Tinker et al. (2008).

Another difference with respect to 3.9 is that the selection is not directly expressed in terms of the cluster mass and redshift. The function $\hat{\chi}(M_{500}, z; l, b)$

Este documento incorpora firma electrónica, y es copia auténtica de un documento electrónico archivado por la ULL según la Ley 39/2015.
Su autenticidad puede ser contrastada en la siguiente dirección <https://sede.ull.es/validacion/>

Identificador del documento: 973742

Código de verificación: Jfg6xBh0

Fecha: 30/06/2017 15:10:10

Firmado por: DENIS TRAMONTE UNIVERSIDAD DE LA LAGUNA	30/06/2017 15:21:31
RAFAEL DELFIN BARRENA DELGADO UNIVERSIDAD DE LA LAGUNA	30/06/2017 15:34:17
JOSE ALBERTO RUBIÑO MARTIN UNIVERSIDAD DE LA LAGUNA	06/07/2017 13:51:19
ERNESTO PEREDA DE PABLO UNIVERSIDAD DE LA LAGUNA	

is related to the selection 3.28 by:

$$\hat{\chi}(M_{500}, z; l, b) = \int dY_{500} \int d\theta_{500} P(M_{500}, z|Y_{500}, \theta_{500}) \chi(Y_{500}, \theta_{500}; l, b), \quad (3.31)$$

which is a variable change, and the function $P(M_{500}, z|Y_{500}, \theta_{500})$ is the probability for a cluster with observables (Y_{500}, θ_{500}) to have a mass M_{500} at a redshift z . Now, we know that for individual clusters the relation between the variables (M_{500}, z) and (Y_{500}, θ_{500}) is given by the scaling relations 3.25 and 3.27. If these relations had no scatter, then the probability distribution $P(M_{500}, z|Y_{500}, \theta_{500})$ would be just a delta function centred in the values of (M_{500}, z) that yield exactly the observables (Y_{500}, θ_{500}) according to the scaling relations. This is actually the case for the cluster angular size θ_{500} , given the equation that relates it to the cluster mass and redshift is analytical. But the equation for the flux is only an average scaling relation, and the probability distribution $P(M_{500}, z|Y_{500})$ widens due to the scatter of the flux around its mean value \bar{Y}_{500} , as expressed by 3.26.

We implemented the computation of the selection this way. For each pair of values (M_{500}, z) , we first computed the average quantities $(\bar{Y}_{500}, \bar{\theta}_{500})$. We used the value \bar{Y}_{500} as the mean for the distribution 3.26, and sampled a proper value of Y_{500} from that distribution: this is the value of the flux we assigned to the cluster. For the size, we simply took the mean value, $\theta_{500} = \bar{\theta}_{500}$. With this pair of values (Y_{500}, θ_{500}) we computed the completeness χ using 3.28. The resulting value is the one we assigned to the scaled selection as a function of mass, $\hat{\chi}(M_{500}, z)$.

One last difference between equations 3.29 and 3.9 is that the dependence of the selection function on the position in the sky prevents us from factorizing out the integral on the comoving volume element. The dependence of the selection function on the sky position comes from the determination of the noise by the MMF algorithm, and is due to foreground residuals. However, once the size of the cluster θ_{500} is fixed, then the noise map is also fixed, and it takes the same values inside each one of the 504 sky patches (figure 3.6). This means that the selection function also changes only when we change the sky patch we are considering. So, instead of letting the galactic coordinates (l, b) vary continuously, we can group the contribution coming from each single patch, and write:

$$\frac{dN}{dz}(z) = \sum_{i=1}^{504} \Omega_i \frac{dV}{dz d\Omega}(z) \int_0^\infty dM_{500} \frac{dn}{dM_{500}}(M_{500}, z) \hat{\chi}_i(M_{500}, z), \quad (3.32)$$

where Ω_i is the solid angle blocked by the i -th patch, and χ_i the value of the

Este documento incorpora firma electrónica, y es copia auténtica de un documento electrónico archivado por la ULL según la Ley 39/2015.
Su autenticidad puede ser contrastada en la siguiente dirección <https://sede.ull.es/validacion/>

Identificador del documento: 973742

Código de verificación: Jfg6xBh0

Fecha: 30/06/2017 15:10:10

Firmado por: DENIS TRAMONTE UNIVERSIDAD DE LA LAGUNA	30/06/2017 15:21:31
RAFAEL DELFIN BARRENA DELGADO UNIVERSIDAD DE LA LAGUNA	30/06/2017 15:34:17
JOSE ALBERTO RUBIÑO MARTIN UNIVERSIDAD DE LA LAGUNA	06/07/2017 13:51:19
ERNESTO PEREDA DE PABLO UNIVERSIDAD DE LA LAGUNA	

selection inside the patch. Equation 3.32 is the one we employed for predicting the yield of a *Planck* cluster survey in the forward problem; once a redshift bin set has been established, the final number count can be computed with 3.10.

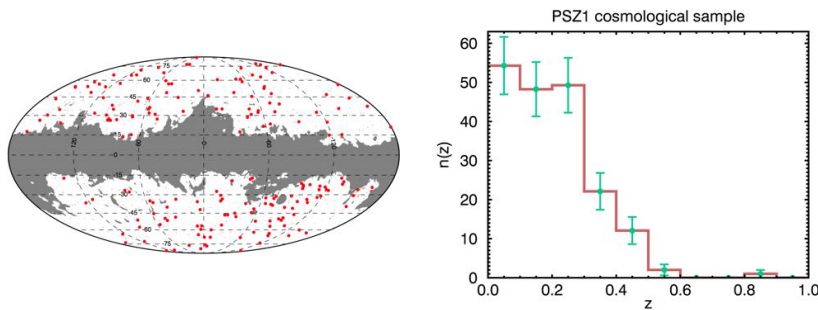


Figure 3.7: *Left:* spatial distribution of the PSZ1 cosmological sample clusters over the sky, together with the $\sim 35\%$ sky mask. *Right:* corresponding cluster number count binned in redshift (errors are Poissonian).

3.3.5 Parameter estimation with *Planck* data

In this section we show the results of parameter estimation using the data issued by the Planck Collaboration. More precisely, we want to reproduce the results in parameter estimation reported in Planck Collaboration et al. (2014g). In that work, a subsample of the PSZ1 cluster catalogue is employed for the cosmological analysis. This subsample is made of 189 confirmed clusters, all but one with determined redshift, and by with a high signal-to-noise ratio ($q > 7$). These clusters were retrieved with the MMF3 algorithm, in a region avoiding the noisier regions close to the initial Galactic mask; the mask used for this analysis, therefore, is larger and covers $\sim 35\%$ of the sky. We show this mask in figure 3.7, together with the cosmological sample number counts: clusters are binned in ten redshift bins of size $\Delta z = 0.1$. The cluster with no redshift information is incorporated in the distribution indirectly, rescaling it by the factor 189/188, which is equivalent to assigning to this cluster a redshift value sampled from the distribution determined by the others.

Parameters are estimated using a MCMC method. The likelihood is written with the Cash formalism defined in 3.14. The cosmological parameter engine is *CosmoMC*, which they modified in order to include the computation of the Cash likelihood. The parameters that are let free to vary, in this case, are

Este documento incorpora firma electrónica, y es copia auténtica de un documento electrónico archivado por la ULL según la Ley 39/2015.
Su autenticidad puede ser contrastada en la siguiente dirección <https://sede.ull.es/validacion/>

Identificador del documento: 973742	Código de verificación: Jfg6xBh0
Firmado por: DENIS TRAMONTE UNIVERSIDAD DE LA LAGUNA	Fecha: 30/06/2017 15:10:10
RAFAEL DELFIN BARRENA DELGADO UNIVERSIDAD DE LA LAGUNA	30/06/2017 15:21:31
JOSE ALBERTO RUBIÑO MARTIN UNIVERSIDAD DE LA LAGUNA	30/06/2017 15:34:17
ERNESTO PEREDA DE PABLO UNIVERSIDAD DE LA LAGUNA	06/07/2017 13:51:19

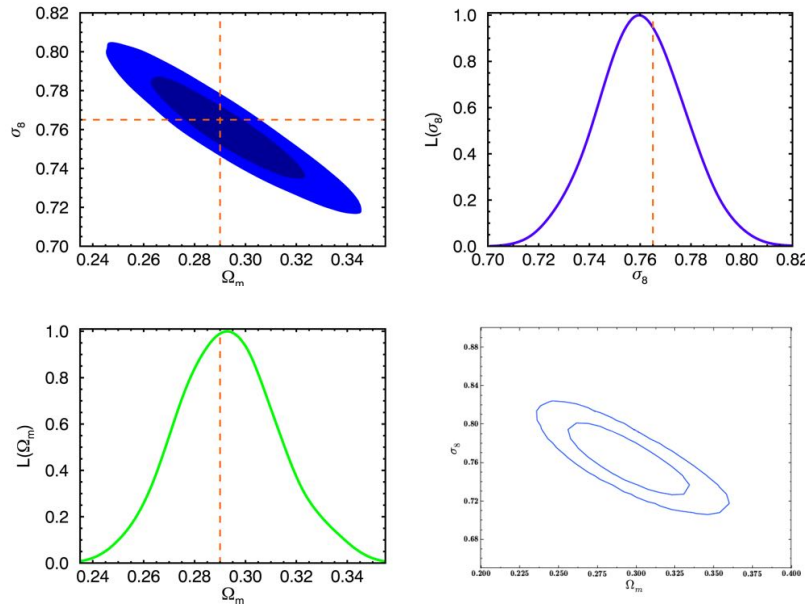


Figure 3.8: Results of cosmological parameter estimation based on the abundance of clusters observed by *Planck*, performed using a combination of cluster+BBN+BAO likelihoods with the mass bias parameter fixed to $(1 - b) = 0.8$. *Upper left*: reconstructed joint posterior probability distribution for the parameters Ω_m and σ_8 . *Upper right*: marginalised probability distribution for Ω_m . *Lower left*: marginalised probability distribution for σ_8 . *Lower right*: the Ω_m - σ_8 correlation plot adapted from [Planck Collaboration et al. \(2014g\)](#).

not only the matter density parameter Ω_m and the amplitude of perturbations σ_8 , but also the baryonic matter density parameter Ω_b , the Hubble parameter H_0 and the spectral index of scalar perturbation n_s . This required the use of additional likelihoods together with the cluster-based one. These were built over the Big Bang nucleosynthesis (BBN) constraints ([Steigman 2008](#)) and the baryon acoustic oscillation (BAO) data, using a combination of the likelihoods from [Hinshaw et al. \(2013\)](#) and [Planck Collaboration et al. \(2014f\)](#). Two cases were considered for the mass bias; in one case it was fixed to the value $(1 - b) = 0.8$, in the other it was let free to vary in the interval $[0.7, 1.0]$ with a flat prior distribution.

Este documento incorpora firma electrónica, y es copia auténtica de un documento electrónico archivado por la ULL según la Ley 39/2015.
Su autenticidad puede ser contrastada en la siguiente dirección <https://sede.ull.es/validacion/>

Identificador del documento: 973742

Código de verificación: Jfg6xBh0

Fecha: 30/06/2017 15:10:10

Firmado por: DENIS TRAMONTE
UNIVERSIDAD DE LA LAGUNA

RAFAEL DELFIN BARRENA DELGADO
UNIVERSIDAD DE LA LAGUNA

JOSE ALBERTO RUBIÑO MARTIN
UNIVERSIDAD DE LA LAGUNA

ERNESTO PEREDA DE PABLO
UNIVERSIDAD DE LA LAGUNA

30/06/2017 15:21:31

30/06/2017 15:34:17

06/07/2017 13:51:19

We performed the same analysis, using our modified version of `CosmoMC`. At each step in the cosmological parameter space, the cluster redshift distribution was determined using 3.32, and the likelihood was computed using 3.14 taking as a reference number count the cluster data plotted in figure 3.7. We launched 8 different chains for the case of a fixed mass bias, and other eight for the case of b with a flat prior. We then used the `getdist` facility to retrieve the posterior distributions for the cosmological parameters we are most interested in, namely Ω_m and σ_8 . Results are plotted in figure 3.8 for the case $b = 0.2$, and in figure 3.9 for the case of a free mass bias. We plot the reconstructed correlation plot between the two parameters, the marginalised one-dimensional probability distributions and the equivalent plot of the joint probability distribution extracted from (Planck Collaboration et al. 2014g).

$(1 - b) = 0.8$		
	Ω_m	σ_8
This work	0.293 ± 0.020	$0.760^{+0.018}_{-0.017}$
<i>Planck</i>	0.290 ± 0.020	0.765 ± 0.021
$(1 - b)$ in $[0.7, 1.0]$		
	Ω_m	σ_8
This work	$0.289^{+0.022}_{-0.020}$	0.750 ± 0.028
<i>Planck</i>	0.290 ± 0.020	0.750 ± 0.030

Table 3.4: Results of parameter estimation, comparing the values for Ω_m and σ_8 retrieved by our code and by the Planck Collaboration, both in the case of a fixed and a free mass bias.

Numerical results for the parameter estimates are reported in table 3.4. As it becomes clear evinced from the plots, our results are fully compatible with the ones reported by the Planck Collaboration. We also see the effect of the mass bias in the final results: letting b free to vary clearly widens the final contours of the posterior joint probability distribution in Ω_m and σ_8 , and results in larger errors in the final estimates, particularly for σ_8 . Contours actually widen in the direction perpendicular to the $\Omega_m - \sigma_8$ degeneracy line, because the bias b is degenerate with the total number of clusters. This can also be understood this way: for a given observed flux and the corresponding estimated SZ mass, a higher value of b implies a higher estimation of the true cluster mass; since the mass function decreases with mass, the predicted abundance of objects with such an SZ flux will be lower, and this requires a higher value of σ_8 to account for the observed number of clusters. The opposite is true if we decrease the value of b , in what case we derive a lower estimate of σ_8 . These results are the final proof of the consistency of our code for estimating cosmological

parameters on the basis of the cluster redshift number count.

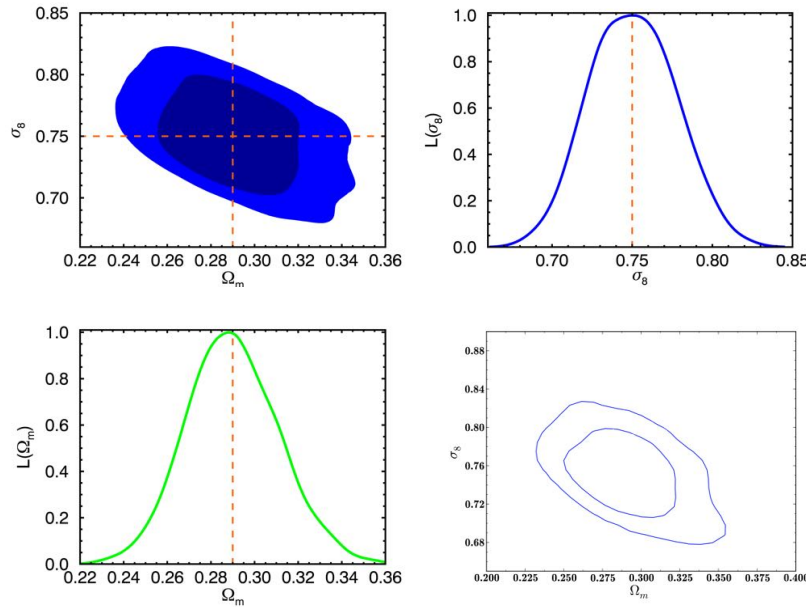


Figure 3.9: Same as in figure 3.8, but this time the mass bias parameter was let free to vary with a flat prior for $(1 - b)$ in $[0.7, 1.0]$.

3.4 Validation of cluster detections

As already stated, the PSZ1 *Planck* catalogue contains in total 1227 cluster detections. The construction of the catalogue passes through a process of validation: each cluster candidate is first searched for in existing cluster catalogues in order to confirm the detection. The search aims especially at finding counterparts of the objects in optical, IR or X-ray observations. Previously identified clusters are searched for within a distance of 5' from the centre of the SZ detection. The Planck Collaboration adopted different existing data at these wavelengths. In X-rays it made use of the ROSAT All Sky Survey (RASS, [Voges et al. 1999](#)). In IR, the all-sky survey with the Wide-field Infrared Survey

Este documento incorpora firma electrónica, y es copia auténtica de un documento electrónico archivado por la ULL según la Ley 39/2015.
Su autenticidad puede ser contrastada en la siguiente dirección <https://sede.ull.es/validacion/>

Identificador del documento: 973742

Código de verificación: Jfg6xBh0

Firmado por: DENIS TRAMONTE
UNIVERSIDAD DE LA LAGUNA

Fecha: 30/06/2017 15:10:10

RAFAEL DELFIN BARRENA DELGADO
UNIVERSIDAD DE LA LAGUNA

30/06/2017 15:21:31

JOSE ALBERTO RUBIÑO MARTIN
UNIVERSIDAD DE LA LAGUNA

30/06/2017 15:34:17

ERNESTO PEREDA DE PABLO
UNIVERSIDAD DE LA LAGUNA

06/07/2017 13:51:19

Explorer (WISE, Wright et al. 2010) was used. Finally, optical data were taken from the Sloan Digital Sky Survey (SDSS, York et al. 2000b). More details on the matching methods can be found in Planck Collaboration et al. (2014i).

Clusters for which a counterpart in existing catalogues could not be found required dedicated observations, in order to verify the detection and to determine its redshift. This *follow-up* is a big effort undertaken by the Planck Collaboration which started early in 2010 with the intermediate SZ catalogues, and is still ongoing. Again, observations in different wavelengths are considered. Clusters are observed in X-rays using the *XMM-Newton* facility (Planck Collaboration et al. 2011b). The analysis on the PSZ1 catalogue considered a subsample of targets, and it allowed to recognise false detections and the determination of redshifts. Independent SZ data were acquired with the Arcminute Microkelvin Imager (AMI, Planck Collaboration et al. 2013), while the *Spitzer* telescope was employed for IR observations. Optical observations from the ground have also given an important contribution to the follow-up programme. From the southern hemisphere, optical imaging was performed with the MPG/ESO 2.2-m telescope using the Wide-Field Imager (WFI), while the 3.5-m New Technology Telescope (NTT) was employed for spectroscopy (for details see Planck Collaboration et al. 2014i). From the northern hemisphere, imaging and spectroscopy were performed with the Russian Turkish Telescope (RTT), using the TFOSC instrument (Planck Collaboration et al. 2015c), and with the facilities in the ENO observatory (Planck Collaboration et al. 2016l).

The ENO observatory is located in the Canary Islands (Spain). The follow-up included imaging and spectroscopic observations. Imaging was performed using mainly three instruments: the Wide-Field Camera (WFC) on the 2.5 m Isaac Newton Telescope (INT); the auxiliary-port camera (ACAM) at the 4.2 m William Herschel Telescope (WHT); and CAMELOT, the optical camera at the 0.82m telescope (IAC80). Observations were taken using the Sloan filters g' , r' , i' , and in most cases also with the z' filter. The combination of the different filter images allowed the identification of the cluster member galaxies; in case the cluster was confirmed, the photometric redshift z_{phot} could be estimated. For spectroscopic observations, the follow-up employed the OSIRIS instrument in the 10.4m Gran Telescopio Canarias (GTC), the DOLORES instrument in the 3.6m Telescopio Nazionale Galileo (TNG), the ALFOSC instrument in the 2.5m Nordic Optical Telescope (NOT), and again the INT with the Intermediate Dispersion Spectrograph (IDS) and the WHT with ACAM⁵. The estimate of the photometric redshift determined the telescope to be employed for spectroscopy; all cases with $z_{\text{phot}} > 0.4$ were tackled with the GTC, the nearest

⁵Apart from being an optical camera, ACAM can be used for low-resolution spectroscopy.

Este documento incorpora firma electrónica, y es copia auténtica de un documento electrónico archivado por la ULL según la Ley 39/2015.
Su autenticidad puede ser contrastada en la siguiente dirección <https://sede.ull.es/validacion/>

Identificador del documento:	973742	Código de verificación:	Jfg6xBh0
Firmado por:	DENIS TRAMONTE UNIVERSIDAD DE LA LAGUNA	Fecha:	30/06/2017 15:10:10
	RAFAEL DELFIN BARRENA DELGADO UNIVERSIDAD DE LA LAGUNA		30/06/2017 15:21:31
	JOSE ALBERTO RUBIÑO MARTIN UNIVERSIDAD DE LA LAGUNA		30/06/2017 15:34:17
	ERNESTO PEREDA DE PABLO UNIVERSIDAD DE LA LAGUNA		06/07/2017 13:51:19

clusters ($z_{\text{phot}} < 0.3$) were observed with INT, WHT or NOT, and the intermediate redshift clusters, $0.3 \leq z_{\text{phot}} \leq 0.4$, were observed with the TNG. In the case of TNG observations the Multi Object Spectroscopy (MOS) technique was employed, which allows the acquisition of spectra for several objects with a single exposure; MOS was also used with the GTC for some clusters with confirmed redshift above 0.5. These data allowed the determination of the spectroscopic redshift. In Planck Collaboration et al. (2016l) the results of this analysis for 78 cluster candidates is reported: optical counterparts were confirmed for 73 detections, and for 53 of them the spectroscopic redshift was determined. We show in figure 3.10 an example of an optical cluster image and its corresponding MOS mask, designed over a TNG pre-imaging observation and used for the acquisition of spectra.

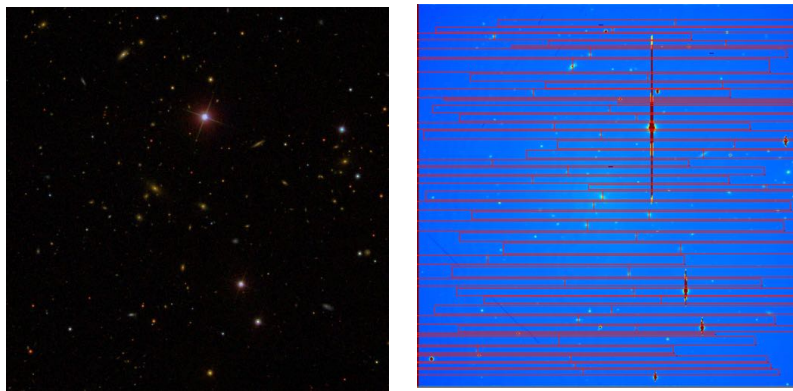


Figure 3.10: A cluster from the PSZ1 catalogue. *Left:* SDSS image of the field. *Right:* MOS mask prepared to select the member galaxies for spectroscopic observations with the TNG.

3.4.1 Results and future works

From the original publication of the PSZ1 cluster catalogue as part of the 2013 Planck Release, the follow-up program has provided new results in characterising the detections; this led to an updated version of the catalogue, which is described in Planck Collaboration et al. (2015a). To sum up, the updated PSZ1 catalogue contains 1227 detections coming from the first 15.5 months of operation of the *Planck* surveyor, among which 947 are confirmed clusters. Of these, 264 are new detections, 214 of which were verified thanks to the results of the follow-up observations. The remaining 280 detections are not confirmed

Este documento incorpora firma electrónica, y es copia auténtica de un documento electrónico archivado por la ULL según la Ley 39/2015.
Su autenticidad puede ser contrastada en la siguiente dirección <https://sede.ull.es/validacion/>

Identificador del documento: 973742

Código de verificación: Jfg6xBh0

Fecha: 30/06/2017 15:10:10

Firmado por: DENIS TRAMONTE
UNIVERSIDAD DE LA LAGUNA

RAFAEL DELFIN BARRENA DELGADO
UNIVERSIDAD DE LA LAGUNA

JOSE ALBERTO RUBIÑO MARTIN
UNIVERSIDAD DE LA LAGUNA

ERNESTO PEREDA DE PABLO
UNIVERSIDAD DE LA LAGUNA

30/06/2017 15:21:31

30/06/2017 15:34:17

06/07/2017 13:51:19

clusters. However, the Planck Collaboration further classified them into three classes of different reliability. Candidates of CLASS 1 are *Planck* SZ detections that have a high probability of being associated with real clusters; they result in high-quality SZ, RASS, and WISE detections. CLASS 2 candidates are reliable cluster candidates, which show good quality criteria in either of the aforementioned detections without fulfilling all of them at once. Finally, candidates of CLASS 3 are the least reliable, consisting in poor SZ detections, or good SZ detections for which there are no clear indications of either X-rays nor optical/IR counterparts. In the updated PSZ1 catalogue 24 detections are CLASS 1, 130 are CLASS 2 and 126 are CLASS 3.

Notice that the second *Planck* Catalogue of Sunyaev-Zel'dovich sources, the PSZ2, has undergone a similar validation process (Planck Collaboration et al. 2016k). The PSZ2 contains 1653 cluster candidates obtained analysing data from the full 29 months of the mission. They were validated using external X-ray, optical, IR and SZ data, both by matching with ancillary data and by dedicated follow-up observations with the facilities described above. The result is a total 1203 confirmed clusters of which 1094 have a redshift estimate. Out of the confirmed clusters, 716 are new detections. A comparison with the PSZ1 results showed good consistency, with 937 candidates in common with the previous catalogue. Detections that did not appear in the PSZ1 are mostly low-significant, and are expected to be confirmed as spurious.

What matters to our work is that the methodology for parameter estimation that we described in section 3.3 with the cosmological sample of clusters from the PSZ1 is a tool that can be applied to broader cluster catalogues. In particular, the analysis of the follow-up observations of PSZ1 candidates is almost complete, and once published it will provide redshifts for about 600 clusters, considerably lowering the signal-to-noise limit of the cosmology cluster sample. We showed in section 3.2.4 that the total number of clusters employed for this analysis dramatically affects the precision in the final parameter estimates. The use of an extended PSZ1 cosmological sample will thus result in a more accurate parameter estimation. Similarly, this methodology can be applied to the extended cosmological sample of the PSZ2 catalogue, once the validation process is over.

3.5 Conclusions

In this chapter we have considered the estimation of cosmological parameters using a cluster catalogue built from SZ observations by the *Planck* satellite. We first described how the output of a cluster survey can be predicted. This involved the implementation of a proper selection function to account for the

Este documento incorpora firma electrónica, y es copia auténtica de un documento electrónico archivado por la ULL según la Ley 39/2015.
Su autenticidad puede ser contrastada en la siguiente dirección <https://sede.ull.es/validacion/>

Identificador del documento:	973742	Código de verificación:	Jfg6xBh0
Firmado por:	DENIS TRAMONTE UNIVERSIDAD DE LA LAGUNA	Fecha:	30/06/2017 15:10:10
	RAFAEL DELFIN BARRENA DELGADO UNIVERSIDAD DE LA LAGUNA		30/06/2017 15:21:31
	JOSE ALBERTO RUBIÑO MARTIN UNIVERSIDAD DE LA LAGUNA		30/06/2017 15:34:17
	ERNESTO PEREDA DE PABLO UNIVERSIDAD DE LA LAGUNA		06/07/2017 13:51:19

instrumental limitation inherent to the survey. We then showed how the results of a cluster survey, more precisely the counts of clusters binned in redshift intervals, can be employed as a cosmological parameter estimator. This involved the use of statistical techniques; in a Bayesian approach, we showed how it is possible to reconstruct the posterior probability distribution on cosmological parameters using MCMC methods. In order to test our numerical implementation, we simulated a cluster survey corresponding to a fiducial cosmology, and we statistically determined the corresponding cosmological parameters; the consistency of the retrieved cosmology with the fiducial one confirmed that our estimator is unbiased. We also showed the importance of the survey selection function in determining the final yield of the survey in terms of the total number of clusters observed, which dramatically affects the precision with which the final cosmological parameters can be constrained.

We turned then our attention to *Planck* data, in particular to a high-quality subsample of the PSZ1 catalogue employed for cosmological analysis. We explained how the catalogue was built, and how it is possible to forecast the output of a *Planck*-like cluster survey. This involved two important steps. First of all, the implementation of the *Planck* selection function, which is dependent on the sky position and the retrieved cluster size θ_{500} and flux Y_{500} . Secondly, the fact that the selection is written in terms of these observables required the use of scaling relations to determine the corresponding mass M_{500} and redshift z of the cluster. These relations are based on a fit over X-rays cluster data, and as already mentioned are characterised both by a scatter and a bias; the latter is quantified by a parameter b , such that the mass related to the X-ray emission gets rescaled by $M_X = (1 - b)M_{500}$. We introduced in our MCMC engine the computation of the cluster abundance as would be observed by *Planck*, and compared it against real data fitting for the value of the cosmological parameters, with particular focus on the matter density parameter Ω_m and on the amplitude of density perturbation σ_8 . Following the analysis performed by the Planck Collaboration, we repeated this analysis in two cases: in the first one the bias parameter is fixed to the value $b = 0.2$; in the second one it is let free to vary with a flat prior in the interval $[0.0, 0.3]$. The resulting joint probability contours on the parameters (Ω_m, σ_8) , together with their marginalised one dimensional estimates, were in excellent agreement with the values published in [Planck Collaboration et al. \(2014g\)](#).

The analysis presented in [Planck Collaboration et al. \(2016i\)](#) extends this work using data coming from the whole duration of the *Planck* survey, collected in the second Planck SZ catalogue PSZ2. The final estimates are in agreement with the estimation performed on the PSZ1 subsample. As we will see in chapter 4, the resulting estimate in $\sigma_8 \simeq 0.76$ is consistent with other

Este documento incorpora firma electrónica, y es copia auténtica de un documento electrónico archivado por la ULL según la Ley 39/2015.
Su autenticidad puede ser contrastada en la siguiente dirección <https://sede.ull.es/validacion/>

Identificador del documento:	973742	Código de verificación:	Jfg6xBh0
Firmado por:	DENIS TRAMONTE UNIVERSIDAD DE LA LAGUNA	Fecha:	30/06/2017 15:10:10
	RAFAEL DELFIN BARRENA DELGADO UNIVERSIDAD DE LA LAGUNA		30/06/2017 15:21:31
	JOSE ALBERTO RUBIÑO MARTIN UNIVERSIDAD DE LA LAGUNA		30/06/2017 15:34:17
	ERNESTO PEREDA DE PABLO UNIVERSIDAD DE LA LAGUNA		06/07/2017 13:51:19

estimates based on the statistical properties of the SZ emission. This value is however quite lower than the one extracted from the analysis of CMB data, $\sigma_8 \simeq 0.83$ (Planck Collaboration et al. 2014f, 2016e). This indicates that there is a tension between the parameters inferred from the late Universe (galaxy clusters) and the early Universe (CMB). This tension is still an open issue and one of the main driving goals in cluster science.

Of course, possible solutions have been proposed. It is clear that the bias b entering the flux-mass scaling relation, at the basis of cluster analysis, can produce important systematic effects in the final parameter estimation: if b is underestimated, then the computed “true” cluster masses are also underestimated; this, in turn, means assigning the observed abundance of clusters to lower mass regions, to which corresponds a lower abundance predicted by the mass function and thus requiring a lower value of σ_8 . It is important, then, to achieve a determination of the bias as accurate as possible. In Planck Collaboration et al. (2016i) different possibilities for b are considered, based on estimates from weak lensing measurements. However, they find that the value of b required to match the prediction from cluster abundance with CMB results is $b \simeq 0.52$, which is quite higher than the values favoured by any available prior. Another possibility is that the systematics come from the parameterisation of the mass function itself. The Tinker et al. (2008) mass function, which is the base parametrisation employed for this analysis, is fitted over N-body dark-matter only simulations; the inclusion of baryonic feedback in simulations would clearly lead to a different fit, actually lowering the predicted abundance of halos (Nagai et al. 2007; Martizzi et al. 2014). This way, a higher value of σ_8 would be required in order to match the observed abundance of clusters. However, the effect does not seem enough to account for the gap with the CMB estimate.

Another possibility is that the observed tension is the first hint for a necessary extension to the base Λ CDM cosmological model. Indeed, while the cluster abundance provides a direct measurement of σ_8 , the same is not true for CMB anisotropies, in whose framework σ_8 is a derived parameter resulting from the linear extrapolation of the theory to the present, which is model dependent. Changing the model would alter the value of the CMB-based σ_8 estimate. The best motivated extension of the standard cosmology is perhaps the inclusion of a non-minimal sum of neutrino masses, $\sum m_\nu > 0.06$ eV. Neutrinos, indeed, damp the growth of perturbations by free-streaming; increasing their total mass would enhance this effect, thus leading to a final lower value of σ_8 ; this goes in the direction of reconciling the tension with the cluster-based estimate. In Planck Collaboration et al. (2016i) this type of analysis is performed, considering the CMB likelihood in different combinations with other

Este documento incorpora firma electrónica, y es copia auténtica de un documento electrónico archivado por la ULL según la Ley 39/2015.
Su autenticidad puede ser contrastada en la siguiente dirección <https://sede.ull.es/validacion/>

Identificador del documento:	973742	Código de verificación:	Jfg6xBh0
Firmado por:	DENIS TRAMONTE UNIVERSIDAD DE LA LAGUNA	Fecha:	30/06/2017 15:10:10
	RAFAEL DELFIN BARRENA DELGADO UNIVERSIDAD DE LA LAGUNA		30/06/2017 15:21:31
	JOSE ALBERTO RUBIÑO MARTIN UNIVERSIDAD DE LA LAGUNA		30/06/2017 15:34:17
	ERNESTO PEREDA DE PABLO UNIVERSIDAD DE LA LAGUNA		06/07/2017 13:51:19

priors. The analysis of the resulting posterior distributions on the parameters shows that lower values of σ_8 are indeed allowed, but this increases the tension with other parameters; for instance, it lowers the value of the CMB-constrained Hubble parameter, which is already rather low compared to direct estimates based on the observations of Type Ia supernovae⁶ (Planck Collaboration et al. 2014f; Riess et al. 2011). Besides, no definite estimate on the total neutrino mass is obtained by combining the CMB and the cluster likelihoods, which only provides upper limits; a reason for this is the lack of a strong prior on the mass bias b , whose estimates are affected by a 10 – 15% error. In order to achieve a definite estimate of the total neutrino mass the mass bias should be known with a precision $\sim 1\%$. The determination of b to these levels of accuracy can be tackled with incoming lensing surveys of galaxies, in space missions like *Euclid* (Laureijs et al. 2011), or in ground-based observational programmes like the Large Synoptic Survey Telescope (LSST, Ivezić et al. 2008).

To sum up, it is then clear the importance of the observational efforts aimed at detecting and characterising galaxy clusters. This is a necessary step towards a better characterisation of the scaling relations used to convert the cluster observables into its mass, a computation that is currently the most important source of systematics in cosmological analysis. Not only will this effort improve the accuracy on the existing estimates of cosmological parameters, but it will also provide a better understanding of the observed tension between the results from study of the low and high redshift Universe. In the short term, the results from the optical follow-up of cluster candidates, with the purpose of verifying the detections and assess their redshift, can increase the size of the available cluster catalogues. This will enhance the scientific impact of the original X-ray or SZ survey missions. In our case, as soon as the redshift estimates from the PSZ1 follow-up are available, we can use the methodology we thoroughly tested throughout this chapter, and provide more accurate estimates of the parameters Ω_m and σ_8 . Besides, following the methodology described in Planck Collaboration et al. (2016i), the larger size of the clusters sample would allow the analysis of a two-dimensional likelihood distribution, as a function of both the redshift and the catalogue signal-to-noise ratio q ; the results presented in this chapter could then be recovered by marginalising over the signal-to-noise for $q > 7$.

⁶The *Planck* estimate of H_0 is also low compared to the WMAP estimate (Hinshaw et al. 2013); hence, the underestimation of the Hubble parameter seems not to be a common result from CMB analysis. The fact that *Planck* predicts such a low value may be ascribed to the inclusion of the high- ℓ data, that are not covered by WMAP.

Firmado por: DENIS TRAMONTE UNIVERSIDAD DE LA LAGUNA	30/06/2017 15:21:31
RAFAEL DELFIN BARRENA DELGADO UNIVERSIDAD DE LA LAGUNA	30/06/2017 15:34:17
JOSE ALBERTO RUBIÑO MARTIN UNIVERSIDAD DE LA LAGUNA	06/07/2017 13:51:19
ERNESTO PEREDA DE PABLO UNIVERSIDAD DE LA LAGUNA	

Este documento incorpora firma electrónica, y es copia auténtica de un documento electrónico archivado por la ULL según la Ley 39/2015.
Su autenticidad puede ser contrastada en la siguiente dirección <https://sede.ull.es/validacion/>

Identificador del documento: 973742

Código de verificación: Jfg6xBh0

Firmado por: DENIS TRAMONTE UNIVERSIDAD DE LA LAGUNA	Fecha: 30/06/2017 15:10:10
RAFAEL DELFIN BARRENA DELGADO UNIVERSIDAD DE LA LAGUNA	30/06/2017 15:21:31
JOSE ALBERTO RUBIÑO MARTIN UNIVERSIDAD DE LA LAGUNA	30/06/2017 15:34:17
ERNESTO PEREDA DE PABLO UNIVERSIDAD DE LA LAGUNA	06/07/2017 13:51:19

4

Cosmology with the Sunyaev-Zel'dovich effect

Apart from being a specific tool used for identifying individual clusters of galaxies, the Sunyaev-Zel'dovich effect can be studied also as a diffuse foreground, and all-sky maps showing the intensity of tSZ can be built. The statistics of these maps can be exploited as a valuable tool in cosmology; in particular, we will concentrate on the tSZ one dimensional probability distribution function (PDF), which happens to be particularly sensitive to the value of the parameter σ_8 . We describe in this chapter a way to theoretically predict the tSZ PDF from a given cosmological model; this will require the use of a proper parametrisation for the pressure profile of galaxy clusters. We will check the consistency of this formalism by comparing its prediction with the distribution obtained from a set of simulated tSZ maps. Finally, we will consider real data from the *Planck* mission and use the derived PDF as a tool to provide an estimate of σ_8 . The results of this analysis are published as part of the Planck 2015 papers release in [Planck Collaboration et al. \(2016h\)](#). In the end, we will also use the tSZ PDF as a forecast tool to assess the precision in the estimate of this parameter by the future COrE mission; this analysis is published in [Melin et al. \(2017\)](#).

4.1 The y map

A map of the thermal Sunyaev-Zel'dovich effect is more conveniently plotted in terms of the corresponding Comptonisation parameter y , which allows the use of a unique reference map independent of frequency. After reminding the

definition and meaning of the Compton parameter, we discuss in the following the way y maps are generated, and take *Planck* data as an example.

4.1.1 The Compton parameter

We already introduced the thermal Sunyaev-Zel'dovich effect in chapter 3. We remind that it is produced by the inverse Compton scattering of CMB photons off high-energy electrons, and that it has a typical spectral signature, resulting in a decrease of the CMB intensity spectrum at frequencies lower than 218 GHz and in an increase at higher frequencies. The fractional CMB temperature shift is quantified by (Carlstrom et al. 2002):

$$\frac{\Delta T}{T_{\text{CMB}}}(\nu) = f(x) y, \quad (4.1)$$

where $\Delta T = T - T_{\text{CMB}}$ and $T_{\text{CMB}} = 2.725 K$. In this equation $g(x)$ is a function that captures the frequency modulations,

$$f(x) = \left[x \coth\left(\frac{x}{2}\right) - 4 \right] [1 + \delta_{\text{SZ}}(x, T_e)], \quad (4.2)$$

where the dimensionless frequency is defined as $x \equiv h\nu/(k_B T_{\text{CMB}})$, and the second factor takes into account possible relativistic corrections depending on the gas electron temperature. The other factor in equation 4.1 is the *Compton parameter* y , which is independent of frequency and is defined as the electron pressure integrated along the line of sight:

$$y = \frac{\sigma_T}{m_e c^2} \int_{\text{LOS}} dl P_e(l) \quad (4.3)$$

which is the same as equation 1.50, but this time we made the dependence on the electron pressure explicit. In the following we are going to focus on the Compton parameter and the information that can be extracted from maps of this parameter.

4.1.2 *Planck* data

Planck primary output consists of time-ordered data (TOD) from its nine frequency channels, spanning the range from 30 GHz to 857 GHz; for each channel, the TOD can be translated into a map. The full pipeline employed for producing individual frequency maps is thoroughly described in Planck Collaboration et al. (2016b), Planck Collaboration et al. (2016c) and Planck Collaboration et al. (2016d). The wide frequency coverage of *Planck* maps allows the identification of the Sunyaev-Zel'dovich effect and the extraction of the corresponding

Este documento incorpora firma electrónica, y es copia auténtica de un documento electrónico archivado por la ULL según la Ley 39/2015.
Su autenticidad puede ser contrastada en la siguiente dirección <https://sede.ull.es/validacion/>

Identificador del documento: 973742

Código de verificación: Jfg6xBh0

Fecha: 30/06/2017 15:10:10

Firmado por: DENIS TRAMONTE
UNIVERSIDAD DE LA LAGUNA

RAFAEL DELFIN BARRENA DELGADO
UNIVERSIDAD DE LA LAGUNA

JOSE ALBERTO RUBIÑO MARTIN
UNIVERSIDAD DE LA LAGUNA

ERNESTO PEREDA DE PABLO
UNIVERSIDAD DE LA LAGUNA

30/06/2017 15:21:31

30/06/2017 15:34:17

06/07/2017 13:51:19

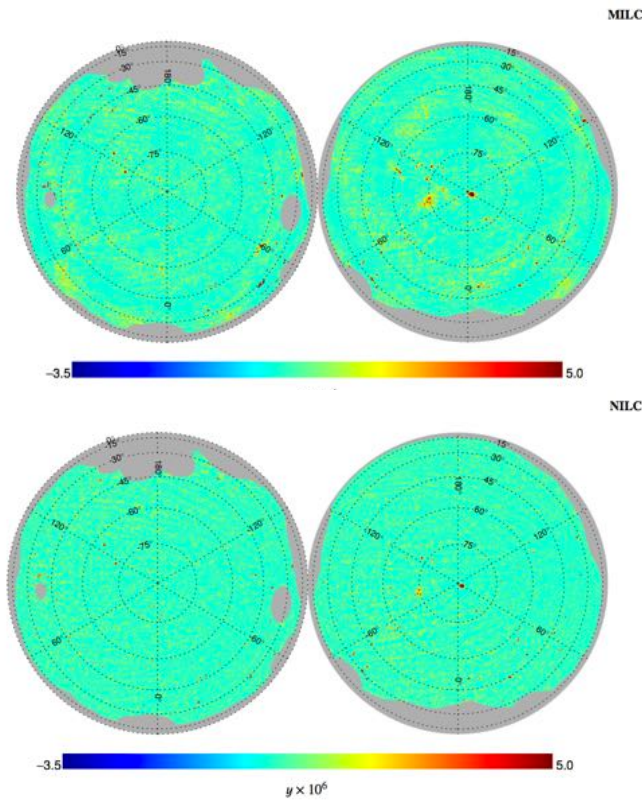


Figure 4.1: Reconstructed Compton-parameter maps from *Planck* data, using the MILCA and NILC algorithms. Maps are plotted in orthographic projection, showing the southern Galactic hemisphere on the left and the northern Galactic hemisphere on the right. Figure taken from [Planck Collaboration et al. \(2016h\)](#).

Compton parameter. The Planck Collaboration employed different algorithms to perform component-separation analyses, and to extract from the individual frequency maps the specific maps for the CMB and various foreground emissions ([Planck Collaboration et al. 2016a, 2014d](#)). These algorithms employed specific methods for separating emission mechanisms entering the individual frequency maps, relying on their different signature in terms of spectral distribution or scale dependence.

Este documento incorpora firma electrónica, y es copia auténtica de un documento electrónico archivado por la ULL según la Ley 39/2015.
Su autenticidad puede ser contrastada en la siguiente dirección <https://sede.ull.es/validacion/>

Identificador del documento: 973742

Código de verificación: Jfg6xBh0

Fecha: 30/06/2017 15:10:10

Firmado por: DENIS TRAMONTE
UNIVERSIDAD DE LA LAGUNA

RAFAEL DELFIN BARRENA DELGADO
UNIVERSIDAD DE LA LAGUNA

JOSE ALBERTO RUBIÑO MARTIN
UNIVERSIDAD DE LA LAGUNA

ERNESTO PEREDA DE PABLO
UNIVERSIDAD DE LA LAGUNA

30/06/2017 15:21:31

30/06/2017 15:34:17

06/07/2017 13:51:19

However, as explained in [Planck Collaboration et al. \(2014h\)](#) and in [Planck Collaboration et al. \(2016h\)](#), these methods are not suitable for reconstructing a map of the tSZ effect, since it is subdominant with respect to the CMB and other foregrounds. Hence, in order to generate a full-sky Compton parameter map, two specifically tailored component separation algorithm were employed, MILCA and NILC, both based on the Internal Linear Combination (ILC) approach, that searches for the optimal linear combination of individual frequency maps in order to preserve the SZ signal with minimum variance while cancelling the other contributions.

The NILC (Needlet Independent Linear Combination) method ([Remazeilles et al. 2011](#)) is a multicomponent extension of the original algorithm developed as a CMB extractor; in this version the covariances are computed independently over a needlet decomposition. The joint dependence on position and scale is exploited to remove CMB contamination and to preserve the tSZ effect. The MILCA (Modified Internal Linear Combination Algorithm) method ([Hurier et al. 2013](#)) imposes preservation of the tSZ effect signal and the removal of the CMB contamination based on their spectral dependence, also minimizing residuals from other foregrounds and from noise. A representation of the final Compton parameter maps obtained using both MILCA and NILC algorithms is shown in figure 4.1.

4.2 The SZ 1D PDF

Let $p(y)$ be a probability density function for the Compton parameter in such a way that the quantity $p(y)dy$ is the probability for the Compton parameter to take value in an infinitesimal interval $[y, y+dy]$. We consider the integrated quantity:

$$P(y) = \int_{y-\Delta y/2}^{y+\Delta y/2} dy' p(y') \quad (4.4)$$

which represents the probability for the Compton parameter to take values in a finite bin of size Δy centered in y . The function $P(y)$ is usually referred to as the SZ one-dimensional probability distribution function (SZ-PDF). The following section deals with the extraction of the $P(y)$ from *Planck* y -maps and its importance as a cosmological tools.

4.2.1 The $P(y)$ from *Planck* data

Building the $P(y)$ from a Compton parameter map means making a histogram of the values of y entering the map. Maps are pixelised in a total number of

Este documento incorpora firma electrónica, y es copia auténtica de un documento electrónico archivado por la ULL según la Ley 39/2015.
Su autenticidad puede ser contrastada en la siguiente dirección <https://sede.ull.es/validacion/>

Identificador del documento: 973742	Código de verificación: Jfg6xBh0	Fecha: 30/06/2017 15:10:10
Firmado por: DENIS TRAMONTE UNIVERSIDAD DE LA LAGUNA		
RAFAEL DELFIN BARRENA DELGADO UNIVERSIDAD DE LA LAGUNA		30/06/2017 15:21:31
JOSE ALBERTO RUBIÑO MARTIN UNIVERSIDAD DE LA LAGUNA		30/06/2017 15:34:17
ERNESTO PEREDA DE PABLO UNIVERSIDAD DE LA LAGUNA		06/07/2017 13:51:19

N_p pixels; once a set of N y -bins has been chosen, $\{y_i\}_{i=1,\dots,N}$, the $P(y)$ can be obtained by binning the values of the map pixel values over the bin set; the resulting histogram must be divided by N_p to get rid of the dependence on the number of pixels. The resulting $P(y)$ still depends on the number of bins over which it is computed; requiring the integral of the $P(y)$ over the considered range to yield unity is enough to make it independent of the number of y bins.

We show in figure 4.2 the $P(y)$ provided by the Planck collaboration, corresponding to the maps shown in figure 4.1 for the MILCA and NILC reconstruction algorithms; we normalized the PDFs integral to unity, which will be useful for the analyses in section 4.5.

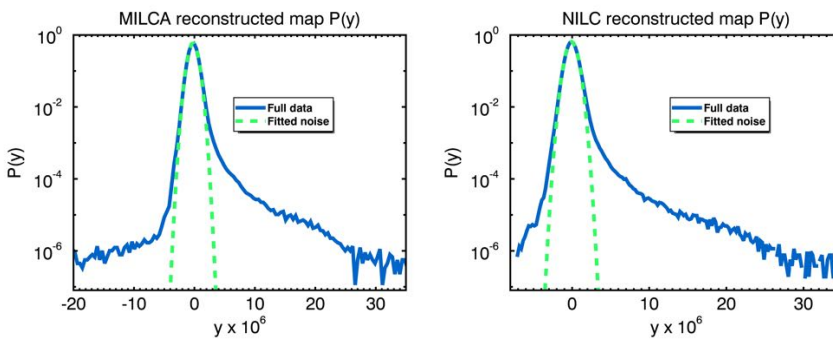


Figure 4.2: SZ 1D-PDF ($P(y)$) corresponding to the two reconstructed y maps shown in figure 4.1, normalized to unit integral. We also show a Gaussian fit to the central noise contribution, as it is defined in section 4.2.2. The galaxy cluster contribution is clearly visible as the high- y tail.

4.2.2 Physical meaning of the $P(y)$

The y -map reconstruction methods described in section 4.1.2 are effective in enhancing the SZ signal over the foregrounds, but they do not completely remove other contaminations. As a result, apart from the signal from galaxy clusters, the $P(y)$ will show also the contribution from the residuals of other galactic and extragalactic emissions. The way different emissions contribute to the PDF is determined by their frequency dependence, and by the particular weights assigned to *Planck* individual frequency maps in the linear combination that maximises the SZ signal. As expected, the cluster emission produces the positive $P(y)$ tail; the negative tail, instead, is produced by the emission from radio sources; finally, the central peak receives the contributions from other

astrophysical signal (CMB, CIB, diffuse galactic emission) and instrumental noise.

Intuitively, the shape of the PDF can be understood by taking as a reference equation 4.1 (see also the detailed work in Rubiño-Martín & Sunyaev 2003). The sign of the ΔT produced by galaxy clusters is the same as the sign of the $f(x)$ function (by definition of the Compton parameter), so y is always positive and this produces the high- y tail in the $P(y)$. The contribution from radio sources, instead, is higher at lower frequencies, where we expect to observe possible residuals from this emission. At low frequencies the function $f(x)$ is negative, so the contribution to y from radio sources will be also negative, producing the low- y tail in the PDF. The ΔT contribution from primordial CMB anisotropies is independent on frequency and Gaussian distributed around zero, and so will be the corresponding y . The CIB and diffuse galactic emission, to a first approximation, also produce symmetric contributions to the PDF around $y = 0$, as is commented in Planck Collaboration et al. (2014h). In the same reference it is shown that the contribution from instrumental noise is also limited to this y region, which can be understood given that the ΔT produced by the noise can be negative or positive regardless of the particular frequency and the corresponding sign of the function $f(x)$. However, we remind that this is only an intuitive explanation; as already stated, the final shape of the $P(y)$ is determined by the effective linear combination of individual frequency maps employed by the MILCA and NILC algorithms to reconstruct the Compton parameter map.

To sum up, there are different sources contributing to the observed $P(y)$, each with its proper distribution: galaxy clusters, $P_{\text{SZ}}(y)$; CMB residuals, $P_{\text{CMB}}(y)$; radio point sources residuals, $P_{\text{PS}}(y)$; the foreground residuals from CIB and galactic diffuse emission, $P_{\text{fgr}}(y)$; and a contribution from instrumental noise $P_{\text{N}}(y)$. The total $P(y)$ can be obtained via a convolution of all different contributions:

$$P(y) = P_{\text{SZ}}(y) \otimes P_{\text{PS}}(y) \otimes P_{\text{CMB}}(y) \otimes P_{\text{fgr}}(y) \otimes P_{\text{N}}(y). \quad (4.5)$$

In the following we will not consider the negative tail, so we can drop the contribution from radio point sources, which becomes important only at negative values of y far from the zero. The CMB, CIB and diffuse galactic residuals can actually be absorbed in a re-definition of the noise PDF, which from now on includes both instrumental and astrophysical contributions. We end up with a simpler expression for the $P(y)$ which can be written, with a slight abuse of notation, as:

$$P(y) \simeq P_{\text{SZ}}(y) \otimes P_{\text{N}}(y). \quad (4.6)$$

Este documento incorpora firma electrónica, y es copia auténtica de un documento electrónico archivado por la ULL según la Ley 39/2015.
Su autenticidad puede ser contrastada en la siguiente dirección <https://sede.ull.es/validacion/>

Identificador del documento: 973742	Código de verificación: Jfg6xBh0	Fecha: 30/06/2017 15:10:10
Firmado por: DENIS TRAMONTE UNIVERSIDAD DE LA LAGUNA		
RAFAEL DELFIN BARRENA DELGADO UNIVERSIDAD DE LA LAGUNA		30/06/2017 15:21:31
JOSE ALBERTO RUBIÑO MARTIN UNIVERSIDAD DE LA LAGUNA		30/06/2017 15:34:17
ERNESTO PEREDA DE PABLO UNIVERSIDAD DE LA LAGUNA		06/07/2017 13:51:19

In order to make theoretical prediction of the PDF, we must be able to model the cluster contribution and the noise component. In figure 4.2 we show a gaussian fit for the noise contribution $P_N(y)$; a way for computing the cluster component is discussed in section 4.3.

4.2.3 The $P(y)$ as a cosmological tool

The importance in the theoretical modeling of the $P(y)$ is given by the fact that the SZ component, being dominated by the contribution from galaxy clusters, is sensitive to their abundance, and ultimately to the cosmological parameter σ_8 (see figure 4.3). The relation between statistics of the tSZ effect and cosmological parameters, and their use as cosmological probes, has been widely discussed in the literature: Komatsu & Seljak (2002), Hill & Sherwin (2013), Hill & Pajer (2013) and Bhattacharya et al. (2012). The work in Hill et al. (2014), in particular, adopts specifically the tSZ PDF for cosmological parameter estimation.

Note that the use of the $P(y)$ for estimating σ_8 is complementary to the analysis based on cluster number counts that we described in chapter 3. The

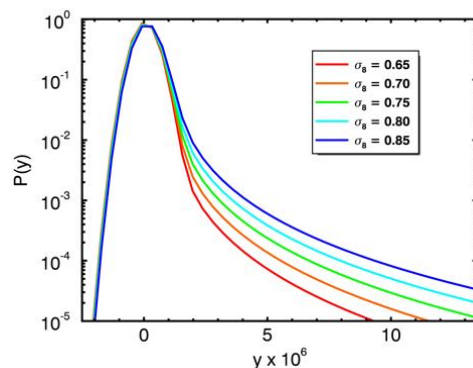


Figure 4.3: Numerical $P(y)$ distributions computed using the formalism described in section 4.3 and the cosmological parameters in table 4.1, but using different values for the parameter σ_8 . The plot clearly shows the strong dependence of the tSZ PDF on this parameter, which makes it an effective cosmological probe.

advantage of this method compared to cluster counts is that it does not require the characterisation of a survey selection function, and is as such free from bias that can arise from a bad modeling of a catalogue completeness or purity.

In this case, all sources enter the statistics, the largest and closer clusters making up the positive tail in the $P(y)$ distribution, and the farthest and faintest ones contributing to the noise around $y = 0$. The downside of this approach is that the cluster pressure profile, which is a necessary element for computing its SZ emission, should be thoroughly understood, for clusters of different masses and redshifts, in order to minimize the systematics that may arise from a bad modelling of the intracluster gas physics. However, the use of a properly-characterised average pressure profile model is quite safe in this context, because it is applied to compute the averaged signal coming from many clusters, and is not intended to reproduce the actual profile of individual objects whose physical conditions may be anomalous, e.g. strong departures from hydrostatic equilibrium (Shaw et al. 2010; Battaglia et al. 2012). In the same way, in this case there is no need to determine the mass of each individual cluster, even though, as we shall see in the following, the mass bias b will still be entering the pressure profile in order to adapt it to the observed scaling relations.

In the following we present the formalism we employed for computing the $P(y)$ contribution from galaxy clusters, and the way we included the noise component. This theoretically-determined distribution, which depends on the assumed underlying cosmology, can be used as a tool to fit the parameter σ_8 against data.

4.3 Computing the PDF

The theoretical prediction of the $P(y)$ is a process that we can divide into different steps. We first have to write a proper parametrisation of the ICM radial pressure profile. This has to be translated into the y signal coming from the cluster along the line of sight, as a function of the angular distance from its center. Then, the contributions from different clusters have to be put together, to yield the total signal entering an individual y bin. To this simple scheme, one has to take into account that the tSZ effect is observed through an instrument with a proper noise and a characteristic beam size, which affect the measured signal. We detail each step in the following.

Ω_m	Ω_b	Ω_Λ	h	n_s	σ_8	b
0.308	4.84×10^{-2}	0.692	0.678	0.968	0.77	0.2

Table 4.1: Fiducial cosmology and mass bias used throughout this chapter.

Throughout this chapter (with the exception of section 4.6) we are going

Este documento incorpora firma electrónica, y es copia auténtica de un documento electrónico archivado por la ULL según la Ley 39/2015.
Su autenticidad puede ser contrastada en la siguiente dirección <https://sede.ull.es/validacion/>

Identificador del documento: 973742	Código de verificación: Jfg6xBh0	Fecha: 30/06/2017 15:10:10
Firmado por: DENIS TRAMONTE UNIVERSIDAD DE LA LAGUNA		
RAFAEL DELFIN BARRENA DELGADO UNIVERSIDAD DE LA LAGUNA		30/06/2017 15:21:31
JOSE ALBERTO RUBIÑO MARTIN UNIVERSIDAD DE LA LAGUNA		30/06/2017 15:34:17
ERNESTO PEREDA DE PABLO UNIVERSIDAD DE LA LAGUNA		06/07/2017 13:51:19

to employ the reference cosmological parameters detailed in table 4.1, and a fixed mass bias $b = 0.2$. All cosmological parameters but σ_8 were taken from the CMB results in Planck Collaboration et al. (2016e); for σ_8 we employed a value closer to the results from the tSZ statistics in Planck Collaboration et al. (2014h).

4.3.1 Cluster pressure profile

We employ the pressure profile for galaxy clusters discussed in Arnaud et al. (2010). They provide a phenomenological pressure profile based on a generalisation of the NFW profile, introducing explicit dependence on cluster mass and redshift. The pressure profile for a cluster of mass M_{500} and redshift z is first written as:

$$P(r, M_{500}, z) = P_{500}(M_{500}, z) p(x, M_{500}), \quad (4.7)$$

where $x = r/R_{500}$. This relation is based on a self-similar model and is normalised to the characteristic pressure P_{500} (Nagai et al. 2007):

$$P_{500} = 1.65 \times 10^{-3} E^{8/3}(z) \left[\frac{M_{500}}{3 \times 10^{14} h_{70}^{-1} M_\odot} \right]^{2/3} h_{70}^2 \text{ keVcm}^{-3}, \quad (4.8)$$

which is basically the pressure at radius R_{500} required to prevent the gravitational collapse of a cluster of mass M_{500} at redshift z . The dependence of the standard pressure profile with mass is further parametrized as:

$$p(x, M_{500}) = \left[\frac{M_{500}}{3 \times 10^{14} h_{70}^{-1} M_\odot} \right]^{\alpha_p + \alpha'_p(x)} p(x) \quad (4.9)$$

with $\alpha_p = 0.12$ and

$$\alpha'_p(x) = 0.10 - (\alpha_p + 0.10) \frac{(x/0.5)^3}{1 + (x/0.5)^3}. \quad (4.10)$$

Equation 4.9 describes a break in the self-similarity of the pressure profile. However, the term α'_p can usually be neglected and the dependence on mass becomes a variation in the profile normalisation. The remaining function $p(x)$ is the universal pressure profile defined in Nagai et al. (2007), obtained as a generalisation of a NWF profile:

$$p(x) = \frac{P_0}{(c_{500}x)^\gamma [1 + (c_{500}x)^\alpha]^{(\beta-\alpha)/\alpha}}. \quad (4.11)$$

Este documento incorpora firma electrónica, y es copia auténtica de un documento electrónico archivado por la ULL según la Ley 39/2015.
Su autenticidad puede ser contrastada en la siguiente dirección <https://sede.ull.es/validacion/>

Identificador del documento: 973742

Código de verificación: Jfg6xBh0

Fecha: 30/06/2017 15:10:10

Firmado por: DENIS TRAMONTE
UNIVERSIDAD DE LA LAGUNA

RAFAEL DELFIN BARRENA DELGADO
UNIVERSIDAD DE LA LAGUNA

JOSE ALBERTO RUBIÑO MARTIN
UNIVERSIDAD DE LA LAGUNA

ERNESTO PEREDA DE PABLO
UNIVERSIDAD DE LA LAGUNA

30/06/2017 15:21:31

30/06/2017 15:34:17

06/07/2017 13:51:19

Parameters in equation 4.11 are determined by fit to observations and simulations, yielding $P_0 = 8.403 h_{70}^{-3/2}$, $c_{500} = 1.177$, $\gamma = 0.3081$, $\alpha = 1.0510$, $\beta = 5.4905$.

Equations from 4.7 to 4.11 are all we need to determine the pressure profile for a cluster of given mass and redshift. However, this assumes we know *a priori* the cluster mass. We know from the previous chapter that the determination of the mass of a galaxy cluster is one of the main sources of systematics in cluster analysis. In order to take this into account, we make use of the fact that the total SZ signal integrated over the cluster extent is proportional to the integrated Compton parameter; since this is in turn the pressure profile integrated along the line of sight, the total SZ signal is proportional to the volume integral of the pressure profile:

$$Y_{\text{SZ}} = \frac{1}{D_A^2 m_e c^2} \int P(\mathbf{r}) dV. \quad (4.12)$$

By explicit integration of the pressure profile defined above, we find:

$$Y_{\text{SZ}} \propto D_A^{-2}(z) E^{2/3}(z) M_{500}^{\alpha_p + 5/3}, \quad (4.13)$$

where we made use of the relation $M_{500} = 4/3\pi\rho_{c,0}R_{500}^3$. In 4.13 we focused on the dependence of the integrated flux on relevant physical quantities, rather than on numerical factors. The *Planck* flux-mass scaling relation reported in [Planck Collaboration et al. \(2014g\)](#) yields:

$$Y_{\text{SZ}} \propto D_A^{-2}(z) E^\beta(z) [(1+b)M_{500}]^\alpha, \quad (4.14)$$

where $\alpha \simeq 1.79$. By comparing 4.13 and 4.14 we see that by integrating the pressure profile we recover the same dependencies of the flux on the angular diameter distance, on the redshift evolution factor ($\beta \simeq 0.66$) and on mass ($\alpha_p + 5/3 \simeq 1.79$). However, the systematics on the mass quantified by the bias b should be explicitly introduced in the relation 4.13. In order for the integrated flux to depend on mass and bias as in equation 4.14, the pressure profile should be modified by rescaling the input mass by $(1+b)$ and also by re-normalizing the profile with a global $(1+b)$ factor. In conclusion, the radial pressure profile that we use for a cluster of mass M_{500} at redshift z is:

$$\begin{aligned} P(r, M_{500}, z) &= 1.65 \times 10^{-3} (1+b) E^{8/3}(z) \\ &\times \left[\frac{(1+b)M_{500}}{3 \times 10^{14} h_{70}^{-1} M_\odot} \right]^{2/3} p(x) h_{70}^2 \text{ keV cm}^{-3}. \end{aligned} \quad (4.15)$$

Este documento incorpora firma electrónica, y es copia auténtica de un documento electrónico archivado por la ULL según la Ley 39/2015.
Su autenticidad puede ser contrastada en la siguiente dirección <https://sede.ull.es/validacion/>

Firmado por:	Identificador del documento:	Código de verificación:	Fecha:
DENIS TRAMONTE UNIVERSIDAD DE LA LAGUNA	973742	Jfg6xBh0	30/06/2017 15:10:10
RAFAEL DELFIN BARRENA DELGADO UNIVERSIDAD DE LA LAGUNA			30/06/2017 15:21:31
JOSE ALBERTO RUBIÑO MARTIN UNIVERSIDAD DE LA LAGUNA			30/06/2017 15:34:17
ERNESTO PEREDA DE PABLO UNIVERSIDAD DE LA LAGUNA			06/07/2017 13:51:19

4.3.2 Compton parameter profile and beam smoothing

Clusters of galaxies observed in a survey appear as two-dimensional objects projected over the sky sphere. The radial pressure profile 4.15 must therefore be translated into an angular profile. Let \mathbf{n} be the unit versor pointing to the center of a cluster of mass M_{500} at redshift z , and let θ be the angular position on the sky referred to the cluster center. According to the definition of Compton parameter, the signal observed at the position θ is (Hill et al. 2014):

$$y(\theta, M_{500}, z) = \frac{\sigma_T}{m_e c^2} \int_{\text{LOS}} dl P \left(\sqrt{l^2 + D_A^2(z)|\theta|^2}, M_{500}, z \right), \quad (4.16)$$

where D_A is the angular diameter distance. In this relation, we make the (safe) assumption that the whole line-of-sight extent of the cluster can be characterised by a single redshift value z . We plot a couple of example Compton profiles in figure 4.4.

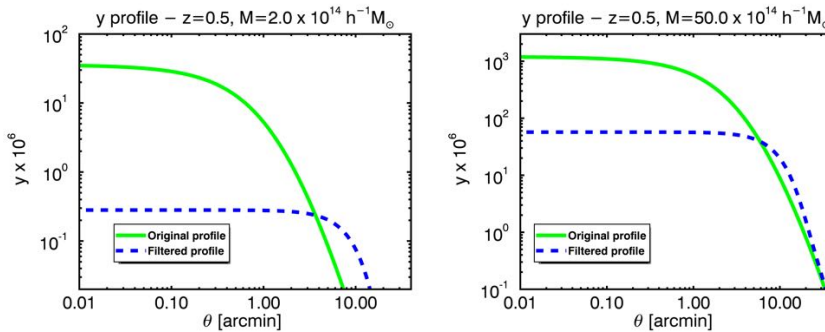


Figure 4.4: Compton parameter profile for a low-mass cluster and a high-mass cluster at redshift $z = 0.5$. In the plot we also include the filtered Compton profile computed with 4.21 using the *Planck* effective smoothing beam of $14.0'$.

Observations in radio frequencies are subject to important instrumental effects. In particular, the spatially diffuse nature of an antenna receptivity implies that each signal from the sky gets diluted over an effective instrumental beam. Mathematically, this degrading of the signal is quantified by a convolution between the source emission profile and the *point spread function* (PSF), which is a function that characterises the antenna spatial emissivity and receptivity (it is also referred to as the antenna power pattern). In most cases, it is common to approximate the antenna PSF as an individual Gaussian centered

Firmado por: DENIS TRAMONTE UNIVERSIDAD DE LA LAGUNA	30/06/2017 15:21:31
RAFAEL DELFIN BARRENA DELGADO UNIVERSIDAD DE LA LAGUNA	30/06/2017 15:34:17
JOSE ALBERTO RUBIÑO MARTIN UNIVERSIDAD DE LA LAGUNA	06/07/2017 13:51:19
ERNESTO PEREDA DE PABLO UNIVERSIDAD DE LA LAGUNA	

on the direction towards which the antenna is pointing and whose extension (or FWHM) is determined by the antenna beam width. We want to model now the effect of such a beam on the cluster Compton profile.

$$\tilde{y}(x_0, w_0) = \int dx \int dw y(x, w) B(x - x_0, w - w_0). \quad (4.17)$$

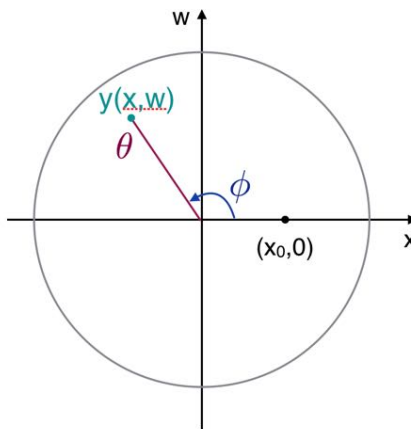


Figure 4.5: Coordinate system used for computing the smoothing of the Compton profile due to an instrumental beam. The computation can be performed at a convenient point $(x_0, 0)$, and the final profile can be easily found by exploiting the circular symmetry of the cluster projected profile.

Let us consider a galaxy cluster located at a position on the sky defined by the versor \mathbf{n} , and let us approximate the neighbouring sky region with the plane tangent to the celestial sphere at the intersection point between the direction \mathbf{n} and the sphere. We introduce a cartesian coordinate system on this plane, (x, w) . The cluster tSZ emission implies that we can define the Compton parameter as a function $y(x, w)$; we shall call θ the radial variable, $\theta^2 = x^2 + w^2$, so that the cluster profile $y(\theta)$ is the one defined by equation 4.16 (see figure 4.5). Let $\tilde{y}(x, w)$ be the profile that describes the cluster emission after being observed through a radio telescope. Let us suppose our antenna is pointing at the direction (x_0, w_0) on the tangent plane. Then its PSF is defined by the function:

$$B(x - x_0, w - w_0) = \frac{1}{2\pi\sigma_B^2} \exp\left[-\frac{(x - x_0)^2 + (w - w_0)^2}{2\sigma_B^2}\right] \quad (4.18)$$

Este documento incorpora firma electrónica, y es copia auténtica de un documento electrónico archivado por la ULL según la Ley 39/2015.
Su autenticidad puede ser contrastada en la siguiente dirección <https://sede.ull.es/validacion/>

Identificador del documento: 973742

Código de verificación: Jfg6xBh0

Firmado por: DENIS TRAMONTE
UNIVERSIDAD DE LA LAGUNA

Fecha: 30/06/2017 15:10:10

RAFAEL DELFIN BARRENA DELGADO
UNIVERSIDAD DE LA LAGUNA

30/06/2017 15:21:31

JOSE ALBERTO RUBIÑO MARTIN
UNIVERSIDAD DE LA LAGUNA

30/06/2017 15:34:17

ERNESTO PEREDA DE PABLO
UNIVERSIDAD DE LA LAGUNA

06/07/2017 13:51:19

where σ_B is related to the antenna FWHM by $\sigma_B = \text{FWHM}/\sqrt{(8 \ln 2)}$. The smoothing effect produced by the beam on the cluster y profile results in a final observed Compton parameter:

In order to simplify the computation of 4.17 we can take advantage of the circular symmetry of the cluster profile: it is sufficient to compute the convolved Compton profile along a preferential direction, e.g. the one defined by $w_0 = 0$, and moving x_0 along the x axis. The computation then simplifies to:

$$\tilde{y}(x_0, w_0 = 0) = \frac{1}{2\pi\sigma_B} \int dx \int dw y(x, w) e^{-(x-x_0)^2/2\sigma_B^2} e^{-w^2/2\sigma_B^2}. \quad (4.19)$$

Notice that, even though with equation 4.19 we have reduced the problem to computing the convolution along a specific direction, we are not performing a one-dimensional convolution. In 4.19 we are still integrating over the two directions x and w , that is, the convolution is still two-dimensional. We are only exploiting the symmetry of the final profile to simplify its computation.

It is convenient to rewrite 4.19 in terms of polar coordinates (θ, ϕ) , such that:

$$x = \theta \cos \phi, \quad w = \theta \sin \phi. \quad (4.20)$$

We find:

$$\tilde{y}(x_0, w_0 = 0) = \frac{1}{2\pi\sigma_B} e^{-x_0^2/2\sigma_B^2} \int d\theta \theta y(\theta) e^{-\theta^2/2\sigma_B^2} \int d\phi e^{x_0\theta \cos \phi/\sigma_B^2}. \quad (4.21)$$

The smoothed Compton profile 4.21 is the one we should use to compute the cluster contribution to the $P(y)$ in equation 4.22 (see section 4.3.3), whenever the final predicted PDF is to be compared with real data acquired by a radiotelescope. From now on we will label it simply as y , understanding that the beam smoothing has already been included.

The value for σ_B we employed for computing the smoothing produced by *Planck* takes into account not only the instrumental beam, but also the additional filtering applied to the individual frequency maps by the component separation algorithms. Both MILCA and NILC apply a filter to the maps to remove the contribution from the CIB and other foregrounds that peak at large scales. This can be taken into account by changing the beam FWHM. The result is like observing cluster through a telescope with effective beam $\sigma_B \simeq 1.73 \times 10^{-3}$, corresponding to a FWHM of $14.0'$.

4.3.3 Cluster contribution to the y map

We discuss now how the signal from individual clusters contributes to the $P(y)$, following the prescription from Hill et al. (2014). We remind that the $P(y)$ is

Este documento incorpora firma electrónica, y es copia auténtica de un documento electrónico archivado por la ULL según la Ley 39/2015.
Su autenticidad puede ser contrastada en la siguiente dirección <https://sede.ull.es/validacion/>

Identificador del documento: 973742

Código de verificación: Jfg6xBh0

Fecha: 30/06/2017 15:10:10

Firmado por: DENIS TRAMONTE
UNIVERSIDAD DE LA LAGUNA

RAFAEL DELFIN BARRENA DELGADO
UNIVERSIDAD DE LA LAGUNA

JOSE ALBERTO RUBIÑO MARTIN
UNIVERSIDAD DE LA LAGUNA

ERNESTO PEREDA DE PABLO
UNIVERSIDAD DE LA LAGUNA

30/06/2017 15:21:31

30/06/2017 15:34:17

06/07/2017 13:51:19

by definition an integrated quantity, whose computation relies on the previous definition of a set of y bins. What we must evaluate is the cluster contribution to a selected bin defined by the extrema values $[y_1, y_2]$, with $y_2 > y_1$. For each cluster, the Compton parameter profile computed with equation 4.16 has a maximum y_{\max} at the center ($\theta = 0$); all clusters for which $y_{\max} < y_1$ will not give any contribution to the selected bin. For the other clusters it is possible to find two angular extents θ_1 and θ_2 , with $\theta_1 > \theta_2$, such that $y_1 = y(\theta_1)$ and $y_2 = y(\theta_2)$. If $y_{\max} < y_2$ we can set $\theta_2 = 0$. The portion of the cluster projected two-dimensional surface correspondent to the annulus comprised between the values θ_2 and θ_1 (or the circle bounded by the radius θ_1 , if $\theta_2 = 0$) is responsible for a tSZ emission whose Compton parameter falls in the bin $[y_1, y_2]$ (see figure 4.6).

In section 4.2.1 we showed that the $P(y)$ can be built by binning the different regions of the y map characterised by different values of the Compton parameter. According to this geometrical meaning of the $P(y)$, the theoretical contribution from a single cluster to a y bin is proportional to the area of the aforementioned annulus (or circle, if $\theta_2 = 0$). In formulae, the contribution from a cluster of mass M_{500} at redshift z to the i -th y bin of the $P(y)$ is:

$$g_i(M_{500}, z) = \pi (\theta^2(y_i, M_{500}, z) - \theta^2(y_{i+1}, M_{500}, z)) = \int_{y_i}^{y_{i+1}} dy f(y, M_{500}, z), \quad (4.22)$$

where with $\theta(y, M_{500}, z)$ we mean the inverse of relation 4.16 (thanks to the circular symmetry of the projected cluster profile we can use the modulus $\theta = |\theta|$), and in the last equality we rewrote the same relation in a differential form, the quantity $f(y, M_{500}, z)dy$ representing the infinitesimal contribution by the selected cluster at the Compton parameter value y . This formalism will turn useful in the following when introducing noise and foreground contaminations; in this case:

$$f(y, M_{500}, z) = -2\pi\theta(y, M_{500}, z). \quad (4.23)$$

We now have to put together the contribution from all clusters; we know from the previous chapter that in order to count all clusters we have to integrate the mass function and the comoving volume element. In a similar way, we can write in this case:

$$P(y_i) = \int dz \frac{d^2V}{dz d\Omega}(z) \int dM_{\text{vir}} \frac{dn}{dM_{\text{vir}}}(M_{\text{vir}}, z) g_i(M_{500}, z). \quad (4.24)$$

In this context it is convenient to use the *virial mass* M_{vir} as the reference mass definition for the clusters. In order to convert between virial and overdensity masses we adopted the method detailed in Appendix D of Komatsu et al.

Este documento incorpora firma electrónica, y es copia auténtica de un documento electrónico archivado por la ULL según la Ley 39/2015.
Su autenticidad puede ser contrastada en la siguiente dirección <https://sede.ull.es/validacion/>

Identificador del documento: 973742

Código de verificación: Jfg6xBh0

Fecha: 30/06/2017 15:10:10

Firmado por: DENIS TRAMONTE
UNIVERSIDAD DE LA LAGUNA

RAFAEL DELFIN BARRENA DELGADO
UNIVERSIDAD DE LA LAGUNA

JOSE ALBERTO RUBIÑO MARTIN
UNIVERSIDAD DE LA LAGUNA

ERNESTO PEREDA DE PABLO
UNIVERSIDAD DE LA LAGUNA

30/06/2017 15:21:31

30/06/2017 15:34:17

06/07/2017 13:51:19

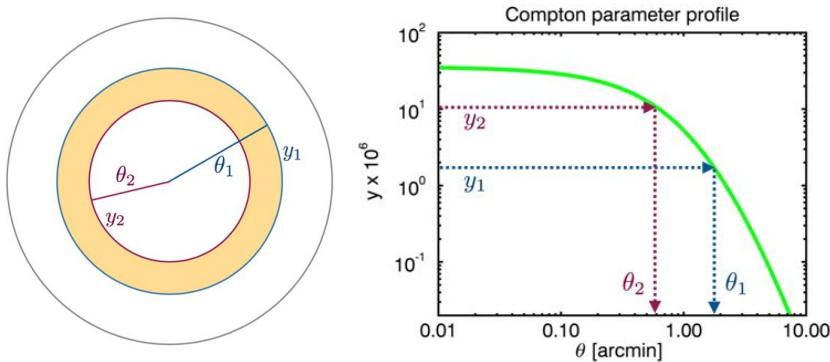


Figure 4.6: Contribution from a single cluster to the tSZ PDF. For a given y bin, it is possible to find an annular region in the cluster projected surface in which the Compton parameter takes values inside the bin. The contribution from that particular cluster to the $P(y)$ is proportional to the area of the annulus.

(2011). The mass function is computed with the Tinker recipe as a function of M_{200} and properly changed into a distribution in M_{vir} ; the mass entering the computation of the pressure profile must be instead the M_{500} corresponding to the given M_{vir} .

Equation 4.24 is the resulting tSZ-PDF computed assuming a noiseless cluster only contribution. The integrals in 4.24 must be defined between proper extrema; we take the redshift in the range $[1 \times 10^{-3}, 1]$, and the virial mass in $[2 \times 10^{14}, 5 \times 10^{15}] h^{-1} M_{\odot}$. We do not take the minimum redshift at zero in order to avoid divergences in the computation of angular extensions, and the choice of the upper limit is justified by the fact that we do not expect to observe clusters with *Planck* at $z > 1$: the signal from clusters at higher redshifts only contributes to the region of the $P(y)$ that is dominated by noise. The upper mass limit has been chosen because clusters more massive than $5 \times 10^{15} h^{-1} M_{\odot}$ are few enough to give a negligible contribution to the total number of clusters (for instance, by setting $1 \times 10^{16} h^{-1} M_{\odot}$ as the upper mass the total number of clusters is only $\sim 0.03\%$ higher). The lower mass limit, instead, ensures that we can neglect effects due to cluster overlaps. The formalism described so far, indeed, makes the assumption that no more than one cluster is intercepted by the same line of sight. Since the low-mass clusters are the most abundant ones, this assumption is easily broken if we further lower the minimum mass. The signal of the clusters that are left out, however, is small and only enters in the noise-dominated region of the $P(y)$.

In order to quantify at what precision the assumption of non-overlap is verified, we compute the total fraction of the sky that is blocked by clusters:

$$F_{\text{clust}} = \int dz \frac{d^2V}{dz d\Omega}(z) \int dM_{\text{vir}} \frac{dn}{dM_{\text{vir}}}(M_{\text{vir}}, z) \pi \theta_{\text{out}}^2(M_{\text{vir}}, z), \quad (4.25)$$

where $\theta_{\text{out}}(M_{\text{vir}}, z)$ is the angular extension of a cluster of mass M_{vir} at redshift z . In the literature it is common to set θ_{out} equal to five times the radius R_{500} :

$$\theta_{\text{out}}(M_{\text{vir}}, z) = 5 \frac{R_{500}(M_{\text{vir}}, z)}{D_A(z)}. \quad (4.26)$$

We checked that this angular extension allows to explore the full Compton parameter profile of the cluster, the ratio of the central to the border values of y being around $\sim 10^4$; even for the closest and most massive clusters that we are considering, this corresponds to a border value of $y \sim 10^{-7}$, that is, fully in the noise-dominated region (see figure 4.2). The non-overlapping cluster approximation is as good as the cluster fraction is smaller than one. With the aforementioned mass and redshift intervals, the total cluster fraction yields $F_{\text{clust}} \simeq 0.3$, which is reasonably small.

To close this section, notice that in order for 4.24 to be normalized at unit integral, the bin containing the value $y = 0$ should take the contribution from all the regions of the sky which are not occupied by clusters, and therefore have no emission. So, an extra term $(1 - F_{\text{clust}})$ should be added to that bin. This makes the cluster-only $P(y)$ to be sharply peaked at $y = 0$.

4.3.4 Modelling the noise contribution

Apart from determining an overall smoothing of the signal structures on the sky, a real telescope also introduces noise to the observed signal. We assume this noise to be Gaussian distributed with a rms σ_N around a central value μ :

$$N(y) = A_N \exp \left[-\frac{(y - \mu_N)^2}{2\sigma_N^2} \right]. \quad (4.27)$$

The gaussian width σ_N quantifies the scatter in the statistical deviation of the observed signal from its nominal value, normalized to a maximum value A_N ; the offset μ_N quantifies possible systematics that can affect the observation. We can actually interpret 4.27 to describe not only instrumental effects, but also all the contributions from other radio emission mechanisms that contaminate the SZ signal, plus the low y emission from low-mass and/or high-redshift clusters (out of the ranges we are considering).

Este documento incorpora firma electrónica, y es copia auténtica de un documento electrónico archivado por la ULL según la Ley 39/2015.
Su autenticidad puede ser contrastada en la siguiente dirección <https://sede.ull.es/validacion/>

Identificador del documento: 973742

Código de verificación: Jfg6xBh0

Fecha: 30/06/2017 15:10:10

Firmado por: DENIS TRAMONTE UNIVERSIDAD DE LA LAGUNA	30/06/2017 15:21:31
RAFAEL DELFIN BARRENA DELGADO UNIVERSIDAD DE LA LAGUNA	30/06/2017 15:34:17
JOSE ALBERTO RUBIÑO MARTIN UNIVERSIDAD DE LA LAGUNA	06/07/2017 13:51:19
ERNESTO PEREDA DE PABLO UNIVERSIDAD DE LA LAGUNA	

We discuss in the following two different ways of implementing this noise in the SZ-PDF computation. In the end of this section we prove their equivalence and make some examples.

Including noise *a posteriori*

We saw in section 4.2.2 that different contributions to the $P(y)$ can be combined via a convolution; in this case, then, the noise can be added to the cluster PDF in the form $P(y) = [P_{\text{SZ}} \otimes N](y)$, where P is computed with equation 4.24. Or, in a more explicit notation:

$$P(y) = \int dy' P(y') N(y - y'). \quad (4.28)$$

An example of convolution between the noise and the noiseless cluster-only PDF is plotted in figure 4.7.

One thing that can be noticed by comparing equations 4.28 and 4.24 is that here we are considering the PDF as if it was a continuous function defined for all values of y , while in section 4.3.3 it was defined as a histogram over a discrete set of non-overlapping bins y_i . Strictly speaking, equation 4.28 should be written with a sum over the N y bins, which is actually the way it is implemented numerically. However, it still makes sense as a limit if we take the bin size Δy sufficiently small to make the continuous approximation safe.

Including noise *a priori*

We present here another way of including the noise contribution, introduced in Hill et al. (2014). Let us consider the i -th Compton parameter bin $[y_i, y_{i+1}]$, and let y be the signal coming from the sky. We define $\rho_i(y)$ as the probability for the signal y to fall inside the bin i ; if there were no noise, the function $\rho_i(y)$ would be equal to unity for $y_i < y < y_{i+1}$ and null elsewhere. The noise introduces a shift and a scatter of the signal around the nominal values y , quantified by the parameters μ_N and σ_N in 4.27, so that the probability $\rho_i(y)$ changes into:

$$\rho_i(y) = \int_{y_i}^{y_{i+1}} dy' N(y' - y). \quad (4.29)$$

Now, the function $g_i(M_{500}, z)$ defined in 4.22, expressing the contribution from a cluster of mass and redshift (M_{500}, z) , should be properly modified to take this alteration of the signal into account. The function $f(y)$, that represents the contribution density by the cluster at the point y , must be multiplied by

Este documento incorpora firma electrónica, y es copia auténtica de un documento electrónico archivado por la ULL según la Ley 39/2015.
Su autenticidad puede ser contrastada en la siguiente dirección <https://sede.ull.es/validacion/>

Identificador del documento: 973742

Código de verificación: Jfg6xBh0

Fecha: 30/06/2017 15:10:10

Firmado por: DENIS TRAMONTE
UNIVERSIDAD DE LA LAGUNA

RAFAEL DELFIN BARRENA DELGADO
UNIVERSIDAD DE LA LAGUNA

JOSE ALBERTO RUBIÑO MARTIN
UNIVERSIDAD DE LA LAGUNA

ERNESTO PEREDA DE PABLO
UNIVERSIDAD DE LA LAGUNA

30/06/2017 15:21:31

30/06/2017 15:34:17

06/07/2017 13:51:19

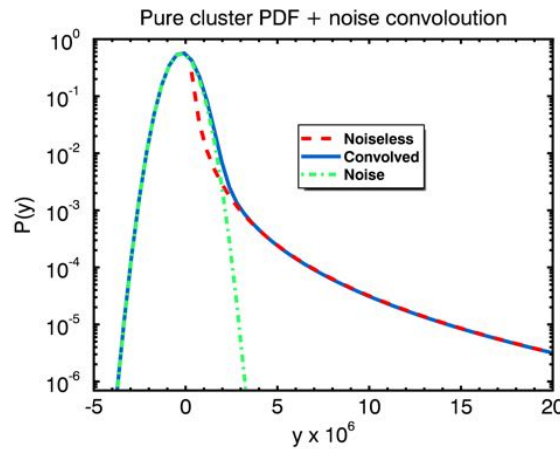


Figure 4.7: Computation of the overall $P(y)$ via convolution between the noise and the noiseless cluster-only contribution.

the probability for y to actually fall in the bin. This allows us to relax the integration extrema in 4.22 and write:

$$\begin{aligned} g_i(M_{500}, z) &= \int dy f(y, M_{500}, z) \rho_i(y) = \\ &= \int d\theta 2\pi\theta \rho_i(y(\theta, M_{500}, z)). \end{aligned} \quad (4.30)$$

Again, the final $P(y)$ is computed by putting together the weighted contribution from all clusters:

$$P(y_i) = (1 - F_{\text{clust}})\rho_i(0) + \int dz \frac{d^2V}{dzd\Omega}(z) \int dM_{\text{vir}} \frac{dn}{dM_{\text{vir}}}(M_{\text{vir}}, z) g_i(M_{500}, z), \quad (4.31)$$

where the first term represents the contribution from the noise to the y bin containing the value $y = 0$. Notice that in the noiseless case, in which $\rho_i(y)$ is equal to unity inside the bin and null elsewhere, equation 4.31 recovers the noiseless case 4.24.

Comparing the two methods

The two methods for including the noise are in fact equivalent. To simplify the notation we will forget about the integrals over mass and redshift and

Este documento incorpora firma electrónica, y es copia auténtica de un documento electrónico archivado por la ULL según la Ley 39/2015.
Su autenticidad puede ser contrastada en la siguiente dirección <https://sede.ull.es/validacion/>

Identificador del documento: 973742

Código de verificación: Jfg6xBh0

Fecha: 30/06/2017 15:10:10

Firmado por: DENIS TRAMONTE UNIVERSIDAD DE LA LAGUNA	30/06/2017 15:21:31
RAFAEL DELFIN BARRENA DELGADO UNIVERSIDAD DE LA LAGUNA	30/06/2017 15:34:17
JOSE ALBERTO RUBIÑO MARTIN UNIVERSIDAD DE LA LAGUNA	06/07/2017 13:51:19
ERNESTO PEREDA DE PABLO UNIVERSIDAD DE LA LAGUNA	

concentrate on the contribution to the $P(y)$ from a single cluster. We shall employ the continuous approximation, so that this contribution can be written as a function $g(y)$, meaning we are considering the value corresponding to a small bin $[y - \delta y/2, y + \delta y/2]$.

The one-cluster $P(y)$ computed with the noise convolution (noise included *a posteriori*), which we label $g_1(y)$, can be written as:

$$\begin{aligned} g_1(y) &= \int dy' N(y - y') g(y') = \\ &= \int dy' N(y - y') \int_{y'-\delta y/2}^{y'+\delta y/2} dy'' f(y'') = \\ &\simeq \int dy' N(y - y') [(\delta y)f(y')] , \end{aligned} \quad (4.32)$$

where in the second line we made the definition of the noiseless contribution g explicit, and in the third line we approximated the integral over the small bin as the bin size times the function evaluated in its center. This is indeed a good approximation whenever the bin size is small compared to the typical variation scale of the integrand function. Notice also that it was possible to include only the contribution $g(y)$ from one cluster because the integrals on mass and redshift factorize outside the integrals over the Compton parameter.

Regarding the *a priori* inclusion of the noise, we can write:

$$\begin{aligned} g_2(y) &= \int dy' f(y') \rho(y') = \\ &= \int dy' f(y') \int_{y-\delta y/2}^{y+\delta y/2} dy'' N(y'' - y') = \\ &\simeq \int dy' f(y') [(\delta y)N(y - y')] , \end{aligned} \quad (4.33)$$

where this time the integral that was approximated is the definition of the probability $\rho(y)$.

We see that the last lines in equation equations 4.32 and 4.33 are the same. To a first approximation, then, the two ways of implementing the noise are the same. The equality becomes exact in the limit of continuous functions; however, it is enough to choose a sufficiently small size Δy for the Compton parameter bins, which is the case in our subsequent analysis. The correspondence is also better where the PDF is a slowly-varying function of y ; in figure 4.8 we show a comparison of the two distributions.

Este documento incorpora firma electrónica, y es copia auténtica de un documento electrónico archivado por la ULL según la Ley 39/2015.
Su autenticidad puede ser contrastada en la siguiente dirección <https://sede.ull.es/validacion/>

Identificador del documento: 973742

Código de verificación: Jfg6xBh0

Fecha: 30/06/2017 15:10:10

Firmado por: DENIS TRAMONTE UNIVERSIDAD DE LA LAGUNA	30/06/2017 15:21:31
RAFAEL DELFIN BARRENA DELGADO UNIVERSIDAD DE LA LAGUNA	30/06/2017 15:34:17
JOSE ALBERTO RUBIÑO MARTIN UNIVERSIDAD DE LA LAGUNA	06/07/2017 13:51:19
ERNESTO PEREDA DE PABLO UNIVERSIDAD DE LA LAGUNA	

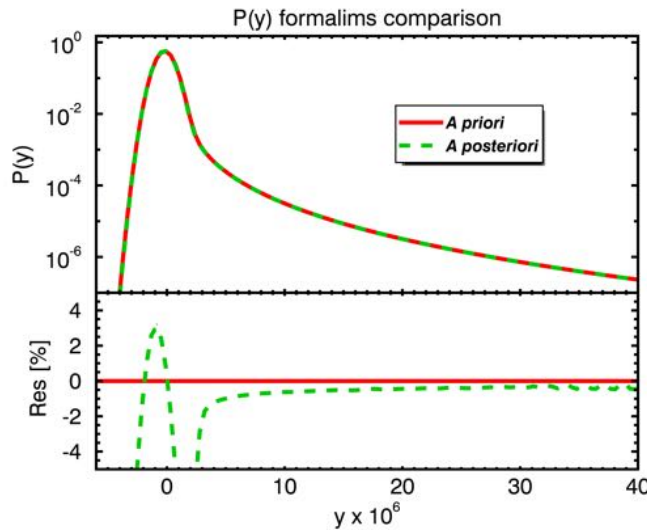


Figure 4.8: Comparison between the two recipes for including noise in the tSZ PDF. The final distributions are the same within a 1% accuracy in the cluster-dominated range, while the difference gets larger where the function has faster variations as a function of y .

4.4 Testing the formalism

Before applying the formalism for computing the cluster plus noise $P(y)$ to real data, we wanted to test the prediction from the recipe described in section 4.3. To this aim we compared the computed $P(y)$ with the one extracted from a set of simulated Compton parameter maps. We describe in the following the method employed for generating the maps and the final results.

4.4.1 Pure cluster tSZ map

In order to simulate a pure SZ Compton map, we first have to determine the total number of clusters that contribute to it. We then have to assign a mass and a redshift to each one of them, which is done according to the (M, z) cluster distribution. The clusters must be placed randomly on the map, and the neighbouring regions will be assigned the corresponding contribution in terms of the y emission. In the end, the SZ map must undergo a transformation to account for the effect of the beam. We detail each step in the following.

Este documento incorpora firma electrónica, y es copia auténtica de un documento electrónico archivado por la ULL según la Ley 39/2015.
Su autenticidad puede ser contrastada en la siguiente dirección <https://sede.ull.es/validacion/>

Identificador del documento: 973742

Código de verificación: Jfg6xBh0

Fecha: 30/06/2017 15:10:10

Firmado por: DENIS TRAMONTE
UNIVERSIDAD DE LA LAGUNA

RAFAEL DELFIN BARRENA DELGADO
UNIVERSIDAD DE LA LAGUNA

JOSE ALBERTO RUBIÑO MARTIN
UNIVERSIDAD DE LA LAGUNA

ERNESTO PEREDA DE PABLO
UNIVERSIDAD DE LA LAGUNA

30/06/2017 15:21:31

30/06/2017 15:34:17

06/07/2017 13:51:19

Total number of clusters

We compute the total number of clusters in our map in the same way as in chapter 3, by integrating over the mass and redshift their number distribution:

$$N_{\text{clust}} = \int_{z_{\min}}^{z_{\max}} dz \int_{M_{\min}}^{M_{\max}} dM_{\text{vir}} \frac{dN}{dM_{\text{vir}} dz}(M_{\text{vir}}, z) \quad (4.34)$$

Again, since we need different definitions for the cluster mass, we employ as a baseline the cluster virial mass, and refer the distributions to it. We take the integration extrema in mass and redshift according to the ranges proposed in section 4.3.3. The distribution of the cluster number in mass and redshift can be written as:

$$\frac{dN}{dM_{\text{vir}} dz}(M_{\text{vir}}, z) = 4\pi \frac{d^2V}{dz d\Omega}(z) \frac{dn}{dM_{200}}(M_{200}(M_{\text{vir}}), z) \frac{dM_{200}}{dM_{\text{vir}}}(M_{\text{vir}}, z) \quad (4.35)$$

where the 4π accounts for the whole sky solid angle, $d^2V/dzd\Omega$ is the comoving volume element, dn/dM_{200} is the Tinker et al. (2008) mass function computed as a function of the mass M_{200} and dM_{200}/dM_{vir} is the jacobian of the transformation to virial masses.

Assigning mass and redshift

For each one of the N_{clust} clusters, values for the mass and the redshift must be assigned. This is done according to the mass and redshift cluster probability distribution. The mass distribution is actually dependent on the redshift. So, first we marginalize the distribution $dN/dMdz$ over the mass to obtain the cluster redshift distribution:

$$\frac{dN}{dz}(z) = \int dM_{\text{vir}} \frac{dN}{dM_{\text{vir}} dz}(M_{\text{vir}}, z). \quad (4.36)$$

The cluster redshift is determined by sampling a value according to this probability distribution.

Once a value has been assigned to the redshift z_c , the mass probability distribution is determined by the joint probability distribution 4.35 computed at that redshift, $dN/(dM_{\text{vir}} dz)(M_{\text{vir}}, z_c)$. By sampling a value from this distribution we obtain the cluster mass M_c .

Placing clusters on map

We assume the simulated cluster map to be defined in Galactic coordinates. The cluster position on the map is determined by considering its position vector

Este documento incorpora firma electrónica, y es copia auténtica de un documento electrónico archivado por la ULL según la Ley 39/2015.
Su autenticidad puede ser contrastada en la siguiente dirección <https://sede.ull.es/validacion/>

Identificador del documento: 973742

Código de verificación: Jfg6xBh0

Fecha: 30/06/2017 15:10:10

Firmado por: DENIS TRAMONTE UNIVERSIDAD DE LA LAGUNA	30/06/2017 15:21:31
RAFAEL DELFIN BARRENA DELGADO UNIVERSIDAD DE LA LAGUNA	30/06/2017 15:34:17
JOSE ALBERTO RUBIÑO MARTIN UNIVERSIDAD DE LA LAGUNA	06/07/2017 13:51:19
ERNESTO PEREDA DE PABLO UNIVERSIDAD DE LA LAGUNA	

and sampling its component x , y , and z from a normalized Gaussian distribution; this ensures that the vector $(x/\lambda, y/\lambda, z/\lambda)$, with $\lambda = (x^2 + y^2 + z^2)^{1/2}$, is uniformly distributed over the sphere. These coordinates can then be translated into the cluster central Galactic longitude and latitude (l_c, b_c) .

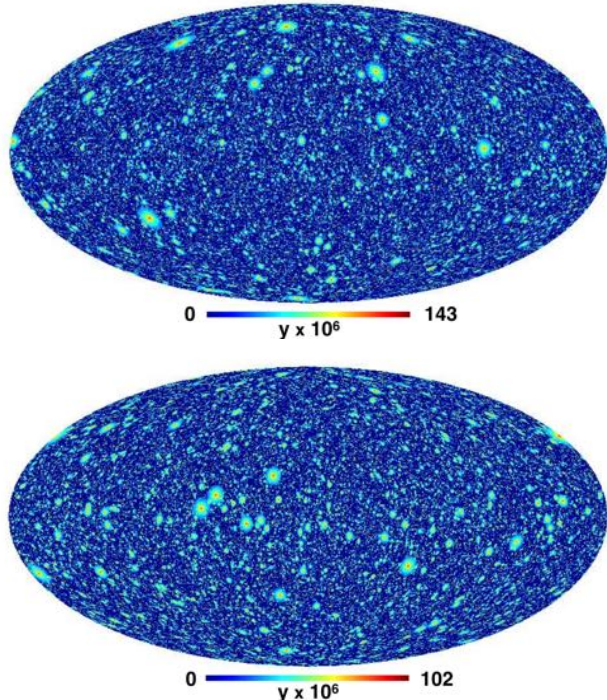


Figure 4.9: Example of two simulated cluster-only Compton parameter maps, without including any instrumental contribution in terms of noise or beam dilution.

To a cluster virial mass M_{vir} it corresponds a proper critical overdensity mass M_{500} . We compute the cluster pressure profile using equation 4.15 with a fixed bias parameter $b = 0.2$. The Compton parameter profile is then derived with 4.16. We considered all pixels located around the cluster center within a radius $R_{\text{TOT}} = 5 R_{500}$ and to each pixel we assign the corresponding value of the Compton parameter depending on its distance from the center. The value of y is computed by integrating the cluster pressure profile 4.16 along the line

Este documento incorpora firma electrónica, y es copia auténtica de un documento electrónico archivado por la ULL según la Ley 39/2015.
Su autenticidad puede ser contrastada en la siguiente dirección <https://sede.ull.es/validacion/>

Identificador del documento: 973742	Código de verificación: Jfg6xBh0
Firmado por: DENIS TRAMONTE UNIVERSIDAD DE LA LAGUNA	Fecha: 30/06/2017 15:10:10
RAFAEL DELFIN BARRENA DELGADO UNIVERSIDAD DE LA LAGUNA	30/06/2017 15:21:31
JOSE ALBERTO RUBIÑO MARTIN UNIVERSIDAD DE LA LAGUNA	30/06/2017 15:34:17
ERNESTO PEREDA DE PABLO UNIVERSIDAD DE LA LAGUNA	06/07/2017 13:51:19

of sight l , in the range $[-5 R_{500}, +5 R_{500}]$ (with the cluster center in $l = 0$). The corresponding integrated Compton profile will then be the cylindrical flux Y^{cyl} , which is the one that is measured on a y map. In our implementation we want to allow possible overlaps between different clusters, so for each pixel we add the y contribution computed this way to any previous value already stored in that pixel.

We use **HEALPix** maps with a base resolution of $N_{\text{side}} = 2048$. This results in a typical pixel angular extension of ≈ 1.7 arcmin. This is roughly the size of the smallest clusters for our mass and redshift ranges. An example of generated cluster maps is shown in figure 4.9.

4.4.2 Including instrumental effects

After generating the pure cluster map, instrumental effects have to be added to it. The alteration to the signal caused by an instrument can be separated into the degrading of the resolution due to its finite beam size, and the injection of a noise component into the signal.

Applying beam dilution

It is possible to apply the beam smoothing at the level of the map. This is done by using the **HEALPix** **smoothing** routine. We choose a beam of $\text{FWHM} = 20'$; the maps only serve for a consistency check of our formalism, so there is no need to use the proper value of the *Planck* beam. In figure 4.10 we show the same maps as in figure 4.9 after applying the beam smoothing.

Adding noise maps

The inclusion of the instrumental noise is done by adding a noise map that is generated separately. To each pixel of the noise map we assign a value taken from a Gaussian distribution, characterised by a mean μ , and a standard deviation σ . The parameter μ accounts for possible systematics, while σ accounts for the scatter introduced by the noise. Together, they determine the importance of the noise compared to the signal that we want to observe (the emission simulated in the pure SZ map). For each pixel, after generating a random number x from a normal distribution (with null mean and unit standard deviation), the simulated noise values can be computed as:

$$n = \mu + \sigma x \quad (4.37)$$

In our case we chose as μ and σ the values obtained from the fit of the MILCA noise component in the $P(y)$ from *Planck* data (figure 4.2). The map obtained

Este documento incorpora firma electrónica, y es copia auténtica de un documento electrónico archivado por la ULL según la Ley 39/2015.
Su autenticidad puede ser contrastada en la siguiente dirección <https://sede.ull.es/validacion/>

Identificador del documento: 973742	Código de verificación: Jfg6xBh0
Firmado por: DENIS TRAMONTE UNIVERSIDAD DE LA LAGUNA	Fecha: 30/06/2017 15:10:10
RAFAEL DELFIN BARRENA DELGADO UNIVERSIDAD DE LA LAGUNA	30/06/2017 15:21:31
JOSE ALBERTO RUBIÑO MARTIN UNIVERSIDAD DE LA LAGUNA	30/06/2017 15:34:17
ERNESTO PEREDA DE PABLO UNIVERSIDAD DE LA LAGUNA	06/07/2017 13:51:19

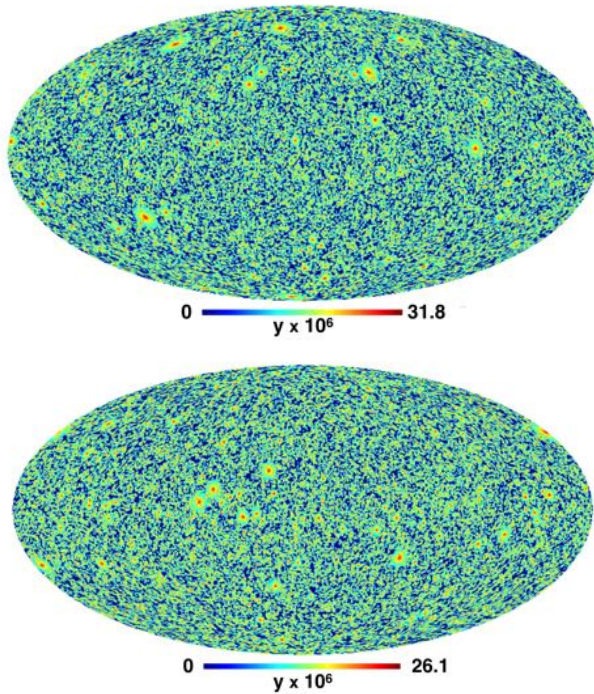


Figure 4.10: The same maps from figure 4.9, after the smoothing with a 20 arcmin beam.

this way should be added to the smoothed SZ cluster map, as in figure 4.11. The addition of the two components at the map level indeed corresponds to a convolution at the level of the PDFs.

4.4.3 Comparison with predicted PDF

As it becomes clear by looking at figure 4.9, generating random cluster masses and redshifts results in the final maps being different from one another, and so will be the corresponding PDF distributions. Hence, when comparing individual $P(y)$ to the one predicted analytically with the recipe described in section 4.3, it will be likely to find substantial differences between them (this effect is usually referred to as sample bias).

Este documento incorpora firma electrónica, y es copia auténtica de un documento electrónico archivado por la ULL según la Ley 39/2015.
Su autenticidad puede ser contrastada en la siguiente dirección <https://sede.ull.es/validacion/>

Identificador del documento: 973742

Código de verificación: Jfg6xBh0

Fecha: 30/06/2017 15:10:10

Firmado por: DENIS TRAMONTE
UNIVERSIDAD DE LA LAGUNA

RAFAEL DELFIN BARRENA DELGADO
UNIVERSIDAD DE LA LAGUNA

JOSE ALBERTO RUBIÑO MARTIN
UNIVERSIDAD DE LA LAGUNA

ERNESTO PEREDA DE PABLO
UNIVERSIDAD DE LA LAGUNA

30/06/2017 15:21:31

30/06/2017 15:34:17

06/07/2017 13:51:19

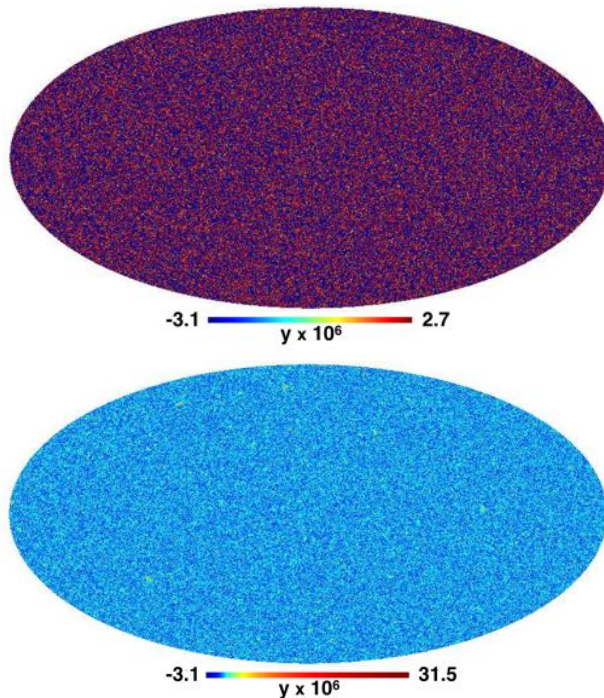


Figure 4.11: Top: example of a simulated noise map using the mean and rms from the MILCA fitted noise in figure 4.2. Bottom: the same map from the top panel of figure 4.10, after adding the noise simulated map.

In order to test the formalism, therefore, we need to consider a large number of simulations of SZ maps, and take the average of the PDFs as the reference one. In 4.12 we show a set of 500 PDFs extracted by different simulations, and their average. This average $P(y)$ is then compared with the one predicted numerically. The comparison shows substantial agreement between the two, the residuals being below 5% in the range of y that is most relevant for our analysis (the lowest y range is dominated by instrumental noise and other backgrounds, while the highest y tail is dominated by emission from the biggest and rarest clusters, so it is more affected by statistical uncertainties).

To sum up, in this section we have proven that our formalism for computing

Este documento incorpora firma electrónica, y es copia auténtica de un documento electrónico archivado por la ULL según la Ley 39/2015.
Su autenticidad puede ser contrastada en la siguiente dirección <https://sede.ull.es/validacion/>

Identificador del documento: 973742

Código de verificación: Jfg6xBh0

Fecha: 30/06/2017 15:10:10

Firmado por: DENIS TRAMONTE
UNIVERSIDAD DE LA LAGUNA

RAFAEL DELFIN BARRENA DELGADO
UNIVERSIDAD DE LA LAGUNA

JOSE ALBERTO RUBIÑO MARTIN
UNIVERSIDAD DE LA LAGUNA

ERNESTO PEREDA DE PABLO
UNIVERSIDAD DE LA LAGUNA

30/06/2017 15:21:31

30/06/2017 15:34:17

06/07/2017 13:51:19

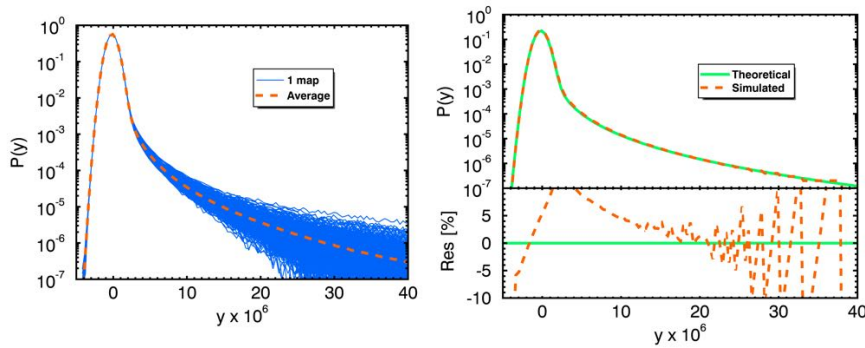


Figure 4.12: Left: PDFs extracted from a set of 500 simulated y maps, together with their average. Right: comparison between the average $P(y)$ with the one computed analytically: we found agreement in the interesting range of y , out of the region dominated by noise.

analytically the $P(y)$ is consistent. The $P(y)$ extracted from the average of a set of simulated Compton parameter maps is properly reproduced by the analytical prescription described in section 4.3, when both PDFs are generated using the same underlying cosmology (for this test we used the reference cosmological model from table 4.1). This implies that we can employ this recipe for the inverse problem of recovering the cosmological parameters, on the basis of the $P(y)$ reconstructed from real data. This topic is tackled in rest of this chapter.

4.5 Application to *Planck* data

In this section we use the tSZ PDF as a cosmological tool. In particular, we already showed in figure 4.3 that the $P(y)$ is highly sensitive to σ_8 , so this is the parameter that we are going to focus on. We are going to consider the *Planck* data shown in figure 4.2. However, we should not employ the full distributions represented there, because in our modelling we are not considering the emission from radio sources responsible for the negative $P(y)$ tail. In order to be consistent, we are going to drop that part and consider only the cluster contributions plus the noise-dominated region around $y = 0$. More precisely, we consider the same $P(y)$ distributions as in figure 4.2, from the reconstructed MILCA and NILC Compton parameter maps, but only for the range $y > 0$; for the negative y range, we continue the distribution using exclusively the fitted noise component, that is also shown in figure 4.2. The resulting data distribution that we are going to consider are the ones plotted in figure 4.13.

Este documento incorpora firma electrónica, y es copia auténtica de un documento electrónico archivado por la ULL según la Ley 39/2015.
Su autenticidad puede ser contrastada en la siguiente dirección <https://sede.ull.es/validacion/>

Identificador del documento: 973742

Código de verificación: Jfg6xBh0

Fecha: 30/06/2017 15:10:10

Firmado por: DENIS TRAMONTE
UNIVERSIDAD DE LA LAGUNA

RAFAEL DELFIN BARRENA DELGADO
UNIVERSIDAD DE LA LAGUNA

JOSE ALBERTO RUBIÑO MARTIN
UNIVERSIDAD DE LA LAGUNA

ERNESTO PEREDA DE PABLO
UNIVERSIDAD DE LA LAGUNA

30/06/2017 15:21:31

30/06/2017 15:34:17

06/07/2017 13:51:19

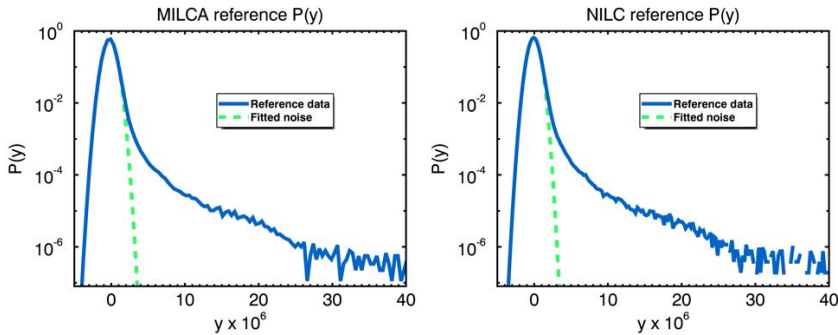


Figure 4.13: Effective SZ PDF distributions from *Planck* reconstructed y maps that we consider for cosmological parameter estimation. These distributions only take the contribution from galaxy clusters and the noise/foregrounds, dropping the negative y tail which would alter the PDFs normalisation.

4.5.1 Methodology

The estimation of a best fit σ_8 parameter relies on building a PDF-based likelihood for this parameter. We fix all cosmological parameters to the *Planck* best-fit 2015 cosmological model (table 4.1), and leave only σ_8 free to vary over a definite range (we chose the interval $[0.72, 0.82]$). For each value of σ_8 , we compute the corresponding $P(y)$ according to the recipe described in 4.3, and compare it to the data, both for the case of MILCA and NILC reconstructed distributions. This comparison requires:

- a proper y interval to be considered. We cannot use the region too close to $y = 0$, since it is dominated by instrumental noise and other foregrounds entering the y map. Even though we include such a noise in the PDF computation, we remind that we extracted it via a fit to the PDF data, so it is not sufficiently well characterised as to be used for cosmological parameter estimation. It is also safer to drop the high y tail, which is the PDF region with higher fluctuations, dominated by the biggest clusters in a mass range where also the mass function abundance predictions begin to suffer from important statistical uncertainties. To sum up, the safe region of y we are going to consider for our fit is roughly $y \simeq [6, 26] \times 10^{-6}$.
- a proper covariance matrix. We remind the $P(y)$ is computed over a set of bins. If these bins were statistically independent, then a simple χ^2 -based likelihood would be sufficient to determine the best-fit $P(y)$. However, in this case a single cluster contributes to different y bins, according to the

Este documento incorpora firma electrónica, y es copia auténtica de un documento electrónico archivado por la ULL según la Ley 39/2015.
Su autenticidad puede ser contrastada en la siguiente dirección <https://sede.ull.es/validacion/>

Identificador del documento: 973742

Código de verificación: Jfg6xBh0

Fecha: 30/06/2017 15:10:10

Firmado por: DENIS TRAMONTE
UNIVERSIDAD DE LA LAGUNA

RAFAEL DELFIN BARRENA DELGADO
UNIVERSIDAD DE LA LAGUNA

JOSE ALBERTO RUBIÑO MARTIN
UNIVERSIDAD DE LA LAGUNA

ERNESTO PEREDA DE PABLO
UNIVERSIDAD DE LA LAGUNA

30/06/2017 15:21:31

30/06/2017 15:34:17

06/07/2017 13:51:19

extension of its Compton parameter profile. This introduces correlations between bins, which have to be taken into account via a proper covariance matrix. We are going to use here the analytical form proposed by Hill et al. (2014):

$$\text{Cov}_{ij} = \frac{P_i}{N_{\text{pix}}} \delta_{ij} + \frac{1}{4\pi f_{\text{sky}}} \int dz \frac{d^2V}{dz d\Omega} \int dM_{\text{vir}} \frac{dn}{dM_{\text{vir}}} \times [g_i - \rho_i(0)\pi\theta_{\text{out}}^2] [g_j - \rho_j(0)\pi\theta_{\text{out}}^2], \quad (4.38)$$

where it is understood that $P_i = P(y_i)$ and that $g_i = g_i(M_{500}, z)$ defined in 4.30. Here N_{pix} is the total number of pixels of the underlying map, and f_{sky} is the covered sky fraction. *Planck* y maps mask the Galactic plane, resulting in $f_{\text{sky}} \simeq 0.64$, and are issued in **HEALPix** maps with $N_{\text{side}} = 2048$, which corresponds to $N_{\text{pix}} \simeq 2.86 \times 10^7$. The first term in 4.38 accounts for the Poissonian error in each bin, normalised to the number of map pixels; if it was the only contribution, the covariance matrix would be diagonal and the likelihood would reduce to a χ^2 form. The second term accounts for bin correlations generated by the cluster profiles. An example of covariance matrix is plotted in figure 4.14.

For each value of σ_8 we determine a distribution $P_i(\sigma_8)$ and a covariance matrix $\text{Cov}(\sigma_8)$. Let \tilde{P}_i be the reference *Planck* PDF; the tSZ PDF-based likelihood distribution for σ_8 can be written as a multivariate gaussian in the form:

$$\mathcal{L}(\sigma_8) = \frac{1}{\sqrt{2\pi \det(\text{Cov}(\sigma_8))}} \times \exp \left[-\frac{1}{2} (P_i(\sigma_8) - \tilde{P}_i)(\text{Cov}^{-1}(\sigma_8))_{ij} (P_j(\sigma_8) - \tilde{P}_j) \right]. \quad (4.39)$$

The likelihood in 4.39 is the one we employed to provide an estimate for the best-fit σ_8 value.

4.5.2 Results

In figure 4.15 we show the likelihood distribution computed with 4.39 for both the cases of MILCA and NILC data. The final estimates are (at 68% C.L.):

$$\text{MILCA } \sigma_8 = 0.769 \pm 0.010, \quad \text{NILC } \sigma_8 = 0.765 \pm 0.010. \quad (4.40)$$

These estimates were included in the publication Planck Collaboration et al. (2016h) as part of *Planck* 2015 Release of Papers. However, the errors reported

Este documento incorpora firma electrónica, y es copia auténtica de un documento electrónico archivado por la ULL según la Ley 39/2015.
Su autenticidad puede ser contrastada en la siguiente dirección <https://sede.ull.es/validacion/>

Identificador del documento: 973742	Código de verificación: Jfg6xBh0
Firmado por: DENIS TRAMONTE UNIVERSIDAD DE LA LAGUNA	Fecha: 30/06/2017 15:10:10
RAFAEL DELFIN BARRENA DELGADO UNIVERSIDAD DE LA LAGUNA	30/06/2017 15:21:31
JOSE ALBERTO RUBIÑO MARTIN UNIVERSIDAD DE LA LAGUNA	30/06/2017 15:34:17
ERNESTO PEREDA DE PABLO UNIVERSIDAD DE LA LAGUNA	06/07/2017 13:51:19

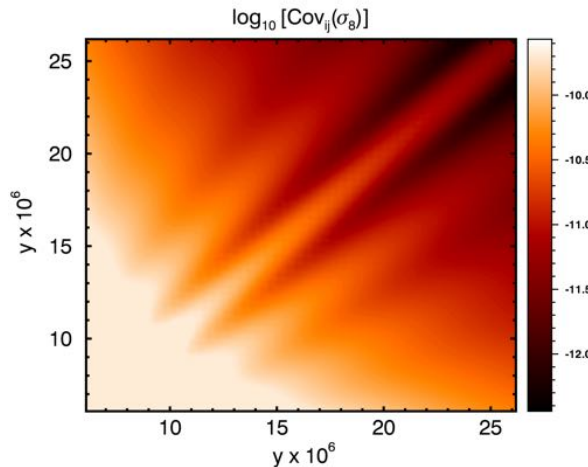


Figure 4.14: Decimal logarithm of the covariance matrix, computed for the best fit solution for the MILCA PDF in figure 4.16.

in 4.40 are only statistical; more conservatively, we estimated also a possible systematic error contribution to be of the same order of the statistical one. Such an error can be due to different assumptions implicit in our modelling of the PDF and to the way we fitted it against data (the choice of the mass and redshift ranges, the y interval actually used for the fit, the way we estimated the noise component or neglecting other radio sources contribution in the PDF). In particular, we tested the dependence of the estimates on the interval of y employed for the fit. We found that the estimate is basically insensitive to the upper y limit, while if we increase the lower y limit the estimate shows variations at the level of $\sim 1 - 2\%$. If the lower limit is decreased, instead, the fit begins to include values of the PDF with a strong noise contribution, and the estimate variations are much larger ($\sim 10\%$). We made sure to leave that region outside the fit for our final estimate, but in order to quantify the variations produced when increasing the lower limit, we introduced a ~ 0.015 systematic error component. As such, the final estimate provided in [Planck Collaboration et al. \(2016h\)](#) is:

$$\sigma_8 = 0.77 \pm 0.02 \quad (68\% \text{ C.L.}) \quad (4.41)$$

Figure 4.16 shows the MILCA and NILC data together with the best-fit $P(y)$ and the region of y actually considered for the fit.

Este documento incorpora firma electrónica, y es copia auténtica de un documento electrónico archivado por la ULL según la Ley 39/2015.
Su autenticidad puede ser contrastada en la siguiente dirección <https://sede.ull.es/validacion/>

Identificador del documento: 973742

Código de verificación: Jfg6xBh0

Fecha: 30/06/2017 15:10:10

Firmado por: DENIS TRAMONTE
UNIVERSIDAD DE LA LAGUNA

RAFAEL DELFIN BARRENA DELGADO
UNIVERSIDAD DE LA LAGUNA

JOSE ALBERTO RUBIÑO MARTIN
UNIVERSIDAD DE LA LAGUNA

ERNESTO PEREDA DE PABLO
UNIVERSIDAD DE LA LAGUNA

30/06/2017 15:21:31

30/06/2017 15:34:17

06/07/2017 13:51:19

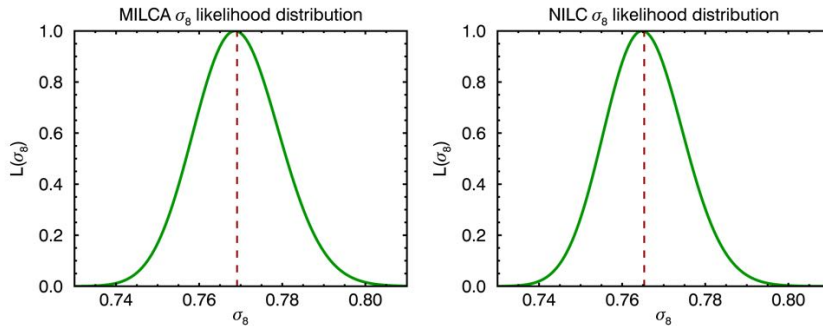


Figure 4.15: Likelihood distributions built using 4.39 with *Planck* MILCA and NILC distribution as a reference. The best fit estimates are marked with the vertical dashed line and are reported in equation 4.40.

This value for σ_8 is in agreement with other estimates coming from cluster statistics (Planck Collaboration et al. 2016h, 2014h, 2016i, 2014g). However, it is in disagreement with the parameter estimated from the CMB, which favours a higher value, $\sigma_8 \simeq 0.83$. This is actually another example of the tension between the estimates of σ_8 from the high-redshift and the low-redshift Universe, which we discussed in the end of chapter 3. It is still an open issue; fixing this tension is actually one of the main driving goals in cluster cosmology.

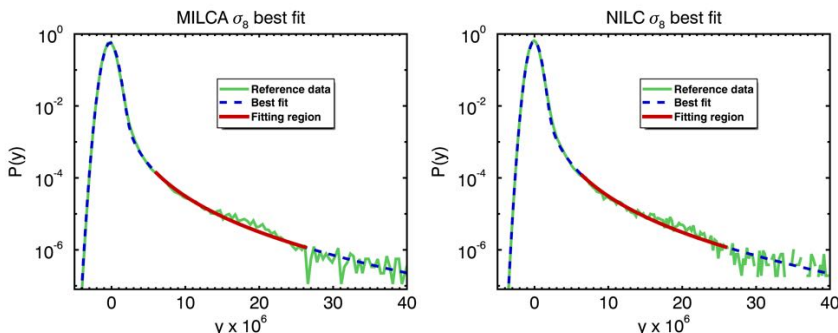


Figure 4.16: MILCA and NILC data together with the corresponding best-fit PDF computed using the σ_8 estimates in 4.40; we also highlight the region of y employed for the fit in both cases.

Este documento incorpora firma electrónica, y es copia auténtica de un documento electrónico archivado por la ULL según la Ley 39/2015.
Su autenticidad puede ser contrastada en la siguiente dirección <https://sede.ull.es/validacion/>

Identificador del documento: 973742

Código de verificación: Jfg6xBh0

Fecha: 30/06/2017 15:10:10

Firmado por: DENIS TRAMONTE
UNIVERSIDAD DE LA LAGUNA

RAFAEL DELFIN BARRENA DELGADO
UNIVERSIDAD DE LA LAGUNA

JOSE ALBERTO RUBIÑO MARTIN
UNIVERSIDAD DE LA LAGUNA

ERNESTO PEREDA DE PABLO
UNIVERSIDAD DE LA LAGUNA

30/06/2017 15:21:31

30/06/2017 15:34:17

06/07/2017 13:51:19

4.6 Forecasts for the COrE mission

We have shown how to use the $P(y)$ as a tool to extract cosmological constraints from real data; however, it can be also used as a forecast tool aimed at assessing the precision that future missions can achieve in the determination of the parameter σ_8 . In this section we consider such a study for the mission COrE. We are going to apply the same analysis performed with *Planck* data, this time with simulated Compton parameter maps.

4.6.1 The mission

COrE (*Cosmic Origins Explorer*) is a fourth-generation full-sky, ESA satellite proposed to be launched around 2030 (The COrE Collaboration et al. 2011), but not selected yet. It will be equipped with polarimeters observing the sky in 15 frequency bands covering the range from 45 GHz to 795 GHz, with resolutions ranging from 23 arcmin to 1.3 arcmin. This frequency range is narrower than the one covered by *Planck*, but COrE will result in a definite improvement in terms of polarisation resolution, sensitivity (10 to 30 times better than *Planck*), systematic control and foreground separation capabilities. Among its scientific goals, the production of polarisation maps will allow to investigate the origins of stars and other cosmic structures, and to push the quest for B-modes to a tensor-to-scalar ratio limit of 10^{-3} (CORE Collaboration et al. 2016); it will also allow to measure the sum of neutrino masses down to 0.03 eV (Di Valentino et al. 2016). The polarisation data at high-frequencies will be the first to cover the whole sky, providing valuable insights into the properties of the Galactic magnetic field and the interstellar medium, apart from characterising a large number of polarized Galactic and extragalactic point-sources (De Zotti et al. 2016).

The frequency range covered by COrE allows the detection of clusters via the tSZ effect (Melin et al. 2017). In particular, the proposed design with a 150 cm primary mirror would result in a total 50000 detected clusters, the most massive ones also at $z > 1.5$. When combined with the expected future outcomes from ACT and SPT telescopes, the final cluster catalogue would amount to ~ 220000 objects down to masses $M_{500} \sim 2 - 3 \times 10^{13} h^{-1} M_\odot$.

We are going to consider now a COrE SZ simulated map and assess the precision achievable from its use to estimate σ_8 .

4.6.2 Simulated data

The COrE Collaboration has produced individual frequency maps, simulated using the current version of the *Planck* Sky Model (Delabrouille et al. 2013).

Este documento incorpora firma electrónica, y es copia auténtica de un documento electrónico archivado por la ULL según la Ley 39/2015.
Su autenticidad puede ser contrastada en la siguiente dirección <https://sede.ull.es/validacion/>

Identificador del documento:	973742	Código de verificación:	Jfg6xBh0
Firmado por:	DENIS TRAMONTE UNIVERSIDAD DE LA LAGUNA	Fecha:	30/06/2017 15:10:10
	RAFAEL DELFIN BARRENA DELGADO UNIVERSIDAD DE LA LAGUNA		30/06/2017 15:21:31
	JOSE ALBERTO RUBIÑO MARTIN UNIVERSIDAD DE LA LAGUNA		30/06/2017 15:34:17
	ERNESTO PEREDA DE PABLO UNIVERSIDAD DE LA LAGUNA		06/07/2017 13:51:19

Signals included in the maps are CMB, Galactic foregrounds (free-free, synchrotron, dust), CIB, radio and IR point sources, and the cluster signal, which is simulated using the Delabrouille-Melin-Bartlett method (Delabrouille et al. 2002). These maps are then smoothed according to the nominal resolution at each frequency.

Ω_m	Ω_b	Ω_Λ	h	n_s	σ_8	b
0.272	4.84×10^{-2}	0.728	0.678	0.968	0.815	0.37

Table 4.2: Fiducial cosmology and mass bias used for COrE forecast.

The Compton parameter map is reconstructed using the NILC method. The high number of COrE frequency bands (19) results in the y map to be reconstructed with unprecedent accuracy. We show in figure 4.17 the final all-sky Compton parameter map with a 37% mask to remove the Galactic plane region. In the same figure we also show the corresponding y PDF distribution, together with the Gaussian fit to the noise-dominated central region. The cosmological parameters used for this realisation are listed in table 4.2.

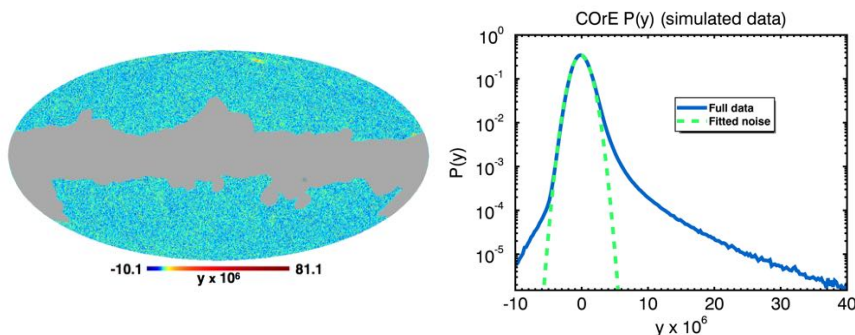


Figure 4.17: COrE simulated all-sky Compton parameter map, together with the corresponding PDF and the fit to its noise component.

4.6.3 Results

We employed the same method used for estimating σ_8 with *Planck* data. We fixed all cosmological parameters to their nominal values employed for simulating the data (table 4.2) with the exception of σ_8 , which is left free. For each value of σ_8 , the likelihood is determined by using equation 4.39; the reference data is the COrE reconstructed $P(y)$ after dropping the negative y tail due to

Este documento incorpora firma electrónica, y es copia auténtica de un documento electrónico archivado por la ULL según la Ley 39/2015.
Su autenticidad puede ser contrastada en la siguiente dirección <https://sede.ull.es/validacion/>

Identificador del documento: 973742

Código de verificación: Jfg6xBh0

Fecha: 30/06/2017 15:10:10

Firmado por: DENIS TRAMONTE
UNIVERSIDAD DE LA LAGUNA

RAFAEL DELFIN BARRENA DELGADO
UNIVERSIDAD DE LA LAGUNA

JOSE ALBERTO RUBIÑO MARTIN
UNIVERSIDAD DE LA LAGUNA

ERNESTO PEREDA DE PABLO
UNIVERSIDAD DE LA LAGUNA

30/06/2017 15:21:31

30/06/2017 15:34:17

06/07/2017 13:51:19

the emission from radio sources. The PDF is computed employing the redshift range $[1 \times 10^{-3}, 3]$, and a virial mass range $[7 \times 10^{13}, 1 \times 10^{16}] h^{-1} M_{\odot}$. The bias parameter employed for the simulation was $b = 0.37$: the theoretical computation of the $P(y)$ also employed that value, and a beam effective FWHM of $4'$. We show in figure 4.18 the resulting likelihood distribution and the best-fit $P(y)$, together with the effective Compton parameter range considered for the fit. The final estimate was:

$$\sigma_8 = 0.814 \pm 0.002 \quad (68\% \text{ C.L.}) \quad (4.42)$$

which is compatible with the nominal value employed for the simulation ($\sigma_8 = 0.815$). This estimate is reported in Melin et al. (2017).

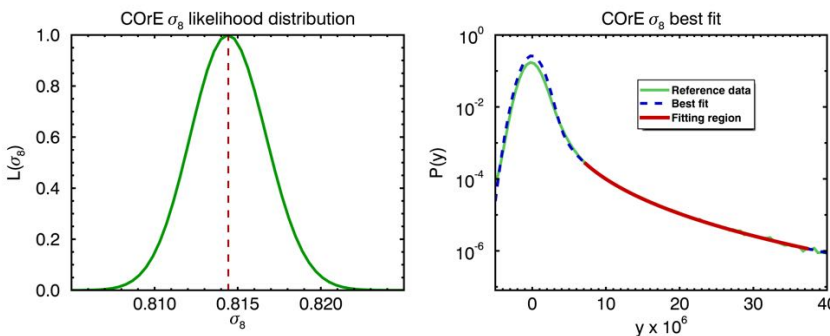


Figure 4.18: Left: likelihood distributions built using 4.39 with the COrE simulated Compton map as a reference. Right: the best-fit $P(y)$ is overplotted on COrE simulated data, showing the y range actually employed for the fit.

The improvement in the precision with respect to the *Planck* estimates 4.40 is evident; if we consider the final estimate 4.41 provided in *Planck* 2015 release, the COrE error bar is reduced by one order of magnitude.

4.7 Conclusions

We have shown in this chapter another way galaxy clusters can be employed as a cosmological probe. Their strict relation with the abundance of matter at large scales can be exploited not only by studying the redshift evolution of their abundance, but also by considering the diffuse tSZ emission they contribute to. This is a change of perspective with respect to the previous chapter: the tSZ effect is no longer just a tool used to detect cluster of galaxies, but it becomes itself the main observable against which cosmological models can be tested.

Este documento incorpora firma electrónica, y es copia auténtica de un documento electrónico archivado por la ULL según la Ley 39/2015.
Su autenticidad puede ser contrastada en la siguiente dirección <https://sede.ull.es/validacion/>

Identificador del documento: 973742

Código de verificación: Jfg6xBh0

Fecha: 30/06/2017 15:10:10

Firmado por: DENIS TRAMONTE
UNIVERSIDAD DE LA LAGUNA

RAFAEL DELFIN BARRENA DELGADO
UNIVERSIDAD DE LA LAGUNA

JOSE ALBERTO RUBIÑO MARTIN
UNIVERSIDAD DE LA LAGUNA

ERNESTO PEREDA DE PABLO
UNIVERSIDAD DE LA LAGUNA

30/06/2017 15:21:31

30/06/2017 15:34:17

06/07/2017 13:51:19

The reference data in this case are full sky maps of the tSZ (Delabrouille et al. 2002), better translated into the corresponding Compton parameter y to get rid of the frequency dependence.

The use of statistics related to the Compton map has already been largely discussed in the literature; among the possible tools that can be used we can list its spectrum (Komatsu & Seljak 2002; Hill & Pajer 2013), bispectrum (Bhattacharya et al. 2012) and other moments of the y probability distribution (Hill & Sherwin 2013). The description of each of these methods goes beyond the scope of this work. We concentrated in particular on the one dimensional probability distribution function for the Compton parameter, or $P(y)$, which turns out to be particularly sensitive to the value of the parameter σ_8 . Its relation with galaxy clusters comes from the particular signature that they produce on this distribution (Rubiño-Martín & Sunyaev 2003), resulting in a clear skewness of the PDF towards higher values of y . In this chapter we employed a formalism to model analytically the tSZ PDF (Hill et al. 2014) and fit it against the data from the *Planck* mission to obtain an estimate of σ_8 .

We described how the emission from individual galaxy clusters contributes to the overall Compton map. This required the assumption of a proper cluster pressure profile; we employed the baseline model proposed by Arnaud et al. (2010) and properly rescaled it in order to match the *Planck* flux-mass scaling relation in terms of the dependence on the mass bias b . This pressure profile in turn determines a Compton parameter profile, whose contribution to the final PDF can be obtained via a geometrical interpretation under the assumption that clusters do not overlap. We also analytically derived a way to include the smoothing that is applied to the signal whenever it is observed by a real radio telescope (this also includes possible filtering performed at the level of the Compton maps). Finally, we addressed the contribution of instrumental noise and other foregrounds to the PDF, and showed two ways it can be implemented analytically: either by convolution of the cluster-only and the noise-only PDFs, or by explicit inclusion of the noise at the level of the Compton parameter for an individual cluster contribution.

We tested this formalism by direct comparison with simulated Compton parameter maps. The pure SZ map was simulated by placing clusters over the sky in random positions, with mass and redshift sampled from the cluster number distribution. The map was then properly smoothed and a separate noise map was added to simulate instrumental response and other foregrounds contamination. We simulated 500 complete maps and averaged the corresponding PDF to avoid sample bias effects. The comparison of the average $P(y)$ with the one computed analytically proved the consistency of our implementation.

We finally considered real *Planck* data and built a σ_8 -based likelihood by

Este documento incorpora firma electrónica, y es copia auténtica de un documento electrónico archivado por la ULL según la Ley 39/2015.
Su autenticidad puede ser contrastada en la siguiente dirección <https://sede.ull.es/validacion/>

Identificador del documento:	973742	Código de verificación:	Jfg6xBh0
Firmado por:	DENIS TRAMONTE UNIVERSIDAD DE LA LAGUNA	Fecha:	30/06/2017 15:10:10
	RAFAEL DELFIN BARRENA DELGADO UNIVERSIDAD DE LA LAGUNA		30/06/2017 15:21:31
	JOSE ALBERTO RUBIÑO MARTIN UNIVERSIDAD DE LA LAGUNA		30/06/2017 15:34:17
	ERNESTO PEREDA DE PABLO UNIVERSIDAD DE LA LAGUNA		06/07/2017 13:51:19

comparing the theoretical PDF with the data. The fit was done over a range of the Compton parameter that was free from foreground contamination and instrumental noise. The extended nature of the Compton profile introduced correlation between y bins, which required the use of a proper covariance matrix to take it into account. The final estimate was $\sigma_8 = 0.77 \pm 0.02$, which is reported in [Planck Collaboration et al. \(2016h\)](#). The final error includes both the statistical estimate from the fit, and an assessed systematic contribution due to the assumptions at the basis of our modelling.

Notice that this method is different from the use of cluster abundance to test cosmological models. Still, the two provide consistent estimates for σ_8 , which are in tension with the ones coming from CMB studies. This tension reflects a difference between cosmology with the low-redshift and the high-redshift Universe which is still an open issue. As already mentioned in the end of chapter 3, there are different proposed solutions to this problem (better characterisation of the mass bias parameter, non-minimal neutrino mass, extension to the Λ C DM model, etc.) but none of them is currently enough to close the issue. Broader data set from future missions will help shedding light on this subject.

In the last part of the chapter we showed indeed how the tSZ PDF can be used also as a forecast tool, to make predictions on the σ_8 estimate with future missions and assess the precision they can achieve. We concentrated on the COrE mission, which will be a fourth-generation ESA CMB satellite. We employed a simulated COrE map and repeated the same estimation technique we employed with *Planck*. The final estimate, $\sigma_8 = 0.814 \pm 0.002$, is compatible with the value used for realising the simulation and has been included in [Melin et al. \(2017\)](#). The error we found is considerably lower than the one coming from the *Planck* estimate.

Este documento incorpora firma electrónica, y es copia auténtica de un documento electrónico archivado por la ULL según la Ley 39/2015.
Su autenticidad puede ser contrastada en la siguiente dirección <https://sede.ull.es/validacion/>

Identificador del documento:	973742	Código de verificación:	Jfg6xBh0
Firmado por:	DENIS TRAMONTE UNIVERSIDAD DE LA LAGUNA	Fecha:	30/06/2017 15:10:10
	RAFAEL DELFIN BARRENA DELGADO UNIVERSIDAD DE LA LAGUNA		30/06/2017 15:21:31
	JOSE ALBERTO RUBIÑO MARTIN UNIVERSIDAD DE LA LAGUNA		30/06/2017 15:34:17
	ERNESTO PEREDA DE PABLO UNIVERSIDAD DE LA LAGUNA		06/07/2017 13:51:19

Este documento incorpora firma electrónica, y es copia auténtica de un documento electrónico archivado por la ULL según la Ley 39/2015.
Su autenticidad puede ser contrastada en la siguiente dirección <https://sede.ull.es/validacion/>

Identificador del documento: 973742

Código de verificación: Jfg6xBh0

Firmado por: DENIS TRAMONTE UNIVERSIDAD DE LA LAGUNA	Fecha: 30/06/2017 15:10:10
RAFAEL DELFIN BARRENA DELGADO UNIVERSIDAD DE LA LAGUNA	30/06/2017 15:21:31
JOSE ALBERTO RUBIÑO MARTIN UNIVERSIDAD DE LA LAGUNA	30/06/2017 15:34:17
ERNESTO PEREDA DE PABLO UNIVERSIDAD DE LA LAGUNA	06/07/2017 13:51:19

5

The QUIJOTE Experiment

In this chapter we focus on the QUIJOTE experiment, which is devoted to the observation of the CMB polarisation. The study of the primordial CMB anisotropies requires a proper characterisation of the foreground emissions. Since November 2012, QUIJOTE has been observing different regions of the sky with the aim of characterising the foreground contributions that have to be removed from the future CMB maps. It is using a multi-frequency instrument (MFI) operating in the range between 10 and 20 GHz and at large angular scales (~ 1 degree).

We begin the Chapter with a general description of the experiment and of the MFI instrument. We will then consider the calibration of the pointing model of the first QUIJOTE telescope, which has been an important part of this thesis. We show how we modelled the telescope non-idealities, the strategy that we employed for their characterisation, and the complications produced by the degeneracy with the focal plane geometry. We will finally show the pointing model solution that we achieved, which provides an absolute pointing error below 1 arcmin, and that has been implemented in the pipeline for the MFI data analysis: in particular, this model has been employed for obtaining the first QUIJOTE scientific results published in Génova-Santos et al. (2015a) and Génova-Santos et al. (2017).

In the last part of the Chapter we will describe the analyses we performed in the Galactic regions W49, W51 and IC443. We will present the work done for producing clean maps of these regions, that we employed for a first determination of the corresponding spectral energy distribution of intensity and polarisation flux densities. Results show hints of anomalous microwave emissions in all regions, and of polarised emission probably due to synchrotron. The results of this work will be presented in Tramonte et al. (in prep.).

5.1 Project overview

The *QUIJOTE Experiment* (Génova-Santos et al. 2015b; Rubiño-Martín et al. 2017), short for *Q-U-I JOint TEnerife Experiment*,¹ is a scientific collabora-

¹*Q*, *U* and *I* are the Stokes parameters.

tion between the *Instituto de Astrofísica de Canarias*, the *Instituto de Física de Cantabria*, the IDOM company, and the Universities of Cantabria, Manchester and Cambridge². The aim of the experiment is to characterise the polarisation of the CMB, and other Galactic and extragalactic physical processes, in the frequency range 10–40 GHz and at angular scales larger than 1 degree; it operates from the Teide Observatory (Tenerife, Spain) at an altitude of 2400 m. The previous experiments hosted in this site, that we mentioned in section 1.3.4, proved that the atmospheric conditions are optimal for CMB observations in the microwave range. QUIJOTE consists of two telescopes and three instruments (Rubiño-Martín et al. 2012b).



Figure 5.1: Picture of the QUIJOTE telescopes in their enclosure at the Teide Observatory: QT1 is visible in the back, QT2 is visible in the front.

The telescopes enclosure and the building hosting the control room were finished in June 2009. The first telescope (QT1) was installed in May 2012, while the second telescope (QT2) was installed in July 2014. Both telescopes are altazimuth-mount type; the primary, 2.25 m, parabolic mirror and the secondary, 1.89 m, hyperbolic mirror are disposed in an offset Gregorian Dracon scheme, which provides optimal cross-polarisation properties (designed to be ≤ -35 dB) and symmetric beams. Each telescope is mounted on its own

²See also the reference website: <https://www.iac.es/proyecto/cmb/pages/en/quipote-cmb-experiment.php>

Este documento incorpora firma electrónica, y es copia auténtica de un documento electrónico archivado por la ULL según la Ley 39/2015.
Su autenticidad puede ser contrastada en la siguiente dirección <https://sede.ull.es/validacion/>

Identificador del documento: 973742	Código de verificación: Jfg6xBh0
Firmado por: DENIS TRAMONTE <i>UNIVERSIDAD DE LA LAGUNA</i>	Fecha: 30/06/2017 15:10:10
RAFAEL DELFIN BARRENA DELGADO <i>UNIVERSIDAD DE LA LAGUNA</i>	30/06/2017 15:21:31
JOSE ALBERTO RUBIÑO MARTIN <i>UNIVERSIDAD DE LA LAGUNA</i>	30/06/2017 15:34:17
ERNESTO PEREDA DE PABLO <i>UNIVERSIDAD DE LA LAGUNA</i>	06/07/2017 13:51:19

platform that can rotate around the azimuth axis at a maximum frequency of 6 rpm (or 36 deg/s). Further information on the telescopes can be found in Gomez et al. (2010) and Sanquince-García et al. (2016).

The first QUIJOTE instrument is the *Multi-Frequency Instrument* (MFI Hoyland et al. 2012), a multichannel instrument providing the frequency coverage between 10 and 20 GHz; it is mounted on the QT1 telescope and started operation in November 2012. It consists of four conical corrugated *feedhorns*³, designed by the University of Manchester, each of which feeds a novel cryogenic on-axis rotating polar modulator which can rotate with a maximum speed of 1 Hz. There are two possible operational modes: the continuous mode, corresponding to a continuous rotation of the polarimeters, and the discrete mode, with changes in the positions of the motors in steps of 22.5°. Mechanical issues related to the use of the continuous spinning of the modulators, that emerged during the laboratory tests, led to the use of the discrete mode alone. Two horns observe at 10 – 14 GHz, and the other two at 16 – 20 GHz, all with two channels with a 2 GHz bandwidth each. The instantaneous sensitivity is $\sim 280 \mu\text{Ks}^{1/2}$ per frequency band. The MFI instrument is devoted primarily to the characterisation of the Galactic emission. It is the instrument we will deal with for the rest of this work, so we will provide further information in section 5.1.2.

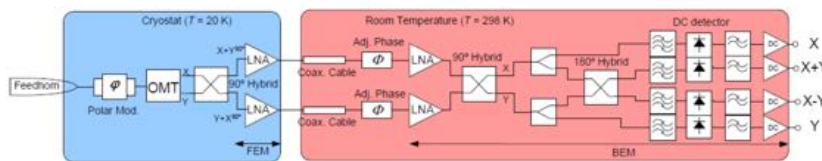


Figure 5.2: Schematic representation of the MFI receiving system.

The second QUIJOTE instrument is the *Thirty-Gigahertz Instrument* (TGI Hoyland et al. 2014), which consists of 31 polarimeters operating at 30 GHz, with a 8 GHz bandwidth and an instantaneous sensitivity of $\sim 50 \mu\text{Ks}^{1/2}$ for the full array. The TGI was installed onto the QT2 telescope in May 2016, when the commissioning of three pixels began. A sketch of the receiving system of a

³A *waveguide horn* is the simplest type of aperture antenna; it consists of a tapered waveguide device, that collects radiation from the large end and hosts the antenna at the narrow end. An advantage of using horn antennas is that they pick up very little ground radiation, being free from external feed-support structures that scatter ground radiation into the receiver; the lack of these external structures also results in an easier determination of the instrument gain, thus allowing the measurement of absolute flux densities.

TGI horn is represented in figure 5.3. Notice that, unlike the MFI, the TGI does not rely in the mechanical movement of polar modulators in order to isolate different polarisation direction; instead, it employs a fixed polariser with the combination of two phase-switches, each with two possible phase states, one at 0/90 degrees and the other at 0/180, generating four polarisation states. This configuration, apart from being able to outputting directly the Stokes parameters I , Q and U , has the advantage that it does not involve movement of mechanical parts, thus being suitable for the long term operations for which the TGI has been designed.

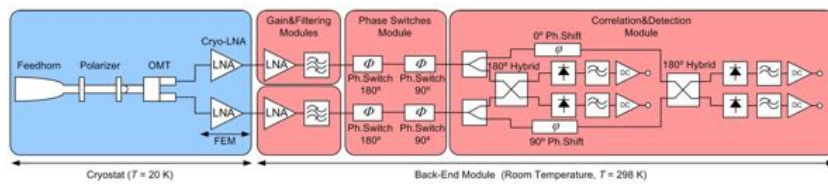


Figure 5.3: Schematic representation of the TGI receiving system.

The third QUIJOTE instrument is the *Forty-Gigahertz Instrument* (FGI), which is currently in the integration phase. It will host 31 polarimeters working at 42 GHz, with a 12 GHz bandwidth and an expected full-array sensitivity of $\sim 52 \mu\text{Ks}^{1/2}$. The design of the FGI resembles that of the TGI, the FGI also employing phase switches to generate different polarisation states. The FGI will be installed in the QT2 telescope. Both the TGI and the FGI are dedicated to CMB science.

The nominal characteristics of the three QUIJOTE instruments are summarised in table 5.1. In the table the *noise equivalent temperature* (NET) is reported, computed as:

$$\text{NET} \equiv \sqrt{2} \frac{T_{\text{sys}}}{\sqrt{\Delta\nu N_{\text{chan}}}}. \quad (5.1)$$

Here, $\Delta\nu$ is the receiver bandwidth, T_{sys} is the total system temperature (sum of the receiver contribution, the estimated contribution of the opto-mechanics, the spillover contribution, the atmospheric contribution at the considered frequency and the CMB contribution) and N_{chan} is the number of channels, computed as the number of horns times the number of output channels per horn. In the case of the TGI and FGI we report the NET for the full array (including all horns), while for the MFI we report the NET computed for each frequency band (8 channels per band). The NET can be used to compute the noise sensitivity

Este documento incorpora firma electrónica, y es copia auténtica de un documento electrónico archivado por la ULL según la Ley 39/2015.
Su autenticidad puede ser contrastada en la siguiente dirección <https://sede.ull.es/validacion/>

Identificador del documento: 973742

Código de verificación: Jfg6xBh0

Firmado por: DENIS TRAMONTE UNIVERSIDAD DE LA LAGUNA	Fecha: 30/06/2017 15:10:10
RAFAEL DELFIN BARRENA DELGADO UNIVERSIDAD DE LA LAGUNA	30/06/2017 15:21:31
JOSE ALBERTO RUBIÑO MARTIN UNIVERSIDAD DE LA LAGUNA	30/06/2017 15:34:17
ERNESTO PEREDA DE PABLO UNIVERSIDAD DE LA LAGUNA	06/07/2017 13:51:19

	MFI				TGI	FGI
Nominal Frequency [GHz]	11	13	17	19	30	42
Bandwidth [GHz]	2	2	2	2	8	12
Number of horns	2	2	2	2	31	31
Channels per horn	4	4	4	4	4	4
Beam FWHM [°]	0.92	0.92	0.60	0.60	0.37	0.28
T_{sys} [K]	25	25	25	25	35	45
NET [$\mu\text{K s}^{1/2}$]	280	280	280	280	50	52
Sensitivity [Jy $\text{s}^{1/2}$]	0.30	0.42	0.31	0.38	0.065	0.074

Table 5.1: Nominal characteristics of the three instruments: MFI, TGI and FGI. Values of NET (and sensitivity) are intended per frequency band in the case of the MFI, and for the full array in the case of the TGI and FGI. Sensitivities are quoted in units of Jansky, $1\text{Jy} = 10^{-26}\text{Wm}^{-2}\text{Hz}^{-1}$, and are referred to Stokes Q and U parameters.

ΔS , which in terms of flux is given by:

$$\Delta S = \text{NET} \frac{2k_B}{c^2} \nu^2 \Omega_B, \quad (5.2)$$

where k_B si the Boltzmann constant, c the speed of light, ν the observing frequency and Ω_B the beam solid angle; sensitivities computed with 5.2 are reported in table 5.1 in units $\text{Jy s}^{1/2}$. For further technical information about QUIJOTE telescopes and instruments see Pérez-de-Taoro et al. (2014) and Pérez-de-Taoro et al. (2016).

5.1.1 Scientific goals

The QUIJOTE Experiment has two primary scientific goals ⁴:

- to detect the imprint of gravitational *B*-modes if they have an amplitude $r \geq 0.05$ (see section 1.3.3);
- to provide essential information of the polarisation of the synchrotron emission and the anomalous microwave emission (see section 1.3.4) from our Galaxy at low frequencies.

In order to accomplish these tasks, QUIJOTE is expected to conduct two large *surveys in polarisation*:

⁴Notice that the sensitivities reported in section 5.1.1 are quoted from Rubiño-Martín et al. (2017) and are more conservative than the nominal values from table 5.1; in the case of the MFI surveys, these sensitivities are measured on the corresponding maps.

Identificador del documento: 973742	Código de verificación: Jfg6xBh0
Firmado por: DENIS TRAMONTE UNIVERSIDAD DE LA LAGUNA	Fecha: 30/06/2017 15:10:10
RAFAEL DELFIN BARRENA DELGADO UNIVERSIDAD DE LA LAGUNA	30/06/2017 15:21:31
JOSE ALBERTO RUBIÑO MARTIN UNIVERSIDAD DE LA LAGUNA	30/06/2017 15:34:17
ERNESTO PEREDA DE PABLO UNIVERSIDAD DE LA LAGUNA	06/07/2017 13:51:19

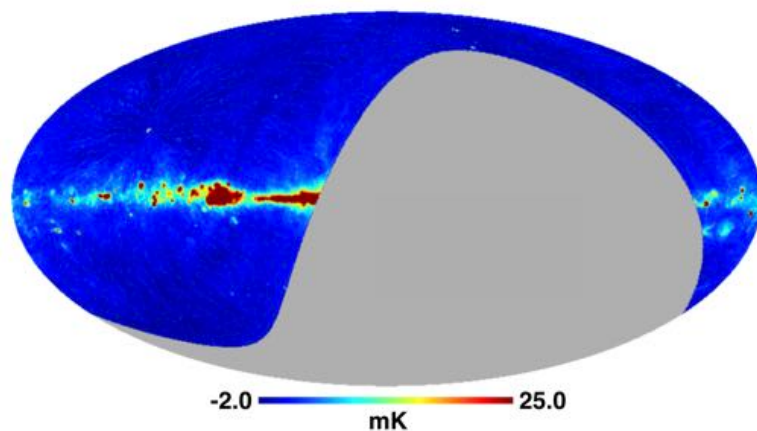


Figure 5.4: Preliminary map of the wide survey at 11 GHz, plotted in Galactic coordinates.
Figure taken from Rubiño-Martín et al. (2017).

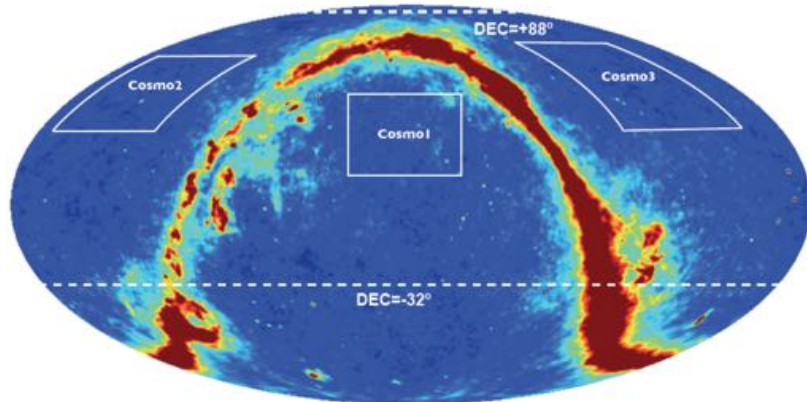


Figure 5.5: WMAP all sky map with the three cosmological (“COSMO”) fields selected for the QUIJOTE deep survey, plotted in equatorial coordinates. Notice that the three fields are selected away from the Galactic plane in order to minimise the contamination from Galactic foregrounds. The two dashed lines mark the limits of the sky region accessible by QUIJOTE.
Figure adapted from Rubiño-Martín et al. (2017).

Este documento incorpora firma electrónica, y es copia auténtica de un documento electrónico archivado por la ULL según la Ley 39/2015.
Su autenticidad puede ser contrastada en la siguiente dirección <https://sede.ull.es/validacion/>

Identificador del documento: 973742

Código de verificación: Jfg6xBh0

Fecha: 30/06/2017 15:10:10

Firmado por: DENIS TRAMONTE
UNIVERSIDAD DE LA LAGUNA

RAFAEL DELFIN BARRENA DELGADO
UNIVERSIDAD DE LA LAGUNA

JOSE ALBERTO RUBIÑO MARTIN
UNIVERSIDAD DE LA LAGUNA

ERNESTO PEREDA DE PABLO
UNIVERSIDAD DE LA LAGUNA

30/06/2017 15:21:31

30/06/2017 15:34:17

06/07/2017 13:51:19

- a shallow Galactic survey, covering a total area of $20\,000 \text{ deg}^2$, with the goal of reaching final sensitivities of $\sim 25 \mu\text{K}$ per beam (at each frequency band) with the MFI, $\sim 4 \mu\text{K}$ per beam with the TGI and $\sim 6 \mu\text{K}$ per beam with the FGI. With a total 9 months of effective observing time with the MFI (figure 5.4), the resulting measured sensitivity is $\sim 80 \mu\text{K}$ per beam in Q and U at elevation above 60 deg.
- a deep “cosmological” survey, covering a sky area of $3\,000 \text{ deg}^2$ split in three separate “COSMO” fields (figure 5.5). After 2 years of dedicated observing time, it is expected to reach final sensitivities of $\sim 5 \mu\text{K}$ per beam with the MFI, and $\sim 1 \mu\text{K}$ per beam with the TGI and FGI. The total observation time with the MFI on the COSMO fields amounts to 6.3 months at the time of writing (June 10, 2017).

The utility of the final maps from the MFI will be twofold. First of all, they constitute a unique low frequency complement to the maps delivered by *Planck*, and as such they can provide a deeper understanding of radio foreground emissions, both in intensity and in polarisation; this information would be particularly useful for future CMB experiments (Errard et al. 2016). Second, the MFI maps of the COSMO fields can be used to clean the future TGI and FGI maps from the foreground contamination, enabling the study of the polarised CMB emission in those fields (we remind that the CMB polarised signal is subdominant compared to the foregrounds, see figure 1.6). It is expected that, after one year of TGI observations in the COSMO fields, it would be possible to constrain the tensor to scalar ratio down to $r = 0.1$ (95% C.L.); by combining three years of observations with the TGI and two years with the FGI this limit can be pushed down to $r = 0.05$ (95% C.L.), which is the ultimate goal of the QUIJOTE experiment.

In addition to these main goals, QUIJOTE is dedicated to other non-core science, based on observations of specific sky regions with the aim of characterising their emission. For instance, observations of the *Perseus* molecular complex were used to study the polarisation of the anomalous microwave emission (AME), providing the first upper limits for polarised intensity in this spectral range (Génova-Santos et al. 2015a). A similar study was conducted on the W43 molecular complex and resulted in the most stringent limits of AME polarisation up to date, reported in Génova-Santos et al. (2017): a polarization limit $< 0.22\%$ is obtained at 40.6 GHz (WMAP frequency), while using QUIJOTE data lowest limit is $< 0.39\%$ at 17 GHz. In the same reference the nearby region W44 (a supernova remnant) is also studied to provide a characterisation of the synchrotron polarised emission. Similar studies are being carried out by the QUIJOTE Collaboration in other Galactic regions, like the Fan region, W63,

Este documento incorpora firma electrónica, y es copia auténtica de un documento electrónico archivado por la ULL según la Ley 39/2015.
Su autenticidad puede ser contrastada en la siguiente dirección <https://sede.ull.es/validacion/>

Identificador del documento:	973742	Código de verificación:	Jfg6xBh0
Firmado por:	DENIS TRAMONTE UNIVERSIDAD DE LA LAGUNA	Fecha:	30/06/2017 15:10:10
	RAFAEL DELFIN BARRENA DELGADO UNIVERSIDAD DE LA LAGUNA		30/06/2017 15:21:31
	JOSE ALBERTO RUBIÑO MARTIN UNIVERSIDAD DE LA LAGUNA		30/06/2017 15:34:17
	ERNESTO PEREDA DE PABLO UNIVERSIDAD DE LA LAGUNA		06/07/2017 13:51:19

3C58 or the Galactic Haze. As part of this work, we will consider in detail the study of the molecular complexes W49 and W51, and of the supernova remnant IC443.

5.1.2 The Multi Frequency Instrument

We give here some additional information about the MFI, which is the instrument we are going to consider for the rest of this Chapter.

Instrument output

The MFI hosts four horns, each one operating at two different frequencies. Conventionally, we call horns 1 and 3 the ones operating at lower frequencies (11 and 13 GHz), and horns 2 and 4 the ones operating at higher frequencies (17 and 19 GHz). The scheme of the receiving system of one MFI horn is represented in figure 5.2. It is divided into two main blocks: a *front-end module* (FEM), in charge of detecting the incoming radio signal and converting it into an electric signal, and a *back-end module*, where the signal is further processed and finally outputted. The FEM is located inside a cryostat that provides cryogenic temperatures (around 20 K) in order to minimise the impact of thermal noise in the detected signal. Behind each horn there is a *polar modulator* (PM) that produces a modulation of the light polarisation quantified by the angle ϕ with respect to a reference direction (e.g. the azimuth axis; see equation 5.5). Although it was initially thought to spin continuously, in order to prevent mechanical damage to the system the modulator has been used by switching between four discrete directions quantified by $\phi_m = 0.0^\circ, 22.5^\circ, 45.0^\circ, 67.5^\circ$, and labelled A, B, C and D respectively. The signal is then processed by an *ortho-mode transducer* that separates the two orthogonal components x and y , which are then correlated by a *90-degree hybrid*, resulting in two separated channels carrying both contributions from x and y polarisation components. Each of these channels passes through a *low-noise amplifier* (LNA) in order to enhance the signal-to-noise ratio. The signal then enters the BEM where further processing of the signal is performed; we do not enter into the details of each electronic component. The final output are four channels labelled as X, Y, X+Y and X-Y. Their relation with the Stokes parameters I , Q and U can be found using the Jones formalism for the Stokes parameters. The output voltage can be expressed by (Jarosik et al. 2003):

$$V = s |\mathbf{E}|^2, \quad (5.3)$$

where s is the detector responsivity and \mathbf{E} is the output electric field, that can be computed using the Jones formalism, with a global MFI Jones matrix

Este documento incorpora firma electrónica, y es copia auténtica de un documento electrónico archivado por la ULL según la Ley 39/2015.
Su autenticidad puede ser contrastada en la siguiente dirección <https://sede.ull.es/validacion/>

Identificador del documento:	973742	Código de verificación:	Jfg6xBh0
Firmado por:	DENIS TRAMONTE UNIVERSIDAD DE LA LAGUNA	Fecha:	30/06/2017 15:10:10
	RAFAEL DELFIN BARRENA DELGADO UNIVERSIDAD DE LA LAGUNA		30/06/2017 15:21:31
	JOSE ALBERTO RUBIÑO MARTIN UNIVERSIDAD DE LA LAGUNA		30/06/2017 15:34:17
	ERNESTO PEREDA DE PABLO UNIVERSIDAD DE LA LAGUNA		06/07/2017 13:51:19

obtained by multiplying the individual Jones matrices of all the optical elements visible in figure 5.2. The final results for the four output channels are:

$$\begin{aligned} V_x &= \frac{s_x}{2} \left[\frac{g_1^2 + g_2^2}{2} I - g_1 g_2 (Q \cos \phi - U \sin \phi) - \frac{g_1^2 - g_2^2}{2} V \right], \\ V_y &= \frac{s_y}{2} \left[\frac{g_1^2 + g_2^2}{2} I + g_1 g_2 (Q \cos \phi - U \sin \phi) - \frac{g_1^2 - g_2^2}{2} V \right], \\ V_{x+y} &= \frac{s_{x+y}}{2} \left[\frac{g_1^2 + g_2^2}{2} I + g_1 g_2 (Q \sin \phi + U \cos \phi) - \frac{g_1^2 - g_2^2}{2} V \right], \\ V_{x-y} &= \frac{s_{x-y}}{2} \left[\frac{g_1^2 + g_2^2}{2} I - g_1 g_2 (Q \sin \phi + U \cos \phi) - \frac{g_1^2 - g_2^2}{2} V \right]. \end{aligned} \quad (5.4)$$

In these relations g_1 and g_2 are the *gain* factors of the amplifiers and the s_i are the responsivities of the four lines from the BEM to the final output channels. The angle ϕ accounts for the rotation of the Stokes parameters when transforming from the sky reference frame to the local instrumental frame. It encodes the contribution from the modulator angle with respect to its zero, ϕ_m , and the parallactic angle ϕ_p :

$$\phi = 4\phi_m + 2\phi_p. \quad (5.5)$$

By different combinations of the equations in 5.4 it is possible to extract the Stokes parameters from the output signals. This receiving scheme is repeated twice for each horn, corresponding to the two operating frequencies; as a result, each horn has a total of eight channels in output. The scientific exploitation of the MFI is done by analyzing the output of its 32 channels.

Before closing this section we mention that the MFI configuration described in this section and represented in figure 5.2 was not implemented from the beginning. Previously, another configuration was employed, with the same scheme as in figure 5.2 but without the two 90° hybrids. In that case, the output of the four channels for each frequency band was given by:

$$\begin{aligned} V_x &= s_x g_1^2 \frac{1}{2} (I + Q \cos \phi - U \sin \phi) \\ V_y &= s_y g_2^2 \frac{1}{2} (I - Q \cos \phi + U \sin \phi) \\ V_{x+y} &= s_{x+y} \frac{1}{2} \left[\frac{g_1^2 + g_2^2}{2} I + \frac{g_1^2 - g_2^2}{2} (Q \cos \phi - U \sin \phi) + g_1 g_2 (Q \sin \phi + U \cos \phi) \right] \\ V_{x-y} &= s_{x-y} \frac{1}{2} \left[\frac{g_1^2 + g_2^2}{2} I + \frac{g_1^2 - g_2^2}{2} (Q \cos \phi - U \sin \phi) - g_1 g_2 (Q \sin \phi + U \cos \phi) \right]. \end{aligned} \quad (5.6)$$

Este documento incorpora firma electrónica, y es copia auténtica de un documento electrónico archivado por la ULL según la Ley 39/2015.
Su autenticidad puede ser contrastada en la siguiente dirección <https://sede.ull.es/validacion/>

Identificador del documento: 973742	Código de verificación: Jfg6xBh0	Fecha: 30/06/2017 15:10:10
Firmado por: DENIS TRAMONTE UNIVERSIDAD DE LA LAGUNA		
RAFAEL DELFIN BARRENA DELGADO UNIVERSIDAD DE LA LAGUNA		30/06/2017 15:21:31
JOSE ALBERTO RUBIÑO MARTIN UNIVERSIDAD DE LA LAGUNA		30/06/2017 15:34:17
ERNESTO PEREDA DE PABLO UNIVERSIDAD DE LA LAGUNA		06/07/2017 13:51:19

The new configuration with the 90° hybrids was implemented in horn 1 in April 2014, and in December 2015 in horns 2, 3 and 4. The Stokes parameters from data acquired before those dates were obtained using equations 5.6.

MFI and the focal plane

The four horns of the MFI are placed in the telescope focal plane. They result in a peculiar configuration determined by the coordinates listed in table 5.2, and shown in figure 5.6. This configuration of the horns represents the MFI focal plane as seen from the secondary mirror.

	x (mm)	y (mm)
Horn 1	90.00	155.88
Horn 2	-155.88	90.00
Horn 3	-90.00	-155.88
Horn 4	155.88	-90.00

Table 5.2: Linear positions of the four MFI horns on QT1 focal plane.

All horns are placed at the same distance from the centre, equal to 180.0 mm. Given the nominal focal length of the QT1 telescope, $f = 3637$ mm, this results in an angular separation on the sky of $\sim 5.6^\circ$ for opposite horns and $\sim 3.9^\circ$ for adjacent horns. The fact that the horns are not placed along the local reference axes x and y implies that during telescope scans (which are always parallel to the reference axes) each horn covers a different sky stripe.

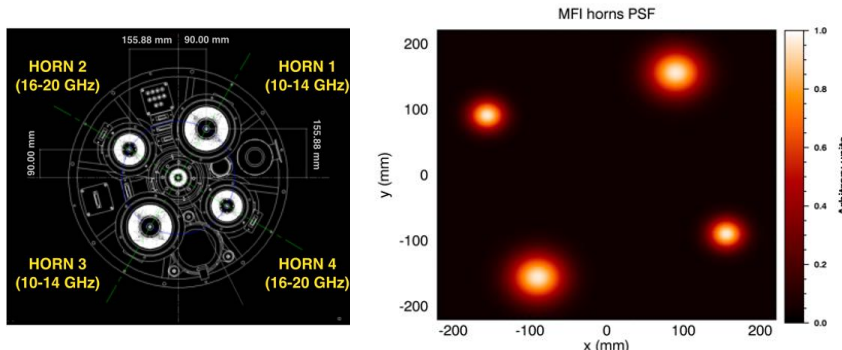


Figure 5.6: *Left:* design of the focal plane horn distribution for the MFI, as seen from the secondary mirror. *Right:* corresponding plot of the horns PSF, computed assuming Gaussian beams with the nominal FWHMs reported in table 5.1.

5.2 Instrumental calibration: the pointing model

We describe now how we tackled a specific aspect of the calibration of the QUIJOTE experiment, that is, the pointing calibration of the QT1 telescope.

In order to properly point a telescope to a sky object, one has to translate the catalogue coordinates of the objects into the local coordinates required by the telescope control software. This process involves two steps: first, the catalogue coordinates (which are usually Galactic or equatorial coordinates) must be translated into local horizontal coordinates, which depend on the observing time and place. This is done via a set of astrometry transformations, and is a standard procedure in astronomy. The second step deals with the fact that any real telescope is affected by non-idealities that produce errors in the pointing. This means that even if we know the local azimuth and elevation (A,E) of a sky object, by entering these values in the telescope encoder the resulting pointing will be shifted from the desired direction, the magnitude of the error depending on the significance of the telescope imperfections. This problem is faced by determining another pair of effective coordinates (A',E'), different from the nominal ones, such that by inputting them in the telescope encoder the telescope will actually be pointing towards the object at (A,E).

The problem of pointing a telescope thus turns into the problem of determining the coordinates (A',E') starting from the nominal ones (A,E). This can be solved by using a set of coordinate transformations that correct for the pointing errors. In such transformations each telescope non-ideality is quantified by a parameter; since correcting the pointing ultimately means changing the telescope direction, these parameters represents the angle quantifying the deviations from the nominal direction. A complete set of pointing parameters constitutes a *pointing model*.

The first step is then determining what are the coordinate transformations required to correct the pointing. Several optical telescopes routinely perform this task, the correction being implemented by a set of codes capable of achieving a precision in the pointing below one arcsecond. For the QUIJOTE experiment this level of accuracy is unnecessary: given that in the MFI the beam FWHM is ~ 0.6 degrees in the best case (table 5.1), it is pointless to employ a complete software correction package that would considerably slow down the data analysis. In our case the goal is achieving a final pointing error below one arcminute. To this aim, we considered the possible types of non-idealities that can affect the QT1 telescope, and we analytically derived the necessary transformation to correct for the corresponding pointing error. The procedure is detailed in sections 5.2.1 and 5.2.2.

The following problem is determining the values of the pointing parameters

Este documento incorpora firma electrónica, y es copia auténtica de un documento electrónico archivado por la ULL según la Ley 39/2015.
Su autenticidad puede ser contrastada en la siguiente dirección <https://sede.ull.es/validacion/>

Identificador del documento:	973742	Código de verificación:	Jfg6xBh0
Firmado por:	DENIS TRAMONTE UNIVERSIDAD DE LA LAGUNA	Fecha:	30/06/2017 15:10:10
	RAFAEL DELFIN BARRENA DELGADO UNIVERSIDAD DE LA LAGUNA		30/06/2017 15:21:31
	JOSE ALBERTO RUBIÑO MARTIN UNIVERSIDAD DE LA LAGUNA		30/06/2017 15:34:17
	ERNESTO PEREDA DE PABLO UNIVERSIDAD DE LA LAGUNA		06/07/2017 13:51:19

for the QT1 telescope. This backward problem requires the use of statistical techniques in order to assess the best-fit value for the parameters, based on the comparison between the predicted direction and data acquired with the telescope. These procedures are considerably complicated by the existence of important degeneracies between the pointing parameters, and by the non-trivial geometry of the MFI focal plane (figure 5.6). This is the subject of section 5.2.3.

5.2.1 Formalism for pointing correction

Let (A, E) be the horizontal coordinates of a sky object and \mathbf{r} the versor defining the corresponding direction. We call \mathcal{H} the correspondence between coordinates and versor (see equation 5.15), so that $\mathbf{r} = \mathcal{H}(A, E)$. If we inputted the pair (A, E) in the encoder of an ideal telescope, it would properly point to the direction \mathbf{r} ; a real telescope, however, will end up pointing to a different direction \mathbf{r}_w (the ‘*w*’ stands for ‘*wrong*’); we refer to the corresponding coordinates as (A_w, E_w) , meaning that $\mathbf{r}_w = \mathcal{H}(A_w, E_w)$. We can define a *pointing function* \mathcal{P} such that, for an ideal telescope, $\mathcal{P} = \mathcal{H}$, while for a real telescope $\mathcal{P}(A, E) = \mathbf{r}_w$. Our goal is to find a pair of coordinates (A_e, E_e) such that, for the real telescope, $\mathcal{P}(A_e, E_e) = \mathbf{r}$.

More precisely, we would like to write a correction function \mathcal{C} that enables the computation of the encoder coordinates starting from the nominal ones:

$$(A_e, E_e) = \mathcal{C}(A, E). \quad (5.7)$$

It is easier to deal with this problem in terms of versors rather than in terms of coordinates. In general, if a specific non-ideality is quantified by a parameter P , then the corresponding pointing correction will be performed by a proper rotation matrix $\hat{R}(P; A_w, E_w)$, that depends on the pointing parameter P and on the initial pointing direction (A_w, E_w) . The matrix is defined in such a way that, when applied to the wrong pointing versor \mathbf{r}_w , it changes its direction towards the nominal one \mathbf{r} :

$$\mathbf{r} = \hat{R}(P; A_w, E_w) \mathbf{r}_w. \quad (5.8)$$

As we will see, there are several different non-idealities that affect a real telescope, each one identified by a parameter P_i . In that case, the overall correction can be obtained by applying equation 5.8 for each one of the parameters P_i , each defining a rotation matrix $\hat{R}(P_i)$. The total correction applied to the vector \mathbf{r}_w by all rotation matrices can be written as a generic function \mathcal{V} ,

$$\mathbf{r} = \mathcal{V}(\mathbf{r}_w). \quad (5.9)$$

Este documento incorpora firma electrónica, y es copia auténtica de un documento electrónico archivado por la ULL según la Ley 39/2015.
Su autenticidad puede ser contrastada en la siguiente dirección <https://sede.ull.es/validacion/>

Identificador del documento: 973742	Código de verificación: Jfg6xBh0	Fecha: 30/06/2017 15:10:10
Firmado por: DENIS TRAMONTE UNIVERSIDAD DE LA LAGUNA		
RAFAEL DELFIN BARRENA DELGADO UNIVERSIDAD DE LA LAGUNA		30/06/2017 15:21:31
JOSE ALBERTO RUBIÑO MARTIN UNIVERSIDAD DE LA LAGUNA		30/06/2017 15:34:17
ERNESTO PEREDA DE PABLO UNIVERSIDAD DE LA LAGUNA		06/07/2017 13:51:19

It is possible to find a relation between the function \mathcal{C} that corrects the coordinates and the function \mathcal{V} that corrects the versors; from figure 5.8, left panel, we can write:

$$(A_e, E_e) = [\mathcal{P}^{-1} \circ \mathcal{V} \circ \mathcal{P}] (A, E). \quad (5.10)$$

The pointing function \mathcal{P} is generally unknown; however, from the right panel of figure 5.8 we see that it can be written as:

$$\mathcal{P} = \mathcal{V}^{-1} \circ \mathbb{1} \circ \mathcal{H} = \mathcal{V}^{-1} \circ \mathcal{H}. \quad (5.11)$$

By substitution of 5.11 into 5.10 we find:

$$(A_e, E_e) = [\mathcal{H}^{-1} \circ \mathcal{V} \circ \mathcal{H}] (A, E). \quad (5.12)$$

Equation 5.12 is our final result: it tells us that, in order to compute the encoder coordinates starting from the nominal ones, we can compute the versor components associated to the nominal coordinates of the sky object, apply the rotations to correct the versor direction, and re-compute its coordinates after the rotation.

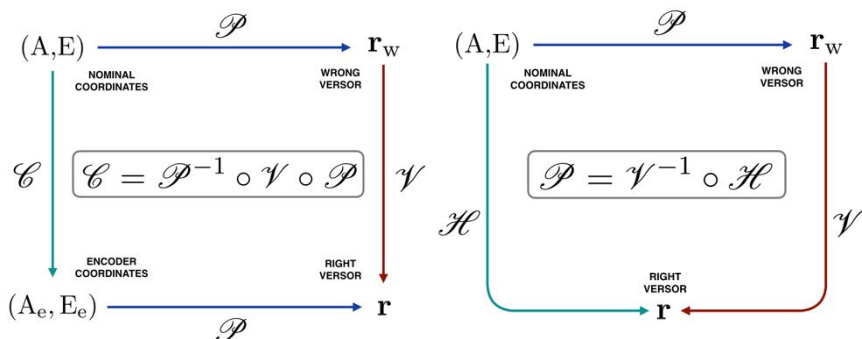


Figure 5.7: Formalism for pointing corrections.

The last step is finding an explicit expression for the function \mathcal{V} . Now, each telescope non-ideality is supposed to be a second-order effect, meaning that the corresponding parameter P is a small quantity. It therefore makes sense to expand the matrix \hat{R} into the sum of the identity transformation $\mathbb{1}$ and a correction:

$$\hat{R}(P; A_w, E_w) \simeq \mathbb{1} + \Delta \hat{R}(P; A_w, E_w), \quad (5.13)$$

Este documento incorpora firma electrónica, y es copia auténtica de un documento electrónico archivado por la ULL según la Ley 39/2015.
Su autenticidad puede ser contrastada en la siguiente dirección <https://sede.ull.es/validacion/>

Identificador del documento: 973742

Código de verificación: Jfg6xBh0

Fecha: 30/06/2017 15:10:10

Firmado por: DENIS TRAMONTE
UNIVERSIDAD DE LA LAGUNA

RAFAEL DELFIN BARRENA DELGADO
UNIVERSIDAD DE LA LAGUNA

JOSE ALBERTO RUBIÑO MARTIN
UNIVERSIDAD DE LA LAGUNA

ERNESTO PEREDA DE PABLO
UNIVERSIDAD DE LA LAGUNA

30/06/2017 15:21:31

30/06/2017 15:34:17

06/07/2017 13:51:19

so that the pointing correction can be written as:

$$\mathbf{r} \simeq [\mathbb{I} + \Delta\hat{R}(P; A_w, E_w)] \mathbf{r}_w = \mathbf{r}_w + \Delta\hat{R}(P; A_w, E_w) \mathbf{r}_w \equiv \mathbf{r}_w + \Delta\mathbf{r}. \quad (5.14)$$

According to equation 5.14, we can correct the pointing direction at the level of the vectors by computing the correction vector $\Delta\mathbf{r}$ and by adding it to the original pointing direction. In general, several non-idealities have to be considered, each quantified by a parameter P_1, P_2, \dots, P_n . In that case, equation 5.14 should be applied for each non-ideality one after the other, the corrected verson \mathbf{r} for the parameter P_1 being the input wrong verson \mathbf{r}_w for the second parameter P_2 , and so on.

5.2.2 Modelling the telescope pointing errors

We detail in this section the different non-idealities considered for the pointing corrections, and the way we derived the linear contribution $\Delta\mathbf{r}$ for each one of them. To be concrete, our horizontal reference frame is defined with the x axis pointing south, the y axis pointing east and the z pointing to the local zenith. The elevation E is measured in the range $[-\pi/2, \pi/2]$, with the zero in the $x - y$ plane; the azimuth A is measured north through east in the range $[0, 2\pi]$. Therefore, the function \mathcal{H} is defined by:

$$\mathbf{r} = \mathcal{H}(A, E) = \begin{pmatrix} x \\ y \\ z \end{pmatrix} = \begin{pmatrix} -\cos E \cos A \\ \cos E \sin A \\ \sin E \end{pmatrix}. \quad (5.15)$$

We considered the telescope non-idealities described in Wallace (2008, from now on W08). In that work the final corrections written with the linear terms $\Delta\mathbf{r}$ are reported. Here we want to derive from scratch the pointing correction rotations, linearise them and check the results against the ones reported in W08. For this reason we will adopt the same convention for the nomenclature of the pointing parameters and their sign definition. These pointing parameters are the ones employed by the TPOINT software (Wallace 1994), which is a common tool used for the analysis of telescope pointing models. In W08 the basic pointing model is made of seven parameters, quantifying the telescope vertical flexure, the misalignment of the azimuth axis, the non-perpendicularity between the two axes and the telescope, and the encoder zero offsets. These non-idealities are shown in figure 5.8 and are described in the following.

Vertical flexure

This non-ideality is related to the flexure of the telescope structure due to gravity. It can be quantified by the angle ζ between the nominal pointing

Este documento incorpora firma electrónica, y es copia auténtica de un documento electrónico archivado por la ULL según la Ley 39/2015.
Su autenticidad puede ser contrastada en la siguiente dirección <https://sede.ull.es/validacion/>

Identificador del documento: 973742

Código de verificación: Jfg6xBh0

Fecha: 30/06/2017 15:10:10

Firmado por: DENIS TRAMONTE UNIVERSIDAD DE LA LAGUNA	30/06/2017 15:21:31
RAFAEL DELFIN BARRENA DELGADO UNIVERSIDAD DE LA LAGUNA	30/06/2017 15:34:17
JOSE ALBERTO RUBIÑO MARTIN UNIVERSIDAD DE LA LAGUNA	06/07/2017 13:51:19
ERNESTO PEREDA DE PABLO UNIVERSIDAD DE LA LAGUNA	

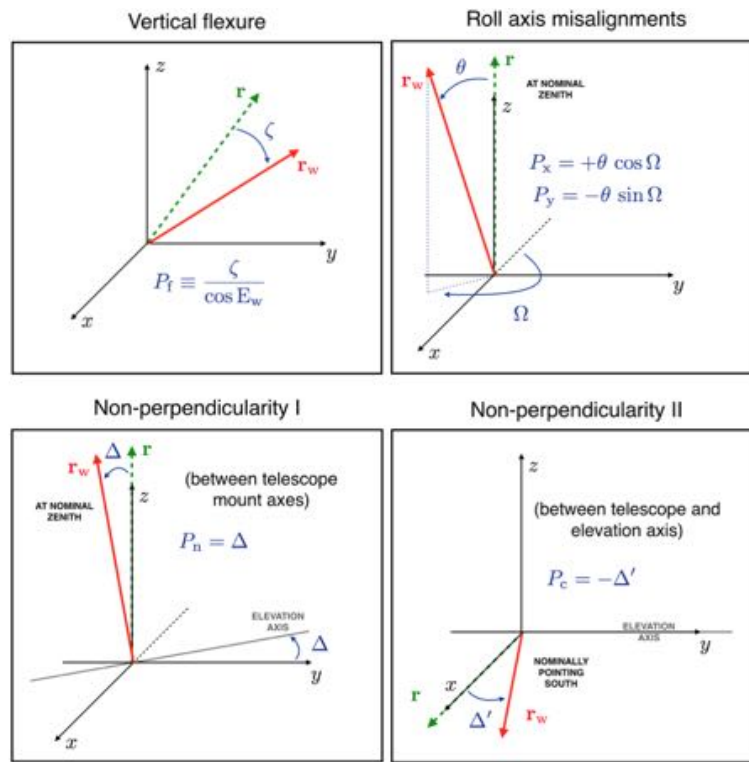


Figure 5.8: Telescope non-idealities considered in this work.

direction and the lower one determined by the flexure (figure 5.8, upper-left panel). This angle will depend on the coordinates (A,E) toward which the telescope is pointing.⁵ In our reference frame the matrix performing the upward

⁵From now on, in order to simplify the notation we will call simply (A,E) the initial, wrong pointing coordinates (A_w, E_w).

rotation of ζ to correct the pointing is:

$$\hat{R}_{\text{VF}} = \begin{pmatrix} \cos^2 A \cos \zeta + \sin^2 A & \cos A \sin A (1 - \cos \zeta) & \cos A \sin \zeta \\ \cos A \sin A (1 - \cos \zeta) & \cos^2 A + \sin^2 A \cos \zeta & -\sin A \sin \zeta \\ -\cos A \sin \zeta & \sin A \sin \zeta & \cos \zeta \end{pmatrix}. \quad (5.16)$$

We can expand the matrix 5.16 to first order in ζ , $\hat{R}_{\text{VF}} \simeq \mathbb{1} + \Delta \hat{R}_{\text{VF}}$. The resulting linear correction to the pointing vector is then:

$$\Delta \mathbf{r}_{\text{VF}} = (\Delta \hat{R})_{\text{VF}} \mathbf{r}' = \begin{pmatrix} \zeta \sin E \cos A \\ -\zeta \sin E \sin A \\ \zeta \cos E \end{pmatrix} = \begin{pmatrix} -P_f z x \\ -P_f z y \\ P_f (x^2 + y^2) \end{pmatrix}, \quad (5.17)$$

where in the last equality we used equation 5.15 to introduce the components (x, y, z) of the pointing verson \mathbf{r} , and we defined:

$$P_f \equiv \frac{\zeta}{\cos E}. \quad (5.18)$$

The linear correction 5.17 coincides with the one quoted in W08. P_f is the pointing parameter quantifying the telescope vertical flexure. In general the flexure depends on the telescope initial tilt, i.e. on the pointed elevation, making the telescope droop in proportion to $\cos E$; equation 5.18 ensures that we can use only one constant value to quantify this effect. Note that both P_f and the matrix 5.16 are undefined when the telescope points to the zenith, in which case the flexure due to gravity is irrelevant.

Azimuth tilt

This non-ideality refers to the misalignment of the azimuth axis with respect to the geodetic vertical (figure 5.8, upper-right panel). In this case we are considering a rigid tilt of the telescope structure as a whole, so that the elevation axis is still perpendicular to the azimuth axis. This kind of non-ideality can be also visualised as a tilt of the telescope basis with respect to the horizontal xy plane.

We can parameterise the tilt of the azimuth axis by means of two parameters: its magnitude, θ , and its direction Ω defined with the same convention as the azimuth (that is, $\Omega = 0$ means the tilt is aligned with the negative x

Este documento incorpora firma electrónica, y es copia auténtica de un documento electrónico archivado por la ULL según la Ley 39/2015.
Su autenticidad puede ser contrastada en la siguiente dirección <https://sede.ull.es/validacion/>

Identificador del documento: 973742

Código de verificación: Jfg6xBh0

Fecha: 30/06/2017 15:10:10

Firmado por: DENIS TRAMONTE UNIVERSIDAD DE LA LAGUNA	30/06/2017 15:21:31
RAFAEL DELFIN BARRENA DELGADO UNIVERSIDAD DE LA LAGUNA	30/06/2017 15:34:17
JOSE ALBERTO RUBIÑO MARTIN UNIVERSIDAD DE LA LAGUNA	06/07/2017 13:51:19
ERNESTO PEREDA DE PABLO UNIVERSIDAD DE LA LAGUNA	

direction). This non-ideality is corrected by rotating the azimuth axis back to the geodetic vertical, resulting in the final transformation:

$$\hat{R}_{\text{AT}} = \begin{pmatrix} \cos^2 \Omega \cos \theta + \sin^2 \Omega & \cos \Omega \sin \Omega(1 - \cos \theta) & \cos \Omega \sin \theta \\ \cos \Omega \sin \Omega(1 - \cos \theta) & \cos^2 \Omega + \sin^2 \Omega \cos \theta & -\sin \Omega \sin \theta \\ -\cos \Omega \sin \theta & \sin \Omega \sin \theta & \cos \theta \end{pmatrix}. \quad (5.19)$$

Note that in this case the matrix does not depend on the telescope pointing direction, given that this non-ideality affects the whole telescope. Again, we can assume the tilt magnitude to be small and simplify the rotation by linearising it with respect to the θ parameter (but not with respect to Ω , which is just the tilt direction and can take any value in $[0, 2\pi]$): $\hat{R}_{\text{AT}} \simeq \mathbb{1} + \Delta\hat{R}_{\text{AT}}$. We now make the following definitions:

$$P_x = +\theta \cos \Omega, \quad (5.20)$$

$$P_y = -\theta \sin \Omega. \quad (5.21)$$

P_x and P_y will be the pointing model parameters for this non-ideality. We observe that $\theta^2 = P_x^2 + P_y^2$, that is, in general both P_x and P_y contribute to the tilt magnitude. In particular, if $\Omega = 0$, then $P_y = 0$ and $\theta = P_x$, so P_x represents the tilt component along the (negative) x axis; and if $\Omega = \pi/2$, then $P_x = 0$ and $\theta = -P_y$, so P_y represents the tilt component along the (negative) y axis. In all other cases the tilt orientation depends on the ratio between the two parameters.

In terms of P_x and P_y we have that the linearised correction for the azimuth tilt is:

$$\Delta\mathbf{r}_{\text{AT}} = (\Delta\hat{R})_{\text{AT}} \mathbf{r} = \begin{pmatrix} P_x z \\ P_y z \\ -P_x x - P_y y \end{pmatrix}, \quad (5.22)$$

which reproduces the result quoted in W08.

Non-perpendicularities

This non-ideality is more complex than the others. We are going to consider two kinds of non-perpendicularities.

- Non-perpendicularity between the mount axes. If the elevation axis is not perpendicular to the azimuth axis it means that at $(A, E) = (0, \pi/2)$ (nominal encoder values), the telescope does not point towards the zenith,

Este documento incorpora firma electrónica, y es copia auténtica de un documento electrónico archivado por la ULL según la Ley 39/2015.
Su autenticidad puede ser contrastada en la siguiente dirección <https://sede.ull.es/validacion/>

Identificador del documento: 973742

Código de verificación: Jfg6xBh0

Fecha: 30/06/2017 15:10:10

Firmado por: DENIS TRAMONTE
UNIVERSIDAD DE LA LAGUNA

RAFAEL DELFIN BARRENA DELGADO
UNIVERSIDAD DE LA LAGUNA

JOSE ALBERTO RUBIÑO MARTIN
UNIVERSIDAD DE LA LAGUNA

ERNESTO PEREDA DE PABLO
UNIVERSIDAD DE LA LAGUNA

30/06/2017 15:21:31

30/06/2017 15:34:17

06/07/2017 13:51:19

but instead has an offset in elevation of an angle that we call Δ (figure 5.8, lower-left panel).

- Non-perpendicularity between the telescope and the elevation axis. This non-ideality implies that at $(A, E) = (\pi, 0)$ (nominal encoder values), it does not point along the positive x axis, but instead along a new direction that we call \tilde{x} and that is shifted in azimuth with respect to x by an angle that we call Δ' (figure 5.8, lower-right panel).

The transformation required to correct for this non-ideality is quite more complex than the ones encountered so far. For this reason, we quote directly the result, leaving the full computation in appendix B. The resulting correction to be added to the wrong pointing vector is:

$$\Delta \mathbf{r}_{NP} = \begin{pmatrix} w(y - w x) \\ -w(x + w y) \\ 0 \end{pmatrix}. \quad (5.23)$$

In 5.23 w is defined as:

$$w = \frac{P_c + P_n z}{\sqrt{x^2 + y^2}}. \quad (5.24)$$

where P_c and P_n are the pointing model parameters employed to quantify the non-perpendicularities. The relation of these parameters with the angles Δ and Δ' defined above is:

$$\begin{aligned} P_c &= -\Delta', \\ P_n &= \Delta. \end{aligned} \quad (5.25)$$

We see that in this first-order derivation the non-ideality correction does not affect z .

Encoder errors

This non-ideality takes into account the possibility that the encoder could be affected by offset errors in handling the input coordinates. This kind of non-ideality is easily corrected at the level of coordinates. Let (A_c, E_c) be the angular coordinates corresponding to the versor corrected for the non-idealities listed so far. Let P_a and P_b be the angles quantifying the offset in azimuth and elevation, respectively. According to the sign convention of the TPOINT software, the correction to be applied reads:

$$\begin{aligned} A_e &= A_c + P_a, \\ E_e &= E_c - P_b. \end{aligned} \quad (5.26)$$

Este documento incorpora firma electrónica, y es copia auténtica de un documento electrónico archivado por la ULL según la Ley 39/2015.
Su autenticidad puede ser contrastada en la siguiente dirección <https://sede.ull.es/validacion/>

Identificador del documento: 973742	Código de verificación: Jfg6xBh0
Firmado por: DENIS TRAMONTE UNIVERSIDAD DE LA LAGUNA	Fecha: 30/06/2017 15:10:10
RAFAEL DELFIN BARRENA DELGADO UNIVERSIDAD DE LA LAGUNA	30/06/2017 15:21:31
JOSE ALBERTO RUBIÑO MARTIN UNIVERSIDAD DE LA LAGUNA	30/06/2017 15:34:17
ERNESTO PEREDA DE PABLO UNIVERSIDAD DE LA LAGUNA	06/07/2017 13:51:19

The coordinates (A_e, E_e) are the ones that we shall finally input to the telescope encoder to ensure it points to the target sky object.

Summary

We have described in this section the set of corrections that transform the nominal horizontal coordinates (A, E) into the encoder requirements (A_e, E_e) . To sum up, the steps to be followed are the following:

1. compute the versor \mathbf{r}_0 associated to the nominal coordinates (A, E) : $\mathbf{r}_0 = \mathcal{H}(A, E)$;
2. apply the vertical flexure correction to \mathbf{r}_0 : $\mathbf{r}_1 = \mathbf{r}_0 + \Delta\mathbf{r}_{VF}(\mathbf{r}_0)$;
3. apply the azimuth tilt correction to \mathbf{r}_1 : $\mathbf{r}_2 = \mathbf{r}_1 + \Delta\mathbf{r}_{AT}(\mathbf{r}_1)$;
4. apply the non-perpendicularities correction to \mathbf{r}_2 : $\mathbf{r}_3 = \mathbf{r}_2 + \Delta\mathbf{r}_{NP}(\mathbf{r}_2)$;
5. compute the resulting corrected coordinates as $(A_c, E_c) = \mathcal{H}^{-1}(\mathbf{r}_3)$;
6. compute the final encoder coordinates (A_e, E_e) by applying the encoder offsets correction 5.26 to (A_c, E_c) .

Sometimes we can be interested in the inverse problem, i.e., by knowing the encoder coordinates we want to know where the telescope is actually pointing. This can be done again by following the previous list, applying the transformation in reverse order and changing the sign of the correction $\Delta\mathbf{r}$. However, this strictly applies only to the transformation in step 6, where the coordinates (A_c, E_c) can be obtained directly by inverting equation 5.26. For the corrections in steps 4, 3 and 2, one has to take into account that the corrections $\Delta\mathbf{r}$ are computed using the “wrong” coordinates (or, equally, the “wrong” components of the versor). The $\Delta\mathbf{r}$ computed when performing the transformations in reverse order will then be different from the one required for the correction.

This problem can be solved by employing an iterative procedure. Let us consider for instance the non-perpendicularities correction, and suppose that we initially know \mathbf{r}_3 and want to compute \mathbf{r}_2 . We can compute an initial guess for the correction as $\Delta\mathbf{r}^{(1)} = \Delta\mathbf{r}_{NP}(\mathbf{r}_3)$, and apply it to get a first corrected vector $\mathbf{r}_3^{(1)} = \mathbf{r}_3 - \Delta\mathbf{r}^{(1)}$. This vector is then used to get an improved estimate of the correction, $\Delta\mathbf{r}^{(2)} = \Delta\mathbf{r}_{NP}(\mathbf{r}_3^{(1)})$, which is in turn applied to the initial \mathbf{r}_3 vector: $\mathbf{r}_3^{(2)} = \mathbf{r}_3 - \Delta\mathbf{r}^{(2)}$. With $\mathbf{r}_3^{(2)}$ we compute the correction $\Delta\mathbf{r}^{(3)}$, and so to continue until the difference between a correction $\Delta\mathbf{r}^{(n)}$ and the previous $\Delta\mathbf{r}^{(n-1)}$ is below the required accuracy.

Este documento incorpora firma electrónica, y es copia auténtica de un documento electrónico archivado por la ULL según la Ley 39/2015.
Su autenticidad puede ser contrastada en la siguiente dirección <https://sede.ull.es/validacion/>

Identificador del documento: 973742	Código de verificación: Jfg6xBh0	Fecha: 30/06/2017 15:10:10
Firmado por: DENIS TRAMONTE UNIVERSIDAD DE LA LAGUNA		
RAFAEL DELFIN BARRENA DELGADO UNIVERSIDAD DE LA LAGUNA		30/06/2017 15:21:31
JOSE ALBERTO RUBIÑO MARTIN UNIVERSIDAD DE LA LAGUNA		30/06/2017 15:34:17
ERNESTO PEREDA DE PABLO UNIVERSIDAD DE LA LAGUNA		06/07/2017 13:51:19

We tested our numerical implementation starting from nominal coordinates, computing the encoder entries and going back to horizontal coordinates, finding that the error in the recovered values remains below ~ 0.2 seconds of arc; the inverse transformation usually requires 3 to 5 iterations for each step to converge.

Summary of coordinate transformations

The pointing model correction is only a part of the whole set of coordinate transformations that are necessary for data reduction with the QUIJOTE experiment. In fact, the coordinates of the celestial objects that we are interested in, are usually quoted with respect to the Galactic reference frame or the equatorial J2000 frame. We describe below the steps that are necessary to know where a given MFI horn is pointing, starting from the telescope encoder inputs.

- *From telescope frame to horizontal frame.* This transformation is performed by the pointing model corrections. We detailed in the previous section how to perform this transformation, both in the horizontal-to-encoder and in the encoder-to-horizontal cases.
- *From focal plane centre to horn.* The pointing model correction retrieves the horizontal coordinates of the axis of the telescope, crossing the centre of the focal plane. The MFI horns, however, lie in different positions defined by the linear coordinates (x, y) on the focal plane (table 5.2 and figure 5.6). This implies that each horn will be pointing to a different direction; the linear separations (x, y) from the centre of the focal plane translates into an angular separation on the sky $(\Delta A, \Delta E)$ from the telescope axis direction (A, E) . This is done using the telescope *focal length* f :

$$\begin{aligned} x &= -f \tan \Delta A \cos E, \\ y &= f \tan \Delta E. \end{aligned} \quad (5.27)$$

The minus sign in the first equation accounts for the fact that the coordinates in table 5.2 determine the horn positions when the MFI focal plane is seen from the secondary mirror; in this case we are considering the MFI from the point of view of an observer, therefore as projected to the sky, and the system undergoes an axial rotation. Besides, we are assuming that the axes x and y are parallel to the local versors of azimuth and elevation defined over a plane tangent to the sphere in the central position (A, E) . Finally, the factor $\cos E$ in the first equation takes into account

Este documento incorpora firma electrónica, y es copia auténtica de un documento electrónico archivado por la ULL según la Ley 39/2015.
Su autenticidad puede ser contrastada en la siguiente dirección <https://sede.ull.es/validacion/>

Identificador del documento: 973742	Código de verificación: Jfg6xBh0	Fecha: 30/06/2017 15:10:10
Firmado por: DENIS TRAMONTE UNIVERSIDAD DE LA LAGUNA		
RAFAEL DELFIN BARRENA DELGADO UNIVERSIDAD DE LA LAGUNA		30/06/2017 15:21:31
JOSE ALBERTO RUBIÑO MARTIN UNIVERSIDAD DE LA LAGUNA		30/06/2017 15:34:17
ERNESTO PEREDA DE PABLO UNIVERSIDAD DE LA LAGUNA		06/07/2017 13:51:19

that the azimuth is not a “true” angle, in the sense that its variations are not proportional to linear variations on the sphere.

Equation 5.27, however, is only approximated; in particular, it cannot be applied close to the poles ($E = \pm\pi/2$). The complete transformation that we shall employ is a *conic projection* (Kovalevsky 1995), that reads:

$$x = -f \frac{\sin \Delta A}{\cos E [\tan E \tan (E + \Delta E) + \cos \Delta A]}, \quad (5.28)$$

$$y = f \frac{\tan (E + \Delta E) - \tan E \cos \Delta A}{\tan E \tan (E + \Delta E) + \cos \Delta A}. \quad (5.29)$$

Equation 5.27 is obtained by expanding 5.28 to first order in the angular shifts.

For our purpose, we want to invert the previous relations in order to compute the angular displacements ($\Delta A, \Delta E$) of the horns given their linear positions (x, y). We find:

$$\begin{aligned} \tan(\Delta A) &= \tilde{x} \cos E \frac{1 + \tan^2 E}{1 - \tilde{y} \tan E}, \\ \tan(\Delta E) &= \frac{K - \tan E}{1 + K \tan E}, \end{aligned} \quad (5.30)$$

where $\tilde{y} = y/f$, $\tilde{x} = -x/f$ and

$$K = \cos \Delta A \frac{\tilde{y} + \tan E}{1 - \tilde{y} \tan E}. \quad (5.31)$$

The coordinates towards which a given horn is pointing are then computed as:

$$A_h = A + \Delta A, \quad (5.32)$$

$$E_h = E + \Delta E. \quad (5.33)$$

- *From horizontal to apparent equatorial.* This transformation changes the azimuth and elevation coordinates (both if they refer to a particular horn or to the telescope axis) into the corresponding right ascension and declination (α, δ) in the equatorial reference frame.⁶ This transformation is

⁶Note that this plane has its origin in the centre of the Earth. Up to now the frame was centred on the Earth surface point where the telescope is placed. In principle, a previous transformation is required, maintaining the direction of the horizontal frame axis but translating its zero to the centre of the Earth: the resulting coordinates are called *topocentric*. However, this transformation has to be taken into account only when dealing with objects in the Solar System (e.g. the Moon, that has been used as a calibrator), otherwise the difference is completely negligible. Since in this work we are dealing with Galactic regions, we can safely skip this step.

a standard rotation between the two reference frames (Lang 1999), that depends on the latitude of the observing site and on the local *sidereal time* (LST). The LST is defined as the time elapsed since the last transit of the spring equinox across the local meridian. The *mean sidereal time* can be computed starting from the civilian date; a further correction due to Earth rotation is then required to obtain the final LST (usually referred to as the equation of the equinoxes). We adopted the convention described in Aoki et al. (1982).

- *From apparent equatorial to J2000*

The apparent celestial coordinates determined so far refers to the current position of the celestial object on the sky, and are therefore called apparent. The motion of *precession* (Newcomb 1895; Lieske et al. 1977; Lieske 1979) and *nutation* (Bradley 1748) of the Earth leads to a drift of the orientation of the axes that define the celestial reference frame; this results in a change in time of the celestial coordinates of sky objects. It is then required to quote celestial coordinates referred to the 12:00 (Terrestrial Time) on the 1st of January 2000: these coordinates are then said to be referred to the *J2000 epoch*.

In astronomy a convenient way of expressing absolute time is the *Julian Date* (JD). The *Julian Day Number* (JDN) is an integer assigned to a whole solar day in a continuous count starting at 12.00 pm on January 1, 4713 BC, in the proleptic Julian Calendar (a calendar in use before the introduction of the currently used Gregorian Calendar and differing from the latter in an overcount of leap years). The JD for a given time *t* is the JDN of the preceding noon plus the fraction of day since *t*. The julian date of the reference J2000 epoch is JD(J2000) = 2451545.

The apparent celestial coordinates can be transformed to the corresponding reference coordinates by knowing the JD and applying the correction for precession and nutation back to the epoch J2000; besides, the apparent displacement from the *aberration* (Bradley 1727) due to the Earth revolution should be taken into account⁷. Detailed equations for correcting for these astrometry effects and compute the J2000 coordinates can be found in Meeus (1998) or in the *Astronomical Almanacs*. When the declination is not within 1 degree from the celestial poles, the equations

⁷There are other effects that can alter the equatorial coordinates of a sky object, like the aberration due to Earth rotation or the deflection of the incoming light around the Sun gravitational field; however, these effects are at the order of 1 second of arc and are too small to matter here.

Este documento incorpora firma electrónica, y es copia auténtica de un documento electrónico archivado por la ULL según la Ley 39/2015. Su autenticidad puede ser contrastada en la siguiente dirección https://sede.ull.es/validacion/		
--	--	--

Identificador del documento: 973742	Código de verificación: Jfg6xBh0
-------------------------------------	----------------------------------

Fecha: 30/06/2017 15:10:10

Firmado por: DENIS TRAMONTE UNIVERSIDAD DE LA LAGUNA

RAFAEL DELFIN BARRENA DELGADO UNIVERSIDAD DE LA LAGUNA

30/06/2017 15:21:31

JOSE ALBERTO RUBIÑO MARTIN UNIVERSIDAD DE LA LAGUNA
--

30/06/2017 15:34:17

ERNESTO PEREDA DE PABLO UNIVERSIDAD DE LA LAGUNA

06/07/2017 13:51:19

found in Lang (1999) can be used.

- *From equatorial J2000 to Galactic*

Sometimes it is useful to work in Galactic longitude and latitude (l, b), rather than in the equatorial coordinates. Since the Galactic reference frame is fixed with respect to the J2000 equatorial frame, this last coordinate transformation is simply a constant matrix that can be found in many textbooks (e.g., Lang 1999).

5.2.3 Parameter estimation

In this section we detail the methodology we employed for the estimation of the pointing parameters, and discuss the final results.

Methodology

The estimation of the pointing model requires the comparison between the predicted observed signal and the real data: in the observation of a radio source, any displacement from the nominal pointing direction will result in a different observed temperature, and this can be exploited to find the pointing parameters that best reproduce the observed intensity pattern.

Point radio sources are usually observed with QUIJOTE in *raster mode*. This means that the telescope moves back and forth in azimuth around the target, while shifting the elevation by a constant step after each scan. Whenever the telescope crosses the meridian passing through the source, it will record an increase of the observed intensity, which will get stronger while the pointing gets closer to the source in elevation, and will decrease once the source elevation has been passed by. The resulting *time-ordered data* (TOD) will then be characterised by a series of peaks in correspondence to the source crossings (see figure 5.9).

It is possible to simulate the TOD numerically. Since we know the catalogue coordinates (Galactic or equatorial J2000) of the target, we can apply the astrometry transformations to compute its apparent equatorial coordinates (α_s, δ_s). From the observation data, we know for each value of the julian date (jd) the telescope encoder coordinates ($A_e(jd), E_e(jd)$). For each MFI horn these coordinates can be transformed into the horizontal telescope coordinates ($A_{tel}(jd), E_{tel}(jd)$) applying the pointing corrections, and then into the coordinates pointed by the selected horn ($A_h(jd), E_h(jd)$) using 5.32; finally, these can be transformed into the apparent equatorial coordinates ($\alpha_h(jd), \delta_h(jd)$). If we assume a Gaussian beam, we can compute the simulated observed temperature

Este documento incorpora firma electrónica, y es copia auténtica de un documento electrónico archivado por la ULL según la Ley 39/2015.
Su autenticidad puede ser contrastada en la siguiente dirección <https://sede.ull.es/validacion/>

Firmado por:	Identificador del documento:	Código de verificación:	Fecha:
DENIS TRAMONTE UNIVERSIDAD DE LA LAGUNA	973742	Jfg6xBh0	30/06/2017 15:10:10
RAFAEL DELFIN BARRENA DELGADO UNIVERSIDAD DE LA LAGUNA			30/06/2017 15:21:31
JOSE ALBERTO RUBIÑO MARTIN UNIVERSIDAD DE LA LAGUNA			30/06/2017 15:34:17
ERNESTO PEREDA DE PABLO UNIVERSIDAD DE LA LAGUNA			06/07/2017 13:51:19

as:

$$T_{\text{sim}}(\text{jd}) = G_T \exp \left[-4 \ln 2 \frac{\Delta^2(\text{jd})}{\text{FWHM}^2} \right], \quad (5.34)$$

where FWHM can be read from table 5.1, $\Delta(\text{jd})$ is the angular separation⁸ between the directions (α_s, δ_s) and $(\alpha_h(\text{jd}), \delta_h(\text{jd}))$, and G_T is a proper gain factor used to transform the units into temperature.

Now, we can define a pointing model \mathbf{P} as any 7-tuple of pointing parameters $\mathbf{P} = \{P_t, P_x, P_y, P_c, P_h, P_a, P_b\}$. With the recipe described above we can compute the simulated TOD corresponding to the pointing model \mathbf{P} , $T_{\text{sim}}(\text{jd}; \mathbf{P})$, and compare it with the acquired data $T_{\text{obs}}(\text{jd})$. The goodness of the pointing model in reproducing the observed intensity can be quantified by the chi-square:

$$\chi^2(\mathbf{P}) = \sum_{i=1}^N [T_{\text{sim}}(\text{jd}_i; \mathbf{P}) - T_{\text{obs}}(\text{jd}_i)]^2. \quad (5.35)$$

We take as our best-fit pointing model the one providing the minimum chi-square.

In order to variate the 7-tuple \mathbf{P} in the pointing parameter space we employed an IDL routine called **AMOEBA**, based on the *Nelder-Mead method* (Nelder & Mead 1965). It is a numerical optimisation method that can be used to find the minimum of a function in a N -dimensional space. It is based on the evaluation of the function values in correspondence to N points that constitute a $(N - 1)$ dimensional simplex; the method generates a new test position that will serve as a new vertex of the simplex, replacing one of the old ones. As a result, the simplex moves in the N -dimensional space, stretching preferentially along directions oriented towards points that yield a lower value of the function; these displacements resemble the movement of a unicellular organism, from where the name is taken. An inconvenient of the **AMOEBA** method is that it can easily fall into a local minimum, that is not necessarily the absolute minimum of the function.

We applied this methodology to each one of the horns. We chose as targets the supernova remnants *Taurus A*, also referred to as the *Crab Nebula* (Crab from now on, Hester 2008), and *Cassiopeia A* (Cas A from now on Fesen et al. 2006). Both are very bright radio sources that are clearly visible at the TOD level. These sources are employed in the QUIJOTE calibration analysis, so they

⁸We chose to make the comparison in the apparent equatorial coordinates because a generic observation is too short for the astrometry transformation to make a difference, so that the source apparent coordinates can be considered constant; this way we avoid performing the astrometry transformations on the telescope coordinates, which would be considerably time consuming.

are observed on a daily basis and a large amount of data is available. Note that the pointing parameters, being related to geometrical properties of the telescope, affect the pointing differently depending on the observation direction; a clear example is the vertical flexure, which is more relevant for low-elevation observations, but in general all parameters contribute differently depending on the telescope configuration. Therefore, in order to achieve a better fit we joined in a single, large TOD, all available observations of Cas A and Crab at different elevations. This not only implied an improvement in the statistics, but it also ensured that we are fitting the pointing model considering the telescope in several geometrical configurations. Since observations are taken at different times, it was possible to include pointings of the telescope at different elevation, both towards the east and the west depending on whether the source was rising or setting. In particular, Crab culminates at $E \sim 86^\circ$, which allowed us to sample high elevations. Besides, Cas A has declination $\sim 59^\circ$, meaning that from the Teide observatory (Lat $\sim 28^\circ$) it is visible towards the north; Crab, instead, having declination $\sim 22^\circ$, was used to cover the southern half of sky. This strategy ensures that the resulting parameters can be used to correct the pointing of observations on any portion of the sky without significative biases.

Initial pointing estimation

We applied the methodology described in the previous section to each horn of the MFI instrument. The resulting pointing parameters are listed in table 5.3.

Horn	P_f	P_x	P_y	P_c	P_n	P_a	P_b
1	361.20	81.91	-27.72	-3891.06	891.80	4509.58	-1225.13
2	-271.86	56.64	-32.97	-1935.40	0.00	3108.03	-1978.78
3	-157.78	62.58	-39.35	-2128.44	0.00	3347.74	-1590.41
4	534.83	64.08	-29.27	-2494.12	0.00	3602.69	-915.94
All	242.57	80.88	-31.03	-2726.60	0.00	3927.13	-1302.10

Table 5.3: First estimation of the pointing model. Parameter values are in arcseconds. The last line reports the results of the estimations considering all horns at the same time.

The most striking feature of table 5.3 is that the recovered pointing model depends on the horn, with major differences among the parameters. This is a

Este documento incorpora firma electrónica, y es copia auténtica de un documento electrónico archivado por la ULL según la Ley 39/2015. Su autenticidad puede ser contrastada en la siguiente dirección https://sede.ull.es/validacion/	
Identificador del documento: 973742	Código de verificación: Jfg6xBh0
Firmado por: DENIS TRAMONTE UNIVERSIDAD DE LA LAGUNA	Fecha: 30/06/2017 15:10:10
RAFAEL DELFIN BARRENA DELGADO UNIVERSIDAD DE LA LAGUNA	30/06/2017 15:21:31
JOSE ALBERTO RUBIÑO MARTIN UNIVERSIDAD DE LA LAGUNA	30/06/2017 15:34:17
ERNESTO PEREDA DE PABLO UNIVERSIDAD DE LA LAGUNA	06/07/2017 13:51:19

very important result, which has to be understood. First of all, we must take into account that the parameters \mathbf{P} are strongly degenerate: even though they have been introduced to quantify different non-idealities, many of them result in the same correction to the pointing coordinates. The clearest example is perhaps the degeneracy between P_f and P_b : the vertical flexure of the telescope results ultimately in a shift in elevation, which can be corrected by an offset in the encoder elevation. Of course, while the elevation shift due to the encoder error is constant, the one associated to the vertical flexure depends on the elevation, and that is the reason why both parameters are necessary for our pointing model. Still, their effect in the pointing correction is the same. This degeneracy exists between other parameter pairs, and as a result there will be different 7-tuples \mathbf{P} that achieve the same pointing correction. When the AMOEBA code looks for a best-fit solution, it may fall into different minima for the χ^2 that achieve the same pointing. Actually, this is not a real issue: our goal is to find a set of parameters capable of correcting the pointing. If different 7-tuples provide the best correction, we can use any of them, even if we do not know the *real* value for the pointing parameters. When fitting the pointing model for different horns, the code may find different solutions, capable of achieving an equally good pointing correction.

However, there is another issue coming into play here. In order to get rid of the degeneracy, we estimated one parameter at a time: we started from P_f , fixing all the other parameters to zero, and get a best-fit estimate \tilde{P}_f . Then, we fixed P_f to the recovered value \tilde{P}_f , and fitted for P_x , maintaining the other five parameters null, and so to continue. We ended up again with four different pointing models, overally achieving a worse fit compared to the results in table 5.3. It is then not possible to find a common pointing model for all the horns. This conclusion can be understood if we assume that the focal plane of the MFI instrument is not ideal. Indeed, the TOD are generated based on the coordinates pointed by the horns, whose positions differ from the telescope central axis. If the real positions of the horns differ from the nominal ones, this will result in a displacement from the nominal pointed direction: this displacement will be absorbed by the pointing errors as if it was one of the telescope non-idealities described in section 5.2.2. This eventually leads to a different set of pointing parameters depending on the horn. Unfortunately, it is not possible to disentangle the focal plane from the telescope non-idealities, due to the lack of a central horn in the MFI instrument. The result is a set of four different pointing models, like the ones in table 5.3.

Este documento incorpora firma electrónica, y es copia auténtica de un documento electrónico archivado por la ULL según la Ley 39/2015.
Su autenticidad puede ser contrastada en la siguiente dirección <https://sede.ull.es/validacion/>

Identificador del documento:	973742	Código de verificación:	Jfg6xBh0
Firmado por:	DENIS TRAMONTE UNIVERSIDAD DE LA LAGUNA	Fecha:	30/06/2017 15:10:10
	RAFAEL DELFIN BARRENA DELGADO UNIVERSIDAD DE LA LAGUNA		30/06/2017 15:21:31
	JOSE ALBERTO RUBIÑO MARTIN UNIVERSIDAD DE LA LAGUNA		30/06/2017 15:34:17
	ERNESTO PEREDA DE PABLO UNIVERSIDAD DE LA LAGUNA		06/07/2017 13:51:19

Horn	δx (mm)	δy (mm)
1	2.26	-0.20
2	-4.40	-6.08
3	-3.84	-0.14
4	-0.11	3.58

Table 5.4: Best-fit displacements of the horn positions with respect to the nominal ones, computed fixing the pointing parameters to the common model from the last line of table 5.3.

Studying the geometry of the focal plane

The results from the first pointing analysis suggest that there may be some non-idealities affecting the geometry of the focal plane. We tried to quantify them, by fitting for the best horn positions while fixing the pointing parameters. To this purpose, we first fitted another time the pointing parameters considering the contribution of all horns at the same time, and found the 7-tuple \mathbf{P}_{All} reported in the last line of table 5.3. This pointing model should serve as a global correction for the whole telescope, without being biased for correcting any one of the horns preferentially.

We wrote the position of each horn as $(x = x_0 + \delta x, y = y_0 + \delta y)$, with (x_0, y_0) the nominal positions from table 5.2, and $(\delta x, \delta y)$ the deviations we want to fit for. We fixed the pointing model to the estimate \mathbf{P}_{All} and used again the full set of Crab and Cas A TODs for each horn. The estimates on the horn displacements are listed in table 5.4.

These displacements are only a few percent of the nominal horn positions, but they are not negligible: a variation of 1 mm on the focal plane corresponds roughly to a separation of 1 minute of arc on the sky, at the level of the precision we want to achieve with the pointing correction. We conclude then that the geometry of the focal plane is different from the ideal one, but there is not a clear pattern of the horn displacements: the variations reported in table 5.4 do not correspond to a rigid translation of the horns, nor to a rotation of the focal plane around its centre. The geometrical transformation emerging from table 5.4 is probably due to a combination of a translation and a rotation, and to a possible *tilt* of the focal plane: a tilt would affect the z direction, which is not represented in this fit. The lack of a clear pattern in the fitted displacements, however, suggests a contribution from a possible curvature of

Este documento incorpora firma electrónica, y es copia auténtica de un documento electrónico archivado por la ULL según la Ley 39/2015.
Su autenticidad puede ser contrastada en la siguiente dirección <https://sede.ull.es/validacion/>

Identificador del documento: 973742

Código de verificación: Jfg6xBh0

Fecha: 30/06/2017 15:10:10

Firmado por: DENIS TRAMONTE
UNIVERSIDAD DE LA LAGUNA

RAFAEL DELFIN BARRENA DELGADO
UNIVERSIDAD DE LA LAGUNA

JOSE ALBERTO RUBIÑO MARTIN
UNIVERSIDAD DE LA LAGUNA

ERNESTO PEREDA DE PABLO
UNIVERSIDAD DE LA LAGUNA

30/06/2017 15:21:31

30/06/2017 15:34:17

06/07/2017 13:51:19

the focal plane, which is difficult to characterise.

We wanted to explore possible displacements of the focal plane along the z direction, that is, parallel to the telescope axis. A variation along this direction would result in a different focal length, which enters the computation of the horn coordinates via equation 5.30. We wanted to find a best-fit focal length. To this aim, we created local-coordinate maps⁹ in (α, δ) around each of the sources Cas A and Crab, using again the common solution for the pointing model \mathbf{P}_{All} . We then extracted the angular positions of the horns *from the map*. For each horn, we considered its angular distance from the other three; we fitted then for a value of the focal length that best reproduced the nominal horn separations when transforming these angular distances into linear separations on the focal plane. More precisely, for each horn we considered an individual focal length f_h , defined as $f_h = f_0 + \delta f_h$, were $f_0 = 3637$ mm is the nominal QUIJOTE focal length, and δf_h is variation to be fitted for the considered horn. The resulting values for the δf_h should map the displacements of the horns along the telescope axis. Note that considering the separation of the horns, and not their absolute positions, has the advantage of separating the effect of the focal length (as a scaling factor) from other possible errors affecting the focal plane, like rotations and translations of the local frame. We also considered a case of a common variation of the focal length, $f = f_0 + \delta f_{\text{all}}$, equally affecting all the horns together: this time we fitted for the value of δf_{all} that best reproduced all the six separations between the four horns. We remind that we fitted only for the focal length variations, while the telescope pointing parameters were kept fixed to the common solution \mathbf{P}_{All} reported in the last line of table 5.3. The results are listed in table 5.5.

We find important differences in the estimated focal lengths. The fit in Cas A and Crab give different results, due to the different sky coverage associated to each one of them, but the pattern emerging from table 5.5 is the same for both sources. This is the confirmation that the focal plane is tilted with respect to the nominal configuration; as seen from the secondary mirror, the lower-right part (horns 3 and especially 4) seems to bend backward, while the upper right-part (horn 1 and especially 2) seems to bend forward; besides, the whole focal plane seems to be shifted backwards by ~ 6 cm, as the fit with all horns at the same time suggests (this time we also find a remarkable agreement between the fits with Cas A and Crab).

⁹For a single horn, a local-coordinate map is a map centered in the nominal position of the source, showing in each pixel the intensity measured by the horn when the telescope axis is pointing towards that pixel. The final local-coordinate map is obtained by adding together the four individual horn maps; the results is similar to the focal plane plot in figure 5.6, right panel.

Firmado por: DENIS TRAMONTE UNIVERSIDAD DE LA LAGUNA	30/06/2017 15:21:31
RAFAEL DELFIN BARRENA DELGADO UNIVERSIDAD DE LA LAGUNA	30/06/2017 15:34:17
JOSE ALBERTO RUBIÑO MARTIN UNIVERSIDAD DE LA LAGUNA	06/07/2017 13:51:19
ERNESTO PEREDA DE PABLO UNIVERSIDAD DE LA LAGUNA	

Horn	δf (mm) - Cas A	δf (mm) - Crab
1	9.84	-10.00
2	52.19	55.94
3	97.81	103.13
4	89.30	103.91
All	62.19	61.25

Table 5.5: Results for the fit of the focal length variation with respect to the nominal value $f_0 = 3637\text{ mm}$, considering each horn individually and all together in the last line. The results are reported separately for Cas A and Crab because the horn angular separations were measured directly from maps in equatorial coordinates.

Best-fit pointing model

The results from the previous section clearly suggest that the focal plane is non-ideal. This should be taken into account in our estimate of the best pointing model for the QT1 telescope. However, the lack of a horn in the centre of the focal plane makes it impossible to disentangle the errors in the pointing of the telescope from the errors in the focal plane. Any fit for the parameters of the pointing will also absorb the contribution from the errors in the horn positions and focal length, and vice-versa.

We tried to go around the degeneracy problem by means of an iterative procedure. We estimated a pointing model with the nominal horn positions and then fitted for the horn positions using that pointing model. These new horn coordinates were employed to repeat the fit for the pointing parameters, and so to continue. However, we found no convergence in this procedure even after several iterations, meaning the degeneracy between the focal plane and the telescope cannot be broken this way.

However, even though we cannot achieve a complete knowledge of the mechanical configuration of the QT1+MFI system, we can still find a practical solution that serves our purpose of pointing corrections. The previous section clearly suggested a displacement of the whole focal plane of $\sim 6\text{ cm}$, so we decided to adopt a new focal length for the QT1 telescope as $f = 3700\text{ mm}$. With this value we repeated the fit for the pointing parameters, using all observations available of Cas A and Crab together. For Cas A, this resulted in 686 observa-

Este documento incorpora firma electrónica, y es copia auténtica de un documento electrónico archivado por la ULL según la Ley 39/2015.
Su autenticidad puede ser contrastada en la siguiente dirección <https://sede.ull.es/validacion/>

Identificador del documento: 973742

Código de verificación: Jfg6xBh0

Fecha: 30/06/2017 15:10:10

Firmado por: DENIS TRAMONTE
UNIVERSIDAD DE LA LAGUNA

RAFAEL DELFIN BARRENA DELGADO
UNIVERSIDAD DE LA LAGUNA

JOSE ALBERTO RUBIÑO MARTIN
UNIVERSIDAD DE LA LAGUNA

ERNESTO PEREDA DE PABLO
UNIVERSIDAD DE LA LAGUNA

30/06/2017 15:21:31

30/06/2017 15:34:17

06/07/2017 13:51:19

tions, taken between November 2012 and November 2016, corresponding to a total observing time of 249.9 hours. For Crab, we considered 650 observations, taken between February 2013 and November 2016, corresponding to a total observing time of 255.6 hours¹⁰.

We maintained the horn positions fixed to their nominal values, and let the resulting pointing parameters account for possible deviations; our goal is indeed to employ a different pointing model depending on the horn. The final results are reported in table 5.6, where for completeness we also reported the resulting pointing model when all horns are considered at the same time.

Horn	P_f	P_x	P_y	P_c	P_n	P_a	P_b
1	485.15	79.86	-65.63	3403.43	-5368.63	308.36	-1071.92
2	-363.26	39.69	-11.91	2455.10	-4434.13	887.69	-2057.83
3	-20.98	40.96	-26.69	6678.65	-7423.40	-1739.25	-1710.67
4	-0.50	103.92	-58.38	1453.48	-2913.73	1196.72	-1350.65
All	483.81	25.47	-24.86	1815.69	-3444.20	1004.42	-1317.71

Table 5.6: Best-fit estimation of the pointing model, using the new estimated focal length $f = 3700\text{ mm}$ and the nominal positions for the horns. Parameter values are reported in arcseconds.

We checked that the solution from table 5.6 is the best in correcting for the pointing errors. In figure 5.9 we show the effect of the pointing correction at the level of a Crab observation TOD. Without the pointing corrections, the peaks corresponding to the source crossings predicted from the encoder coordinates are completely shifted with respect to the real data. After applying the pointing correction, instead, the prediction matches very well the observed data.

In figure 5.10 we show the effect of the pointing corrections at the level of Crab maps in Galactic coordinates. These maps were obtained by stacking together all the observations of Crab that were employed for fitting the pointing model: such observations were taken at different elevations, so that the pointing errors affect differently each one of them. As a result, when superimposing the corresponding maps, the source results elongated and not centred in its nominal position (marked with a cross in the plots), as it is visible from the left panels

¹⁰This total observation times are actually slightly overestimated, because part of the data is automatically flagged by the data reduction software; this is better explained in section 5.3.2.

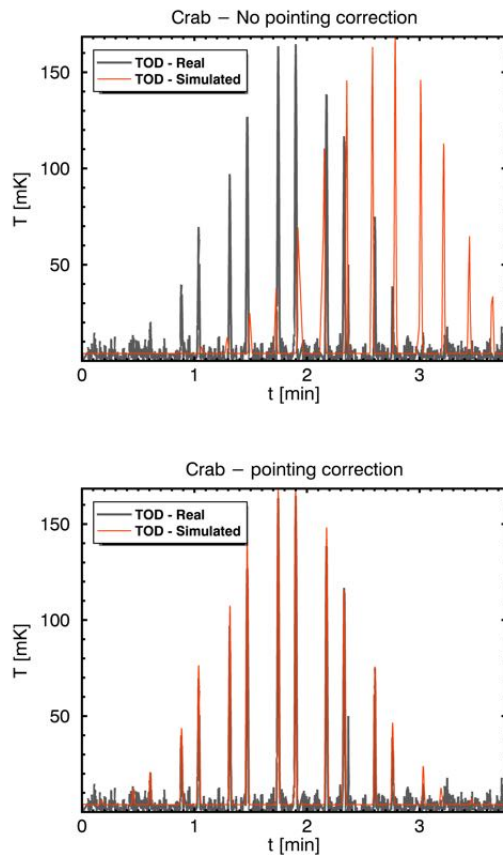


Figure 5.9: Effect of the pointing model correction at the level of the TOD for an observation of Crab. We plot the data with the simulation superimposed, in the case of no pointing correction (*top*) and with the pointing correction using the parameters from table 5.6 (*bottom*). The improvement resulting from applying the pointing model is evident.

of figure 5.10. After correcting the pointing with our best fit model, instead, all observations tend to agree in reproducing a much more rounded beam shape centred in the expected source position (right panels of figure 5.10). In order

Este documento incorpora firma electrónica, y es copia auténtica de un documento electrónico archivado por la ULL según la Ley 39/2015.
Su autenticidad puede ser contrastada en la siguiente dirección <https://sede.ull.es/validacion/>

Identificador del documento: 973742

Código de verificación: Jfg6xBh0

Fecha: 30/06/2017 15:10:10

Firmado por: DENIS TRAMONTE
UNIVERSIDAD DE LA LAGUNA

RAFAEL DELFIN BARRENA DELGADO
UNIVERSIDAD DE LA LAGUNA

JOSE ALBERTO RUBIÑO MARTIN
UNIVERSIDAD DE LA LAGUNA

ERNESTO PEREDA DE PABLO
UNIVERSIDAD DE LA LAGUNA

30/06/2017 15:21:31

30/06/2017 15:34:17

06/07/2017 13:51:19

Horn	δl (arcmin)	δb (arcmin)	FWHM _l (arcmin)	FWHM _b (arcmin)	e
1-lf	-0.29	0.72	54.88	54.55	3.0×10^{-3}
2-lf	-0.33	-0.55	38.31	39.12	1.1×10^{-2}
3-lf	-0.71	-0.72	54.75	54.33	3.9×10^{-3}
4-lf	-0.13	-0.84	38.03	38.15	1.6×10^{-3}
1-hf	-0.25	0.30	54.84	54.51	3.0×10^{-3}
2-hf	-0.38	-0.43	38.81	39.87	1.3×10^{-2}
3-hf	-0.69	-0.53	54.77	54.11	6.0×10^{-3}
4-hf	-0.06	-0.81	38.81	38.80	2.0×10^{-3}

Table 5.7: Results from the Gaussian fits to the horn PSF from the stack in Galactic coordinates of several Crab observations. For each horn we fit for its angular displacement from the expected source position and the FWHM of the beam in two orthogonal directions. In the table we also report the corresponding horn ellipticities, computed with equation 5.36. We report results for both low frequency (lf) and high frequency maps (hf).

to quantify the precision achieved with our pointing model, we performed a Gaussian fit over the beams to determine their angular shift ($\delta l, \delta b$) from the nominal Crab position, and assess the level of residual ellipticities. For each horn we computed the ellipticity as:

$$e = \frac{|FWHM_l - FWHM_b|}{FWHM_l + FWHM_b}, \quad (5.36)$$

where FWHM_l and FWHM_b are the full width at half maximum of the horn PSF along the Galactic longitude and latitude directions, respectively. The results are reported in table 5.7. Notice that the maps in figure 5.10 are only the temperature maps for the lower frequency band of each horn; the higher frequency maps look very much alike them and there is no need to plot them as well. However, in table 5.7 we report the results for both low and high frequency maps.

We see that the errors in the recovered positions of the source remain below one minute of arc, which was our initial goal for the accuracy in the pointing

Este documento incorpora firma electrónica, y es copia auténtica de un documento electrónico archivado por la ULL según la Ley 39/2015.
Su autenticidad puede ser contrastada en la siguiente dirección <https://sede.ull.es/validacion/>

Identificador del documento: 973742

Código de verificación: Jfg6xBh0

Fecha: 30/06/2017 15:10:10

Firmado por: DENIS TRAMONTE
UNIVERSIDAD DE LA LAGUNA

RAFAEL DELFIN BARRENA DELGADO
UNIVERSIDAD DE LA LAGUNA

JOSE ALBERTO RUBIÑO MARTIN
UNIVERSIDAD DE LA LAGUNA

ERNESTO PEREDA DE PABLO
UNIVERSIDAD DE LA LAGUNA

30/06/2017 15:21:31

30/06/2017 15:34:17

06/07/2017 13:51:19

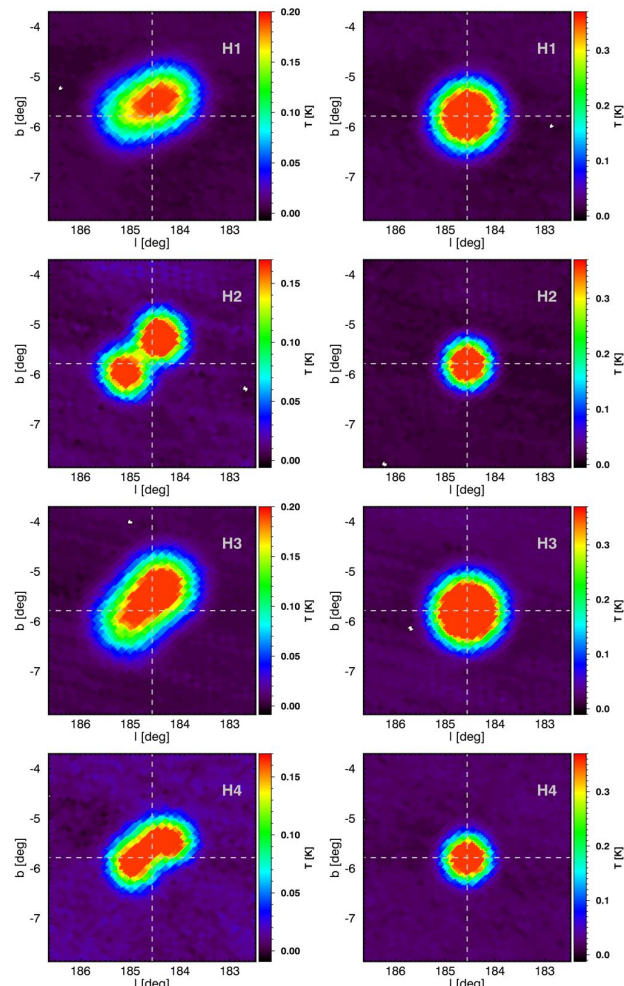


Figure 5.10: Stack of 650 Crab observations in Galactic coordinates for horns 1 to 4 (top to bottom) in the low frequency band, with no pointing correction (left panels) after applying the pointing from table 5.6 (right panel).

Este documento incorpora firma electrónica, y es copia auténtica de un documento electrónico archivado por la ULL según la Ley 39/2015.
Su autenticidad puede ser contrastada en la siguiente dirección <https://sede.ull.es/validacion/>

Identificador del documento: 973742

Código de verificación: Jfg6xBh0

Firmado por: DENIS TRAMONTE
UNIVERSIDAD DE LA LAGUNA

Fecha: 30/06/2017 15:10:10

RAFAEL DELFIN BARRENA DELGADO
UNIVERSIDAD DE LA LAGUNA

30/06/2017 15:21:31

JOSE ALBERTO RUBIÑO MARTIN
UNIVERSIDAD DE LA LAGUNA

30/06/2017 15:34:17

ERNESTO PEREDA DE PABLO
UNIVERSIDAD DE LA LAGUNA

06/07/2017 13:51:19

correction. We also see that the ellipticity are negligible, the beams resulting rounded in projection, and with values for the FWHMs comparable with the theoretical values from table 5.1. Notice, however, that the MFI beams may possess an intrinsic ellipticity. Anyway, in the maps that we are using to test the goodness of the pointing model we are averaging over several rasters, taken at different elevations, meaning that the beam will correspondingly appear with different orientations. In the final stack of all observations, therefore, the intrinsic beam ellipticity should average out to a first approximation.

The results reported in this section show that the individual pointing model solution per horn reported in table 5.6 solves the problem of the telescope pointing calibration. It has been included in the MFI pipeline for data reduction, and it is routinely employed by the QUIJOTE Collaboration in the scientific exploitation of QUIJOTE data.

5.2.4 Conclusions about QUIJOTE pointing model

In this section we have presented the way we implemented numerically the coordinate transformations useful when analyzing data coming from an observation of QUIJOTE. We also described the corrections for the pointing of the telescope, and explained the meaning of the different parameters. A detailed study has been made to obtain the best estimates for these parameters, reported in table 5.6. The main conclusions of the above analysis can be summarised as follows.

- The pointing parameters are highly degenerate. This means that different sets of parameters can be equally good in correcting the pointing of the telescope, and for this reason different estimations can give a different value for each individual parameter.
- The estimation of the pointing model is sensitive to the observed sky region. For this reason it is advisable to always employ the largest sky coverage as possible and the widest ranges of azimuth and elevation values, by combining observations of different radio sources.
- We found that the initial best-fit pointing model depends on the horn, meaning that the geometry of the focal plane is not ideal. The non-ideality is not simple, though, being probably a combination of a displacement along the telescope axis and a tilt of the whole focal plane. The results suggest a better estimation of the focal length as $f = 3700$ mm, about 6 cm longer than the nominal value.

Este documento incorpora firma electrónica, y es copia auténtica de un documento electrónico archivado por la ULL según la Ley 39/2015.
Su autenticidad puede ser contrastada en la siguiente dirección <https://sede.ull.es/validacion/>

Identificador del documento:	973742	Código de verificación:	Jfg6xBh0
Firmado por:	DENIS TRAMONTE UNIVERSIDAD DE LA LAGUNA	Fecha:	30/06/2017 15:10:10
	RAFAEL DELFIN BARRENA DELGADO UNIVERSIDAD DE LA LAGUNA		30/06/2017 15:21:31
	JOSE ALBERTO RUBIÑO MARTIN UNIVERSIDAD DE LA LAGUNA		30/06/2017 15:34:17
	ERNESTO PEREDA DE PABLO UNIVERSIDAD DE LA LAGUNA		06/07/2017 13:51:19

- The lack of a horn in the centre of the focal plane prevents us from disentangling the parameters of the focal plane geometry and of the telescope pointing. This forces us to employ a different set of parameters depending on the horn, which absorbs also the deviation of the horn position from its nominal coordinates.
- Our final fit for the pointing parameters employed the nominal positions for the horns and the new estimated focal length. Even if we lack a complete understanding of the focal plane geometry and the telescope mechanical non-idealities, the final solution, as a set of four individual pointing model per horn, is capable of correcting the pointing within the required accuracy and is routinely employed for QUIJOTE data analysis.

A similar procedure is planned to be used for calibrating the pointing of the QT2 telescope with the TGI instrument. However, the TGI is equipped with a horn in the centre of the focal plane. This will allow the estimation of the pointing parameters of the telescope using the central horn. Once a best-fit solution has been found, the pointing can be fixed and the data from the other horns can be used to explore the geometry of the TGI focal plane.

5.3 Study of Galactic foreground emissions with the MFI

In this last section we turn to the scientific exploitation of data acquired with the MFI. In particular, we will consider three Galactic regions, W49, W51 and IC443. Our aim is to analyse the radio emission from these regions, both in intensity and polarisation, with particular interest in finding possible evidences of anomalous microwave emission. The process starts with the analysis of the raw data and the selection of good observations. The selected observations are then stacked together to create a calibrated map of the region in Galactic coordinates. From this map we can then extract the integrated flux densities at different frequencies, to build the corresponding spectral energy distribution. We detail each step in the following, and conclude with a discussion of the results.

5.3.1 Galactic regions

We begin by giving a brief description of the Galactic regions that we are going to consider. Their locations on the Galactic plane are shown in figure 5.11.

Este documento incorpora firma electrónica, y es copia auténtica de un documento electrónico archivado por la ULL según la Ley 39/2015.
Su autenticidad puede ser contrastada en la siguiente dirección <https://sede.ull.es/validacion/>

Identificador del documento:	973742	Código de verificación:	Jfg6xBh0
Firmado por:	DENIS TRAMONTE UNIVERSIDAD DE LA LAGUNA	Fecha:	30/06/2017 15:10:10
	RAFAEL DELFIN BARRENA DELGADO UNIVERSIDAD DE LA LAGUNA		30/06/2017 15:21:31
	JOSE ALBERTO RUBIÑO MARTIN UNIVERSIDAD DE LA LAGUNA		30/06/2017 15:34:17
	ERNESTO PEREDA DE PABLO UNIVERSIDAD DE LA LAGUNA		06/07/2017 13:51:19

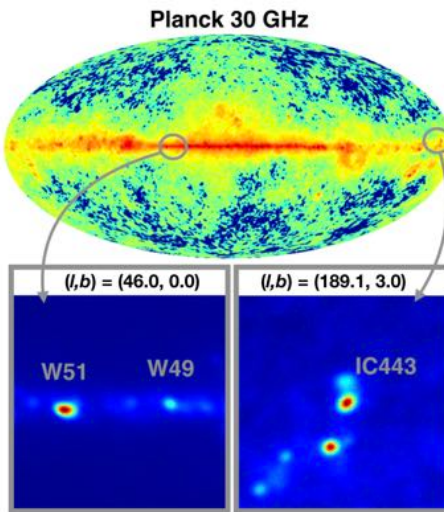


Figure 5.11: Location of the considered regions in Galactic coordinates, plotted using *Planck*'s lowest frequency map.

W49

W49 (*Westerhout 49*, Brun et al. 2011; Wu et al. 2016) is a Galactic radio source in *Aquila*, located on the plane of the Milky Way at Galactic coordinates¹¹ $(l, b) = (43.2^\circ, 0.0^\circ)$. Emission from this region can be separated in a thermal part W49A, centred in $(l, b) = (43.17^\circ, 0.00^\circ)$, which is a star forming region, and a non-thermal part from a supernova remnant in W49B $(l, b) = (43.27^\circ, -0.19^\circ)$ (Mezger et al. 1967). W49A is a giant molecular cloud with several HII regions associated with star formation activity; it has an estimated mass of $10^6 M_\odot$, a total extension of 100 pc (Simon et al. 2001) and an estimated distance of ~ 11 kpc. W49B is a supernova remnant from a former super-massive star, with an estimated age between 1 and 4 kyr (Pye et al. 1984; Hwang et al. 2000), and a distance between 8 and 12 kpc (Brogan & Troland 2001).

With QUIJOTE resolution it is not possible to resolve the source into the two components. In this work we will consider W49 as an individual region, whose emission is made from the contribution of both the thermal and non-

¹¹All nominal coordinates quoted for the description of the Galactic regions are taken from the SIMBAD astronomical database website, <http://simbad.u-strasbg.fr/simbad/>.

thermal part.

W51

W51 (*Westerhout 51*, [Ginsburg et al. 2016](#)) is a Galactic molecular cloud also in *Aquila*, located west of W49 with central coordinates $(l, b) = (49.1^\circ, -0.6^\circ)$; its position marks the region where the Orion Galactic arm originates, detaching from the Sagittarius arm. It subtends an angular extension of $\sim 30'$ on the sky and is located at a distance of ~ 5.5 kpc ([Sato et al. 2010](#)). It can be divided into three sub-components ([Aleksić et al. 2012](#)), labelled W51A, W51B and W51C.

W51A and W51B are star forming regions: their combination makes W51 one of the largest of these regions in our Galaxy; from here the importance of radio observation of this source ([Mufson & Liszt 1979](#)), that have been used to map its structure ([Carpenter & Sanders 1998](#)).

W51C is a supernova remnant with an age of 30 kyr ([Hanabata et al. 2013](#)); it is responsible for the non-thermal emission from this region. With QUIJOTE it will be observed together with the thermal component from W51A and W51B.

IC443

IC443 (*Index Catalogue 443*, [Kundu & Velusamy 1972](#); [Green 1986](#); [Mitra et al. 2014](#)) is a supernova remnant located in the constellation of *Gemini* at Galactic coordinates $(l, b) = (189.06^\circ, 3.24^\circ)$; it is therefore found close to the Galactic anticentre, with a lower emission from the neighbouring background compared to W49 and W51, which are much closer (in projection) to the Galactic bulge. Observed in radio waves, it shows two spherical shells of synchrotron emission ([Castelletti et al. 2011](#)). It has been extensively observed in X-rays and γ -rays ([Torres et al. 2003](#)). In particular, γ -ray emission deriving from the decay of pions (the “pion-decay bump”) has been detected in IC443 by [Ackermann et al. \(2013\)](#); these pions are produced in collisions between accelerated cosmic-ray protons and interstellar material, so that the detection of the pion bump provides information on the source of cosmic rays and on the proton energy distribution. The IC443 supernova event occurred between 3 ([Petre et al. 1988](#)) and 30 kyr ago ([Olbert et al. 2001](#)). Its distance is estimated between 0.7 and 1.5 kpc ([Lozinskaya 1981](#); [Fesen 1984](#)), and its angular size is $\sim 45'$.

Este documento incorpora firma electrónica, y es copia auténtica de un documento electrónico archivado por la ULL según la Ley 39/2015.
Su autenticidad puede ser contrastada en la siguiente dirección <https://sede.ull.es/validacion/>

Identificador del documento: 973742	Código de verificación: Jfg6xBh0
Firmado por: DENIS TRAMONTE UNIVERSIDAD DE LA LAGUNA	Fecha: 30/06/2017 15:10:10
RAFAEL DELFIN BARRENA DELGADO UNIVERSIDAD DE LA LAGUNA	30/06/2017 15:21:31
JOSE ALBERTO RUBIÑO MARTIN UNIVERSIDAD DE LA LAGUNA	30/06/2017 15:34:17
ERNESTO PEREDA DE PABLO UNIVERSIDAD DE LA LAGUNA	06/07/2017 13:51:19

5.3.2 Data selection

We considered all data taken with the MFI on the three Galactic regions. W49 was observed in 193 dedicated observations performed between June and August 2015, for a total observing time of ~ 235 hours; these observations were raster scans in which the telescope elevation was maintained fixed (in this case one usually talks about a *drift scan*, or *transit*), and the pointing is switched back and forth in azimuth with a ~ 15 degree amplitude on the sky for each scan; the crossing of the source was ensured by the apparent motion of the sky. Observations for W51 were performed between October and December 2016, with 162 drift scans again with a ~ 15 degree azimuth amplitude on the sky, corresponding in total to 184 hours. Finally, observations of IC443 were 553 raster scans with an amplitude of ~ 12 degrees in elevation and ~ 15 degrees in azimuth (on the sky), performed between October 2014 and June 2015 for a total observing time of 263 hours.

However, it is not possible to use the full set of data for our analysis. Raw data must be checked in order to discard the observations affected by bad weather, external interference, gain variations or other issues related to bad instrumental behavior. Part of this check is performed automatically: the data reduction software flags data at the TOD level, on the basis of different criteria. These are, e.g. values of the cryostat temperature and pressure out of range, pointing too close to the Sun or the Moon ($< 10^\circ$) or to satellites ($< 5^\circ$), bad weather (precipitable water vapour data above the accepted threshold), too high values of the dispersion of data (computed in 60 ms intervals) or data with strong drifts of the baseline level. However, there are features that cannot be detected by the software, requiring an eye inspection of provisional maps built daily for each individual observation; this allowed us to assess if the overall signal-to-noise of each observation was acceptable, and to detect possible spurious contribution entering the maps. For every horn we considered the eight maps obtained from the output of all its channels; if any particularly evident feature was found affecting the appearance of the source in any of the channels, the corresponding observation was discarded. This resulted in a different selection per horn, made of a subset of the complete list of observations. We list the relative percentage of used time in table 5.8. We see that in general a 20 – 30% of observations is finally discarded. Notice, however, that these time fractions are computed using all the observations accepted on the basis of the eye inspection, and considering the full length of their TODs. The automatic data flagging further reduces the total fraction of effective time, so that the values reported in table 5.8 are to be intended as upper limits.

Este documento incorpora firma electrónica, y es copia auténtica de un documento electrónico archivado por la ULL según la Ley 39/2015.
Su autenticidad puede ser contrastada en la siguiente dirección <https://sede.ull.es/validacion/>

Firmado por:	Identificador del documento:	Código de verificación:	Fecha:
DENIS TRAMONTE UNIVERSIDAD DE LA LAGUNA	973742	Jfg6xBh0	30/06/2017 15:10:10
RAFAEL DELFIN BARRENA DELGADO UNIVERSIDAD DE LA LAGUNA			30/06/2017 15:21:31
JOSE ALBERTO RUBIÑO MARTIN UNIVERSIDAD DE LA LAGUNA			30/06/2017 15:34:17
ERNESTO PEREDA DE PABLO UNIVERSIDAD DE LA LAGUNA			06/07/2017 13:51:19

	N_{obs}	t_{tot} [hrs]	f_t (H1) [%]	f_t (H2) [%]	f_t (H3) [%]	f_t (H4) [%]
W49	193	235.5	85.0	54.0	79.5	78.8
W51	162	184.2	79.8	80.2	80.9	69.1
IC443	553	263.6	76.0	73.1	74.6	70.5

Table 5.8: Results from the data selection. For each region we report the total number of dedicated observations N_{obs} , the corresponding total time in hours t_{tot} , and the time fraction of accepted observations f_t for each one of the horn, in terms of the ratio of the effective hours of observations used against the total t_{tot} . These fractions are computed on the basis of the eye inspection only, so they do not take into account the further loss of data deriving from the automatic flagging.

5.3.3 Gain calibration

The output signal from the MFI horns is measured in Volts; for the subsequent measurements of flux densities from the Galactic sources, these voltages must be transformed into temperatures. This is done using proper *gain factors* for the 32 MFI output channels. For an individual channel, we define the gain factor g as the factor that converts the observed temperature into the output voltage (units of g are usually mV/mK).

The gain factors are calibrated using observations of a radio source whose flux density at the observation frequency is known. Cas A is a bright source that can serve for this purpose (the same source that we also employed for the pointing calibration in section 5.2). As explained in Génova-Santos et al. (2015a), the average gain factors are estimated as the ratio:

$$g_{\text{avg}} = \left\langle \frac{V_{\text{Cas}}}{T_{\text{Cas}}} \right\rangle, \quad (5.37)$$

where V_{Cas} is the output voltage from the channel we are considering, while T_{Cas} is the temperature of Cas A at the corresponding frequency, determined using the spectrum from Weiland et al. (2011) and estimating the source secular variation using the model of Hafez et al. (2008). The average in 5.37 means that the final estimates for g are taken as the median (for each channel) over a set of several observations of Cas A, which is observed on a daily basis.

For this work we considered a more refined way of calibrating the gain factors. In the electronics of the MFI a diode is integrated; this diode injects a signal of constant amplitude in the MFI channels at regular time intervals

Este documento incorpora firma electrónica, y es copia auténtica de un documento electrónico archivado por la ULL según la Ley 39/2015.
Su autenticidad puede ser contrastada en la siguiente dirección <https://sede.ull.es/validacion/>

Identificador del documento: 973742	Código de verificación: Jfg6xBh0
Firmado por: DENIS TRAMONTE UNIVERSIDAD DE LA LAGUNA	Fecha: 30/06/2017 15:10:10
RAFAEL DELFIN BARRENA DELGADO UNIVERSIDAD DE LA LAGUNA	30/06/2017 15:21:31
JOSE ALBERTO RUBIÑO MARTIN UNIVERSIDAD DE LA LAGUNA	30/06/2017 15:34:17
ERNESTO PEREDA DE PABLO UNIVERSIDAD DE LA LAGUNA	06/07/2017 13:51:19

(one second-long signal every 30 seconds). The amplitude of the measured diode signal is then sensitive to variations in time of the instrumental gain. For each observation of W49, W51 or IC443, the diode amplitude is averaged over all the activations during the considered raster or transit; let us call \tilde{A}_d the corresponding median of the diode activation amplitudes. Let then $\tilde{A}_{d, \text{Cas}}$ be the same median computed with the observation of Cas A taken in the same day. The gain factor (for an individual channel) is then defined as:

$$g_d = g_{\text{avg}} \frac{\tilde{A}_d}{\tilde{A}_{d, \text{Cas}}}, \quad (5.38)$$

where g_{avg} is defined in equation 5.37. The gain factors g_d achieve a more reliable conversion between voltage and temperature compared to the average estimates g_{avg} , because they are calibrated over each particular observation.

The conversion between voltage and temperature is performed using the factors g_d at the TOD level. Notice that this calibration of the output signal from the MFI channels is not a specific tool for this work, but has been recently been used within the QUIJOTE Collaboration for any kind of analyses requiring the estimation of flux densities.

5.3.4 Map-making

For each region, the final maps in intensity and polarisation were created by stacking all accepted observations together. Each pixel of the maps receives the average contribution of the intensity and polarisation signals from all the observations, properly calibrated as detailed in section 5.3.3, corresponding to the TOD value at each crossing of the telescope through the considered point. The use of a properly calibrated pointing model ensures that it is possible to combine, for each source, observations taken at different azimuth and elevations, without a significative bias (this procedure was also employed for the test with Crab in figure 5.10).

However, this naïve method for generating maps suffers from a systematic effect. Apart from the uncorrelated white noise that affects all observations, a combination of changes in the atmospheric brightness and drifts in the instrumental temperature and gain, produce a noise that is correlated over large time scales (or low frequencies). In Fourier space, the contribution of this correlated noise can be modelled as (Zacchei et al. 2011; Zonca et al. 2013):

$$P(k) \propto \left[1 + \left(\frac{f_k}{f} \right) \right], \quad (5.39)$$

Este documento incorpora firma electrónica, y es copia auténtica de un documento electrónico archivado por la ULL según la Ley 39/2015.
Su autenticidad puede ser contrastada en la siguiente dirección <https://sede.ull.es/validacion/>

Identificador del documento: 973742	Código de verificación: Jfg6xBh0
Firmado por: DENIS TRAMONTE UNIVERSIDAD DE LA LAGUNA	Fecha: 30/06/2017 15:10:10
RAFAEL DELFIN BARRENA DELGADO UNIVERSIDAD DE LA LAGUNA	30/06/2017 15:21:31
JOSE ALBERTO RUBIÑO MARTIN UNIVERSIDAD DE LA LAGUNA	30/06/2017 15:34:17
ERNESTO PEREDA DE PABLO UNIVERSIDAD DE LA LAGUNA	06/07/2017 13:51:19

where f_k is a “knee frequency” at which the contribution from the correlated noise and the white noise are the same. For $f < f_k$ the noise scales with frequency as f^{-1} , so that it is referred to as *1/f noise* (or *pink noise* or *flicker noise*). The 1/f noise affects the final maps, determining the appearance of a series of bright and dark stripes superimposed to the observed signal.

The 1/f can be removed at the map level by using tailored techniques, which are generally referred to as *desstriping algorithms*. The subject of desstriping algorithms has been largely discussed in the literature, being a common tool necessary to clean CMB maps (e.g., Delabrouille 1998; Maino et al. 2002; Kurki-Suonio et al. 2009; Planck Collaboration et al. 2016d). The algorithm employed by the QUIJOTE Collaboration, and that we used for generating the final maps for our regions, is described in Génova-Santos et al. (2017). Notice that the 1/f contribution was not important for the Crab maps in figure 5.10, were we were only interested in the position and geometry of the recovered PSF. However, it is of crucial importance now for the subsequent flux estimation that we want to perform.

We show the desstriped maps for W49, W51 and IC443 in figures 5.12, 5.13 and 5.14 respectively. Results are presented for all the observed frequency bands, and for the three Stokes parameters I , Q and U . Note that the regions W49 and W51 are neighbouring, and the amplitude of the drift scans in many cases allowed to observe both of them in the same transit. However, in the observations dedicated to W49 (that were the first to be made, in 2015), the source W51 was not always completely covered by all horns. For this reason it was decided to repeat a set of observations specifically centred on W51 in the end of 2016. In principle, for generating maps it is possible to stack together all the observations, whether they are centred on W49 or W51. However, we found that the final desstriped maps for each source are cleaner when generated using only the observations dedicated to that source. Therefore, we decided not to combine the two sets of observations; the maps for each source were generated using only the dedicated observations.

Note that at low frequencies we plotted only maps obtained with horn 3, because polarisation measurements with horn 1 cannot be trusted. A mechanical problem with horn 1 prevents the switch of the orientation of its modulator; this implies that it is not possible to average over the four positions of the modulator in order to minimise possible leakages from different channels. This is particularly important for polarisation, because a few percent leakage from intensity is at the level of the polarisation signal itself; the opposite case of leakage from polarisation to intensity is also possible, but the resulting relative error is much lower. Hence, data from horn 1 can be used for studying emission from the three regions only in intensity.

Este documento incorpora firma electrónica, y es copia auténtica de un documento electrónico archivado por la ULL según la Ley 39/2015.
Su autenticidad puede ser contrastada en la siguiente dirección <https://sede.ull.es/validacion/>

Identificador del documento:	973742	Código de verificación:	Jfg6xBh0
Firmado por:	DENIS TRAMONTE UNIVERSIDAD DE LA LAGUNA	Fecha:	30/06/2017 15:10:10
	RAFAEL DELFIN BARRENA DELGADO UNIVERSIDAD DE LA LAGUNA		30/06/2017 15:21:31
	JOSE ALBERTO RUBIÑO MARTIN UNIVERSIDAD DE LA LAGUNA		30/06/2017 15:34:17
	ERNESTO PEREDA DE PABLO UNIVERSIDAD DE LA LAGUNA		06/07/2017 13:51:19

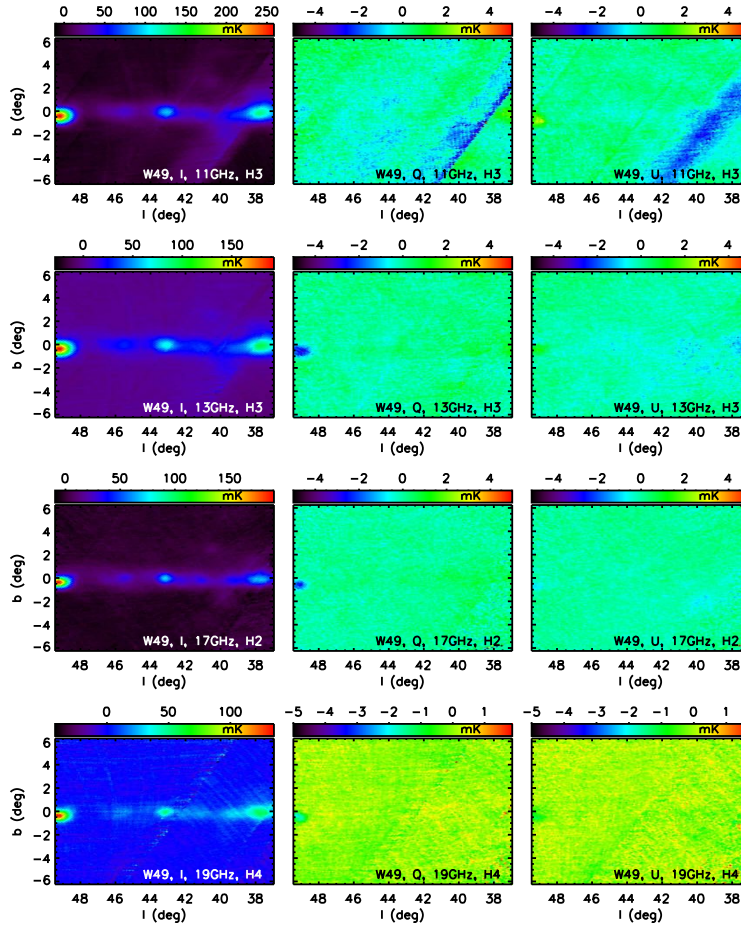


Figure 5.12: Intensity and polarisation W49 destriped maps, for the four QUIJOTE observing frequencies. From top to bottom, we show the maps at 11 GHz (horn 3), 13 GHz (horn 3), 17 GHz (horn 2) and 19 GHz (horn 4); the signal plotted in the maps is intensity I in the left column, the Stokes parameter Q in the middle column and the Stokes parameter U in the right column. In the intensity maps, the sources W51, W49 and W47 (left to right) are clearly visible.

Este documento incorpora firma electrónica, y es copia auténtica de un documento electrónico archivado por la ULL según la Ley 39/2015.
Su autenticidad puede ser contrastada en la siguiente dirección <https://sede.ull.es/validacion/>

Identificador del documento: 973742

Código de verificación: Jfg6xBh0

Firmado por: DENIS TRAMONTE
UNIVERSIDAD DE LA LAGUNA

Fecha: 30/06/2017 15:10:10

RAFAEL DELFIN BARRENA DELGADO
UNIVERSIDAD DE LA LAGUNA

30/06/2017 15:21:31

JOSE ALBERTO RUBIÑO MARTIN
UNIVERSIDAD DE LA LAGUNA

30/06/2017 15:34:17

ERNESTO PEREDA DE PABLO
UNIVERSIDAD DE LA LAGUNA

06/07/2017 13:51:19

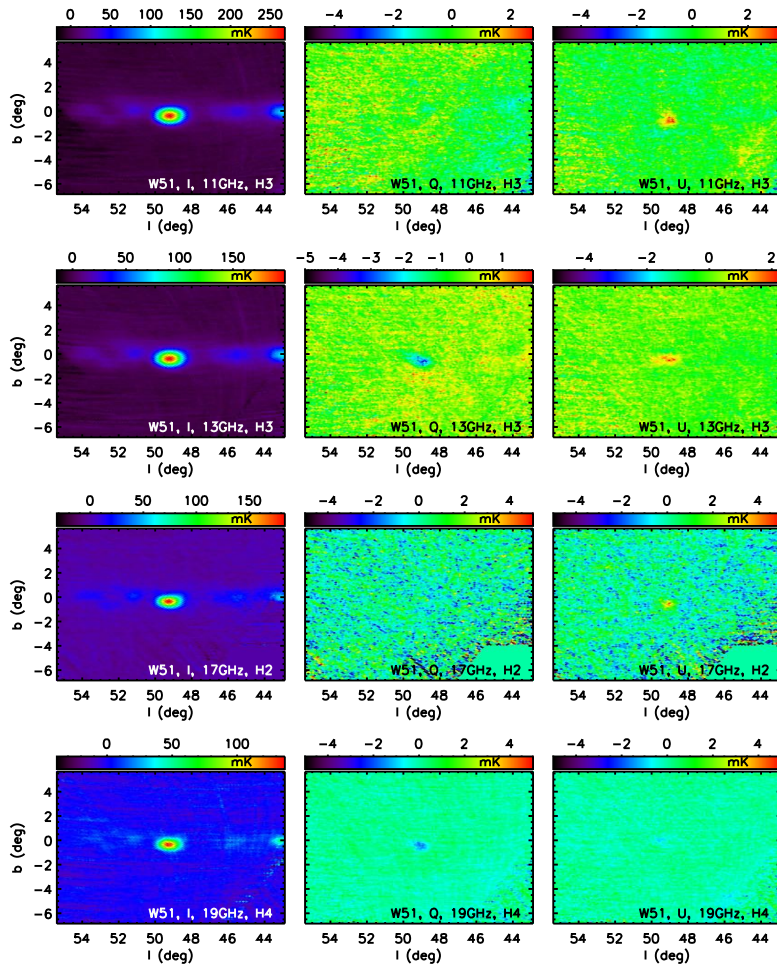


Figure 5.13: Same as figure 5.12, but for W51.

Interference correction

In the destriped maps of W49 for horn 3 at low frequency (figure 5.12, uppermost panels) a clear stripe in the low-right corner is visible, particularly in

Este documento incorpora firma electrónica, y es copia auténtica de un documento electrónico archivado por la ULL según la Ley 39/2015.
Su autenticidad puede ser contrastada en la siguiente dirección <https://sede.ull.es/validacion/>

Identificador del documento: 973742

Código de verificación: Jfg6xBh0

Firmado por: DENIS TRAMONTE
UNIVERSIDAD DE LA LAGUNA

Fecha: 30/06/2017 15:10:10

RAFAEL DELFIN BARRENA DELGADO
UNIVERSIDAD DE LA LAGUNA

30/06/2017 15:21:31

JOSE ALBERTO RUBIÑO MARTIN
UNIVERSIDAD DE LA LAGUNA

30/06/2017 15:34:17

ERNESTO PEREDA DE PABLO
UNIVERSIDAD DE LA LAGUNA

06/07/2017 13:51:19

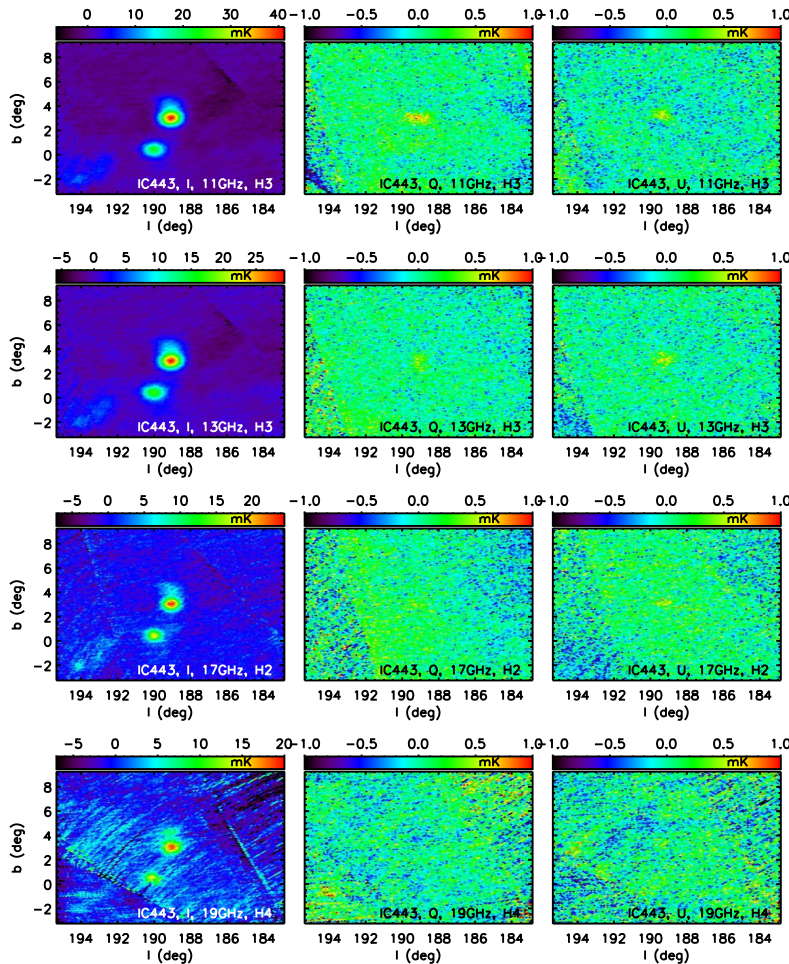


Figure 5.14: Same as figure 5.12, but for IC443.

polarisation. This signal contributes to the map at the level of a few mK, so it is important to characterise its origin.

First of all, we tried to isolate the observations contributing to this con-

Este documento incorpora firma electrónica, y es copia auténtica de un documento electrónico archivado por la ULL según la Ley 39/2015.
Su autenticidad puede ser contrastada en la siguiente dirección <https://sede.ull.es/validacion/>

Identificador del documento: 973742

Código de verificación: Jfg6xBh0

Firmado por: DENIS TRAMONTE
UNIVERSIDAD DE LA LAGUNA

Fecha: 30/06/2017 15:10:10

RAFAEL DELFIN BARRENA DELGADO
UNIVERSIDAD DE LA LAGUNA

30/06/2017 15:21:31

JOSE ALBERTO RUBIÑO MARTIN
UNIVERSIDAD DE LA LAGUNA

30/06/2017 15:34:17

ERNESTO PEREDA DE PABLO
UNIVERSIDAD DE LA LAGUNA

06/07/2017 13:51:19

tamination. Observations of W49 can be divided into four groups, identified by the values of the central azimuth and elevation of the drift scans:

- Group 1 : (AZ,EL)=(110°,49°), 66 observations
- Group 2 : (AZ,EL)=(138°,65°), 29 observations
- Group 3 : (AZ,EL)=(250°,48°), 67 observations
- Group 4 : (AZ,EL)=(262°,33°), 30 observations

We found that only observations from Group 1 produced the stripe: the fact that this signal is limited to a group of observations with the same base pointing suggests that it may be an interference signal coming from a nearby source, and that manages to enter the observation via the side-lobes of horn 3 when the telescope is pointing toward that direction. A possibility is that this interference comes from an artificial satellite. It affects only horn 3 because it is probably the one geometrically closer to the interference region when the focal plane is projected to the sky, and only its lowest frequency band because 11 GHz falls inside the *X-band*, which is a microwave band (8 to 12 GHz) employed by communication satellites.

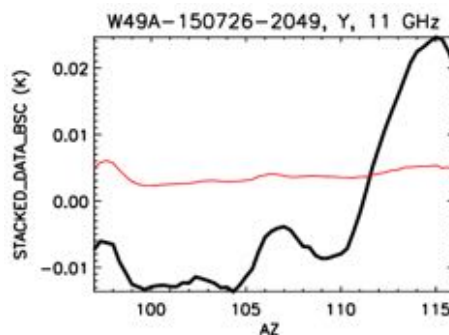


Figure 5.15: Azimuth stack of a W49 observation from Group 1, comparing the signal from QUIJOTE (black) and WMAP (red): the satellite interference clearly emerges at AZ > 104°.

The simplest solution for this interference would be to discard all observations in Group 1. However, since they are quite a large fraction of the available observations of W49 ($\sim 34\%$), we adopted a more conservative approach. We considered individually each one of Group 1 observations and examined what fraction of the TOD was directly affected by the interference. To this aim, we considered *azimuth stacks*, that are histograms of the observed intensity over a

Este documento incorpora firma electrónica, y es copia auténtica de un documento electrónico archivado por la ULL según la Ley 39/2015.
Su autenticidad puede ser contrastada en la siguiente dirección <https://sede.ull.es/validacion/>

Identificador del documento: 973742

Código de verificación: Jfg6xBh0

Fecha: 30/06/2017 15:10:10

Firmado por: DENIS TRAMONTE UNIVERSIDAD DE LA LAGUNA	30/06/2017 15:21:31
RAFAEL DELFIN BARRENA DELGADO UNIVERSIDAD DE LA LAGUNA	30/06/2017 15:34:17
JOSE ALBERTO RUBIÑO MARTIN UNIVERSIDAD DE LA LAGUNA	06/07/2017 13:51:19
ERNESTO PEREDA DE PABLO UNIVERSIDAD DE LA LAGUNA	

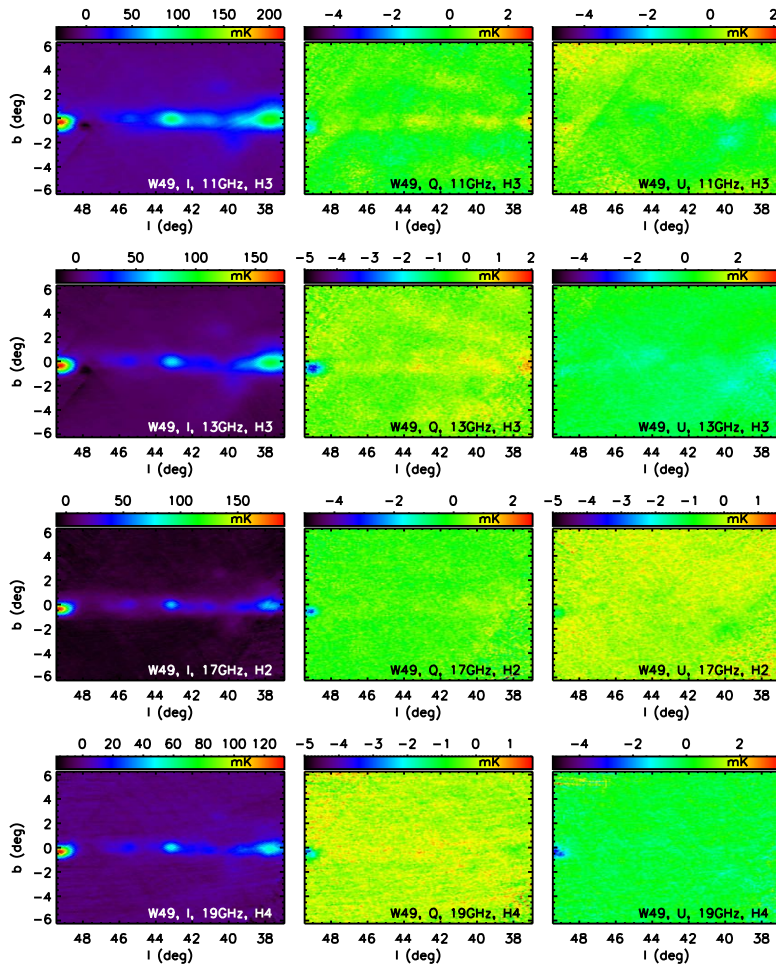


Figure 5.16: Intensity and polarisation W49 destriped maps after correcting for the interference contamination which was present in figure 5.12.

set of azimuth bins (more precisely, in each bin is reported the average of the intensities measured every time the pointing crosses the corresponding azimuth

Este documento incorpora firma electrónica, y es copia auténtica de un documento electrónico archivado por la ULL según la Ley 39/2015.
Su autenticidad puede ser contrastada en la siguiente dirección <https://sede.ull.es/validacion/>

Identificador del documento: 973742

Código de verificación: Jfg6xBh0

Fecha: 30/06/2017 15:10:10

Firmado por: DENIS TRAMONTE
UNIVERSIDAD DE LA LAGUNA

RAFAEL DELFIN BARRENA DELGADO
UNIVERSIDAD DE LA LAGUNA

JOSE ALBERTO RUBIÑO MARTIN
UNIVERSIDAD DE LA LAGUNA

ERNESTO PEREDA DE PABLO
UNIVERSIDAD DE LA LAGUNA

30/06/2017 15:21:31

30/06/2017 15:34:17

06/07/2017 13:51:19

value). All azimuth stacks of Group 1 observations look like the one we show in figure 5.15, right panel. To the QUIJOTE data we overplot the corresponding signal extracted from WMAP data at the lowest frequency (~ 23 GHz), which is made only of astrophysical contributions. We see that QUIJOTE data at higher azimuth show a strong bump which has no counterpart in WMAP data. This is indeed the contribution coming from the interference: since it is limited to $AZ > 104^\circ$, it is safe to maintain the observations of W49 from Group 1 if we discard this region from the TODs. After this correction, we get the final destriped maps for W49 that are shown in figure 5.16.

5.3.5 Flux extraction

In the maps of figures 5.16, 5.13 and 5.14 the three sources we are considering are clearly visible in intensity. In polarisation the signal to noise ratio is lower, but some emission is still visible in the position of the source for W51 and IC443; this suggests the actual existence of a polarised emission in this regions. The same cannot be said for W49, which seems not to emit a polarised signal.

In order to be more quantitative we proceeded to the estimation of flux density coming from the sources at the different frequencies. The technique we employed is called *aperture photometry*, and consists in the integration of the signal from all pixels inside a circle centred in the source; the background level is estimated by averaging the signal from pixels enclosed in an external annulus, and is then subtracted from the integrated signal from the inner disc. This technique has already been used for the estimation of the level of AME emission (López-Caraballo et al. 2011; Rubiño-Martín et al. 2012a; Génova-Santos et al. 2015a, 2017). In formulae, the flux is computed as:

$$S_\nu = a(\nu) \left[\frac{1}{n_1} \sum_{i=1}^{n_1} T_i - \frac{1}{n_2} \sum_{j=1}^{n_2} T_j \right] \quad (5.40)$$

where n_1 and n_2 are the total number of pixels in the internal aperture and in the background annulus, respectively, and T_i and T_j are the corresponding pixel calibrated temperatures from the map (in intensity or polarisation). $a(\nu)$ is the conversion factor between temperature and flux density,

$$a(\nu) = \frac{h^2 \nu^4}{2k_B T_0 c^2} \sinh^{-2} \left(\frac{h\nu}{k_B T_0} \right) n_1 \Omega_{\text{pix}}, \quad (5.41)$$

with Ω_{pix} the solid angle subtended by each pixel. The error associated to the

Este documento incorpora firma electrónica, y es copia auténtica de un documento electrónico archivado por la ULL según la Ley 39/2015.
Su autenticidad puede ser contrastada en la siguiente dirección <https://sede.ull.es/validacion/>

Identificador del documento: 973742

Código de verificación: Jfg6xBh0

Fecha: 30/06/2017 15:10:10

Firmado por: DENIS TRAMONTE UNIVERSIDAD DE LA LAGUNA	30/06/2017 15:21:31
RAFAEL DELFIN BARRENA DELGADO UNIVERSIDAD DE LA LAGUNA	30/06/2017 15:34:17
JOSE ALBERTO RUBIÑO MARTIN UNIVERSIDAD DE LA LAGUNA	06/07/2017 13:51:19
ERNESTO PEREDA DE PABLO UNIVERSIDAD DE LA LAGUNA	

estimate 5.40 can be evaluated as (Rubiño-Martín et al. 2012a):

$$\sigma(S_\nu) = a(\nu) \left[\frac{1}{n_1^2} \sum_{i,i'}^{n_1,n_1} C(\theta_{ii'}) + \frac{1}{n_2^2} \sum_{j,j'}^{n_2,n_2} C(\theta_{jj'}) - \frac{2}{n_1 n_2} \sum_{i,j}^{n_1,n_2} C(\theta_{ij}) \right]^{1/2}, \quad (5.42)$$

where the indices i and i' run over the n_1 pixels in the internal aperture and the indices j and j' run over the n_2 pixels in the external annulus. The angle θ_{ij} is the separation between the pixels i and j , while $C(\theta_{ij})$ is the pixel-to-pixel two-point correlation function. Since we do not know the noise correlation function we estimated the errors using the approximated relation provided in the same reference:

$$\sigma(S_\nu) \simeq a(\nu) \sigma(T_{\text{bg}}) \left[\frac{1}{n_{\text{ap}}^2} + \frac{1}{n_{\text{bg}}^2} \right]^{1/2}, \quad (5.43)$$

where $\sigma(T_{\text{bg}})$ is the pixel-to-pixel standard deviation, while n_{ap} and n_{bg} are the numbers of independent pixels in the aperture and in the background (Rubiño-Martín et al. 2012a).

In our implementation we chose an inner aperture with a 60 arcmin radius, and an external annulus comprised between the radii of 80 and 100 arcmin. For this work, we employed a dedicated software for performing aperture photometry that is available within the QUIJOTE Collaboration. The fluxes obtained for the three sources at all QUIJOTE frequencies are listed in table 5.9 for intensity, in table 5.10 for Q and in table 5.11 for U . Notice that for QUIJOTE eight different frequencies are reported, corresponding to the measured value for each horn output (which may be different from the nominal values).

In order to extend the frequency range in which we study the sources, we considered also ancillary data from other surveys and missions, and performed the flux extractions on the corresponding maps. More precisely, at low frequency we considered the map at 408 MHz from Haslam et al. (1982), which covers the whole sky and was carried out using different facilities (Jodrell Bank MkI, Bonn-100 m, Parkes-64 m and Jodrell Bank MkIA telescopes). At 820 MHz we employed the Berkhuijsen (1972) map, obtained from a survey with the Dwingeloo-25 m telescope (Netherlands). We considered the Reich & Reich (1986) survey at 1420 MHz conducted with the Stockert-25m telescope (Germany) and the (Jonas et al. 1998) survey from the HartRAO-26 m radio telescope (South Africa). Note that IC443 is not covered by the HartRAO, so for the latter survey we can only compute the fluxes for W49 and W51. At higher frequencies we employed data from the CMB satellite missions described in Chapter 1. We used the five WMAP bands at 23, 33, 41, 61, and 94

Este documento incorpora firma electrónica, y es copia auténtica de un documento electrónico archivado por la ULL según la Ley 39/2015.
Su autenticidad puede ser contrastada en la siguiente dirección <https://sede.ull.es/validacion/>

Identificador del documento: 973742

Código de verificación: Jfg6xBh0

Fecha: 30/06/2017 15:10:10

Firmado por: DENIS TRAMONTE UNIVERSIDAD DE LA LAGUNA	30/06/2017 15:21:31
RAFAEL DELFIN BARRENA DELGADO UNIVERSIDAD DE LA LAGUNA	30/06/2017 15:34:17
JOSE ALBERTO RUBIÑO MARTIN UNIVERSIDAD DE LA LAGUNA	06/07/2017 13:51:19
ERNESTO PEREDA DE PABLO UNIVERSIDAD DE LA LAGUNA	

ν [GHz]	Intensity I flux densities			Survey/Telescope
	W49 [Jy]	W51 [Jy]	IC443 [Jy]	
0.408	223 ± 12	434 ± 14	127 ± 5	Haslam
0.82	167 ± 10	417 ± 9	129 ± 1	Dwingeloo
1.42	133 ± 7	353 ± 6	103 ± 1	Reich
2.33	163 ± 9	385 ± 9	—	HartRao
11.15	143 ± 3	345 ± 2	49 ± 1	QUIJOTE (H3)
11.22	123 ± 4	346 ± 2	57 ± 1	QUIJOTE (H1)
12.84	130 ± 4	342 ± 2	55 ± 1	QUIJOTE (H1)
12.89	111 ± 2	332 ± 2	54 ± 1	QUIJOTE (H3)
16.75	159 ± 4	378 ± 2	55 ± 1	QUIJOTE (H2)
17.00	143 ± 3	371 ± 3	53 ± 1	QUIJOTE (H4)
18.71	159 ± 4	363 ± 3	55 ± 1	QUIJOTE (H2)
19.00	138 ± 3	357 ± 3	51 ± 1	QUIJOTE (H14)
22.7	162 ± 7	341 ± 6	53 ± 2	WMAP
28.4	150 ± 7	330 ± 6	43 ± 1	<i>Planck</i>
32.9	145 ± 6	326 ± 6	42 ± 1	WMAP
40.6	135 ± 6	308 ± 5	38 ± 1	WMAP
44.1	133 ± 6	302 ± 5	36 ± 1	<i>Planck</i>
60.5	130 ± 6	286 ± 5	31 ± 1	WMAP
70.4	138 ± 7	284 ± 6	29 ± 1	<i>Planck</i>
93.0	187 ± 11	307 ± 9	31 ± 1	WMAP
100	220 ± 13	329 ± 11	35 ± 2	<i>Planck</i>
143	498 ± 33	484 ± 28	54 ± 5	<i>Planck</i>
217	2018 ± 144	1540 ± 118	204 ± 20	<i>Planck</i>
353	9679 ± 687	6909 ± 556	915 ± 91	<i>Planck</i>
545	$(3.57 \pm 0.25) \times 10^4$	$(2.67 \pm 0.20) \times 10^4$	3055 ± 292	<i>Planck</i>
857	$(1.18 \pm 0.08) \times 10^5$	$(9.42 \pm 0.65) \times 10^4$	8320 ± 782	<i>Planck</i>
1249	$(2.63 \pm 0.18) \times 10^5$	$(2.35 \pm 0.14) \times 10^5$	$(1.62 \pm 0.14) \times 10^4$	DIRBE
2141	$(4.11 \pm 0.26) \times 10^5$	$(4.80 \pm 0.20) \times 10^5$	$(2.08 \pm 0.17) \times 10^4$	DIRBE
2997	$(2.12 \pm 0.11) \times 10^5$	$(3.57 \pm 0.09) \times 10^5$	$(1.08 \pm 0.09) \times 10^4$	DIRBE

Table 5.9: Intensity fluxes computed with aperture photometry in the regions W49, W51 and IC443. For QUIJOTE we used the maps described in section 5.3.4. The other fluxes were computed using ancillary maps from other surveys. All maps were degraded to a common resolution of 1 degree before extracting the fluxes.

Este documento incorpora firma electrónica, y es copia auténtica de un documento electrónico archivado por la ULL según la Ley 39/2015.
Su autenticidad puede ser contrastada en la siguiente dirección <https://sede.ull.es/validacion/>

Identificador del documento: 973742

Código de verificación: Jfg6xBh0

Fecha: 30/06/2017 15:10:10

Firmado por: DENIS TRAMONTE
UNIVERSIDAD DE LA LAGUNA

RAFAEL DELFIN BARRENA DELGADO
UNIVERSIDAD DE LA LAGUNA

JOSE ALBERTO RUBIÑO MARTIN
UNIVERSIDAD DE LA LAGUNA

ERNESTO PEREDA DE PABLO
UNIVERSIDAD DE LA LAGUNA

30/06/2017 15:21:31

30/06/2017 15:34:17

06/07/2017 13:51:19

ν [GHz]	<i>Q</i> Stokes parameter, flux densities			Survey/Telescope
	W49 [Jy]	W51 [Jy]	IC443 [Jy]	
11.15	1.8 ± 0.1	-0.2 ± 0.2	0.73 ± 0.06	QUIJOTE (H3)
11.22	1.9 ± 0.6	0.5 ± 0.1	0.1 ± 0.1	QUIJOTE (H1)
12.84	1.9 ± 0.4	0.5 ± 0.2	0.4 ± 0.1	QUIJOTE (H1)
12.89	1.2 ± 0.1	-4.2 ± 0.2	0.39 ± 0.07	QUIJOTE (H3)
16.75	0.7 ± 0.2	-0.8 ± 0.7	0.7 ± 0.1	QUIJOTE (H2)
17.00	0.6 ± 0.1	-2.6 ± 0.2	-0.1 ± 0.1	QUIJOTE (H4)
18.71	2.7 ± 0.8	0.5 ± 0.8	-0.3 ± 0.5	QUIJOTE (H2)
19.00	1.7 ± 0.2	-3.7 ± 0.2	-0.2 ± 0.2	QUIJOTE (H4)
22.7	1.01 ± 0.05	-3.38 ± 0.05	0.4 ± 0.02	WMAP
28.4	0.70 ± 0.04	-4.19 ± 0.05	0.6 ± 0.02	<i>Planck</i>
32.9	0.82 ± 0.04	-3.30 ± 0.05	0.4 ± 0.03	WMAP
40.6	0.51 ± 0.03	-3.05 ± 0.05	0.1 ± 0.03	WMAP
44.1	0.40 ± 0.06	-2.90 ± 0.04	0.5 ± 0.03	<i>Planck</i>
60.5	-0.02 ± 0.06	-2.39 ± 0.06	0.4 ± 0.07	WMAP
70.4	1.04 ± 0.07	-2.69 ± 0.04	-0.2 ± 0.08	<i>Planck</i>
93.0	1.4 ± 0.2	0.007 ± 0.129	-0.2 ± 0.2	WMAP

Table 5.10: Q fluxes computed with aperture photometry in the regions W49, W51 and IC443.

GHz considering the maps from the 9-year data release (Bennett et al. 2013); the nine individual frequency maps from *Planck* (Planck Collaboration et al. 2016a) at 30, 44, 70, 100, 143, 217, 353, 545 and 857 GHz; and three high-frequency channels from the DIRBE instrument on the COBE mission (Hauser et al. 1998) at 1249, 2141, 2998 GHz. In polarisation, apart from QUIJOTE data, we employed the five WMAP bands and the three *Planck* LFI bands (in this preliminary analysis we are not correcting for the intensity to polarization leakage affecting the 28 GHz LFI band). Note that in order to make results comparable, before computing the aperture fluxes, all maps were degraded to a common resolution of 1 degree.

5.3.6 Spectral Energy Distributions

We show now the spectral energy distribution (SED) in intensity, corresponding to the photometry results of section 5.3.5. For all three regions, we show the SED in intensity in figure 5.17.

Este documento incorpora firma electrónica, y es copia auténtica de un documento electrónico archivado por la ULL según la Ley 39/2015.
Su autenticidad puede ser contrastada en la siguiente dirección <https://sede.ull.es/validacion/>

Identificador del documento: 973742	Código de verificación: Jfg6xBh0
Firmado por: DENIS TRAMONTE UNIVERSIDAD DE LA LAGUNA	Fecha: 30/06/2017 15:10:10
RAFAEL DELFIN BARRENA DELGADO UNIVERSIDAD DE LA LAGUNA	30/06/2017 15:21:31
JOSE ALBERTO RUBIÑO MARTIN UNIVERSIDAD DE LA LAGUNA	30/06/2017 15:34:17
ERNESTO PEREDA DE PABLO UNIVERSIDAD DE LA LAGUNA	06/07/2017 13:51:19

ν [GHz]	<i>U</i> Stokes parameter, flux densities			Survey/Telescope
	W49 [Jy]	W51 [Jy]	IC443 [Jy]	
11.15	-0.5 ± 0.1	3.2 ± 0.2	0.52 ± 0.07	QUIJOTE (H3)
11.22	0.1 ± 0.5	1.1 ± 0.1	0.5 ± 0.1	QUIJOTE (H1)
12.84	0.2 ± 0.4	1.1 ± 0.1	0.4 ± 0.1	QUIJOTE (H1)
12.89	-0.2 ± 0.1	2.4 ± 0.2	0.8 ± 0.1	QUIJOTE (H3)
16.75	-0.6 ± 0.2	6.1 ± 0.8	0.5 ± 0.2	QUIJOTE (H2)
17.00	-0.1 ± 0.2	-3.5 ± 0.3	0.5 ± 0.2	QUIJOTE (H4)
18.71	-0.1 ± 0.5	5 ± 1	1.6 ± 0.8	QUIJOTE (H2)
19.00	-0.6 ± 0.3	-1.2 ± 0.3	0.4 ± 0.3	QUIJOTE (H4)
22.7	0.33 ± 0.06	-1.98 ± 0.03	0.71 ± 0.02	WMAP
28.4	0.53 ± 0.06	-0.56 ± 0.03	0.44 ± 0.02	<i>Planck</i>
32.9	0.07 ± 0.05	-1.34 ± 0.02	0.48 ± 0.03	WMAP
40.6	0.28 ± 0.05	-1.08 ± 0.02	0.61 ± 0.03	WMAP
44.1	0.07 ± 0.04	-0.99 ± 0.03	0.58 ± 0.03	<i>Planck</i>
60.5	0.43 ± 0.08	-1.02 ± 0.05	0.63 ± 0.09	WMAP
70.4	0.45 ± 0.05	-0.87 ± 0.04	0.96 ± 0.05	<i>Planck</i>
93.0	-0.3 ± 0.2	-1.2 ± 0.1	-0.5 ± 0.1	WMAP

Table 5.11: *U* fluxes computed with aperture photometry in the regions W49, W51 and IC443.

Qualitatively, the intensity SEDs clearly show the contribution from different astrophysical emissions. The lowest frequency data fall with frequency as expected for synchrotron and/or free-free emissions. The highest frequencies are dominated by thermal dust. The central frequencies, between 10 and 30 GHz, show a clear bump, particularly in W49 and W51, which may be the signature of AME contribution. However, care must be taken when constraining the emission with the lowest frequency data, which have a high statistical weight when fitting for the different emission components: this has to be taken into account in the characterisation of the errors for these points. In particular, the HartRAO point seems to be an outlier, maybe due to an erroneous calibration.

Notice that the results from tables 5.10 and 5.11 show that QUIJOTE detects polarised emission from all three regions. It is therefore interesting to consider the total polarisation intensity:

$$P = (Q^2 + U^2)^{1/2}, \quad (5.44)$$

Este documento incorpora firma electrónica, y es copia auténtica de un documento electrónico archivado por la ULL según la Ley 39/2015.
Su autenticidad puede ser contrastada en la siguiente dirección <https://sede.ull.es/validacion/>

Firmado por: DENIS TRAMONTE <i>UNIVERSIDAD DE LA LAGUNA</i>	Identificador del documento: 973742	Código de verificación: Jfg6xBh0	Fecha: 30/06/2017 15:10:10
RAFAEL DELFIN BARRENA DELGADO <i>UNIVERSIDAD DE LA LAGUNA</i>			30/06/2017 15:21:31
JOSE ALBERTO RUBIÑO MARTIN <i>UNIVERSIDAD DE LA LAGUNA</i>			30/06/2017 15:34:17
ERNESTO PEREDA DE PABLO <i>UNIVERSIDAD DE LA LAGUNA</i>			06/07/2017 13:51:19

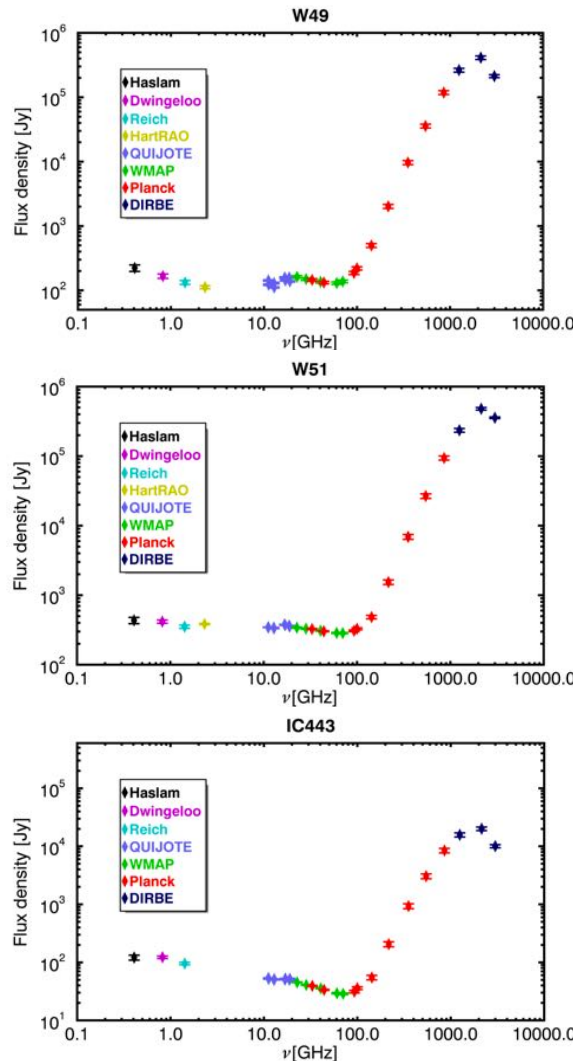


Figure 5.17: Intensity SED for the three regions, joining results from the eight QUIJOTE frequencies and all the other ancillary data listed in section 5.3.5.

Este documento incorpora firma electrónica, y es copia auténtica de un documento electrónico archivado por la ULL según la Ley 39/2015.
Su autenticidad puede ser contrastada en la siguiente dirección <https://sede.ull.es/validacion/>

Identificador del documento: 973742

Código de verificación: Jfg6xBh0

Fecha: 30/06/2017 15:10:10

Firmado por: DENIS TRAMONTE
UNIVERSIDAD DE LA LAGUNA

RAFAEL DELFIN BARRENA DELGADO
UNIVERSIDAD DE LA LAGUNA

JOSE ALBERTO RUBIÑO MARTIN
UNIVERSIDAD DE LA LAGUNA

ERNESTO PEREDA DE PABLO
UNIVERSIDAD DE LA LAGUNA

30/06/2017 15:21:31

30/06/2017 15:34:17

06/07/2017 13:51:19

and its spectral distribution. However, there are still some calibration issues affecting the determination of polarised flux. Indeed, from tables 5.10 we see that we do not find consistency between different horns at the same frequency. We mentioned already that there are some issues associated with the determination of polarisation fluxes with horn 1. However, even if we consider only the other horns, there is not a clear dependence of the fluxes on frequency. Besides, due to the non-linear definition 5.44, the polarised intensity P is not Gaussian distributed, so that the total polarised fluxes must be properly *debiased* (Vailancourt 2006; Rubiño-Martín et al. 2012a)

We plan to properly recalibrate the polarisation maps and compute the debiased polarised fluxes in the next months; this will allow us to study the spectral distribution of the polarised emission from the sources. The results of this analysis will be discussed in the paper Tramonte et al. (in prep.). For this work, however, we only focus on the analysis of the intensity emissions, and on the assessment of the level of the AME component in the three regions.

5.3.7 Multicomponent fit of the intensity SEDs

In this section we address the theoretical modelling of the intensity SEDs from figure 5.17 in order to obtain quantitative results on the level of the different emission mechanisms; we considered the four components mentioned in the previous section, namely free-free, synchrotron, thermal dust and spinning dust. We followed the same implementation described in Génova-Santos et al. (2017). For the free-free spectrum we only fit for its amplitude, quantified by the emission measure (EM), maintaining the standard parametrisation for the spectrum shape described in Planck Collaboration et al. (2011a). We include the synchrotron component assuming a power law spectral dependence, and fit for its amplitude at 1 GHz, $S_{\text{sync}}^{\text{1GHz}}$ and its spectral index β_{sync} . The AME is fitted assuming a model of spinning dust emission consisting of a parabola in the logarithmic space ($\log S_{\nu} - \log \nu$), as proposed by Bonaldi et al. (2007). This model is defined by three parameters: the peak frequency $\nu_{\text{AME}}^{\text{peak}}$, the peak amplitude $S_{\text{AME}}^{\text{peak}}$ and the slope at 60 GHz, m_{60} , which quantifies the width of the fitting parabola. The thermal dust component is fitted as a modified blackbody: fitting parameters are its temperature T_{dust} , the optical depth at 250 GHz τ_{250} and the emissivity spectra index β_{dust} .

We tried different combinations of these components, trying to find the one that achieved the best fit, in terms of a lower reduced chi-square χ_{red}^2 . We found that the best fit in W49 is obtained without including the free-free component, while in W51 is obtained without including the synchrotron contribution. For IC443, the use of all components provided the best fit. The inclusion of AME

Este documento incorpora firma electrónica, y es copia auténtica de un documento electrónico archivado por la ULL según la Ley 39/2015.
Su autenticidad puede ser contrastada en la siguiente dirección <https://sede.ull.es/validacion/>

Identificador del documento:	973742	Código de verificación:	Jfg6xBh0
Firmado por:	DENIS TRAMONTE UNIVERSIDAD DE LA LAGUNA	Fecha:	30/06/2017 15:10:10
	RAFAEL DELFIN BARRENA DELGADO UNIVERSIDAD DE LA LAGUNA		30/06/2017 15:21:31
	JOSE ALBERTO RUBIÑO MARTIN UNIVERSIDAD DE LA LAGUNA		30/06/2017 15:34:17
	ERNESTO PEREDA DE PABLO UNIVERSIDAD DE LA LAGUNA		06/07/2017 13:51:19

	W49	W51	IC443
EM(cm^{-6}pc)	-	3983 ± 85	300 ± 30
$S_{\text{sync}}^{\text{1GHz}}(\text{Jy})$	157 ± 7	-	74 ± 3
β_{sync}	-0.40 ± 0.08	-	-0.54 ± 0.04
m_{60}	1.0 ± 0.3	4.2 ± 0.8	3.3 ± 0.9
$S_{\text{AME}}^{\text{peak}}(\text{Jy})$	109 ± 33	72 ± 308	11 ± 39
$\nu_{\text{AME}}^{\text{peak}}$	28.7 ± 0.6	23.0 ± 0.4	18.1 ± 0.5
$10^3\tau_{250}$	1.4 ± 0.1	0.9 ± 0.1	0.15 ± 0.02
β_{dust}	1.59 ± 0.04	1.64 ± 0.05	1.67 ± 0.08
$T_{\text{dust}}(\text{T})$	20.7 ± 0.5	24.1 ± 0.6	18.3 ± 0.5
χ_{red}^2	8.0	9.2	4.5

Table 5.12: Results of the multicomponent fit on the three regions.

always resulted in an improvement in the fit.

The best-fit parameters for this model are listed in tabel 5.12, while in figure 5.18 we show the resulting best fit models overplotted on top of the measured flux densities. Notice that for the fit we decided to discard the HartRAO point, whose absolute flux was dependent on the flux calibration. The results suggest the presence of AME in all regions; however, as it can be seen in table 5.12, the error associated to the amplitude makes it compatible with zero for W51 and IC443. Therefore the detection of AME is not robust. The thermal dust is well fitted, with similar values of the fitting parameters between the three sources. At low frequency, however, the degeneracy between the synchrotron and free-free emissions makes it difficult to assess the effective contribution of the two components.

5.3.8 Summary of this analysis

To conclude, we have shown in the last part of this Chapter the study of the Galactic regions W49, W51 and IC443. We have provided calibrated, clean

Este documento incorpora firma electrónica, y es copia auténtica de un documento electrónico archivado por la ULL según la Ley 39/2015.
Su autenticidad puede ser contrastada en la siguiente dirección <https://sede.ull.es/validacion/>

Identificador del documento: 973742 Código de verificación: Jfg6xBh0

Firmado por: DENIS TRAMONTE <i>UNIVERSIDAD DE LA LAGUNA</i>	Fecha: 30/06/2017 15:10:10
RAFAEL DELFIN BARRENA DELGADO <i>UNIVERSIDAD DE LA LAGUNA</i>	30/06/2017 15:21:31
JOSE ALBERTO RUBIÑO MARTIN <i>UNIVERSIDAD DE LA LAGUNA</i>	30/06/2017 15:34:17
ERNESTO PEREDA DE PABLO <i>UNIVERSIDAD DE LA LAGUNA</i>	06/07/2017 13:51:19

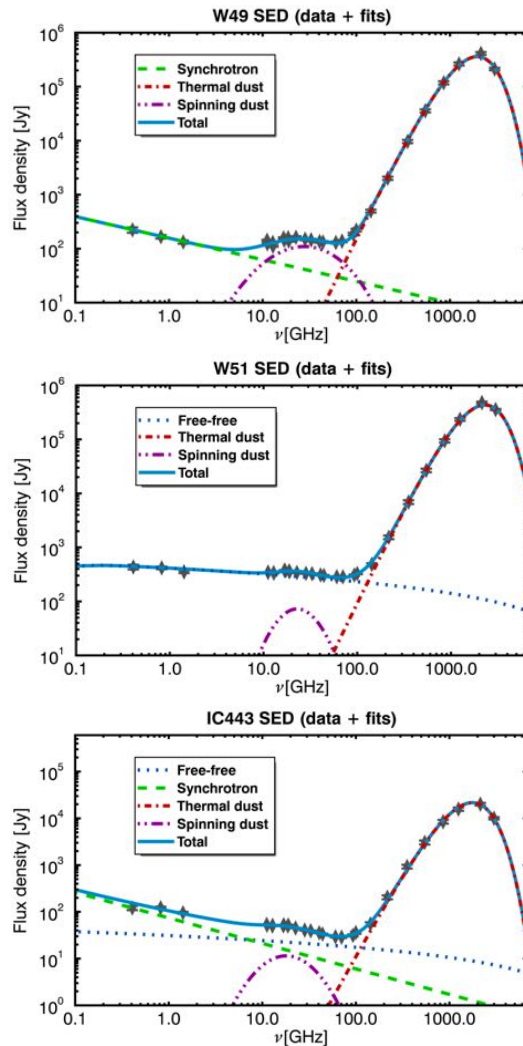


Figure 5.18: The same SEDs from figure 5.17 without the HartRAO point, with the best fit model superimposed.

Este documento incorpora firma electrónica, y es copia auténtica de un documento electrónico archivado por la ULL según la Ley 39/2015.
Su autenticidad puede ser contrastada en la siguiente dirección <https://sede.ull.es/validacion/>

Identificador del documento: 973742

Código de verificación: Jfg6xBh0

Fecha: 30/06/2017 15:10:10

Firmado por: DENIS TRAMONTE
UNIVERSIDAD DE LA LAGUNA

RAFAEL DELFIN BARRENA DELGADO
UNIVERSIDAD DE LA LAGUNA

JOSE ALBERTO RUBIÑO MARTIN
UNIVERSIDAD DE LA LAGUNA

ERNESTO PEREDA DE PABLO
UNIVERSIDAD DE LA LAGUNA

30/06/2017 15:21:31

30/06/2017 15:34:17

06/07/2017 13:51:19

maps for the regions, and made an estimation of the corresponding fluxes in intensity and polarisation. The combination of these results with ancillary data allowed us to build SEDs to assess the contribution from different emission mechanisms in the regions. We found hints of anomalous microwave emission in all the regions, which would be particularly important for the case of the supernova remnant IC443; it is possible, however, that the observed signal derives from a background contribution, which is difficult to separate from the proper source emission given the poor angular resolution of the MFI beams. We also detected polarised emission in the QUIJOTE frequencies.

The results from the modelling of the SEDs in intensity show that the best fit (in terms of lowest reduced chi-square) is provided by including the contribution from thermal dust and AME in all regions (even though in W51 and IC443 the detection is not robust, given the high final error on the estimated peak amplitude), and with different combinations of the synchrotron and free-free emissions, depending on the source. In any case, we found it hard to assess the effective contribution from synchrotron and free-free, due to their degeneracy at low frequencies; besides, the amplitude of the AME has large errors and is compatible with zero for W51 and IC443. With respect to polarisation, the points from QUIJOTE show a large scatter and do not seem to follow a particular frequency dependence.

In fact, there are still open issues, related to the implementation of the aperture photometry flux estimation, and the lack of points in the range from 3 to 10 GHz. In polarisation, in particular, there seem to be issues in the flux extraction. A proper recalibration of the polarised maps, and an implementation of the polarised flux debiasing, is expected for the next months. The results of this analysis can help setting upper limits to possible contribution of AME in polarisation, which can be compared with previous estimates (Rubiño-Martín et al. 2012a; Génova-Santos et al. 2015a, 2017).

In what concerns intensity, the crucial part of the SED is then the low-frequency end. More points are needed to enhance the statistical significance of the fit, and clearly assess the relative contribution of the synchrotron and the free-free emissions. This issue is still open, and it is one of the goals for the final work to present in the paper in preparation.

Este documento incorpora firma electrónica, y es copia auténtica de un documento electrónico archivado por la ULL según la Ley 39/2015.
Su autenticidad puede ser contrastada en la siguiente dirección <https://sede.ull.es/validacion/>

Identificador del documento:	973742	Código de verificación:	Jfg6xBh0
Firmado por:	DENIS TRAMONTE UNIVERSIDAD DE LA LAGUNA	Fecha:	30/06/2017 15:10:10
	RAFAEL DELFIN BARRENA DELGADO UNIVERSIDAD DE LA LAGUNA		30/06/2017 15:21:31
	JOSE ALBERTO RUBIÑO MARTIN UNIVERSIDAD DE LA LAGUNA		30/06/2017 15:34:17
	ERNESTO PEREDA DE PABLO UNIVERSIDAD DE LA LAGUNA		06/07/2017 13:51:19

6

Conclusions

In this thesis we have considered three independent cosmological probes: the large scale structure of the Universe (LSS), the galaxy clusters and the cosmic microwave background (CMB). The aim of this work was to contribute to the cosmological research in these fields; for each probe, we have developed analytical and numerical tools that are necessary for its exploitation, and, when possible, we have provided independent estimates on some cosmological parameters. We list in the following the results obtained for each topic.

Study of the conditional mass function

In chapter 2 we tackled the study of the conditional mass function (CMF), i.e. the mass distribution of the number density of dark matter halos inside regions with a definite density contrast with respect to the background. Although some recipes have been provided in the literature for computing the CMF, it has not been as thoroughly tested as the unconditional mass function (UMF), which predicts the halo abundance over an homogeneous background. In this work:

- we considered two different recipes for computing the CMF, already proposed in the literature: a standard rescaling which is applied globally inside the condition, and one that is implemented locally. We tested that none of them verifies the normalisation condition.
- We explicitly modified the recipes for computing the CMF by including an additional parameter α , in such a way that the CMF results prop-

erly normalised. We found that small-scale conditions $Q \sim 8h^{-1}\text{Mpc}$ are effective in constraining the value $\alpha = 1.25$, while the parameter is basically unconstrained in the case of larger conditions.

- We tested the prediction from the two rescalings against numerical N-body simulations, for conditions with Eulerian radii in the range 5 to $30 h^{-1}\text{Mpc}$ and for halo masses in $[10^{11}, 10^{14}] h^{-1} M_\odot$. We verified that the use of the parameter $\alpha = 1.25$ improves the CMF normalisation also at large scales. We found that the explicitly normalised CMF provides excellent agreement with the simulated halo abundances in underdense regions at all scales and in overdense regions at large scales. These results apply both to the global and the local CMF, the latter providing a slightly better prediction in underdense regions.
- We provided a fitting formula to speed up the computation of the matter-to-halo bias function in underdense regions. We extended a fit already proposed in the literature; the resulting function is capable of reproducing the halo bias with an error below 2% for the reference cosmology, and below 9% when considering different values of redshift or σ_8 . This result is useful for the study of void statistics.
- We finally considered an alternative method for computing the CMF, based on the rescaling of the cosmological parameters locally inside the condition. We considered three different implementations of this recipe, and found good agreement with the standard CMF, except at very large scales where errors can grow larger than 20%.

Constraining cosmological parameters with the abundance of galaxy clusters

In chapter 3 we considered how the redshift distribution of the abundance of galaxy clusters can be used for constraining cosmological parameters. To this aim:

- we first described how to implement the computation of the cluster abundance as observed by a cluster survey. This work implied the implementation of a specific interface to the Boltzmann code **CAMB**, to compute the matter power spectrum for a specific cosmological model. We showed how the total number of observed clusters crucially depends on the survey selection function.

Este documento incorpora firma electrónica, y es copia auténtica de un documento electrónico archivado por la ULL según la Ley 39/2015.
Su autenticidad puede ser contrastada en la siguiente dirección <https://sede.ull.es/validacion/>

Identificador del documento: 973742	Código de verificación: Jfg6xBh0	Fecha: 30/06/2017 15:10:10
Firmado por: DENIS TRAMONTE UNIVERSIDAD DE LA LAGUNA		
RAFAEL DELFIN BARRENA DELGADO UNIVERSIDAD DE LA LAGUNA		30/06/2017 15:21:31
JOSE ALBERTO RUBIÑO MARTIN UNIVERSIDAD DE LA LAGUNA		30/06/2017 15:34:17
ERNESTO PEREDA DE PABLO UNIVERSIDAD DE LA LAGUNA		06/07/2017 13:51:19

- We turned then to the inverse problem of reconstructing the cosmological model starting from a cluster catalogue. This implied the use of statistical techniques, in our case MCMC methods with the *CosmoMC* engine, to reconstruct the posterior probability distribution on the cosmological parameters. We checked that the recovered cosmology was the same as the one employed for the initial survey simulation, thus confirming that our implementation is unbiased and can be applied to real data. We stressed in particular how the total number of observed clusters critically determines the magnitude of the final errors on the parameter estimates.
- We applied our statistical tool to a subsample of the PSZ1 cluster catalogue provided by *Planck*. To this aim it was necessary to implement the *Planck* selection function: this is written in terms of the cluster observables, so that proper scaling relations are required to determine the selection in terms of the cluster mass and redshift. We detailed how these scaling relations are affected by systematic uncertainties, quantified by the cluster mass bias b ; we showed how these systematics can affect the values of the estimated cosmological parameters.
- We concentrated on the parameters Ω_m and σ_8 , which we estimated from *Planck* data using our cluster-based likelihood in combination with likelihoods from BBN and BAO. When fixing the bias parameter to the value $b = 0.2$, we found the final estimates $\Omega_m = 0.293 \pm 0.020$ and $\sigma_8 = 0.760_{-0.017}^{+0.018}$ (68% C.L.). When b is let free to vary with a flat prior in the range $[0.0, 0.3]$ we found the estimates $\Omega_m = 0.289_{-0.020}^{+0.022}$ and $\sigma_8 = 0.750 \pm 0.028$. These results are in very good agreement with the ones provided by the Planck Collaboration for the same data set, in the 2013 paper release.
- These results confirm that our code for the estimation of cosmological parameters can be applied to broader data sets to reduce the final errors on the estimated parameters. An example is the extended subsample of the PSZ1, that is the result of an optical follow-up of PSZ1 cluster candidates undertaken from the Canary Islands Observatories, and that will be soon publicly available.

Constraining cosmology with the SZ 1D PDF

Chapter 4 was dedicated to the study of the thermal Sunyaev-Zel'dovich effect, this time not as a tool for detecting galaxy clusters, but as a cosmological probe

Este documento incorpora firma electrónica, y es copia auténtica de un documento electrónico archivado por la ULL según la Ley 39/2015.
Su autenticidad puede ser contrastada en la siguiente dirección <https://sede.ull.es/validacion/>

Firmado por:	Identificador del documento:	Código de verificación:	Fecha:
DENIS TRAMONTE UNIVERSIDAD DE LA LAGUNA	973742	Jfg6xBh0	30/06/2017 15:10:10
RAFAEL DELFIN BARRENA DELGADO UNIVERSIDAD DE LA LAGUNA			30/06/2017 15:21:31
JOSE ALBERTO RUBIÑO MARTIN UNIVERSIDAD DE LA LAGUNA			30/06/2017 15:34:17
ERNESTO PEREDA DE PABLO UNIVERSIDAD DE LA LAGUNA			06/07/2017 13:51:19

itself. It is indeed possible to construct all-sky maps of the Compton parameter y . In this work:

- we considered the first order statistics of such maps, i.e. the 1-dimensional probability distribution function (PDF) for the Compton parameter. We described how different astrophysical emissions (SZ effect, radio sources, CMB, CIB etc.) contribute to different features of the $P(y)$.
- We showed that the amplitude of the high- y tail of the $P(y)$, which is dominated by the contribution from galaxy clusters, is sensitive to the value of the parameter σ_8 , and can be used as a tool for its estimation.
- We implemented the computation of the PDF for a given cosmology. We modelled the galaxy cluster contribution assuming a pressure profile normalised according to the *Planck* mass-flux scaling relation. The noise component was modelled as a Gaussian; we compared two methods for including the noise contribution, finding overall agreement.
- We tested this formalism for computing the $P(y)$ against a set of simulated Compton parameter maps, generated by including the cluster contribution and the noise component. We found that the resulting PDF is properly reproduced by our analytical implementation.
- We then used the $P(y)$ as a cosmological tool, and fitted for the parameter σ_8 comparing the predicted PDF against the one extracted from *Planck* data. We have considered only values for $y \gtrsim 4.5 \times 10^{-6}$ in order to leave out contamination from instrumental noise and other astrophysical foregrounds, and obtained the final estimate $\sigma_8 = 0.77 \pm 0.02$ (68% C.L.). This result is compatible with other cluster-based estimates, and shows a tension with the value obtained from the CMB (~ 0.83). This tension is still an open issue in cluster cosmology.
- We finally employed the same formalism to forecast the final precision that the future COrE mission can achieve in the determination of σ_8 . The reference y map was the result of a simulation performed by the COrE collaboration. The final estimate that we found is $\sigma_8 = 0.814 \pm 0.002$ (68% C.L.), which is compatible with the value used for simulating the data; the final error is an order of magnitude lower than the one obtained with *Planck* data.

Este documento incorpora firma electrónica, y es copia auténtica de un documento electrónico archivado por la ULL según la Ley 39/2015.
Su autenticidad puede ser contrastada en la siguiente dirección <https://sede.ull.es/validacion/>

Identificador del documento: 973742	Código de verificación: Jfg6xBh0	Fecha: 30/06/2017 15:10:10
Firmado por: DENIS TRAMONTE UNIVERSIDAD DE LA LAGUNA		
RAFAEL DELFIN BARRENA DELGADO UNIVERSIDAD DE LA LAGUNA		30/06/2017 15:21:31
JOSE ALBERTO RUBIÑO MARTIN UNIVERSIDAD DE LA LAGUNA		30/06/2017 15:34:17
ERNESTO PEREDA DE PABLO UNIVERSIDAD DE LA LAGUNA		06/07/2017 13:51:19

Calibration of the QUIJOTE experiment and preliminary analysis of the emission from galactic regions

In Chapter 5 we focused on the QUIJOTE experiment, providing an overall description of its goals and of its first instrument, the MFI. We tackled the problem of the pointing calibration of the first QUIJOTE telescope, and performed a preliminary analysis of MFI data on galactic regions. More precisely:

- we described the possible non-idealities that can affect an altazimuth-type telescope, and the errors they produce on the final pointing. We detailed our formalism for modelling these non-idealities and derived the corresponding pointing corrections, in the form of a set of coordinate transformations. These transformations depend on a set of parameters that constitute the pointing model of the telescope.
- We fitted the best pointing parameters, by comparing the predicted TOD against observations of the bright radio sources Crab and Cas A. We found that the best-fit pointing model depends on the horn. This suggested that the MFI focal plane may not be ideal. Indeed, we found that the best-fit horn positions differ from their nominal values, and that the best-fit focal length is ~ 6 cm longer than the nominal one. However, the degeneracy between the telescope and focal plane non-idealities made it impossible to obtain a common solution for the pointing model.
- Our final determination of the pointing model therefore employed the new focal lengths, the nominal horn positions and allows the pointing parameters to depend on the horn. This solution is capable of correcting the pointing with a final error below 1 arcminute, which is sufficient for the MFI requirements. This pointing model has been implemented in the data reduction software and is routinely employed by the QUIJOTE collaboration.
- We then turned to the scientific exploitation of the MFI data, in the galactic regions W49, W51 (supernova remnants with molecular clouds) and IC443 (supernova remnant). We described how we generated clean maps of these regions, and performed aperture photometry to determine their flux densities at the QUIJOTE frequencies in intensity and in polarization (in terms of the Stokes parameters Q and U). We combined these results with ancillary data to build spectral energy distributions (SEDs) of the sources.

Este documento incorpora firma electrónica, y es copia auténtica de un documento electrónico archivado por la ULL según la Ley 39/2015.
Su autenticidad puede ser contrastada en la siguiente dirección <https://sede.ull.es/validacion/>

Identificador del documento: 973742

Código de verificación: Jfg6xBh0

Fecha: 30/06/2017 15:10:10

Firmado por: DENIS TRAMONTE
UNIVERSIDAD DE LA LAGUNA

RAFAEL DELFIN BARRENA DELGADO
UNIVERSIDAD DE LA LAGUNA

JOSE ALBERTO RUBIÑO MARTIN
UNIVERSIDAD DE LA LAGUNA

ERNESTO PEREDA DE PABLO
UNIVERSIDAD DE LA LAGUNA

30/06/2017 15:21:31

30/06/2017 15:34:17

06/07/2017 13:51:19

- We performed a multicomponent fit to the intensity SEDs to assess the relative contribution of different emission mechanisms (synchrotron, free-free, thermal dust and AME). We found evidence for AME emission in all regions, even though only in W49 we obtained a clear detection. At low frequencies it was generally difficult to disentangle the contributions from synchrotron and free-free. We also detected non-null polarised emission at the QUIJOTE frequencies, but data show a large scatter, probably due to issues in the calibration.
- These are preliminary results, and further work is to be done. In particular, it is planned to recalibrate the polarisation maps and consider the full debiased polarisation fraction. In intensity, the goal is to achieve a better reconstruction of the SED at low frequencies by considering additional ancillary data; this will then lead to a more robust result on the effective contribution of AME in the QUIJOTE frequencies.

Este documento incorpora firma electrónica, y es copia auténtica de un documento electrónico archivado por la ULL según la Ley 39/2015.
Su autenticidad puede ser contrastada en la siguiente dirección <https://sede.ull.es/validacion/>

Identificador del documento: 973742

Código de verificación: Jfg6xBh0

Fecha: 30/06/2017 15:10:10

Firmado por: DENIS TRAMONTE
UNIVERSIDAD DE LA LAGUNA

RAFAEL DELFIN BARRENA DELGADO
UNIVERSIDAD DE LA LAGUNA

JOSE ALBERTO RUBIÑO MARTIN
UNIVERSIDAD DE LA LAGUNA

ERNESTO PEREDA DE PABLO
UNIVERSIDAD DE LA LAGUNA

30/06/2017 15:21:31

30/06/2017 15:34:17

06/07/2017 13:51:19

A

Fitting tables and procedures for the halo bias

In section 2.5 we introduced a fitting function to reproduce the halo bias in underdense regions. The fitting parameters A , b and c defined in (2.41) inherit from the bias the dependence on the object mass m , the condition size Q , the redshift z and the cosmological parameters. In this section we want to explore these residual dependences and provide fitting formulae to compute the parameters A , b and c in different situations. To begin, it is convenient to split the dependence on the variables Q and m from the cosmological variables (including z).

For a given cosmology the dependence on the condition can be fitted by a polynomial function in powers of Q and $\ln(m)$. More precisely, the fitting functions we employed are:

$$\begin{aligned} A(m, Q) &= \sum_{i=0}^3 \left(\sum_{j=0}^3 a_{ij} Q'^j \right) \ln(m')^i, \\ b(m, Q) &= \sum_{i=0}^3 \left(\sum_{j=0}^3 b_{ij} Q'^j \right) \ln(m')^i, \\ c(m, Q) &= \sum_{i=0}^3 \left(\sum_{j=0}^3 c_{ij} Q'^j \right) \ln(m')^i, \end{aligned} \quad (\text{A.1})$$

where $m' = m/3.51 \times 10^{11} h^{-1} M_\odot$ and $Q' = Q/8 h^{-1} \text{Mpc}$. Polynomials are third degree in both radius and mass, resulting in 16 a_{ij} fitting terms for A , 16

Table A.1: Complete list of fitting terms for computing the parameters A , b and c in the reference cosmology, using eq. (A.1). Index i runs over lines, index j runs over columns.

a_{ij}	0	1	2	3
0	-0.91	-0.15	0.69	-0.13
1	1.08	0.42	-0.59	0.10
2	-0.12	-0.20	0.17	-0.03
3	-0.00	0.02	-0.02	0.00
b_{ij}	0	1	2	3
0	5.38	-2.75	0.23	0.03
1	-4.69	2.88	-0.42	-0.00
2	1.48	-0.99	0.18	-0.01
3	-0.15	0.11	-0.02	0.00
c_{ij}	0	1	2	3
0	0.89	1.70	-0.85	0.09
1	-0.25	-1.84	0.85	-0.09
2	0.09	0.55	-0.26	0.03
3	-0.02	-0.04	0.02	-0.00

Table A.2: Complete list of fitting terms to transform the A parameter to the chosen values of z and σ_8 , using eqs. (A.4) and (A.3). Index i selects a line, index j selects a column.

ξ_{ij}^A	0	1	2	3	4
0	-601.87	515.84	-142.68	11.74	0.28
1	480.91	-349.49	59.17	6.42	-1.73
2	-151.77	89.94	-0.73	-7.22	1.04
3	24.26	-12.77	-1.32	1.58	-0.21
4	-1.67	0.95	0.03	-0.09	0.01

b_{ij} fitting terms for b and 16 c_{ij} fitting terms for c . For our reference cosmology, these terms are listed in table A.1. They were obtained allowing the Lagrangian radius to vary in the range $[18.0, 34.0] h^{-1}$ Mpc, and the halo mass in the range $[10^{13}, 6 \times 10^{13}] h^{-1} M_\odot$; the intervals also fix the limits in which the parameters in table A.1 can be applied. Using these tabulated values and eq. (A.1), it is possible to quickly compute the bias with a typical error $\sim 1\text{--}2\%$

The dependence on cosmology is better fitted first in terms of the combination $D(z)\sigma_8$, with $D(z)$ the growth factor of linear perturbation at redshift z , normalized to unity at $z = 0$. Indeed, other combinations of the variables z and σ_8 produce quite a large scatter in the points, making this 1-d fit impossible. This can be understood since the mass function does not depend separately on

Este documento incorpora firma electrónica, y es copia auténtica de un documento electrónico archivado por la ULL según la Ley 39/2015.
Su autenticidad puede ser contrastada en la siguiente dirección <https://sede.ull.es/validacion/>

Identificador del documento: 973742 Código de verificación: Jfg6xBh0

Firmado por: DENIS TRAMONTE UNIVERSIDAD DE LA LAGUNA	Fecha: 30/06/2017 15:10:10
RAFAEL DELFIN BARRENA DELGADO UNIVERSIDAD DE LA LAGUNA	30/06/2017 15:21:31
JOSE ALBERTO RUBIÑO MARTIN UNIVERSIDAD DE LA LAGUNA	30/06/2017 15:34:17
ERNESTO PEREDA DE PABLO UNIVERSIDAD DE LA LAGUNA	06/07/2017 13:51:19

η_{ij}^A	0	1	2	3	4
0	1314.85	-996.58	184.93	13.28	-4.48
1	-942.80	479.62	78.01	-71.26	9.16
2	274.40	-62.62	-92.19	41.22	-4.65
3	-45.12	6.77	18.44	-7.77	0.86
4	3.51	-1.16	-0.88	0.45	-0.05

ζ_{ij}^A	0	1	2	3	4
0	-1357.21	951.22	-109.53	-40.10	7.36
1	957.06	-396.99	-172.61	102.48	-12.41
2	-280.42	32.45	127.75	-53.09	5.89
3	47.90	-4.19	-23.22	9.53	-1.05
4	-3.86	1.25	1.05	-0.53	0.06

z and σ_8 . In order to fit this dependence, we introduced the variable

$$\mathcal{C} \equiv D(z) \frac{\sigma_8}{\tilde{\sigma}_8}, \quad (\text{A.2})$$

where $\tilde{\sigma}_8$ is the value for the reference cosmology. In our case, our reference choice was $\tilde{z} = 0$, $\tilde{\sigma}_8 = 0.8$, to which corresponds $\mathcal{C} = 1$. We considered redshift values in $[0, 1]$ and σ_8 values in $[0.6, 1.0]$. Now, given the parameters A , b and c for the reference cosmology, we found that a convenient function to fit the

ω_{ij}^A	0	1	2	3	4
0	646.58	-516.54	107.32	3.35	-2.02
1	-485.83	297.08	3.29	-27.64	3.98
2	149.69	-64.78	-25.95	16.04	-1.97
3	-24.88	9.90	5.18	-2.94	0.36
4	1.84	-0.96	-0.18	0.16	-0.02

Este documento incorpora firma electrónica, y es copia auténtica de un documento electrónico archivado por la ULL según la Ley 39/2015.
Su autenticidad puede ser contrastada en la siguiente dirección <https://sede.ull.es/validacion/>

Identificador del documento: 973742 Código de verificación: Jfg6xBh0

Firmado por: DENIS TRAMONTE UNIVERSIDAD DE LA LAGUNA	Fecha: 30/06/2017 15:10:10
RAFAEL DELFIN BARRENA DELGADO UNIVERSIDAD DE LA LAGUNA	30/06/2017 15:21:31
JOSE ALBERTO RUBIÑO MARTIN UNIVERSIDAD DE LA LAGUNA	30/06/2017 15:34:17
ERNESTO PEREDA DE PABLO UNIVERSIDAD DE LA LAGUNA	06/07/2017 13:51:19

Table A.3: Complete list of fitting terms to transform the b parameter to the chosen values of z and σ_8 , using eqs. (A.4) and (A.3). Index i selects a line, index j selects a column.

ξ_{ij}^b	0	1	2	3	4
0	-5098.88	3004.96	-36.68	-248.98	37.40
1	5948.68	-4065.13	526.96	148.63	-29.76
2	-2635.03	2035.06	-435.59	-6.77	7.41
3	517.88	-440.23	120.16	-8.72	-0.48
4	-37.68	34.46	-10.82	1.24	-0.02

η_{ij}^b	0	1	2	3	4
0	-7.31	15936.67	-13941.07	4094.47	-400.37
1	-6188.86	-8012.52	10187.80	-3312.39	339.99
2	4944.70	-371.62	-2216.28	907.10	-101.58
3	-1294.53	673.68	76.99	-89.84	12.17
4	110.78	-81.52	14.21	1.60	-0.45

parameters change when moving the value of z or σ_8 is:

$$\begin{aligned}
 & \ln \left[\frac{A(m, Q; z, \sigma_8)}{A(m, Q; \tilde{z}, \tilde{\sigma}_8)} \right] = \\
 &= \ln \mathcal{C} [\xi_A(m, Q) + \eta_A(m, Q)\mathcal{C} + \zeta_A(m, Q)\mathcal{C}^2 + \omega_A(m, Q)\mathcal{C}^3], \\
 & \ln \left[\frac{b(m, Q; z, \sigma_8)}{b(m, Q; \tilde{z}, \tilde{\sigma}_8)} \right] = \\
 &= \ln \mathcal{C} [\xi_b(m, Q) + \eta_b(m, Q)\mathcal{C} + \zeta_b(m, Q)\mathcal{C}^2 + \omega_b(m, Q)\mathcal{C}^3], \\
 & \ln \left[\frac{c(m, Q; z, \sigma_8)}{c(m, Q; \tilde{z}, \tilde{\sigma}_8)} \right] = \\
 &= \ln \mathcal{C} [\xi_c(m, Q) + \eta_c(m, Q)\mathcal{C} + \zeta_c(m, Q)\mathcal{C}^2 + \omega_c(m, Q)\mathcal{C}^3].
 \end{aligned} \tag{A.3}$$

The fitting function is the product of a logarithm of \mathcal{C} and a polynomial in

ζ_{ij}^b	0	1	2	3	4
0	-16937.67	1881.75	7188.21	-3034.33	344.50
1	24667.19	-11863.01	-2414.89	2031.29	-266.51
2	-12435.60	8586.89	-1080.03	-343.33	67.33
3	2627.79	-2160.41	532.22	-17.38	-5.38
4	-198.39	180.62	-55.52	5.84	-0.04

Este documento incorpora firma electrónica, y es copia auténtica de un documento electrónico archivado por la ULL según la Ley 39/2015.
Su autenticidad puede ser contrastada en la siguiente dirección <https://sede.ull.es/validacion/>

Identificador del documento: 973742 Código de verificación: Jfg6xBh0

Firmado por: DENIS TRAMONTE UNIVERSIDAD DE LA LAGUNA	Fecha: 30/06/2017 15:10:10
RAFAEL DELFIN BARRENA DELGADO UNIVERSIDAD DE LA LAGUNA	30/06/2017 15:21:31
JOSE ALBERTO RUBIÑO MARTIN UNIVERSIDAD DE LA LAGUNA	30/06/2017 15:34:17
ERNESTO PEREDA DE PABLO UNIVERSIDAD DE LA LAGUNA	06/07/2017 13:51:19

ω_{ij}^b	0	1	2	3	4
0	2523.95	4337.38	-5179.53	1679.53	-173.02
1	-6083.56	279.16	2962.50	-1212.21	136.61
2	3702.39	-1958.01	-217.79	265.72	-36.47
3	-858.07	643.84	-117.70	-11.54	3.51
4	68.11	-59.61	16.85	-1.31	-0.06

Table A.4: Complete list of fitting terms to transform the c parameter to the chosen values of z and σ_8 , using eqs. (A.4) and (A.3). Index i selects a line, index j selects a column.

ξ_{ij}^c	0	1	2	3	4
0	748.68	-72.63	-320.20	131.82	-14.59
1	-1142.51	618.11	48.90	-73.50	9.99
2	574.04	-434.57	82.90	5.72	-2.02
3	-118.26	104.21	-29.84	2.53	0.06
4	8.61	-8.27	2.77	-0.36	0.01

\mathcal{C} up to the third power. Note that with this definition of the fitting function, when $\mathcal{C} = 1$ the reference values for the parameters are recovered exactly. The fit for each parameter now depends on 4 coefficients, ξ , η , ζ and ω , which in turn still depend on m and Q .

The next step is to fit the residual dependence of these coefficients. We use a fitting function similar to the one in eq. (A.1), but since the dependence of these coefficients on mass and radius is more complex than it was for A , b and

η_{ij}^c	0	1	2	3	4
0	-1221.81	-1707.65	2094.52	-672.53	67.91
1	2894.40	-639.47	-924.38	420.64	-48.04
2	-1695.05	1094.91	-81.54	-65.14	10.68
3	374.61	-313.11	79.72	-3.58	-0.63
4	-28.23	26.57	-8.59	1.02	-0.03

Este documento incorpora firma electrónica, y es copia auténtica de un documento electrónico archivado por la ULL según la Ley 39/2015.
Su autenticidad puede ser contrastada en la siguiente dirección <https://sede.ull.es/validacion/>

Identificador del documento: 973742 Código de verificación: Jfg6xBh0

Firmado por: DENIS TRAMONTE UNIVERSIDAD DE LA LAGUNA	Fecha: 30/06/2017 15:10:10
RAFAEL DELFIN BARRENA DELGADO UNIVERSIDAD DE LA LAGUNA	30/06/2017 15:21:31
JOSE ALBERTO RUBIÑO MARTIN UNIVERSIDAD DE LA LAGUNA	30/06/2017 15:34:17
ERNESTO PEREDA DE PABLO UNIVERSIDAD DE LA LAGUNA	06/07/2017 13:51:19

ζ_{ij}^c	0	1	2	3	4
0	-484.44	4245.93	-3390.87	958.13	-90.91
1	-1646.29	-1238.83	1889.74	-634.97	65.44
2	1381.05	-612.86	-168.43	121.24	-15.28
3	-343.50	263.65	-53.79	-2.33	1.12
4	27.28	-24.96	7.74	-0.83	0.01

ω_{ij}^c	0	1	2	3	4
0	-272.51	-999.77	956.32	-286.49	27.94
1	1016.88	-84.11	-409.65	168.12	-18.58
2	-646.65	415.56	-40.68	-20.78	3.61
3	146.42	-125.71	35.66	-2.88	-0.09
4	-11.07	10.74	-3.73	0.52	-0.02

c , we employed a 4-degree polynomial in both m and Q . In formulae:

$$\begin{aligned}\xi(m, Q) &= \sum_{i=0}^4 \left(\sum_{j=0}^4 \xi_{ij} Q^{ij} \right) \ln(m')^i, \\ \eta(m, Q) &= \sum_{i=0}^4 \left(\sum_{j=0}^4 \eta_{ij} Q^{ij} \right) \ln(m')^i, \\ \zeta(m, Q) &= \sum_{i=0}^4 \left(\sum_{j=0}^4 \zeta_{ij} Q^{ij} \right) \ln(m')^i, \\ \omega(m, Q) &= \sum_{i=0}^4 \left(\sum_{j=0}^4 \omega_{ij} Q^{ij} \right) \ln(m')^i.\end{aligned}\quad (\text{A.4})$$

In this case we have 25 terms $\xi_{i,j}$ for ξ , 25 terms $\eta_{i,j}$ for η and so on. The whole set must be repeated three times (for A , b and c), ending up with 300 parameters for this last fit. Tables A.2, A.3 and A.4 list these parameters for A , b and c respectively. This set of fitting parameters allows the computation of the bias for any value of Q , m , z and σ_8 in the specified ranges, with a final error below $\sim 8\%$.

The last step is the dependence of fitting parameters A , b and c on the matter density parameter Ω_m and the Hubble parameter h . We found that the same parameters obtained for the reference cosmology can still be employed,

Este documento incorpora firma electrónica, y es copia auténtica de un documento electrónico archivado por la ULL según la Ley 39/2015.
Su autenticidad puede ser contrastada en la siguiente dirección <https://sede.ull.es/validacion/>

Identificador del documento: 973742 Código de verificación: Jfg6xBh0

Firmado por: DENIS TRAMONTE <i>UNIVERSIDAD DE LA LAGUNA</i>	Fecha: 30/06/2017 15:10:10
RAFAEL DELFIN BARRENA DELGADO <i>UNIVERSIDAD DE LA LAGUNA</i>	30/06/2017 15:21:31
JOSE ALBERTO RUBIÑO MARTIN <i>UNIVERSIDAD DE LA LAGUNA</i>	30/06/2017 15:34:17
ERNESTO PEREDA DE PABLO <i>UNIVERSIDAD DE LA LAGUNA</i>	06/07/2017 13:51:19

Table A.5: Complete list of fitting terms for computing the exponent $f(h, \Omega_m)$ using eq. (A.6), entering the mass scaling (A.5). Index i selects a line, index j selects a column.

f_{ij}	0	1	2	3	4
0	7824.37	25237.25	3138.79	-323056.91	351919.38
1	55357.30	15986.33	-244637.95	-256695.08	598394.06
2	72768.05	-31325.23	-342372.66	74755.55	391854.50
3	20716.17	6647.99	-158499.00	43559.96	161916.81
4	-1549.50	4181.00	6828.17	-51471.20	55152.71

provided the mass is scaled as:

$$m \rightarrow m \left(\frac{\Omega_m h^4}{\tilde{\Omega}_m \tilde{h}^4} \right)^{f(h, \Omega_m)}, \quad (\text{A.5})$$

where \tilde{h} and $\tilde{\Omega}_m$ are the values for the reference cosmology, and

$$f(h, \Omega_m) = \sum_{i=0}^4 \left(\sum_{j=0}^4 f_{ij} \Omega_m^j \right) h^i. \quad (\text{A.6})$$

The terms f_{ij} are listed in table A.5. We computed them allowing h to vary in $[0.65, 0.75]$, and Ω_m in $[0.25, 0.35]$. With this recipe it is possible to compute the bias using the same fitting parameters listed in tables A.1 to A.4. In this case, the final relative error with respect to the bias computed analytically is usually in the range $\sim 10\text{--}20\%$, but in some cases it can grow up to 40%.

Implementation

To sum up, in order to determine the value of the bias, given as input a chosen cosmology and the values of Q , m , z , and δ_l , one should:

1. for the chosen values of the Hubble parameter and the matter density parameter, compute the exponent $f(h, \Omega_m)$ using eq. (A.6) with the parameters from table A.5;
2. scale the mass according to eq. (A.5), with the value of f just computed. From now on this is the new mass that has to be used;
3. compute the parameters $A(m, Q; \tilde{z}, \tilde{\sigma}_8)$, $b(m, Q; \tilde{z}, \tilde{\sigma}_8)$ and $c(m, Q; \tilde{z}, \tilde{\sigma}_8)$ for the reference cosmology, using eq. (A.1) and the parameters listed in table A.1;

Este documento incorpora firma electrónica, y es copia auténtica de un documento electrónico archivado por la ULL según la Ley 39/2015.
Su autenticidad puede ser contrastada en la siguiente dirección <https://sede.ull.es/validacion/>

Identificador del documento: 973742	Código de verificación: Jfg6xBh0
Firmado por: DENIS TRAMONTE UNIVERSIDAD DE LA LAGUNA	Fecha: 30/06/2017 15:10:10
RAFAEL DELFIN BARRENA DELGADO UNIVERSIDAD DE LA LAGUNA	30/06/2017 15:21:31
JOSE ALBERTO RUBIÑO MARTIN UNIVERSIDAD DE LA LAGUNA	30/06/2017 15:34:17
ERNESTO PEREDA DE PABLO UNIVERSIDAD DE LA LAGUNA	06/07/2017 13:51:19

4. compute the parameters $(\xi_A, \eta_A, \zeta_A, \omega_A)$, $(\xi_b, \eta_b, \zeta_b, \omega_b)$ and $(\xi_c, \eta_c, \zeta_c, \omega_c)$, using the fit described in eq. (A.4) with parameters from tables A.2, A.3 and A.4;
5. evolve A , b and c to the chosen values of z and σ_8 using eq. (A.3);
6. compute the final bias with eq. (2.45).

This computation, though requiring storing a large number of fitting parameters, is much faster than the implementation of the full expression (2.41). Reading the parameters from files and computing polynomials is a task that can easily be implemented in a numerical code, and is efficiently handled by a processor.

Este documento incorpora firma electrónica, y es copia auténtica de un documento electrónico archivado por la ULL según la Ley 39/2015.
Su autenticidad puede ser contrastada en la siguiente dirección <https://sede.ull.es/validacion/>

Identificador del documento:	973742	Código de verificación:	Jfg6xBh0
Firmado por:	DENIS TRAMONTE UNIVERSIDAD DE LA LAGUNA	Fecha:	30/06/2017 15:10:10
	RAFAEL DELFIN BARRENA DELGADO UNIVERSIDAD DE LA LAGUNA		30/06/2017 15:21:31
	JOSE ALBERTO RUBIÑO MARTIN UNIVERSIDAD DE LA LAGUNA		30/06/2017 15:34:17
	ERNESTO PEREDA DE PABLO UNIVERSIDAD DE LA LAGUNA		06/07/2017 13:51:19

B

Pointing correction for non-perpendicularities

We detail in this section the derivation of the pointing correction 5.23 for the non-perpendicularity errors. We take as a reference the orientation of the telescope when the encoder coordinates are $(A,E) = (\pi, 0)$. We know that, due to the non-perpendicularity between the telescope and the elevation axis, in this configuration the telescope is not aligned with the x axis of the horizontal frame, but it is shifted by the angle Δ' (figure 5.8, lower-right panel). We define a new reference frame $(\tilde{x}, \tilde{y}, \tilde{z})$, which we call the “telescope frame”, in which \tilde{x} is aligned with the telescope in the configuration we have just described, \tilde{y} is aligned with the telescope elevation axis and \tilde{z} is directed towards the zenith,¹ as in the usual horizontal frame (x, y, z) .

We will first derive the pointing correction in the telescope frame, and then change it back to the horizontal frame. Our strategy is the following. Let us call \mathbf{e} the versor aligned with the \tilde{x} axis. If we enter the nominal coordinates (A,E) in the encoder, the telescope will be pointing towards a wrong pointing direction \mathbf{r}_w , which will be different from the nominal direction \mathbf{r} that points to the target. We call \tilde{R}_w the rotation matrix that aligns the versor \mathbf{e} with the wrong pointing direction \mathbf{r}_w , in the telescope frame:

$$\mathbf{r}_w = \tilde{R}_w \mathbf{e}, \quad (B.1)$$

and we call \tilde{R} the rotation matrix that brings the versor \mathbf{e} along with the right

¹Note that the axes of the telescope frame are not orthogonal; this is not an issue for the formalism described in this section.

pointing direction \mathbf{r} , also in the telescope frame:

$$\mathbf{r} = \tilde{\mathcal{R}} \mathbf{e}. \quad (\text{B.2})$$

The correction matrix that brings the wrong pointing direction \mathbf{r}_w towards the nominal \mathbf{r} can then be computed as:

$$\mathbf{r} = (\tilde{\mathcal{R}} (\tilde{\mathcal{R}}_w)^{-1}) \mathbf{r}_w = \tilde{\mathcal{R}}_{NP} \mathbf{r}_w, \quad (\text{B.3})$$

where the tilde sign in $\tilde{\mathcal{R}}_{NP}$ stresses that this correction is written in the telescope frame.

The expression for $\tilde{\mathcal{R}}_w$

The matrix $\tilde{\mathcal{R}}_w$ can be written by making use of the meaning of the coordinates (A,E) as encoder inputs. The entries “A” and “E” tell the telescope control system the angular magnitude of the rotations it has to perform around the azimuth and elevation axes. In our formalism this is equivalent to performing the rotations around the telescope frame axes \hat{y} (of an angle E) and \hat{z} (of an angle A, or better $\pi - A$ given the initial direction of the \mathbf{e} versor). The corresponding matrix reads:

$$\tilde{\mathcal{R}}_w = \begin{pmatrix} -c_A c_E & -s_A & c_A s_E \\ s_A c_E & -c_A & -s_A s_E \\ s_E & 0 & c_E \end{pmatrix}. \quad (\text{B.4})$$

In this section, in order to shorten the analytical expressions, we use the notation $c_A \equiv \cos A$, $c_E \equiv \cos E$, $s_A \equiv \sin A$ and $s_E \equiv \sin E$.

The rotation B.4 can be easily understood if we apply it to the \mathbf{e} versor:

$$\mathbf{r}_w = \tilde{\mathcal{R}}_w \mathbf{e} = \begin{pmatrix} -c_A c_E \\ s_A c_E \\ s_E \end{pmatrix}. \quad (\text{B.5})$$

The components in B.5 are the same as the components (5.15) of a vector pointing towards the generic direction (A,E) in the horizontal frame. Indeed, the matrix B.4 is the one that brings the reference direction towards the coordinates (A,E) on the sky, with the difference that now we are working in the telescope frame and not in the usual horizon frame.

Este documento incorpora firma electrónica, y es copia auténtica de un documento electrónico archivado por la ULL según la Ley 39/2015.
Su autenticidad puede ser contrastada en la siguiente dirección <https://sede.ull.es/validacion/>

Identificador del documento: 973742

Código de verificación: Jfg6xBh0

Fecha: 30/06/2017 15:10:10

Firmado por: DENIS TRAMONTE UNIVERSIDAD DE LA LAGUNA	30/06/2017 15:21:31
RAFAEL DELFIN BARRENA DELGADO UNIVERSIDAD DE LA LAGUNA	30/06/2017 15:34:17
JOSE ALBERTO RUBIÑO MARTIN UNIVERSIDAD DE LA LAGUNA	06/07/2017 13:51:19
ERNESTO PEREDA DE PABLO UNIVERSIDAD DE LA LAGUNA	

The expression for \tilde{R}

The derivation of an expression for \tilde{R} implies implementing the correction for the telescope non-idealities. We are still working in the telescope frame, but this time, apart from the two rotations in azimuth and elevations, we will need two additional rotations to compensate for the deviations quantified by Δ and Δ' . We proceed as explained in the following.

- The first rotation we perform is to correct for the nonperpendicularity between the telescope and the elevation axis, that produces the displacements of the e versor by an angle Δ' from the x direction. The first thing we do is therefore to re-align e with the horizontal x axis, with a counterclockwise rotation around the \tilde{z} axis (the misalignment lying in the $x - y$ plane); the associated matrix is:

$$\tilde{R}_1 = \begin{pmatrix} \cos \Delta' & -\sin \Delta' & 0 \\ \sin \Delta' & \cos \Delta' & 0 \\ 0 & 0 & 1 \end{pmatrix}, \quad (\text{B.6})$$

where we have defined $c_{\Delta'} \equiv \cos \Delta'$ and $s_{\Delta'} \equiv \sin \Delta'$.

- Now we rotate the versor around the \tilde{y} axis of an angle equal to its nominal elevation E . This transformation reads:

$$\tilde{R}_2 = \begin{pmatrix} c_E & 0 & -s_E \\ 0 & 1 & 0 \\ s_E & 0 & c_E \end{pmatrix}. \quad (\text{B.7})$$

- At this point we correct for the nonperpendicularity between the mount axes. Indeed, even though in the last rotation we started with a vector lying in the $x - z$ plane, the fact that \tilde{y} is not perpendicular to z makes the rotating vector go out of that plane (with a maximum displacement for a 90° rotation); we now want to take it back on the plane by means of a rotation around the \tilde{x} axis, whose magnitude is equal to the nonperpendicularity angle Δ :

$$\tilde{R}_3 = \begin{pmatrix} 1 & 0 & 0 \\ 0 & c_\Delta & -s_\Delta \\ 0 & s_\Delta & c_\Delta \end{pmatrix}, \quad (\text{B.8})$$

Este documento incorpora firma electrónica, y es copia auténtica de un documento electrónico archivado por la ULL según la Ley 39/2015.
Su autenticidad puede ser contrastada en la siguiente dirección <https://sede.ull.es/validacion/>

Identificador del documento: 973742

Código de verificación: Jfg6xBh0

Firmado por: DENIS TRAMONTE
UNIVERSIDAD DE LA LAGUNA

Fecha: 30/06/2017 15:10:10

RAFAEL DELFIN BARRENA DELGADO
UNIVERSIDAD DE LA LAGUNA

30/06/2017 15:21:31

JOSE ALBERTO RUBIÑO MARTIN
UNIVERSIDAD DE LA LAGUNA

30/06/2017 15:34:17

ERNESTO PEREDA DE PABLO
UNIVERSIDAD DE LA LAGUNA

06/07/2017 13:51:19

where as usual $c_\Delta \equiv \cos \Delta$ and $s_\Delta \equiv \sin \Delta$.

- Now the versor lies in the xz plane and is in the right position for the last rotation, which is performed around the \hat{z} axis by an amount equal to the nominal azimuth:

$$\tilde{R}_4 = \begin{pmatrix} -c_A & s_A & 0 \\ -s_A & -c_A & 0 \\ 0 & 0 & 1 \end{pmatrix}. \quad (\text{B.9})$$

We can now compute the total matrix as $\tilde{R} = \tilde{R}_4 \tilde{R}_3 \tilde{R}_2 \tilde{R}_1$. It is not convenient to write down the full analytical expression, which is rather long and does not add any further information.

The pointing correction in the telescope frame

We show now the result for the final matrix $\tilde{R}_{\text{NP}} = \tilde{R} \tilde{R}_w^{-1}$. Again, the complete expression is quite long, and we will not report it in here (its determination only involves algebraic calculations). However, we can quote its linearized version, obtained by expanding \tilde{R}_{NP} to first order in Δ and Δ' . We found:

$$\tilde{R}_{\text{NP}}^{(\text{lin})} = \begin{pmatrix} 1 & -\Delta' c_E & \Delta s_A - \Delta' s_A s_E \\ \Delta' c_E & 1 & \Delta c_A - \Delta' c_A s_E \\ -\Delta s_A + \Delta' s_A s_E & -\Delta c_A + \Delta' c_A s_E & 1 \end{pmatrix}. \quad (\text{B.10})$$

We can now proceed as we did with the other non-idealities in section 5.2.2. We apply the linearized transformation to the vector \mathbf{r}_w that, in the reference frame we are using, is described by the components listed in equation (B.5)). We see that the matrix (B.10) can be decomposed into the sum of the identity and a correction,

$$\tilde{R}_{\text{NP}}^{(\text{lin})} = \mathbb{1} + (\Delta \tilde{R})_{\text{NP}}, \quad (\text{B.11})$$

so that the vector to be added to the wrong pointing vector \mathbf{r}' is, performing all the calculations:

Este documento incorpora firma electrónica, y es copia auténtica de un documento electrónico archivado por la ULL según la Ley 39/2015.
Su autenticidad puede ser contrastada en la siguiente dirección <https://sede.ull.es/validacion/>

Identificador del documento: 973742

Código de verificación: Jfg6xBh0

Fecha: 30/06/2017 15:10:10

Firmado por: DENIS TRAMONTE UNIVERSIDAD DE LA LAGUNA	30/06/2017 15:21:31
RAFAEL DELFIN BARRENA DELGADO UNIVERSIDAD DE LA LAGUNA	30/06/2017 15:34:17
JOSE ALBERTO RUBIÑO MARTIN UNIVERSIDAD DE LA LAGUNA	06/07/2017 13:51:19
ERNESTO PEREDA DE PABLO UNIVERSIDAD DE LA LAGUNA	

$$\Delta \mathbf{r} = (\Delta \tilde{R})_{\text{NP}} \mathbf{r}_w = \begin{pmatrix} s_A c_E & \frac{-\Delta' + \Delta \sin E}{c_E} \\ c_A c_E & \frac{-\Delta' + \Delta \sin E}{c_E} \\ 0 & 0 \end{pmatrix} = \begin{pmatrix} \tilde{y} \frac{P_c + P_n \tilde{z}}{\sqrt{\tilde{x}^2 + \tilde{y}^2}} \\ -\tilde{x} \frac{P_c + P_n \tilde{z}}{\sqrt{\tilde{x}^2 + \tilde{y}^2}} \\ 0 \end{pmatrix} = \begin{pmatrix} w\tilde{y} \\ -w\tilde{x} \\ 0 \end{pmatrix}, \quad (\text{B.12})$$

where $(\tilde{x}, \tilde{y}, \tilde{z})$ are the components of the \mathbf{r}_w vector. In equation B.12 we have introduced the pointing model parameters P_c (non-perpendicularity between telescope and elevation axis) and P_n (non-perpendicularity between mount axis), defined according to the TPOINT conventions as:

$$\begin{aligned} P_c &= -\Delta', \\ P_n &= \Delta, \end{aligned} \quad (\text{B.13})$$

(as in equation 5.25). In the last equality of B.12 we simplified the notation by introducing the parameter:

$$w = \frac{P_c + P_n \tilde{z}}{\sqrt{\tilde{x}^2 + \tilde{y}^2}}. \quad (\text{B.14})$$

We see that in this first-order derivation the non-ideality correction does not affect \tilde{z} .

The pointing correction in the horizontal frame

The correction B.12 requires the computation of the vector \mathbf{r}_w in the telescope frame; however, all the other corrections that we have implemented are performed in the horizontal frame. Here, the components of \mathbf{r}_w are computed using B.5, but those components as computed in the horizontal frame yield the corrected vector components. When we perform the pointing model correction, we follow the scheme detailed in the summary of section 5.2.2: our input are the “wrong” versor components in the horizontal frame, which are not given by B.5. Therefore, in the horizontal frame the components \tilde{x} and \tilde{y} appearing in B.12 are actually the corrected versor component x and y , which can be written as the wrong components plus the correction: $x = x_w + \Delta x$,

Este documento incorpora firma electrónica, y es copia auténtica de un documento electrónico archivado por la ULL según la Ley 39/2015.
Su autenticidad puede ser contrastada en la siguiente dirección <https://sede.ull.es/validacion/>

Identificador del documento: 973742

Código de verificación: Jfg6xBh0

Fecha: 30/06/2017 15:10:10

Firmado por: DENIS TRAMONTE UNIVERSIDAD DE LA LAGUNA	30/06/2017 15:21:31
RAFAEL DELFIN BARRENA DELGADO UNIVERSIDAD DE LA LAGUNA	30/06/2017 15:34:17
JOSE ALBERTO RUBIÑO MARTIN UNIVERSIDAD DE LA LAGUNA	06/07/2017 13:51:19
ERNESTO PEREDA DE PABLO UNIVERSIDAD DE LA LAGUNA	

$y = y_w + \Delta y$. So, we can write²:

$$\begin{aligned}\Delta x &= w y = w (y_w + \Delta y) = w (y_w - w x) \simeq w (y_w - w x_w), \\ \Delta y &= -w x = -w (x_w + \Delta x) = -w (x_w + w y) \simeq -w (x_w + w y_w),\end{aligned}\quad (\text{B.15})$$

where in the last equality we approximated x with x_w and y with y_w when they are multiplied by w^2 , which is second-order. Hence, we can finally write the versor correction for non-perpendicularities as:

$$\Delta \mathbf{r} = \begin{pmatrix} w (y_w - w x_w) \\ -w (x_w + w y_w) \\ 0 \end{pmatrix}, \quad (\text{B.16})$$

that is the same correction reported in equation 5.23.

²The expression for w should be transformed as well, but it remains unchanged to first order because it actually depends only on the z component which, as we commented, undergoes no correction.

List of Figures

1.1 Redshift evolution of the Universe, according to the standard cosmological model. Credits:NASA/WMAP Science Team.	8
1.2 Numerical simulations showing the evolution of the LSS, from initial small perturbations on the homogeneous background to the present structures; the figure shows different snapshots from an initial redshift $z = 30$ to the present $z = 0$. Credit: simulations were performed at the National Center for Supercomputer Applications by Andrey Kravtsov (The University of Chicago) and Anatoly Klypin (New Mexico State University). Visualisations by Andrey Kravtsov.	13
1.3 Matter power spectrum 1.28 computed at $z = 0$ using the cosmology from table 1.2 (“Reference”). We also show the effect on the spectrum of changing one cosmological parameter at a time. When different from their reference values, cosmological parameters are set to: $\Omega_b = 0.08$, $\Omega_m = 0.45$, $h = 0.75$, $A_s = 3.4 \times 10^9$, $n_s = 1.25$	15
1.4 Effect of changing one cosmological parameter at a time on the CMB angular power spectrum. When different from their reference values, cosmological parameters are set to: $\Omega_b = 0.08$, $\Omega_m = 0.45$, $h = 0.75$, $A_s = 3.4 \times 10^9$, $n_s = 1.25$, as in figure 1.3.	21
1.5 Auto-correlation power spectra C_ℓ^{TT} , C_ℓ^{EE} , C_ℓ^{BB} and cross-correlation power spectrum C_ℓ^{TE} , computed for our reference cosmology from table 1.2, in the case of purely scalar (<i>left</i>) and purely tensor (<i>right</i>) primordial perturbations. Discontinuous line means the cross-correlation C_ℓ^{TE} becomes negative.	24

243

Este documento incorpora firma electrónica, y es copia auténtica de un documento electrónico archivado por la ULL según la Ley 39/2015.
Su autenticidad puede ser contrastada en la siguiente dirección <https://sede.ull.es/validacion/>

Identificador del documento: 973742	Código de verificación: Jfg6xBh0
Firmado por: DENIS TRAMONTE UNIVERSIDAD DE LA LAGUNA	Fecha: 30/06/2017 15:10:10
RAFAEL DELFIN BARRENA DELGADO UNIVERSIDAD DE LA LAGUNA	30/06/2017 15:21:31
JOSE ALBERTO RUBIÑO MARTIN UNIVERSIDAD DE LA LAGUNA	30/06/2017 15:34:17
ERNESTO PEREDA DE PABLO UNIVERSIDAD DE LA LAGUNA	06/07/2017 13:51:19

1.6 Brightness of foregrounds contribution compared to the CMB signal, in the case of intensity (<i>left</i>) and polarisation (<i>right</i>). We see that in intensity there is a frequency window in which the CMB is dominant, while it is always subdominant in polarisation. Figure taken from Planck Collaboration et al. (2016a)	29
1.7 Summary of CMB space missions.	30
1.8 Pictures of ACT, SPT, BICEP2 and the two C-BASS telescopes.	32
1.9 A composite, multi-wavelength image of the Toothbrush Cluster. Image credit: X-ray: NASA/CXC/SAO/R. van Weeren et al; Radio: LOFAR/ASTRON; Optical: NAOJ/Subaru.	34
1.10 The Abell cluster in optical light, observed by the Hubble Space Telescope. The effect of gravitational lensing of background light is also visible. Credit: NASA, ESA, Hubble Heritage Team (STScI/AURA), and J. Blakeslee (NRC Herzberg, DAO) & H. Ford (JHU).	36
1.11 X-ray image of the Coma cluster, observed with XMM-Newton. Credit: ESA/XMM-Newton; image courtesy of U. Briel, MPE Garching.	38
1.12 <i>Left:</i> shift of the CMB spectrum produced by the tSZ. <i>Right:</i> spectral distortions produced by the thermal and kinetic SZ effects, together with the rescaled CMB spectrum (dotted line). Figures from Carlstrom et al. (2002).	41
1.13 The typical tSZ spectral signature in a galaxy cluster observed by <i>Planck</i> . Each panel shows a CLASS 1 cluster candidate (see section 3.4.1) for an individual <i>Planck</i> frequency channel, over a $\sim 2.5 \times 2.5$ square degrees area. The spectral distortion plotted in figure 1.12 can easily be traced. Plots are taken from Planck Collaboration et al. (2014i).	44
2.1 Comparison between different mass functions parametrisations, computed using the cosmological parameters from table 2.1: PS74, ST99, J01, W06 and T08 with $\Delta = 200$ (see the text for details). Lower panel shows percent difference with respect to the T08 mass function, which is the reference parametrisation used in this work. The PS74 function is indeed the most inaccurate, clearly underestimating the abundance of most massive halos. The W06 function is the closest to the T08 one, sharing the same functional form.	54

Este documento incorpora firma electrónica, y es copia auténtica de un documento electrónico archivado por la ULL según la Ley 39/2015.
Su autenticidad puede ser contrastada en la siguiente dirección <https://sede.ull.es/validacion/>

Identificador del documento: 973742	Código de verificación: Jfg6xBh0	Fecha: 30/06/2017 15:10:10
Firmado por: DENIS TRAMONTE UNIVERSIDAD DE LA LAGUNA		
RAFAEL DELFIN BARRENA DELGADO UNIVERSIDAD DE LA LAGUNA		30/06/2017 15:21:31
JOSE ALBERTO RUBIÑO MARTIN UNIVERSIDAD DE LA LAGUNA		30/06/2017 15:34:17
ERNESTO PEREDA DE PABLO UNIVERSIDAD DE LA LAGUNA		06/07/2017 13:51:19

2.2 Graphic representation of the difference between the Eulerian radius R and the Lagrangian radius Q . While the former evolves according to the local density contrast, the latter remains invariant throughout all redshifts.	58
2.3 Representation of the basic framework for developing the formalism of the local CMF. The condition is represented as a sphere with Lagrangian radius Q_1 and density contrast δ_1 . At a distance q from its centre, we consider another region, with Lagrangian radius $Q_2 < Q_1$, and density contrast $\delta_2 > \delta_1$: such region encloses a total mass m , which is going to be the collapsed halo.	60
2.4 Comparison between the UMF and different CMF rescalings computed using the T08 parametrisation, in small-scale regions (upper panels), large scale regions (lower panels), underdensities (left panels) and overdensities (right panels). We consider the CMF computed with the standard rescaling and three cases of the locally rescaled CMF, namely the CMF evaluated in the centre of the condition ($q = 0$), at the condition border ($q = Q$) and its volume average inside the condition computed with equation 2.29. The vertical dashed line marks the fraction 1/30 of the condition mass, above which the formalism for computing the CMF is no longer reliable.	62
2.5 Regions showing the allowed values for the normalisation parameter α , as a function of the mass, in order to have the normalisation condition satisfied with 10%, 5% and 3% accuracy, respectively. The conditional mass function is computed using the T08 parametrisation with the local rescaling. The plots show how the contours evolve when the condition size increases: larger conditions are less effective in determining a unique value for the normalisation parameter, ultimately leaving α unconstrained.	66
2.6 Same as Figure 2.5, but computing the mass function with the standard rescaling.	67

Este documento incorpora firma electrónica, y es copia auténtica de un documento electrónico archivado por la ULL según la Ley 39/2015.
Su autenticidad puede ser contrastada en la siguiente dirección <https://sede.ull.es/validacion/>

Identificador del documento:	973742	Código de verificación:	Jfg6xBh0
Firmado por:	DENIS TRAMONTE UNIVERSIDAD DE LA LAGUNA		Fecha: 30/06/2017 15:10:10
	RAFAEL DELFIN BARRENA DELGADO UNIVERSIDAD DE LA LAGUNA		30/06/2017 15:21:31
	JOSE ALBERTO RUBIÑO MARTIN UNIVERSIDAD DE LA LAGUNA		30/06/2017 15:34:17
	ERNESTO PEREDA DE PABLO UNIVERSIDAD DE LA LAGUNA		06/07/2017 13:51:19

- 2.7 Unconditional mass function test for the simulation set. Upper panel: points mark the halo number density as a function of mass, obtained from the Small Scale Simulation (circles) and the Large Scale Simulation (diamonds); the line shows the abundance predicted by the T08 UMF computed with the same underlying cosmology and an overdensity parameter $\Delta = 200$. Lower panel: same as the upper panel but showing the percent residuals with respect to the theoretical UMF. Poissonian errors are overplotted (darker error bars), together with numerical errors computed dividing each box into eight subsets of equal volume (lighter error bars). Although the abundances extracted from simulations reproduce the overall shape of the T08 UMF, they are affected by systematics that can produce deviations from the theoretical prediction at the level of $\sim 10\%$. These offsets, which could in principle be strongly reduced by averaging over a large number of simulations, must be accounted for in the subsequent analysis. 70
- 2.8 Examples of a snapshot slice from the SSS box, showing a $50 \times 50 h^{-2} \text{Mpc}^2$ area with a $1 h^{-1} \text{Mpc}$ depth. Simulation particles are shown as black dots, while red spots represent identified halos. Green circles show the randomly placed spheres. The abundance of particles inside each sphere defines its density contrast, while the mass distribution of the encompassed halos is the simulated CMF. 72
- 2.9 Same as figure 2.8, this time showing a $300 \times 300 h^{-2} \text{Mpc}^2$ area slice from the LSS, with a $3 h^{-1} \text{Mpc}$ depth. 72
- 2.10 Posterior distributions for the quantities characterising the conditions, resulting from randomly placed spheres over the simulations with a top-hat prior for their Eulerian radius (see the text for details). From top to bottom: normalised distribution for the Lagrangian radius Q , the physical density contrast δ_m and the linear density contrast δ_l . Left column: Small Scale Simulation, with a total 6×10^4 spheres; right column: Large Scale Simulation, with a total 4.4×10^5 spheres. 74

Este documento incorpora firma electrónica, y es copia auténtica de un documento electrónico archivado por la ULL según la Ley 39/2015.
Su autenticidad puede ser contrastada en la siguiente dirección <https://sede.ull.es/validacion/>

Identificador del documento:	973742	Código de verificación:	Jfg6xBh0
Firmado por:	DENIS TRAMONTE UNIVERSIDAD DE LA LAGUNA	Fecha:	30/06/2017 15:10:10
	RAFAEL DELFIN BARRENA DELGADO UNIVERSIDAD DE LA LAGUNA		30/06/2017 15:21:31
	JOSE ALBERTO RUBIÑO MARTIN UNIVERSIDAD DE LA LAGUNA		30/06/2017 15:34:17
	ERNESTO PEREDA DE PABLO UNIVERSIDAD DE LA LAGUNA		06/07/2017 13:51:19

2.11 Normalisation test for the CMF, for both the SSS (left column) and the LSS (right column). Points are halo abundances from simulation with Poissonian errors; we also plot the standard and the local CMF, both with no explicit normalisation and normalised with $\alpha = 1.25$. Middle panels show the residual of the simulated abundances with respect to the simulated UMF plotted with points in figure 2.7. Lower panels show the residuals of the analytical CMFs with respect to the T08 UMF.	76
2.12 Comparison between simulation and theoretical CMFs, in the case of the SSS (left column) and the LSS (right column). From top to bottom we show a strongly underdense region, a region with moderate underdensity and an overdense region. We plot the simulation points with Poissonian errors and both the standard and the local rescaling, without explicit normalisation. The vertical dotted line represents a fraction 1/30 of the average condition mass.	79
2.13 Same plot as in figure 2.12, but showing the effect of the normalisation parameter on the local CMF. We plot the CMF with no explicit normalisation, with normalisation parameter $\alpha = 1.25$, and with a more conservative value $\alpha = 1.5$	80
2.14 Same plot as in figure 2.13, but considering this time the effect of the normalisation parameter on the standard rescaling.	81
2.15 Bias between the integrated CMF and UMF plotted as a function of the linear density contrast. We compare the prediction from the two-parameter fit 2.44 and the three-parameter fit 2.45, together with the theoretical bias computed with 2.41, for different values of condition radius, mass, redshift and σ_8 (the case is made explicit in the title).	83
2.16 Comparison between the standard CMF and the mass function computations based on a locally defined cosmology: we consider the local parameter rescaling (CPR), the power spectrum rescaling (PSR), and the rescaling defined in Chiang (2015). Residuals are computed with respect to the standard CMF. We show results for underdensities and overdensities at both small and large scale.	91
3.1 <i>Left:</i> mass function from Tinker et al. (2008) computed at different redshifts as a function of M_{200} . <i>Right:</i> comoving volume element, as a function of redshift.	97

Este documento incorpora firma electrónica, y es copia auténtica de un documento electrónico archivado por la ULL según la Ley 39/2015.
Su autenticidad puede ser contrastada en la siguiente dirección <https://sede.ull.es/validacion/>

Firmado por:	Identificador del documento:	Código de verificación:	Fecha:
DENIS TRAMONTE UNIVERSIDAD DE LA LAGUNA	973742	Jfg6xBh0	30/06/2017 15:10:10
RAFAEL DELFIN BARRENA DELGADO UNIVERSIDAD DE LA LAGUNA			30/06/2017 15:21:31
JOSE ALBERTO RUBIÑO MARTIN UNIVERSIDAD DE LA LAGUNA			30/06/2017 15:34:17
ERNESTO PEREDA DE PABLO UNIVERSIDAD DE LA LAGUNA			06/07/2017 13:51:19

3.2 <i>Left:</i> Albrecht et al. (2006) selection function computed at $z = 0$ for three different values of the threshold mass. <i>Right:</i> selection function at three different redshift, in the case of a $10^{14.6} h^{-1} M_\odot$ threshold mass.	100
3.3 <i>Left:</i> redshift distribution of the cluster number density, for three simulated surveys with different selection thresholds. <i>Right:</i> corresponding number counts over a set of redshift bins.	102
3.4 Posterior probability distributions obtained with the modified CosmoMC. Fiducial values for the cosmological parameter are marked with dashed line. <i>Upper panel:</i> correlation plot between Ω_m and σ_8 . <i>Lower panel:</i> marginalised probability distributions for the individual parameters.	109
3.5 Effect of the threshold mass on the estimation of the cosmological parameters Ω_m and σ_8 . The higher number of clusters detectable with a lower threshold mass results in a dramatic improvement of the precision in the final parameter estimates.	111
3.6 Noise maps (<i>left</i>) with corresponding completeness functions (<i>right</i>), for an angular size of $\theta_{500} = 1'$ (<i>top</i>) and $\theta_{500} = 30'$ (<i>bottom</i>).	118
3.7 <i>Left:</i> spatial distribution of the PSZ1 cosmological sample clusters over the sky, together with the $\sim 35\%$ sky mask. <i>Right:</i> corresponding cluster number count binned in redshift (errors are Poissonian).	120
3.8 Results of cosmological parameter estimation based on the abundance of clusters observed by <i>Planck</i> , performed using a combination of cluster+BBN+BAO likelihoods with the mass bias parameter fixed to $(1 - b) = 0.8$. <i>Upper left:</i> reconstructed joint posterior probability distribution for the parameters Ω_m and σ_8 . <i>Upper right:</i> marginalised probability distribution for Ω_m . <i>Lower left:</i> marginalised probability distribution for σ_8 . <i>Lower right:</i> the Ω_m – σ_8 correlation plot adapted from Planck Collaboration et al. (2014g).	121
3.9 Same as in figure 3.8, but this time the mass bias parameter was let free to vary with a flat prior for $(1 - b)$ in $[0.7, 1.0]$	123
3.10 A cluster from the PSZ1 catalogue. <i>Left:</i> SDSS image of the field. <i>Right:</i> MOS mask prepared to select the member galaxies for spectroscopic observations with the TNG.	125

Este documento incorpora firma electrónica, y es copia auténtica de un documento electrónico archivado por la ULL según la Ley 39/2015.
Su autenticidad puede ser contrastada en la siguiente dirección <https://sede.ull.es/validacion/>

Identificador del documento: 973742	Código de verificación: Jfg6xBh0	Fecha: 30/06/2017 15:10:10
Firmado por: DENIS TRAMONTE UNIVERSIDAD DE LA LAGUNA		
RAFAEL DELFIN BARRENA DELGADO UNIVERSIDAD DE LA LAGUNA		30/06/2017 15:21:31
JOSE ALBERTO RUBIÑO MARTIN UNIVERSIDAD DE LA LAGUNA		30/06/2017 15:34:17
ERNESTO PEREDA DE PABLO UNIVERSIDAD DE LA LAGUNA		06/07/2017 13:51:19

4.1	Reconstructed Compton-parameter maps from <i>Planck</i> data, using the MILCA and NILC algorithms. Maps are plotted in orthographic projection, showing the southern Galactic hemisphere on the left and the northern Galactic hemisphere on the right. Figure taken from Planck Collaboration et al. (2016h)	133
4.2	SZ 1D-PDF ($P(y)$) corresponding to the two reconstructed y maps shown in figure 4.1, normalized to unit integral. We also show a Gaussian fit to the central noise contribution, as it is defined in section 4.2.2. The galaxy cluster contribution is clearly visible as the high- y tail.	135
4.3	Numerical $P(y)$ distributions computed using the formalism described in section 4.3 and the cosmological parameters in table 4.1, but using different values for the parameter σ_8 . The plot clearly shows the strong dependence of the tSZ PDF on this parameter, which makes it an effective cosmological probe.	137
4.4	Compton parameter profile for a low-mass cluster and a high-mass cluster at redshift $z = 0.5$. In the plot we also include the filtered Compton profile computed with 4.21 using the <i>Planck</i> effective smoothing beam of $14.0'$	141
4.5	Coordinate system used for computing the smoothing of the Compton profile due to an instrumental beam. The computation can be performed at a convenient point $(x_0, 0)$, and the final profile can be easily found by exploiting the circular symmetry of the cluster projected profile.	142
4.6	Contribution from a single cluster to the tSZ PDF. For a given y bin, it is possible to find an annular region in the cluster projected surface in which the Compton parameter takes values inside the bin. The contribution from that particular cluster to the $P(y)$ is proportional to the area of the annulus.	145
4.7	Computation of the overall $P(y)$ via convolution between the noise and the noiseless cluster-only contribution.	148
4.8	Comparison between the two recipes for including noise in the tSZ PDF. The final distributions are the same within a 1% accuracy in the cluster-dominated range, while the difference gets larger where the function has faster variations as a function of y .	150
4.9	Example of two simulated cluster-only Compton parameter maps, without including any instrumental contribution in terms of noise or beam dilution.	152
4.10	The same maps from figure 4.9, after the smoothing with a 20 arcmin beam.	154

Este documento incorpora firma electrónica, y es copia auténtica de un documento electrónico archivado por la ULL según la Ley 39/2015.
Su autenticidad puede ser contrastada en la siguiente dirección <https://sede.ull.es/validacion/>

Identificador del documento:	973742	Código de verificación:	Jfg6xBh0
Firmado por:	DENIS TRAMONTE UNIVERSIDAD DE LA LAGUNA	Fecha:	30/06/2017 15:10:10
	RAFAEL DELFIN BARRENA DELGADO UNIVERSIDAD DE LA LAGUNA		30/06/2017 15:21:31
	JOSE ALBERTO RUBIÑO MARTIN UNIVERSIDAD DE LA LAGUNA		30/06/2017 15:34:17
	ERNESTO PEREDA DE PABLO UNIVERSIDAD DE LA LAGUNA		06/07/2017 13:51:19

4.11 <i>Top:</i> example of a simulated noise map using the mean and rms from the MILCA fitted noise in figure 4.2. <i>Bottom:</i> the same map from the top panel of figure 4.10, after adding the noise simulated map.	155
4.12 Left: PDFs extracted from a set of 500 simulated y maps, together with their average. Right: comparison between the average $P(y)$ with the one computed analytically: we found agreement in the interesting range of y , out of the region dominated by noise.	156
4.13 Effective SZ PDF distributions from <i>Planck</i> reconstructed y maps that we consider for cosmological parameter estimation. These distributions only take the contribution from galaxy clusters and the noise/foregrounds, dropping the negative y tail which would alter the PDFs normalisation.	157
4.14 Decimal logarithm of the covariance matrix, computed for the best fit solution for the MILCA PDF in figure 4.16.	159
4.15 Likelihood distributions built using 4.39 with <i>Planck</i> MILCA and NILC distribution as a reference. The best fit estimates are marked with the vertical dashed line and are reported in equation 4.40.	160
4.16 MILCA and NILC data together with the corresponding best-fit PDF computed using the σ_8 estimates in 4.40; we also highlight the region of y employed for the fit in both cases.	160
4.17 COrE simulated all-sky Compton parameter map, together with the corresponding PDF and the fit to its noise component.	162
4.18 Left: likelihood distributions built using 4.39 with the COrE simulated Compton map as a reference. Right: the best-fit $P(y)$ is overplotted on COrE simulated data, showing the y range actually employed for the fit.	163
5.1 Picture of the QUIJOTE telescopes in their enclosure at the Teide Observatory: QT1 is visible in the back, QT2 is visible in the front.	168
5.2 Schematic representation of the MFI receiving system.	169
5.3 Schematic representation of the TGI receiving system.	170
5.4 Preliminary map of the wide survey at 11 GHz, plotted in Galactic coordinates. Figure taken from Rubiño-Martín et al. (2017).	172

Este documento incorpora firma electrónica, y es copia auténtica de un documento electrónico archivado por la ULL según la Ley 39/2015.
Su autenticidad puede ser contrastada en la siguiente dirección <https://sede.ull.es/validacion/>

Identificador del documento: 973742	Código de verificación: Jfg6xBh0	Fecha: 30/06/2017 15:10:10
Firmado por: DENIS TRAMONTE UNIVERSIDAD DE LA LAGUNA		
RAFAEL DELFIN BARRENA DELGADO UNIVERSIDAD DE LA LAGUNA		30/06/2017 15:21:31
JOSE ALBERTO RUBIÑO MARTIN UNIVERSIDAD DE LA LAGUNA		30/06/2017 15:34:17
ERNESTO PEREDA DE PABLO UNIVERSIDAD DE LA LAGUNA		06/07/2017 13:51:19

5.5 WMAP all sky map with the three cosmological (“COSMO”) field selected for the QUIJOTE deep survey, plotted in equatorial coordinates. Notice that the three fields are selected away from the Galactic plane in order to minimise the contamination from Galactic foregrounds. The two dashed lines mark the limits of the sky region accessible by QUIJOTE. Figure adapted from Rubiño-Martín et al. (2017).	172
5.6 <i>Left:</i> design of the focal plane horn distribution for the MFI, as seen from the secondary mirror. <i>Right:</i> corresponding plot of the horns PSF, computed assuming Gaussian beams with the nominal FWHMs reported in table 5.1.	176
5.7 Formalism for pointing corrections.	179
5.8 Telescope non-idealities considered in this work.	181
5.9 Effect of the pointing model correction at the level of the TOD for an observation of Crab. We plot the data with the simulation superimposed, in the case of no pointing correction (<i>top</i>) and with the pointing correction using the parameters from table 5.6 (<i>bottom</i>). The improvement resulting from applying the pointing model is evident.	197
5.10 Stack of 650 Crab observations in Galactic coordinates for horns 1 to 4 (top to bottom) in the low frequency band, with no pointing correction (left panels) after applying the pointing from table 5.6 (right panel).	199
5.11 Location of the considered regions in Galactic coordinates, plotted using <i>Planck</i> ’s lowest frequency map.	202
5.12 Intensity and polarisation W49 destriped maps, for the four QUIJOTE observing frequencies. From top to bottom, we show the maps at 11 GHz (horn 3), 13 GHz (horn 3), 17 GHz (horn 2) and 19 GHz (horn 4); the signal plotted in the maps is intensity I in the left column, the Stokes parameter Q in the middle column and the Stokes parameter U in the right column. In the intensity maps, the sources W51, W49 and W47 (left to right) are clearly visible.	208
5.13 Same as figure 5.12, but for W51.	209
5.14 Same as figure 5.12, but for IC443.	210
5.15 Azimuth stack of a W49 observation from Group 1, comparing the signal from QUIJOTE (black) and WMAP (red): the satellite interference clearly emerges at $AZ > 104^\circ$	211
5.16 Intensity and polarisation W49 destriped maps after correcting for the interference contamination which was present in figure 5.12.	212

Este documento incorpora firma electrónica, y es copia auténtica de un documento electrónico archivado por la ULL según la Ley 39/2015.
Su autenticidad puede ser contrastada en la siguiente dirección <https://sede.ull.es/validacion/>

Identificador del documento: 973742	Código de verificación: Jfg6xBh0	Fecha: 30/06/2017 15:10:10
Firmado por: DENIS TRAMONTE UNIVERSIDAD DE LA LAGUNA		
RAFAEL DELFIN BARRENA DELGADO UNIVERSIDAD DE LA LAGUNA		30/06/2017 15:21:31
JOSE ALBERTO RUBIÑO MARTIN UNIVERSIDAD DE LA LAGUNA		30/06/2017 15:34:17
ERNESTO PEREDA DE PABLO UNIVERSIDAD DE LA LAGUNA		06/07/2017 13:51:19

5.17 Intensity SED for the three regions, joining results from the eight QUIJOTE frequencies and all the other ancillary data listed in section 5.3.5.	218
5.18 The same SEDs from figure 5.17 without the HartRAO point, with the best fit model superimposed.	221

Este documento incorpora firma electrónica, y es copia auténtica de un documento electrónico archivado por la ULL según la Ley 39/2015.
Su autenticidad puede ser contrastada en la siguiente dirección <https://sede.ull.es/validacion/>

Identificador del documento: 973742

Código de verificación: Jfg6xBh0

Firmado por: DENIS TRAMONTE
UNIVERSIDAD DE LA LAGUNA

Fecha: 30/06/2017 15:10:10

RAFAEL DELFIN BARRENA DELGADO
UNIVERSIDAD DE LA LAGUNA

30/06/2017 15:21:31

JOSE ALBERTO RUBIÑO MARTIN
UNIVERSIDAD DE LA LAGUNA

30/06/2017 15:34:17

ERNESTO PEREDA DE PABLO
UNIVERSIDAD DE LA LAGUNA

06/07/2017 13:51:19

List of Tables

1.1	Evolution of the energy density and of the scale factor, for different components dominating the expansion of the Universe.	4
1.2	Cosmological model used for the examples in this chapter.	9
2.1	Values of cosmological parameters for our reference model.	63
2.2	Table summarising the properties of the two simulations used in this work.	68
3.1	Fiducial cosmology used for simulating a cluster survey.	96
3.2	Total number of clusters observed depending on the threshold mass used for the selection function.	102
3.3	Total number of clusters and final parameter estimates depending on the selected threshold mass.	112
3.4	Results of parameter estimation, comparing the values for Ω_m and σ_8 retrieved by our code and by the Planck Collaboration, both in the case of a fixed and a free mass bias.	122
4.1	Fiducial cosmology and mass bias used throughout this chapter.	138
4.2	Fiducial cosmology and mass bias used for COrE forecast.	162
5.1	Nominal characteristics of the three instruments: MFI, TGI and FGI. Values of NET (and sensitivity) are intended per frequency band in the case of the MFI, and for the full array in the case of the TGI and FGI. Sensitivities are quoted in units of Jansky, $1 \text{ Jy} = 10^{-26} \text{ W m}^{-2} \text{ Hz}^{-1}$, and are referred to Stokes Q and U parameters.	171
5.2	Linear positions of the four MFI horns on QT1 focal plane.	176

Identificador del documento:	973742	Código de verificación:	Jfg6xBh0
Firmado por:	DENIS TRAMONTE UNIVERSIDAD DE LA LAGUNA		Fecha: 30/06/2017 15:10:10
	RAFAEL DELFIN BARRENA DELGADO UNIVERSIDAD DE LA LAGUNA		30/06/2017 15:21:31
	JOSE ALBERTO RUBIÑO MARTIN UNIVERSIDAD DE LA LAGUNA		30/06/2017 15:34:17
	ERNESTO PEREDA DE PABLO UNIVERSIDAD DE LA LAGUNA		06/07/2017 13:51:19

5.3	First estimation of the pointing model. Parameter values are in arcseconds. The last line reports the results of the estimations considering all horns at the same time.	191
5.4	Best-fit displacements of the horn positions with respect to the nominal ones, computed fixing the pointing parameters to the common model from the last line of table 5.3.	193
5.5	Results for the fit of the focal length variation with respect to the nominal value $f_0 = 3637$ mm, considering each horn individually and all together in the last line. The results are reported separately for Cas A and Crab because the horn angular separations were measured directly from maps in equatorial coordinates.	195
5.6	Best-fit estimation of the pointing model, using the new estimated focal length $f = 3700$ mm and the nominal positions for the horns. Parameter values are reported in arcseconds.	196
5.7	Results from the Gaussian fits to the horn PSF from the stack in Galactic coordinates of several Crab observations. For each horn we fit for its angular displacement from the expected source position and the FWHM of the beam in two orthogonal directions. In the table we also report the corresponding horn ellipticities, computed with equation 5.36. We report results for both low frequency (lf) and high frequency maps (hf).	198
5.8	Results from the data selection. For each region we report the total number of dedicated observations N_{obs} , the corresponding total time in hours t_{tot} , and the time fraction of accepted observations f_t for each one of the horn, in terms of the ratio of the effective hours of observations used against the total t_{tot} . These fractions are computed on the basis of the eye inspection only, so they do not take into account the further loss of data deriving from the automatic flagging.	205
5.9	Intensity fluxes computed with aperture photometry in the regions W49, W51 and IC443. For QUIJOTE we used the maps described in section 5.3.4. The other fluxes were computed using ancillary maps from other surveys. All maps were degraded to a common resolution of 1 degree before extracting the fluxes.	215
5.10	Q fluxes computed with aperture photometry in the regions W49, W51 and IC443.	216
5.11	U fluxes computed with aperture photometry in the regions W49, W51 and IC443.	217
5.12	Results of the multicomponent fit on the three regions.	220

Este documento incorpora firma electrónica, y es copia auténtica de un documento electrónico archivado por la ULL según la Ley 39/2015.
Su autenticidad puede ser contrastada en la siguiente dirección <https://sede.ull.es/validacion/>

Identificador del documento: 973742	Código de verificación: Jfg6xBh0	Fecha: 30/06/2017 15:10:10
Firmado por: DENIS TRAMONTE UNIVERSIDAD DE LA LAGUNA		
RAFAEL DELFIN BARRENA DELGADO UNIVERSIDAD DE LA LAGUNA		30/06/2017 15:21:31
JOSE ALBERTO RUBIÑO MARTIN UNIVERSIDAD DE LA LAGUNA		30/06/2017 15:34:17
ERNESTO PEREDA DE PABLO UNIVERSIDAD DE LA LAGUNA		06/07/2017 13:51:19

A.1	Complete list of fitting terms for computing the parameters A , b and c in the reference cosmology, using eq. (A.1). Index i runs over lines, index j runs over columns.	230
A.2	Complete list of fitting terms to transform the A parameter to the chosen values of z and σ_8 , using eqs. (A.4) and (A.3). Index i selects a line, index j selects a column.	230
A.3	Complete list of fitting terms to transform the b parameter to the chosen values of z and σ_8 , using eqs. (A.4) and (A.3). Index i selects a line, index j selects a column.	232
A.4	Complete list of fitting terms to transform the c parameter to the chosen values of z and σ_8 , using eqs. (A.4) and (A.3). Index i selects a line, index j selects a column.	233
A.5	Complete list of fitting terms for computing the exponent $f(h, \Omega_m)$ using eq. (A.6), entering the mass scaling (A.5). Index i selects a line, index j selects a column.	235

Este documento incorpora firma electrónica, y es copia auténtica de un documento electrónico archivado por la ULL según la Ley 39/2015.
Su autenticidad puede ser contrastada en la siguiente dirección <https://sede.ull.es/validacion/>

Identificador del documento: 973742

Código de verificación: Jfg6xBh0

Fecha: 30/06/2017 15:10:10

Firmado por: DENIS TRAMONTE
UNIVERSIDAD DE LA LAGUNA

RAFAEL DELFIN BARRENA DELGADO
UNIVERSIDAD DE LA LAGUNA

JOSE ALBERTO RUBIÑO MARTIN
UNIVERSIDAD DE LA LAGUNA

ERNESTO PEREDA DE PABLO
UNIVERSIDAD DE LA LAGUNA

30/06/2017 15:21:31

30/06/2017 15:34:17

06/07/2017 13:51:19

Este documento incorpora firma electrónica, y es copia auténtica de un documento electrónico archivado por la ULL según la Ley 39/2015.
Su autenticidad puede ser contrastada en la siguiente dirección <https://sede.ull.es/validacion/>

Identificador del documento: 973742

Código de verificación: Jfg6xBh0

Firmado por: DENIS TRAMONTE UNIVERSIDAD DE LA LAGUNA	Fecha: 30/06/2017 15:10:10
RAFAEL DELFIN BARRENA DELGADO UNIVERSIDAD DE LA LAGUNA	30/06/2017 15:21:31
JOSE ALBERTO RUBIÑO MARTIN UNIVERSIDAD DE LA LAGUNA	30/06/2017 15:34:17
ERNESTO PEREDA DE PABLO UNIVERSIDAD DE LA LAGUNA	06/07/2017 13:51:19

Bibliography

- Abazajian, K. N., & Kaplinghat, M. 2016, Annual Review of Nuclear and Particle Science, 66, 401
- Abbott, L. F., & Wise, M. B. 1984, ApJ, 282, L47
- Abell, G. O. 1958, ApJS, 3, 211
- Abell, G. O., Corwin, Jr., H. G., & Olowin, R. P. 1989, ApJS, 70, 1
- Abramowitz, M., & Stegun, I. A. 1972, Handbook of Mathematical Functions
- Ackermann, M., Ajello, M., Allafort, A., et al. 2013, Science, 339, 807
- Acquaviva, V., Bartolo, N., Matarrese, S., & Riotto, A. 2003, Nuclear Physics B, 667, 119
- Ade, P. A. R., Aghanim, N., Ahmed, Z., et al. 2015, Phys. Rev. Lett., 114, 101301
- Aghanim, N., de Luca, A., Bouchet, F. R., Gispert, R., & Puget, J. L. 1997, A&A, 325, 9
- Aghanim, N., Majumdar, S., & Silk, J. 2008, Reports on Progress in Physics, 71, 066902
- Albrecht, A., Bernstein, G., Cahn, R., et al. 2006, ArXiv Astrophysics e-prints, astro-ph/0609591
- Aleksić, J., Alvarez, E. A., Antonelli, L. A., et al. 2012, A&A, 541, A13
- Allen, S. W., Evrard, A. E., & Mantz, A. B. 2011, ARA&A, 49, 409
- Allen, S. W., Rapetti, D. A., Schmidt, R. W., et al. 2008a, MNRAS, 383, 879

- . 2008b, MNRAS, 383, 879
- Allen, S. W., Schmidt, R. W., Ebeling, H., Fabian, A. C., & van Speybroeck, L. 2004, in COSPAR Meeting, Vol. 35, 35th COSPAR Scientific Assembly, ed. J.-P. Paillé, 998
- Angulo, R. E., Springel, V., White, S. D. M., et al. 2012, MNRAS, 426, 2046
- Aoki, S., Kinoshita, H., Guinot, B., et al. 1982, A&A, 105, 359
- Arnaud, M., Pratt, G. W., Piffaretti, R., et al. 2010, A&A, 517, A92
- Audren, B., Bellini, E., Cuesta, A. J., et al. 2015, JCAP, 3, 036
- Barbosa, D., Bartlett, J. G., Blanchard, A., & Oukbir, J. 1996, A&A, 314, 13
- Barkana, R., & Loeb, A. 2001, Phys. Rep., 349, 125
- Barkats, D., Aikin, R., Bischoff, C., et al. 2014, ApJ, 783, 67
- Bartelmann, M., & Schneider, P. 2001, Phys. Rep., 340, 291
- Bassett, B., & Hlozek, R. 2010, Baryon acoustic oscillations, ed. P. Ruiz-Lapuente, 246
- Battaglia, N., Bond, J. R., Pfrommer, C., & Sievers, J. L. 2012, ApJ, 758, 75
- Bennett, C. L., Halpern, M., Hinshaw, G., et al. 2003, ApJS, 148, 1
- Bennett, C. L., Larson, D., Weiland, J. L., et al. 2013, ApJS, 208, 20
- Benoit, A., Ade, P., Amblard, A., et al. 2004, A&A, 424, 571
- Berkhuijsen, E. M. 1972, A&AS, 5, 263
- Betancort-Rijo, J., Patiri, S. G., Prada, F., & Romano, A. E. 2009, MNRAS, 400, 1835
- Betancort-Rijo, J., Tramonte, D., & Rubiño-Martín, J. A. in prep.
- Betancort-Rijo, J. E., & Montero-Dorta, A. D. 2006a, ApJ, 650, L95
- . 2006b, ApJ, 653, L77
- Betancort-Rijo, J. E., Sanchez-Conde, M. A., Prada, F., & Patiri, S. G. 2006, ApJ, 649, 579

Este documento incorpora firma electrónica, y es copia auténtica de un documento electrónico archivado por la ULL según la Ley 39/2015.
Su autenticidad puede ser contrastada en la siguiente dirección <https://sede.ull.es/validacion/>

Identificador del documento: 973742

Código de verificación: Jfg6xBh0

Fecha: 30/06/2017 15:10:10

Firmado por: DENIS TRAMONTE UNIVERSIDAD DE LA LAGUNA	30/06/2017 15:21:31
RAFAEL DELFIN BARRENA DELGADO UNIVERSIDAD DE LA LAGUNA	30/06/2017 15:34:17
JOSE ALBERTO RUBIÑO MARTIN UNIVERSIDAD DE LA LAGUNA	06/07/2017 13:51:19
ERNESTO PEREDA DE PABLO UNIVERSIDAD DE LA LAGUNA	

- Bhattacharya, S., Nagai, D., Shaw, L., Crawford, T., & Holder, G. P. 2012, ApJ, 760, 5
- BICEP2 Collaboration, Ade, P. A. R., Aikin, R. W., et al. 2014, Physical Review Letters, 112, 241101
- BICEP2 Collaboration, Keck Array Collaboration, Ade, P. A. R., et al. 2016, Physical Review Letters, 116, 031302
- Birkinshaw, M. 1991, in Physical Cosmology, ed. A. Blanchard, L. Celnikier, M. Lachieze-Rey, & J. Tran Thanh Van, 177
- Birkinshaw, M. 1999, Phys. Rep., 310, 97
- Birkinshaw, M., Gull, S. F., & Northover, K. J. E. 1978a, Nature, 275, 40
- . 1978b, MNRAS, 185, 245
- Birkinshaw, M., & Hughes, J. P. 1994, ApJ, 420, 33
- Bischoff, C., Brizius, A., Buder, I., et al. 2013, ApJ, 768, 9
- Biviano, A. 2000, in Constructing the Universe with Clusters of Galaxies
- Bleem, L. E., Stalder, B., de Haan, T., et al. 2015, ApJS, 216, 27
- Bocquet, S., Saro, A., Dolag, K., & Mohr, J. J. 2016, MNRAS, 456, 2361
- Boesgaard, A. M., & Steigman, G. 1985, ARA&A, 23, 319
- Böhringer, H., Schuecker, P., Guzzo, L., et al. 2004, A&A, 425, 367
- Bonaldi, A., Ricciardi, S., Leach, S., et al. 2007, MNRAS, 382, 1791
- Bonamente, M., Joy, M., LaRoque, S. J., et al. 2008, ApJ, 675, 106
- Bonamente, M., Joy, M. K., LaRoque, S. J., et al. 2006, ApJ, 647, 25
- Bond, J. R., Cole, S., Efstathiou, G., & Kaiser, N. 1991, ApJ, 379, 440
- Bond, J. R., & Efstathiou, G. 1984, ApJ, 285, L45
- Bond, J. R., & Myers, S. T. 1996, ApJS, 103, 1
- Bondi, H. 1990, The Steady-State Theory of the Universe, ed. J. Leslie, 70
- Bradley, J. 1727, Philosophical Transactions of the Royal Society of London Series I, 35, 637

Este documento incorpora firma electrónica, y es copia auténtica de un documento electrónico archivado por la ULL según la Ley 39/2015.
Su autenticidad puede ser contrastada en la siguiente dirección <https://sede.ull.es/validacion/>

Identificador del documento: 973742

Código de verificación: Jfg6xBh0

Fecha: 30/06/2017 15:10:10

Firmado por: DENIS TRAMONTE
 UNIVERSIDAD DE LA LAGUNA

RAFAEL DELFIN BARRENA DELGADO
 UNIVERSIDAD DE LA LAGUNA

JOSE ALBERTO RUBIÑO MARTIN
 UNIVERSIDAD DE LA LAGUNA

ERNESTO PEREDA DE PABLO
 UNIVERSIDAD DE LA LAGUNA

30/06/2017 15:21:31

30/06/2017 15:34:17

06/07/2017 13:51:19

- . 1748, Philosophical Transactions of the Royal Society of London Series I, 45, 1
- Brogan, C. L., & Troland, T. H. 2001, ApJ, 550, 799
- Brun, F., de Naurois, M., Hofmann, W., et al. 2011, in SF2A-2011: Proceedings of the Annual meeting of the French Society of Astronomy and Astrophysics, ed. G. Alecian, K. Belkacem, R. Samadi, & D. Valls-Gabaud, 545–548
- Bucher, M. 2015, International Journal of Modern Physics D, 24, 1530004
- Bundy, K., Bershadsky, M. A., Law, D. R., et al. 2015, ApJ, 798, 7
- Burenin, R. A., Vikhlinin, A., Hornstrup, A., et al. 2007, ApJS, 172, 561
- Carlstrom, J. E., Holder, G. P., & Reese, E. D. 2002, ARA&A, 40, 643
- Carpenter, J. M., & Sanders, D. B. 1998, AJ, 116, 1856
- Carvalho, P., Rocha, G., Hobson, M. P., & Lasenby, A. 2012, MNRAS, 427, 1384
- Cash, W. 1979, ApJ, 228, 939
- Castelletti, G., Dubner, G., Clarke, T., & Kassim, N. E. 2011, A&A, 534, A21
- Cavaliere, A., & Fusco-Femiano, R. 1976, A&A, 49, 137
- . 1978, A&A, 70, 677
- Chevallier, M., & Polarski, D. 2001, International Journal of Modern Physics D, 10, 213
- Chiang, C.-T. 2015, ArXiv e-prints, arXiv:1508.03256
- Cole, S., & Kaiser, N. 1989, MNRAS, 237, 1127
- Colless, M., Dalton, G., Maddox, S., et al. 2001, MNRAS, 328, 1039
- CORE Collaboration, Finelli, F., Bucher, M., et al. 2016, ArXiv e-prints, arXiv:1612.08270
- Corey, B. E., & Wilkinson, D. T. 1976, in BAAS, Vol. 8, Bulletin of the American Astronomical Society, 351
- Courtin, J., Rasera, Y., Alimi, J.-M., et al. 2011, MNRAS, 410, 1911

Este documento incorpora firma electrónica, y es copia auténtica de un documento electrónico archivado por la ULL según la Ley 39/2015.
Su autenticidad puede ser contrastada en la siguiente dirección <https://sede.ull.es/validacion/>

Identificador del documento:	973742	Código de verificación:	Jfg6xBh0
Firmado por:	DENIS TRAMONTE UNIVERSIDAD DE LA LAGUNA	Fecha:	30/06/2017 15:10:10
	RAFAEL DELFIN BARRENA DELGADO UNIVERSIDAD DE LA LAGUNA		30/06/2017 15:21:31
	JOSE ALBERTO RUBIÑO MARTIN UNIVERSIDAD DE LA LAGUNA		30/06/2017 15:34:17
	ERNESTO PEREDA DE PABLO UNIVERSIDAD DE LA LAGUNA		06/07/2017 13:51:19

- Crites, A. T., Henning, J. W., Ade, P. A. R., et al. 2015, ApJ, 805, 36
- Crocce, M., Fosalba, P., Castander, F. J., & Gaztañaga, E. 2010, MNRAS, 403, 1353
- Crocce, M., Pueblas, S., & Scoccimarro, R. 2006, MNRAS, 373, 369
- Dalton, G. B., Maddox, S. J., Sutherland, W. J., & Efstathiou, G. 1997, MNRAS, 289, 263
- Danese, L., & Partridge, R. B. 1989, ApJ, 342, 604
- Das, S., Sherwin, B. D., Aguirre, P., et al. 2011, Physical Review Letters, 107, 021301
- Davies, R. D., Lasenby, A. N., Watson, R. A., et al. 1987, Nature, 326, 462
- Davis, M., Efstathiou, G., Frenk, C. S., & White, S. D. M. 1985, ApJ, 292, 371
- Dawson, K. S., Schlegel, D. J., Ahn, C. P., et al. 2013, AJ, 145, 10
- Dawson, K. S., Kneib, J.-P., Percival, W. J., et al. 2016, AJ, 151, 44
- de Bernardis, P., Ade, P. A. R., Bock, J. J., et al. 2001, in American Institute of Physics Conference Series, Vol. 555, Cosmology and Particle Physics, ed. R. Durrer, J. Garcia-Bellido, & M. Shaposhnikov, 85–94
- de Vaucouleurs, G., de Vaucouleurs, A., Corwin, Jr., H. G., et al. 1991, Third Reference Catalogue of Bright Galaxies. Volume I: Explanations and references. Volume II: Data for galaxies between 0^h and 12^h . Volume III: Data for galaxies between 12^h and 24^h .
- De Zotti, G., Gonzalez-Nuevo, J., Lopez-Caniego, M., et al. 2016, ArXiv e-prints, arXiv:1609.07263
- Delabrouille, J. 1998, A&AS, 127, 555
- Delabrouille, J., Melin, J.-B., & Bartlett, J. G. 2002, in Astronomical Society of the Pacific Conference Series, Vol. 257, AMiBA 2001: High-Z Clusters, Missing Baryons, and CMB Polarization, ed. L.-W. Chen, C.-P. Ma, K.-W. Ng, & U.-L. Pen, 81
- Delabrouille, J., Betoule, M., Melin, J.-B., et al. 2013, A&A, 553, A96
- Despali, G., Giocoli, C., Angulo, R. E., et al. 2016, MNRAS, 456, 2486

Este documento incorpora firma electrónica, y es copia auténtica de un documento electrónico archivado por la ULL según la Ley 39/2015.
Su autenticidad puede ser contrastada en la siguiente dirección <https://sede.ull.es/validacion/>

Identificador del documento:	973742	Código de verificación:	Jfg6xBh0
Firmado por:	DENIS TRAMONTE UNIVERSIDAD DE LA LAGUNA	Fecha:	30/06/2017 15:10:10
	RAFAEL DELFIN BARRENA DELGADO UNIVERSIDAD DE LA LAGUNA		30/06/2017 15:21:31
	JOSE ALBERTO RUBIÑO MARTIN UNIVERSIDAD DE LA LAGUNA		30/06/2017 15:34:17
	ERNESTO PEREDA DE PABLO UNIVERSIDAD DE LA LAGUNA		06/07/2017 13:51:19

- Di Valentino, E., Brinckmann, T., Gerbino, M., et al. 2016, ArXiv e-prints, arXiv:1612.00021
- Dicke, R. H., Peebles, P. J. E., Roll, P. G., & Wilkinson, D. T. 1965, ApJ, 142, 414
- Dickinson, C., Battye, R. A., Carreira, P., et al. 2004, MNRAS, 353, 732
- Dole, H., Lagache, G., Puget, J.-L., et al. 2006, A&A, 451, 417
- Draine, B. T., & Lazarian, A. 1998, ApJ, 494, L19
- Ebeling, H., Edge, A. C., Boehringer, H., et al. 1998, MNRAS, 301, 881
- Ebeling, H., Edge, A. C., Mantz, A., et al. 2010, MNRAS, 407, 83
- Efstathiou, G., Frenk, C. S., White, S. D. M., & Davis, M. 1988, MNRAS, 235, 715
- Eisenstein, D. J., & Hu, W. 1998, ApJ, 496, 605
- Errard, J., Feeney, S. M., Peiris, H. V., & Jaffe, A. H. 2016, JCAP, 3, 052
- Falco, E. E., Kurtz, M. J., Geller, M. J., et al. 1999, PASP, 111, 438
- Fassbender, R., Böhringer, H., Nastasi, A., et al. 2011, New Journal of Physics, 13, 125014
- Femenía, B., Rebolo, R., Gutiérrez, C. M., Limón, M., & Piccirillo, L. 1998, ApJ, 498, 117
- Fesen, R. A. 1984, ApJ, 281, 658
- Fesen, R. A., Hammell, M. C., Morse, J., et al. 2006, ApJ, 645, 283
- Fixsen, D. J., Cheng, E. S., Gales, J. M., et al. 1996, ApJ, 473, 576
- Fixsen, D. J., & Mather, J. C. 2002, ApJ, 581, 817
- Forman, W., Kellogg, E., Gursky, H., Tananbaum, H., & Giacconi, R. 1972, ApJ, 178, 309
- Frieman, J. A., Turner, M. S., & Huterer, D. 2008a, ARA&A, 46, 385
- Frieman, J. A., Bassett, B., Becker, A., et al. 2008b, AJ, 135, 338
- Furlanetto, S. R., & Piran, T. 2006, MNRAS, 366, 467

Este documento incorpora firma electrónica, y es copia auténtica de un documento electrónico archivado por la ULL según la Ley 39/2015.
Su autenticidad puede ser contrastada en la siguiente dirección <https://sede.ull.es/validacion/>

Identificador del documento: 973742

Código de verificación: Jfg6xBh0

Fecha: 30/06/2017 15:10:10

Firmado por: DENIS TRAMONTE UNIVERSIDAD DE LA LAGUNA	30/06/2017 15:21:31
RAFAEL DELFIN BARRENA DELGADO UNIVERSIDAD DE LA LAGUNA	30/06/2017 15:34:17
JOSE ALBERTO RUBIÑO MARTIN UNIVERSIDAD DE LA LAGUNA	06/07/2017 13:51:19
ERNESTO PEREDA DE PABLO UNIVERSIDAD DE LA LAGUNA	

- Gallegos, J. E., Macías-Pérez, J. F., Gutiérrez, C. M., et al. 2001, MNRAS, 327, 1178
- Gaustad, J. E., McCullough, P. R., Rosing, W., & Van Buren, D. 2001, PASP, 113, 1326
- Ge, J., Mahadevan, S., Lee, B., et al. 2008, in Astronomical Society of the Pacific Conference Series, Vol. 398, Extreme Solar Systems, ed. D. Fischer, F. A. Rasio, S. E. Thorsett, & A. Wolszczan, 449
- Génova-Santos, R., Rubiño-Martín, J. A., Rebolo, R., et al. 2015a, MNRAS, 452, 4169
- Génova-Santos, R., Rubiño-Martín, J. A., Rebolo, R., et al. 2015b, in Highlights of Spanish Astrophysics VIII, ed. A. J. Cenarro, F. Figueras, C. Hernández-Monteagudo, J. Trujillo Bueno, & L. Valdivielso, 207–212
- Génova-Santos, R., Rubiño-Martín, J. A., Peláez-Santos, A., et al. 2017, MNRAS, 464, 4107
- George, E. M., Reichardt, C. L., Aird, K. A., et al. 2015, ApJ, 799, 177
- Ginsburg, A., Goss, W. M., Goddi, C., et al. 2016, A&A, 595, A27
- Gladders, M. D., & Yee, H. K. C. 2000, AJ, 120, 2148
- . 2005, ApJS, 157, 1
- Goldberg, D. M., & Vogeley, M. S. 2004, ApJ, 605, 1
- Goldberg, J. N., Macfarlane, A. J., Newman, E. T., Rohrlich, F., & Sudarshan, E. C. G. 1967, Journal of Mathematical Physics, 8, 2155
- Gomez, A., Murga, G., Etxeita, B., et al. 2010, in Proc. SPIE, Vol. 7733, Ground-based and Airborne Telescopes III, 77330Z
- Gordon, C., Wands, D., Bassett, B. A., & Maartens, R. 2001, Phys. Rev. D, 63, 023506
- Górski, K. M., & Hivon, E. 2011, HEALPix: Hierarchical Equal Area isoLatitude Pixelization of a sphere, Astrophysics Source Code Library, ascl:1107.018
- Gottlöber, S., Lokas, E. L., Klypin, A., & Hoffman, Y. 2003, MNRAS, 344, 715

Este documento incorpora firma electrónica, y es copia auténtica de un documento electrónico archivado por la ULL según la Ley 39/2015.
Su autenticidad puede ser contrastada en la siguiente dirección <https://sede.ull.es/validacion/>

Identificador del documento: 973742

Código de verificación: Jfg6xBh0

Fecha: 30/06/2017 15:10:10

Firmado por: DENIS TRAMONTE
UNIVERSIDAD DE LA LAGUNA

RAFAEL DELFIN BARRENA DELGADO
UNIVERSIDAD DE LA LAGUNA

JOSE ALBERTO RUBIÑO MARTIN
UNIVERSIDAD DE LA LAGUNA

ERNESTO PEREDA DE PABLO
UNIVERSIDAD DE LA LAGUNA

30/06/2017 15:21:31

30/06/2017 15:34:17

06/07/2017 13:51:19

- Grainge, K., Jones, M. E., Pooley, G., et al. 2002, MNRAS, 333, 318
- Grainge, K., Carreira, P., Cleary, K., et al. 2003, MNRAS, 341, L23
- Green, D. A. 1986, MNRAS, 221, 473
- Grieb, J. N., Sánchez, A. G., Salazar-Albornoz, S., & Dalla Vecchia, C. 2016, MNRAS, 457, 1577
- Gursky, H., Kellogg, E., Murray, S., et al. 1971, ApJ, 167, L81
- Guth, A. H. 1981, Phys. Rev. D, 23, 347
- Guzzetti, M., Bartolo, N., Liguori, M., & Matarrese, S. 2016, ArXiv e-prints, arXiv:1605.01615
- Hafez, Y. A., Davies, R. D., Davis, R. J., et al. 2008, MNRAS, 388, 1775
- Haffner, L. M., Reynolds, R. J., Tufte, S. L., et al. 2003, ApJS, 149, 405
- Hanabata, Y., Sawada, M., Katagiri, H., Bamba, A., & Fukazawa, Y. 2013, PASJ, 65, 42
- Hand, N., Addison, G. E., Aubourg, E., et al. 2012, Physical Review Letters, 109, 041101
- Hanson, D., Hoover, S., Crites, A., et al. 2013, Physical Review Letters, 111, 141301
- Harrison, D. L., Rubiño-Martin, J. A., Melhuish, S. J., et al. 2000, MNRAS, 316, L24
- Harrison, E. R. 1970, Phys. Rev. D, 1, 2726
- Haslam, C. G. T., Salter, C. J., Stoffel, H., & Wilson, W. E. 1982, A&AS, 47, 1
- Hasselfield, M., Hilton, M., Marriage, T. A., et al. 2013, JCAP, 7, 008
- Hastings, W. K. 1970, 57, 97, this paper introduces what is now known as the Metropolis–Hastings algorithm, a generalization of the work in [Metropolis et al. \(1953\)](#).
- Hauser, M. G., & Dwek, E. 2001, ARA&A, 39, 249
- Hauser, M. G., Arendt, R. G., Kelsall, T., et al. 1998, ApJ, 508, 25

Este documento incorpora firma electrónica, y es copia auténtica de un documento electrónico archivado por la ULL según la Ley 39/2015.
Su autenticidad puede ser contrastada en la siguiente dirección <https://sede.ull.es/validacion/>

Identificador del documento:	973742	Código de verificación:	Jfg6xBh0
Firmado por:	DENIS TRAMONTE UNIVERSIDAD DE LA LAGUNA	Fecha:	30/06/2017 15:10:10
	RAFAEL DELFIN BARRENA DELGADO UNIVERSIDAD DE LA LAGUNA		30/06/2017 15:21:31
	JOSE ALBERTO RUBIÑO MARTIN UNIVERSIDAD DE LA LAGUNA		30/06/2017 15:34:17
	ERNESTO PEREDA DE PABLO UNIVERSIDAD DE LA LAGUNA		06/07/2017 13:51:19

- Hernández-Monteagudo, C., Ma, Y.-Z., Kitaura, F. S., et al. 2015, Physical Review Letters, 115, 191301
- Herranz, D., Sanz, J. L., Hobson, M. P., et al. 2002, MNRAS, 336, 1057
- Hester, J. J. 2008, ARA&A, 46, 127
- Hicks, A. K., Ellingson, E., Bautz, M., et al. 2008, ApJ, 680, 1022
- Hill, J. C., & Pajer, E. 2013, Phys. Rev. D, 88, 063526
- Hill, J. C., & Sherwin, B. D. 2013, Phys. Rev. D, 87, 023527
- Hill, J. C., Sherwin, B. D., Smith, K. M., et al. 2014, ArXiv e-prints, arXiv:1411.8004
- Hinder, R. A. 1970, Nature, 225, 614
- Hinshaw, G., Larson, D., Komatsu, E., et al. 2013, ApJS, 208, 19
- Hinton, S. R., Kazin, E., Davis, T. M., et al. 2017, MNRAS, 464, 4807
- Hogg, D. W. 1999, ArXiv Astrophysics e-prints, astro-ph/9905116
- Hoyland, R., Aguiar-González, M., Génova-Santosa, R., et al. 2014, in Proc. SPIE, Vol. 9153, Millimeter, Submillimeter, and Far-Infrared Detectors and Instrumentation for Astronomy VII, 915332
- Hoyland, R. J., Aguiar-González, M., Aja, B., et al. 2012, in Proc. SPIE, Vol. 8452, Millimeter, Submillimeter, and Far-Infrared Detectors and Instrumentation for Astronomy VI, 845233
- Hoyle, F. 1954, The Observatory, 74, 253
- Hu, W., & Dodelson, S. 2002, ARA&A, 40, 171
- Hu, W., Fukugita, M., Zaldarriaga, M., & Tegmark, M. 2001, ApJ, 549, 669
- Hu, W., Seljak, U., White, M., & Zaldarriaga, M. 1998, Phys. Rev. D, 57, 3290
- Hu, W., & White, M. 1997, New Astronomy, 2, 323
- Huchra, J. P., Macri, L. M., Masters, K. L., et al. 2012, ApJS, 199, 26
- Hughes, J. P., & Birkinshaw, M. 1998, ApJ, 501, 1

Este documento incorpora firma electrónica, y es copia auténtica de un documento electrónico archivado por la ULL según la Ley 39/2015.
Su autenticidad puede ser contrastada en la siguiente dirección <https://sede.ull.es/validacion/>

Identificador del documento: 973742

Código de verificación: Jfg6xBh0

Fecha: 30/06/2017 15:10:10

Firmado por: DENIS TRAMONTE
UNIVERSIDAD DE LA LAGUNA

RAFAEL DELFIN BARRENA DELGADO
UNIVERSIDAD DE LA LAGUNA

JOSE ALBERTO RUBIÑO MARTIN
UNIVERSIDAD DE LA LAGUNA

ERNESTO PEREDA DE PABLO
UNIVERSIDAD DE LA LAGUNA

30/06/2017 15:21:31

30/06/2017 15:34:17

06/07/2017 13:51:19

- Hughes, J. P., Yamashita, K., Okumura, Y., Tsunemi, H., & Matsuoka, M. 1988, ApJ, 327, 615
- Hurier, G., Macías-Pérez, J. F., & Hildebrandt, S. 2013, A&A, 558, A118
- Hwang, U., Petre, R., & Hughes, J. P. 2000, ApJ, 532, 970
- Irfan, M. O., Dickinson, C., Davies, R. D., et al. 2015, MNRAS, 448, 3572
- Ivezic, Z., Axelrod, T., Brandt, W. N., et al. 2008, Serbian Astronomical Journal, 176, 1
- Jarosik, N., Bennett, C. L., Halpern, M., et al. 2003, ApJS, 145, 413
- Jenkins, A., Frenk, C. S., White, S. D. M., et al. 2001, (J01), MNRAS, 321, 372
- Jennings, E., Li, Y., & Hu, W. 2013, MNRAS, 434, 2167
- Jonas, J. L., Baart, E. E., & Nicolson, G. D. 1998, MNRAS, 297, 977
- Jones, D. H., Read, M. A., Saunders, W., et al. 2009, MNRAS, 399, 683
- Jones, M., Saunders, R., Alexander, P., et al. 1993, Nature, 365, 320
- Kamionkowski, M., Kosowsky, A., & Stebbins, A. 1997, Phys. Rev. D, 55, 7368
- Kashlinsky, A., & Atrio-Barandela, F. 2000, ApJ, 536, L67
- Kashlinsky, A., Mather, J. C., Odenwald, S., & Hauser, M. G. 1996, ApJ, 470, 681
- Keisler, R., Hoover, S., Harrington, N., et al. 2015, ApJ, 807, 151
- King, O. G., Copley, C., Davies, R., et al. 2010, in Proc. SPIE, Vol. 7741, Millimeter, Submillimeter, and Far-Infrared Detectors and Instrumentation for Astronomy V, 77411I
- Koester, B. P., McKay, T. A., Annis, J., et al. 2007, ApJ, 660, 239
- Kolb, E. W., & Turner, M. S. 1990, The early universe.
- Komatsu, E., & Seljak, U. 2002, MNRAS, 336, 1256
- Komatsu, E., Smith, K. M., Dunkley, J., et al. 2011, ApJS, 192, 18
- Kovalevsky, J. 1995, Modern Astrometry, 137

Este documento incorpora firma electrónica, y es copia auténtica de un documento electrónico archivado por la ULL según la Ley 39/2015.
Su autenticidad puede ser contrastada en la siguiente dirección <https://sede.ull.es/validacion/>

Identificador del documento: 973742

Código de verificación: Jfg6xBh0

Fecha: 30/06/2017 15:10:10

Firmado por: DENIS TRAMONTE
 UNIVERSIDAD DE LA LAGUNA

RAFAEL DELFIN BARRENA DELGADO
 UNIVERSIDAD DE LA LAGUNA

JOSE ALBERTO RUBIÑO MARTIN
 UNIVERSIDAD DE LA LAGUNA

ERNESTO PEREDA DE PABLO
 UNIVERSIDAD DE LA LAGUNA

30/06/2017 15:21:31

30/06/2017 15:34:17

06/07/2017 13:51:19

- Kravtsov, A. V., Vikhlinin, A., & Nagai, D. 2006, ApJ, 650, 128
- Kundu, M. R., & Velusamy, T. 1972, A&A, 20, 237
- Kurki-Suonio, H., Keihänen, E., Keskitalo, R., et al. 2009, A&A, 506, 1511
- Lacey, C., & Cole, S. 1993, MNRAS, 262, 627
- . 1994, MNRAS, 271, 676
- Lahav, O., Lilje, P. B., Primack, J. R., & Rees, M. J. 1991, MNRAS, 251, 128
- Lang, K. R. 1999, Astrophysical formulae
- LaRoque, S. J., Bonamente, M., Carlstrom, J. E., et al. 2006, ApJ, 652, 917
- LaRoque, S. J., Carlstrom, J. E., Reese, E. D., et al. 2002, ArXiv Astrophysics e-prints, astro-ph/0204134
- Laureijs, R., Amiaux, J., Arduini, S., et al. 2011, ArXiv e-prints, arXiv:1110.3193
- Leinert, C., Bowyer, S., Haikala, L. K., et al. 1997, VizieR Online Data Catalog, 412
- Leitch, E. M., Kovac, J. M., Halverson, N. W., et al. 2005, ApJ, 624, 10
- Lewis, A., & Bridle, S. 2002, Phys. Rev. D, 66, 103511
- Lewis, A., Challinor, A., & Lasenby, A. 2000, ApJ, 538, 473
- Lieske, J. H. 1979, A&A, 73, 282
- Lieske, J. H., Lederle, T., Fricke, W., & Morando, B. 1977, A&A, 58, 1
- Linde, A. 2008, in Lecture Notes in Physics, Berlin Springer Verlag, Vol. 738, Inflationary Cosmology, ed. M. Lemoine, J. Martin, & P. Peter, 1
- Longair, M. S., ed. 1998, Galaxy formation
- Lopez, R. E., Dodelson, S., Heckler, A., & Turner, M. S. 1999, Physical Review Letters, 82, 3952
- López-Caraballo, C. H., Rubiño-Martín, J. A., Rebolo, R., & Génova-Santos, R. 2011, ApJ, 729, 25
- Lozinskaya, T. A. 1981, Soviet Astronomy Letters, 7, 29

Este documento incorpora firma electrónica, y es copia auténtica de un documento electrónico archivado por la ULL según la Ley 39/2015.
Su autenticidad puede ser contrastada en la siguiente dirección <https://sede.ull.es/validacion/>

Identificador del documento: 973742

Código de verificación: Jfg6xBh0

Firmado por: DENIS TRAMONTE UNIVERSIDAD DE LA LAGUNA	Fecha: 30/06/2017 15:10:10
RAFAEL DELFIN BARRENA DELGADO UNIVERSIDAD DE LA LAGUNA	30/06/2017 15:21:31
JOSE ALBERTO RUBIÑO MARTIN UNIVERSIDAD DE LA LAGUNA	30/06/2017 15:34:17
ERNESTO PEREDA DE PABLO UNIVERSIDAD DE LA LAGUNA	06/07/2017 13:51:19

- Lubin, L. M., & Bahcall, N. A. 1993, ApJ, 415, L17
- Lubin, P. M., Epstein, G. L., & Smoot, G. F. 1983, Physical Review Letters, 50, 616
- Lumsden, S. L., Nichol, R. C., Collins, C. A., & Guzzo, L. 1992, MNRAS, 258, 1
- Lyth, D. H., & Liddle, A. R. 2009, The Primordial Density Perturbation
- Macellari, N., Pierpaoli, E., Dickinson, C., & Vaillancourt, J. E. 2011, MNRAS, 418, 888
- Maino, D., Burigana, C., Górska, K. M., Mandolesi, N., & Bersanelli, M. 2002, A&A, 387, 356
- Majewski, S. R., APOGEE Team, & APOGEE-2 Team. 2016, Astronomische Nachrichten, 337, 863
- Majewski, S. R., Schiavon, R. P., Frinchaboy, P. M., et al. 2015, ArXiv e-prints, arXiv:1509.05420
- Martínez, V. J., & Saar, E. 2002, Statistics of the Galaxy Distribution (Chapman &)
- Martizzi, D., Mohammed, I., Teyssier, R., & Moore, B. 2014, MNRAS, 440, 2290
- Masi, S. 2002, Progress in Particle and Nuclear Physics, 48, 243
- Massey, R., Kitching, T., & Richard, J. 2010, Reports on Progress in Physics, 73, 086901
- Mather, J. C., Cheng, E. S., Eplee, Jr., R. E., et al. 1990, ApJ, 354, L37
- Mather, J. C., Cheng, E. S., Cottingham, D. A., et al. 1994, ApJ, 420, 439
- Mazzotta, P., Rasia, E., Moscardini, L., & Tormen, G. 2004, MNRAS, 354, 10
- Meeus, J. 1998, Astronomical algorithms
- Mehrtens, N., Romer, A. K., Hilton, M., et al. 2012, MNRAS, 423, 1024
- Melin, J.-B., Bartlett, J. G., & Delabrouille, J. 2006, A&A, 459, 341
- Melin, J.-B., Bonaldi, A., Remazeilles, M., et al. 2017, ArXiv e-prints, arXiv:1703.10456

Este documento incorpora firma electrónica, y es copia auténtica de un documento electrónico archivado por la ULL según la Ley 39/2015.
Su autenticidad puede ser contrastada en la siguiente dirección <https://sede.ull.es/validacion/>

Identificador del documento: 973742

Código de verificación: Jfg6xBh0

Fecha: 30/06/2017 15:10:10

Firmado por: DENIS TRAMONTE
UNIVERSIDAD DE LA LAGUNA

RAFAEL DELFIN BARRENA DELGADO
UNIVERSIDAD DE LA LAGUNA

JOSE ALBERTO RUBIÑO MARTIN
UNIVERSIDAD DE LA LAGUNA

ERNESTO PEREDA DE PABLO
UNIVERSIDAD DE LA LAGUNA

30/06/2017 15:21:31

30/06/2017 15:34:17

06/07/2017 13:51:19

- Metropolis, N., Rosenbluth, A. W., Rosenbluth, M. N., Teller, A. H., & Teller, E. 1953, J. Chem. Phys., 21, 1087
- Mezger, P. G., Schraml, J., & Terzian, Y. 1967, ApJ, 150, 807
- Mitra, D., Green, D. A., & Rao, A. P. 2014, in IAU Symposium, Vol. 296, Supernova Environmental Impacts, ed. A. Ray & R. A. McCray, 376–377
- Mo, H. J., & White, S. D. M. 1996, MNRAS, 282, 347
- Mueller, E.-M., de Bernardis, F., Bean, R., & Niemack, M. D. 2015, ApJ, 808, 47
- Mufson, S. L., & Liszt, H. S. 1979, ApJ, 232, 451
- Musso, M., Paranjape, A., & Sheth, R. K. 2012, MNRAS, 427, 3145
- Naess, S., Hasselfield, M., McMahon, J., et al. 2014, JCAP, 10, 007
- Nagai, D., Kravtsov, A. V., & Vikhlinin, A. 2007, ApJ, 668, 1
- Navarro, J. F., Frenk, C. S., & White, S. D. M. 1997, ApJ, 490, 493
- Nelder, J. A., & Mead, R. 1965, Computer Journal, 7, 308
- Newcomb, S. 1895, AJ, 15, 185
- Neyrinck, M. C., Aragón-Calvo, M. A., Jeong, D., & Wang, X. 2014, MNRAS, 441, 646
- Olbert, C. M., Clearfield, C. R., Williams, N. E., Keohane, J. W., & Frail, D. A. 2001, ApJ, 554, L205
- Osterbrock, D. E., & Ferland, G. J. 2006, Astrophysics of gaseous nebulae and active galactic nuclei
- Ostriker, J. P., & Vishniac, E. T. 1986, ApJ, 306, L51
- Pacaud, F., Pierre, M., Adami, C., et al. 2007, MNRAS, 382, 1289
- Padin, S., Cartwright, J. K., Mason, B. S., et al. 2001, ApJ, 549, L1
- Padmanabhan, T. 1993, Structure Formation in the Universe, 499
- Paranjape, A., Lam, T. Y., & Sheth, R. K. 2012, MNRAS, 420, 1648
- Patiri, S. G., Betancort-Rijo, J., & Prada, F. 2006, MNRAS, 368, 1132

Este documento incorpora firma electrónica, y es copia auténtica de un documento electrónico archivado por la ULL según la Ley 39/2015.
Su autenticidad puede ser contrastada en la siguiente dirección <https://sede.ull.es/validacion/>

Identificador del documento: 973742

Código de verificación: Jfg6xBh0

Fecha: 30/06/2017 15:10:10

Firmado por: DENIS TRAMONTE
 UNIVERSIDAD DE LA LAGUNA

RAFAEL DELFIN BARRENA DELGADO
 UNIVERSIDAD DE LA LAGUNA

JOSE ALBERTO RUBIÑO MARTIN
 UNIVERSIDAD DE LA LAGUNA

ERNESTO PEREDA DE PABLO
 UNIVERSIDAD DE LA LAGUNA

30/06/2017 15:21:31

30/06/2017 15:34:17

06/07/2017 13:51:19

- Peacock, J. A. 1999, Cosmological Physics, 704
- Peacock, J. A., & Dodds, S. J. 1994, MNRAS, 267, 1020
- Peebles, P. J., & Ratra, B. 2003, Reviews of Modern Physics, 75, 559
- Peebles, P. J. E. 1980, The large-scale structure of the universe
—. 1982, ApJ, 263, L1
—. 1993, Principles of Physical Cosmology
- Penzias, A. A., & Wilson, R. W. 1965, ApJ, 142, 419
- Percival, W. J. 2013, ArXiv e-prints, arXiv:1312.5490
- Pérez-de-Taoro, M. R., Aguiar-González, M., Génova-Santos, R., et al. 2014,
in Proc. SPIE, Vol. 9145, Ground-based and Airborne Telescopes V, 91454T
- Pérez-de-Taoro, M. R., Aguiar-González, M., Cárdenas-Castellano, J., et al. 2016,
in Proc. SPIE, Vol. 9906, Ground-based and Airborne Telescopes VI, 99061K
- Perlmutter, S., Aldering, G., Goldhaber, G., et al. 1999, ApJ, 517, 565
- Persic, M., Salucci, P., & Stel, F. 1996, MNRAS, 281, 27
- Petre, R., Szymkowiak, A. E., Seward, F. D., & Willingale, R. 1988, ApJ, 335,
215
- Phillips, P. R. 1995, ApJ, 455, 419
- Planck Collaboration, Ade, P. A. R., Aghanim, N., et al. 2011a, A&A, 536, A1
- Planck Collaboration, Aghanim, N., Arnaud, M., et al. 2011b, A&A, 536, A9
- Planck Collaboration, Ade, P. A. R., Aghanim, N., et al. 2011c, A&A, 536, A7
—. 2011d, A&A, 536, A18
—. 2011e, A&A, 536, A22
—. 2011f, A&A, 536, A23
- Planck Collaboration, AMI Collaboration, Ade, P. A. R., et al. 2013, A&A,
550, A128
- Planck Collaboration, Aghanim, N., Armitage-Caplan, C., et al. 2014a, A&A,
571, A2

Este documento incorpora firma electrónica, y es copia auténtica de un documento electrónico archivado por la ULL según la Ley 39/2015.
Su autenticidad puede ser contrastada en la siguiente dirección <https://sede.ull.es/validacion/>

Identificador del documento: 973742

Código de verificación: Jfg6xBh0

Fecha: 30/06/2017 15:10:10

Firmado por: DENIS TRAMONTE UNIVERSIDAD DE LA LAGUNA	30/06/2017 15:21:31
RAFAEL DELFIN BARRENA DELGADO UNIVERSIDAD DE LA LAGUNA	30/06/2017 15:34:17
JOSE ALBERTO RUBÍÑO MARTÍN UNIVERSIDAD DE LA LAGUNA	06/07/2017 13:51:19
ERNESTO PEREDA DE PABLO UNIVERSIDAD DE LA LAGUNA	

- Planck Collaboration, Ade, P. A. R., Aghanim, N., et al. 2014b, A&A, 571, A6
- Planck Collaboration, Abergel, A., Ade, P. A. R., et al. 2014c, A&A, 571, A11
- Planck Collaboration, Ade, P. A. R., Aghanim, N., et al. 2014d, A&A, 571, A12
- . 2014e, A&A, 571, A14
- . 2014f, A&A, 571, A16
- . 2014g, A&A, 571, A20
- . 2014h, A&A, 571, A21
- . 2014i, A&A, 571, A29
- . 2014j, A&A, 571, A28
- . 2015a, A&A, 581, A14
- . 2015b, A&A, 576, A104
- . 2015c, A&A, 582, A29
- Planck Collaboration, Adam, R., Ade, P. A. R., et al. 2016a, A&A, 594, A1
- Planck Collaboration, Ade, P. A. R., Aghanim, N., et al. 2016b, A&A, 594, A2
- Planck Collaboration, Adam, R., Ade, P. A. R., et al. 2016c, A&A, 594, A7
- . 2016d, A&A, 594, A8
- Planck Collaboration, Ade, P. A. R., Aghanim, N., et al. 2016e, A&A, 594, A13
- . 2016f, A&A, 594, A17
- . 2016g, A&A, 594, A20
- Planck Collaboration, Aghanim, N., Arnaud, M., et al. 2016h, A&A, 594, A22
- Planck Collaboration, Ade, P. A. R., Aghanim, N., et al. 2016i, A&A, 594, A24
- . 2016j, A&A, 594, A25
- . 2016k, A&A, 594, A27

Este documento incorpora firma electrónica, y es copia auténtica de un documento electrónico archivado por la ULL según la Ley 39/2015.
Su autenticidad puede ser contrastada en la siguiente dirección <https://sede.ull.es/validacion/>

Identificador del documento: 973742

Código de verificación: Jfg6xBh0

Fecha: 30/06/2017 15:10:10

Firmado por: DENIS TRAMONTE
UNIVERSIDAD DE LA LAGUNA

RAFAEL DELFIN BARRENA DELGADO
UNIVERSIDAD DE LA LAGUNA

JOSE ALBERTO RUBIÑO MARTIN
UNIVERSIDAD DE LA LAGUNA

ERNESTO PEREDA DE PABLO
UNIVERSIDAD DE LA LAGUNA

30/06/2017 15:21:31

30/06/2017 15:34:17

06/07/2017 13:51:19

- . 2016l, A&A, 586, A139
- . 2016m, A&A, 586, A140
- Press, W. H., & Schechter, P. 1974, (PS74), ApJ, 187, 425
- Pye, J. P., Becker, R. H., Seward, F. D., & Thomas, N. 1984, MNRAS, 207, 649
- QUIET Collaboration, Bischoff, C., Brizius, A., et al. 2011, ApJ, 741, 111
- QUIET Collaboration, Araujo, D., Bischoff, C., et al. 2012, ApJ, 760, 145
- Rabii, B., Winant, C. D., Collins, J. S., et al. 2006, Review of Scientific Instruments, 77, 071101
- Rebolo, R., Gutiérrez, C. M., Watson, R. A., & Gallegos, J. 2000, Astrophysical Letters and Communications, 37, 293
- Rebolo, R., Battye, R. A., Carreira, P., et al. 2004, MNRAS, 353, 747
- Reed, D. S., Bower, R., Frenk, C. S., Jenkins, A., & Theuns, T. 2007, MNRAS, 374, 2
- Rees, M. J., & Sciama, D. W. 1968, Nature, 217, 511
- Reese, E. 2000, in Bulletin of the American Astronomical Society, Vol. 32, American Astronomical Society Meeting Abstracts, 1605
- Refregier, A. 1999, in Astronomical Society of the Pacific Conference Series, Vol. 181, Microwave Foregrounds, ed. A. de Oliveira-Costa & M. Tegmark, 219
- Reich, P., & Reich, W. 1986, A&AS, 63, 205
- Reichardt, C. L., Ade, P. A. R., Bock, J. J., et al. 2009, ApJ, 694, 1200
- Reichardt, C. L., Stalder, B., Bleem, L. E., et al. 2013, ApJ, 763, 127
- Reiprich, T. H., & Böhringer, H. 2002, ApJ, 567, 716
- Remazeilles, M., Delabrouille, J., & Cardoso, J.-F. 2011, MNRAS, 410, 2481
- Riess, A. G., Filippenko, A. V., Challis, P., et al. 1998, AJ, 116, 1009
- Riess, A. G., Macri, L., Casertano, S., et al. 2011, ApJ, 730, 119

Este documento incorpora firma electrónica, y es copia auténtica de un documento electrónico archivado por la ULL según la Ley 39/2015.
Su autenticidad puede ser contrastada en la siguiente dirección <https://sede.ull.es/validacion/>

Identificador del documento: 973742

Código de verificación: Jfg6xBh0

Fecha: 30/06/2017 15:10:10

Firmado por: DENIS TRAMONTE
UNIVERSIDAD DE LA LAGUNA

RAFAEL DELFIN BARRENA DELGADO
UNIVERSIDAD DE LA LAGUNA

JOSE ALBERTO RUBIÑO MARTIN
UNIVERSIDAD DE LA LAGUNA

ERNESTO PEREDA DE PABLO
UNIVERSIDAD DE LA LAGUNA

30/06/2017 15:21:31

30/06/2017 15:34:17

06/07/2017 13:51:19

- Rockosi, C. M. 2012, in American Astronomical Society Meeting Abstracts, Vol. 219, American Astronomical Society Meeting Abstracts #219, 205.01
- Rosati, P., Della Ceca, R., Norman, C., & Giacconi, R. 1998, ApJ, 492, L21
- Rubiño-Martín, J. A., Betancort-Rijo, J., & Patiri, S. G. 2008, (RBP08), MNRAS, 386, 2181
- Rubiño-Martín, J. A., López-Caraballo, C. H., Génova-Santos, R., & Rebolo, R. 2012a, Advances in Astronomy, 2012, 351836
- Rubiño-Martín, J. A., & Sunyaev, R. A. 2003, MNRAS, 344, 1155
- Rubiño-Martín, J. A., Rebolo, R., Aguiar, M., et al. 2012b, in Proc. SPIE, Vol. 8444, Ground-based and Airborne Telescopes IV, 84442Y
- Rubiño-Martín, J. A., Génova-Santos, R., Rebolo, R., et al. 2017, in Highlights on Spanish Astrophysics IX, ed. S. Arribas, A. Alonso-Herrero, F. Figueras, C. Hernández-Monteagudo, A. Sánchez-Lavega, & S. Pérez-Hoyos, 99–107
- Rubin, V. C., Ford, Jr., W. K., & Thonnard, N. 1980, ApJ, 238, 471
- Rubiño-Martín, J., Rebolo, R., & Mediavilla, E. 2009, The Cosmic Microwave Background: From Quantum Fluctuations to the Present Universe, Canary Islands Winter School of Astrophysics (Cambridge University Press)
- Rykoff, E. S., Rozo, E., Busha, M. T., et al. 2014, ApJ, 785, 104
- Sachs, R. K., & Wolfe, A. M. 1967, ApJ, 147, 73
- Sadler, E. M., Ricci, R., Ekers, R. D., et al. 2006, MNRAS, 371, 898
- Sánchez, A. G., Kazin, E. A., Beutler, F., et al. 2013, MNRAS, 433, 1202
- Sanquirce-García, R., Sainz-Pardo, I., Etxeita-Arriaga, B., et al. 2016, in Proc. SPIE, Vol. 9906, Ground-based and Airborne Telescopes VI, 99064N
- Sarazin, C. L. 1988, X-ray emission from clusters of galaxies
- Sato, M., Reid, M. J., Brunthaler, A., & Menten, K. M. 2010, ApJ, 720, 1055
- Saunders, W., Rowan-Robinson, M., Lawrence, A., et al. 1990, MNRAS, 242, 318
- Saunders, W., Sutherland, W. J., Maddox, S. J., et al. 2000, MNRAS, 317, 55

Este documento incorpora firma electrónica, y es copia auténtica de un documento electrónico archivado por la ULL según la Ley 39/2015.
Su autenticidad puede ser contrastada en la siguiente dirección <https://sede.ull.es/validacion/>

Identificador del documento: 973742

Código de verificación: Jfg6xBh0

Fecha: 30/06/2017 15:10:10

Firmado por: DENIS TRAMONTE
UNIVERSIDAD DE LA LAGUNA

RAFAEL DELFIN BARRENA DELGADO
UNIVERSIDAD DE LA LAGUNA

JOSE ALBERTO RUBIÑO MARTÍN
UNIVERSIDAD DE LA LAGUNA

ERNESTO PEREDA DE PABLO
UNIVERSIDAD DE LA LAGUNA

30/06/2017 15:21:31

30/06/2017 15:34:17

06/07/2017 13:51:19

- Schechter, P. 1976, ApJ, 203, 297
- Schlegel, D. J., Finkbeiner, D. P., & Davis, M. 1998, ApJ, 500, 525
- Schmidt, R. W., Allen, S. W., & Fabian, A. C. 2004, MNRAS, 352, 1413
- Scott, D., & Smoot, G. 2006, ArXiv Astrophysics e-prints, astro-ph/0601307
- Seljak, U., & Zaldarriaga, M. 1997, Physical Review Letters, 78, 2054
- Shane, C. D. 1956, Vistas in Astronomy, 2, 1574
- Shaw, L. D., Nagai, D., Bhattacharya, S., & Lau, E. T. 2010, ApJ, 725, 1452
- Shectman, S. A., Landy, S. D., Oemler, A., et al. 1996, ApJ, 470, 172
- Sherwin, B. D., Dunkley, J., Das, S., et al. 2011, Physical Review Letters, 107, 021302
- Sheth, R. K., & Lemson, G. 1999, MNRAS, 304, 767
- Sheth, R. K., Mo, H. J., & Tormen, G. 2001, MNRAS, 323, 1
- Sheth, R. K., & Tormen, G. 1999, (ST99), MNRAS, 308, 119
—. 2002, MNRAS, 329, 61
- Sheth, R. K., & van de Weygaert, R. 2004, MNRAS, 350, 517
- Sievers, J. L., Hlozek, R. A., Nolta, M. R., et al. 2013, JCAP, 10, 060
- Silk, J. 1968, ApJ, 151, 459
- Simon, R., Jackson, J. M., Clemens, D. P., Bania, T. M., & Heyer, M. H. 2001, ApJ, 551, 747
- Smoot, G. F. 1998, ArXiv Astrophysics e-prints, astro-ph/9801121
- Smoot, G. F., Bennett, C. L., Kogut, A., et al. 1992, ApJ, 396, L1
- Spiegel, D. N., Verde, L., Peiris, H. V., et al. 2003, The Astrophysical Journal Supplement Series, 148, 175
- Springel, V., White, S. D. M., Tormen, G., & Kauffmann, G. 2001, MNRAS, 328, 726
- Springel, V., White, S. D. M., Jenkins, A., et al. 2005, Nature, 435, 629

Este documento incorpora firma electrónica, y es copia auténtica de un documento electrónico archivado por la ULL según la Ley 39/2015.
Su autenticidad puede ser contrastada en la siguiente dirección <https://sede.ull.es/validacion/>

Identificador del documento: 973742

Código de verificación: Jfg6xBh0

Fecha: 30/06/2017 15:10:10

Firmado por: DENIS TRAMONTE UNIVERSIDAD DE LA LAGUNA	30/06/2017 15:21:31
RAFAEL DELFIN BARRENA DELGADO UNIVERSIDAD DE LA LAGUNA	30/06/2017 15:34:17
JOSE ALBERTO RUBIÑO MARTIN UNIVERSIDAD DE LA LAGUNA	06/07/2017 13:51:19
ERNESTO PEREDA DE PABLO UNIVERSIDAD DE LA LAGUNA	

- Steigman, G. 2004, Measuring and Modeling the Universe, 169
- . 2008, ArXiv e-prints, arXiv:0807.3004
- Stompor, R., Hanany, S., Abroe, M. E., et al. 2003, ArXiv Astrophysics e-prints, astro-ph/0309409
- Story, K. T., Reichardt, C. L., Hou, Z., et al. 2013, ApJ, 779, 86
- Strauss, M. A., & Willick, J. A. 1995, Phys. Rep., 261, 271
- Sunyaev, R. A., & Zeldovich, Y. B. 1970, Ap&SS, 7, 3
- . 1972, Comments on Astrophysics and Space Physics, 4, 173
- Takey, A., Schwope, A., & Lammer, G. 2011, A&A, 534, A120
- The COrE Collaboration, Armitage-Caplan, C., Avillez, M., et al. 2011, ArXiv e-prints, arXiv:1102.2181
- The Polarbear Collaboration: P. A. R. Ade, Akiba, Y., Anthony, A. E., et al. 2014, ApJ, 794, 171
- Tinker, J., Kravtsov, A. V., Klypin, A., et al. 2008, (T08), ApJ, 688, 709
- Tormen, G. 1998, MNRAS, 297, 648
- Torres, D. F., Romero, G. E., Dame, T. M., Combi, J. A., & Butt, Y. M. 2003, Phys. Rep., 382, 303
- Tramonte, D., Rubiño-Martín, J. A., Betancort-Rijo, J., & Dalla Vecchia, C. 2017, MNRAS, 467, 3424
- Tramonte, D., Rubiño-Martín, J. A., & Génova-Santos, R.T. in prep.
- Vaillancourt, J. E. 2006, PASP, 118, 1340
- van Engelen, A., Sherwin, B. D., Sehgal, N., et al. 2015, ApJ, 808, 7
- Velliscig, M., van Daalen, M. P., Schaye, J., et al. 2014, MNRAS, 442, 2641
- Vikhlinin, A., Kravtsov, A. V., Burenin, R. A., et al. 2009, ApJ, 692, 1060
- Voges, W., Aschenbach, B., Boller, T., et al. 1999, A&A, 349, 389
- Voit, G. M. 2005, Reviews of Modern Physics, 77, 207

Este documento incorpora firma electrónica, y es copia auténtica de un documento electrónico archivado por la ULL según la Ley 39/2015.
Su autenticidad puede ser contrastada en la siguiente dirección <https://sede.ull.es/validacion/>

Identificador del documento:	973742	Código de verificación:	Jfg6xBh0
Firmado por:	DENIS TRAMONTE UNIVERSIDAD DE LA LAGUNA	Fecha:	30/06/2017 15:10:10
	RAFAEL DELFIN BARRENA DELGADO UNIVERSIDAD DE LA LAGUNA		30/06/2017 15:21:31
	JOSE ALBERTO RUBIÑO MARTIN UNIVERSIDAD DE LA LAGUNA		30/06/2017 15:34:17
	ERNESTO PEREDA DE PABLO UNIVERSIDAD DE LA LAGUNA		06/07/2017 13:51:19

- Wallace, P. T. 1994, Starlink User Note, 100
- Wallace, P. T. 2008, in Proc. SPIE, Vol. 7019, Advanced Software and Control for Astronomy II, 701908
- Warren, M. S., Abazajian, K., Holz, D. E., & Teodoro, L. 2006, (W06), ApJ, 646, 881
- Watson, R. A., Rebolo, R., Rubiño-Martín, J. A., et al. 2005, ApJ, 624, L89
- Watson, W. A., Iliev, I. T., D'Aloisio, A., et al. 2013, MNRAS, 433, 1230
- Weiland, J. L., Odegard, N., Hill, R. S., et al. 2011, ApJS, 192, 19
- Weinberg, S. 1972, Gravitation and Cosmology: Principles and Applications of the General Theory of Relativity, 688
- Wen, Z. L., Han, J. L., & Liu, F. S. 2012, ApJS, 199, 34
- White, M., Scott, D., & Silk, J. 1994, ARA&A, 32, 319
- Wilson, T. L., Rohlfs, K., & Hüttemeister, S. 2009, Tools of Radio Astronomy (Springer-Verlag), doi:10.1007/978-3-540-85122-6
- Wright, E. L., & Reese, E. D. 2000, ApJ, 545, 43
- Wright, E. L., Eisenhardt, P. R. M., Mainzer, A. K., et al. 2010, AJ, 140, 1868
- Wu, S.-W., Bik, A., Bestenlehner, J. M., et al. 2016, A&A, 589, A16
- Xue, Y.-J., & Wu, X.-P. 2000, ApJ, 538, 65
- Yanny, B., Rockosi, C., Newberg, H. J., et al. 2009, AJ, 137, 4377
- York, D. G., Adelman, J., Anderson, Jr., J. E., et al. 2000a, AJ, 120, 1579
- . 2000b, AJ, 120, 1579
- Zacchei, A., Maino, D., Baccigalupi, C., et al. 2011, A&A, 536, A5
- Zaldarriaga, M. 1998, ApJ, 503, 1
- Zaldarriaga, M., & Seljak, U. 1997, Phys. Rev. D, 55, 1830
- Zaroubi, S. 2013, in Astrophysics and Space Science Library, Vol. 396, The First Galaxies, ed. T. Wiklind, B. Mobasher, & V. Bromm, 45

Este documento incorpora firma electrónica, y es copia auténtica de un documento electrónico archivado por la ULL según la Ley 39/2015.
Su autenticidad puede ser contrastada en la siguiente dirección <https://sede.ull.es/validacion/>

Identificador del documento: 973742

Código de verificación: Jfg6xBh0

Fecha: 30/06/2017 15:10:10

Firmado por: DENIS TRAMONTE UNIVERSIDAD DE LA LAGUNA	30/06/2017 15:21:31
RAFAEL DELFIN BARRENA DELGADO UNIVERSIDAD DE LA LAGUNA	30/06/2017 15:34:17
JOSE ALBERTO RUBIÑO MARTIN UNIVERSIDAD DE LA LAGUNA	06/07/2017 13:51:19
ERNESTO PEREDA DE PABLO UNIVERSIDAD DE LA LAGUNA	

Zeldovich, Y. B. 1972, MNRAS, 160, 1P

Zonca, A., Williams, B., Meinholt, P., & Lubin, P. 2013, Astronomy and Computing, 3, 13

Este documento incorpora firma electrónica, y es copia auténtica de un documento electrónico archivado por la ULL según la Ley 39/2015.
Su autenticidad puede ser contrastada en la siguiente dirección <https://sede.ull.es/validacion/>

Identificador del documento: 973742

Código de verificación: Jfg6xBh0

Firmado por: DENIS TRAMONTE
UNIVERSIDAD DE LA LAGUNA

Fecha: 30/06/2017 15:10:10

RAFAEL DELFIN BARRENA DELGADO
UNIVERSIDAD DE LA LAGUNA

30/06/2017 15:21:31

JOSE ALBERTO RUBIÑO MARTIN
UNIVERSIDAD DE LA LAGUNA

30/06/2017 15:34:17

ERNESTO PEREDA DE PABLO
UNIVERSIDAD DE LA LAGUNA

06/07/2017 13:51:19